Mechanics of Unsaturated Geomaterials

This book is dedicated to the memory of our dear colleague,
Dr. Olivier Coussy, who tragically passed away
while working on a chapter for this book

Mechanics of Unsaturated Geomaterials

Edited by
Lyesse Laloui

ISTE WILEY

First published 2010 in Great Britain and the United States by ISTE Ltd and John Wiley & Sons, Inc.

ISTE Ltd
27-37 St George's Road
London SW19 4EU
UK

www.iste.co.uk

John Wiley & Sons, Inc.
111 River Street
Hoboken, NJ 07030
USA

www.wiley.com

Library of Congress Cataloging-in-Publication Data

Mechanics of unsaturated geomaterials / edited by Lyesse Laloui.
p. cm.
Includes bibliographical references and index.
ISBN 978-1-84821-266-4
1. Soil mechanics. 2. Soil moisture. 3. Soil permeability. I. Laloui, Lyesse.
TA710.U684 2010
624.1'5136--dc22

2010015718

British Library Cataloguing-in-Publication Data
A CIP record for this book is available from the British Library
ISBN 978-1-84821-266-4

Printed and bound in Great Britain by CPI Antony Rowe, Chippenham and Eastbourne.

Table of Contents

Preface

An understanding of the mechanics of unsaturated geomaterials has become an important component of the background for a geo-engineer operating in various fields of geomechanics.

Several geotechnical operations, such as compaction and excavation processes, are linked to the mechanics of unsaturated geomaterials. As more than one-third of the Earth's surface is arid or semi-arid, in addition to the less extreme cases of seasonal droughts and diurnal variations of the water table in soils, it is obvious that most soils and rocks are in a general state of partial water saturation. In other words, the pore space within geomaterials (e.g. soil, rock, and concrete) is generally filled with water and air. It means that the mechanics and physics of the considered material are those of a three-phase material: solid mineral and two immiscible fluid phases.

Even though most natural and engineered geomaterials are only partially saturated with water, a persistent assumption made in geomechanics and geotechnical engineering over the past decades has been the assumption of complete saturation. The study of the mechanics of unsaturated geomaterials was initiated approximately 50 years ago as a natural extension of the knowledge developed in the conventional areas of the mechanics of (saturated) soils and rocks. The mechanics of saturated geomaterials is primarily based on the concept of effective stress and on the consolidation theory. In the hydromechanical frameworks for saturated materials that have been developed, the pore fluid (water) pressure mainly contributes to the mechanical behavior through the field equations (consolidation theory). Its contribution to the constitutive behavior of the solid skeleton is considered

"neutral" (no effect of the pore fluid pressure on the effective material compressibility or strength, for instance). When this particular assumption about materials saturated with a fluid under compression was no longer considered valid, the conventional theories needed to be revised. This was the first major development in defining the mechanics of unsaturated materials. The field equations were found to need an extension to address the effect of the degree of saturation on water permeability and compressibility; the gas flow also had to be considered in some situations. The solid skeleton constitutive behavior must incorporate the effect of the gas pressure, or more specifically, its difference with respect to the liquid pressure, known as suction. In addition, the extension of the effective stress concept to the unsaturated conditions revealed a need to take into account the important contribution of the water retention behavior, linking the degree of saturation to suction.

In the past decade, the advancement of knowledge regarding the mechanics of unsaturated geomaterials has been significant. Some fundamental issues were solved, and important achievements were made in certain areas, including application of the effective stress concept and measurement of volume variations. The multiphysical interactions were then extended to non-isothermal conditions. This spectacular progress in the field also included engineering applications. In many cases, new tools were developed and advanced analysis became possible.

The objective of this book is to supply the reader with an exhaustive overview on new trends in the field of the mechanics of unsaturated geomaterials, starting from the basic issues and covering the most recent theories and applications (i.e. natural disasters and nuclear waste disposal). The presentation of the fundamental concepts is based on an interdisciplinary approach and includes chapters on the topics of soil-, rock-, and cement-based mechanics.

The book begins with the introduction of several fundamental notions concerning the mechanics of unsaturated materials. Basic concepts about the state of water in soils are presented in Chapter 1, and Chapter 2 introduces the concepts of mechanics in unsaturated geomaterials. Chapter 3 reviews the phenomenon of soil cracking during soil desaturation. Part II of the book is devoted to experimental techniques that allow testing of soils and rocks in unsaturated conditions. Chapter 4 reviews the techniques for controlling and measuring suction and presents mechanical testing devices.

The characterization of highly overconsolidated clayey unsaturated materials is presented in Chapter 5. Field measurement techniques (of suction, water content, and water permeability) are presented in Chapter 6. In Part III of the book, the main theoretical concepts are established. The numerical treatment of the field equations is emphasized, with special attention devoted to the analysis of the strain localization in coupled transient phenomena. The conservation laws in unsaturated porous materials are discussed in Chapter 7, while the hydromechanical coupling theory and its numerical integration methods are presented in Chapter 8. Strain localization in coupled transient phenomena is the topic of Chapter 9. Part IV of the book presents engineering applications that show the importance of the mechanics of unsaturated geomaterials in many fields of practical interest. Numerical modeling of landslides is investigated in Chapter 10. Moisture transport and pore pressure generation in nearly saturated geomaterials are the main topics of Chapter 11. Chapter 12 deals with application to nuclear waste storage. Chapter 13 reviews experimental results and modeling of soil–pipeline interactions. The engineering behaviors of different unsaturated zones are described in Chapter 14, where the modeling of consolidation and swelling in fine soils is also considered. River embankments are geomechanically analyzed in Chapter 15.

This book was written for postgraduate students, researchers and practitioners in the fields where unsaturated conditions play a fundamental role, such as soil mechanics, soil physics, rock mechanics, petroleum engineering, hydrology, and nuclear waste engineering.

I would like to express my appreciation to all of my colleagues who chose to contribute to this book. Special thanks are due to Prof. Tomasz Hueckel and Prof. Félix Darve for their encouragement, which made the book possible. My thanks are also directed to the Alert Geomaterials network that supported this initiative.

Lyesse LALOUI
June 2010

PART I

Fundamental Concepts

Chapter 1

Basic Concepts in the Mechanics and Hydraulics of Unsaturated Geomaterials

Unsaturated geomaterials are geomaterials with void spaces partially filled with liquid and partially with gas. The liquid (wetting) phase is an aqueous solution, generically referred to as *water*, whereas, the gaseous (non-wetting) phase is a mixture of air and water vapor, generically referred to as *air*. The mutual interaction between these two phases and their interaction with the solid phase plays a key role in the mechanical and hydraulic response of unsaturated geomaterials. The basic mechanisms and thermodynamics of the interaction between the liquid, gaseous, and solid phases are not commonly covered in undergraduate and graduate courses. As a result, students and engineers with geotechnical background may find it difficult to approach the mechanics and hydraulics of unsaturated soils. The purpose of this chapter is to fill this gap and to illustrate the basic elementary mechanisms behind water retention, water flow, and mechanical behavior of unsaturated geomaterials. Special emphasis has been given to capillary mechanisms arising from surface tension at the air–water interface and from the angle formed by the air–water interface at the solid–liquid–gas junction (contact angle). Capillary actions play a major role in the response of unsaturated geomaterials and can conveniently serve as a basis to introduce the most distinctive features of the hydraulic and mechanical response of unsaturated geomaterials.

Chapter written by Alessandro TARANTINO.

1.1. Water retention mechanisms in capillary systems

1.1.1. *Surface tension, contact angle, and water tension*

Liquid surfaces act as if they are in tension as a result of an imbalance between intermolecular attractions at a surface. In bulk liquid, the forces acting on a molecule are effectively equal in all directions and the molecule feels no net force. As a molecule moves to the surface, it loses some nearest neighbors, thus leaving it with unbalanced attractive forces with a downward resultant force (Figure 1.1(a)). For a molecule to stay in the surface region, it must gain excess energy (and entropy) over those in the bulk liquid. This excess energy (surface free energy) is the surface tension and causes the surface to act like a membrane in tension. When in contact with a solid surface, the interface will curve near that surface to form a *meniscus*. If adhesive forces between solid and liquid prevail on cohesive forces in the liquid, the interface will curve up and will form an angle lower than 90° with the solid surface (Figure 1.1(b)). Contact angles, which are measured *through* the liquid, lower than 90° are typical for soil water on soil minerals.

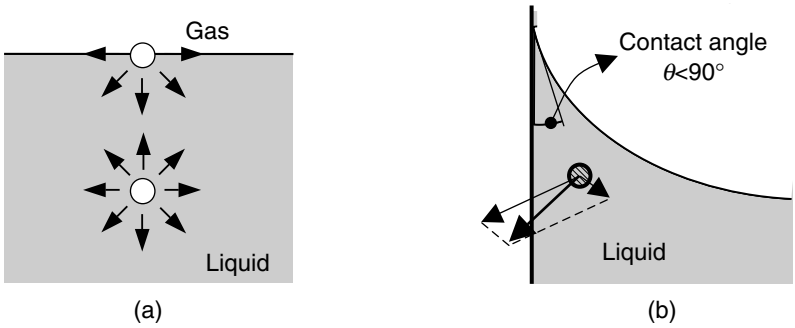

Figure 1.1. *(a) Development of surface tension at the gas–liquid interface and (b) curvature of the gas–liquid interface in proximity of a solid surface*

Menisci concave on the air side generate water pressures lower than the air pressure. Let us consider a meniscus in a capillary tube of diameter d (Figure 1.2). The water pressure at the back of the meniscus can be calculated by considering the vertical force equilibrium of the air–water interface:

$$u_{\mathrm{w}} - u_{\mathrm{a}} = -\frac{4T\cos\theta}{d} = -\frac{2T}{R}, \qquad [1.1]$$

where u_{w} is the water pressure at the back of the meniscus, u_{a} the air pressure, T the surface tension, θ the contact angle, and R the radius of curvature of the interface. If the contact angle is lower than 90°, the gauge water pressure u_{w}–u_{a} becomes negative.

Using equation [1.1], it is instructive to calculate the gauge and the absolute water pressure for capillary tubes having diameters of the same order of magnitude as the size of pores in clay, silt, and sand. For the sake of simplicity, let us assume that pore size is about 1/10 of the grain size and contact angle is $\theta = 0$. As shown in Table 1.1, if the pore size is sufficiently small, as in the case of clays, *absolute* water pressure may be negative. Water can, therefore, be held in tension (i.e. it is being stretched) in unsaturated geomaterials.

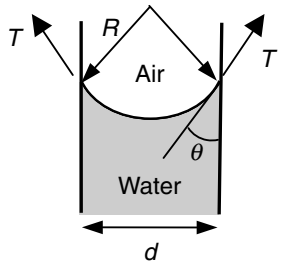

Figure 1.2. *Negative water pressure generated by meniscus concave on the air side*

Water can indeed sustain high tensile stresses as recognized earlier by Berthelot [BER 50] and confirmed by several experiments carried out using metal and glass Berthelot-type systems (see [MAR 95]). The magnitude of negative pressure and the duration over which the negative pressure can be sustained is limited by the phase relationships of the pore fluid and the phenomenon of heterogenous cavitation [MAR 08]. Heterogenous cavitation of water typically occurs at negative gauge pressures close to –100 kPa, but this pressure should not be mistaken for the tensile strength of water.

	Sand	**Silt**	**Clay**
d_{grain} (mm)	2	0.075	0.002
d_{pore} (mm)	0.2	0.0075	0.0002
u_w–u_a (kPa)	–1.4	–38	–1440
u_w (kPa)	+98.6	+62	–1340
k_{sat} (m/s)	6×10^{-3}	2×10^{-6}	6×10^{-9}

Table 1.1. *Minimum sustainable gauge and absolute water pressure and hydraulic conductivity in capillary tubes having diameters representative of typical geomaterial pore size ($\theta = 0°$, $T = 0.072$ N/m, $u_a = 100$ kPa, $\eta = 10^{-6}$ m^2/s)*

1.1.2. *Hysteresis of contact angle*

Gibbs [GIB 48] showed that only one stable contact angle exists for a given system of smooth, homogenous, and non-deformable solids. In practice, however, this is rarely, if ever, the situation. If these assumptions are removed, within the framework of classical thermodynamics it can be shown that many different stable angles exist for a given system, i.e. the contact angle shows hysteresis [JOH 69].

The concept of contact angle hysteresis can perhaps be best explained by considering a drop of water placed on a surface. The water drop contact angle attains an equilibrium value θ_c when the surface is horizontal (Figure 1.3(a)). If the surface is progressively tilted, the contact angles at the leading and trailing edge of the drop will increase and decrease, respectively, to prevent the drop periphery from moving. In this way, the tangential component of the drop weight can be equilibrated by the tangential component of the surface tension forces T acting at the drop periphery. This will continue until a limiting condition is attained when these angles become the advancing and receding angles, θ_a and $\theta_{r,}$, respectively, at which point the drop will roll off the plate (Figure 1.3(b)). Thus, a number of macroscopic stable contact angles exist for a given system in the range from θ_r to θ_a. The hysteresis of the contact angle can be produced by surface roughness and surface heterogeneity [JOH 69].

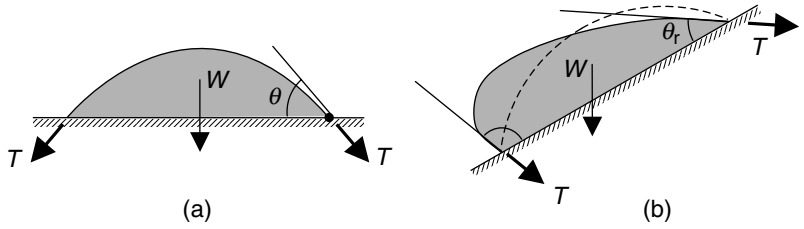

Figure 1.3. *Hysteresis of the contact angle: (a) water drop on horizontal surface and (b) water drop on a tilted surface*

1.1.3. *Evaporation from capillary systems and geomaterials*

Unsaturated geomaterials are found in earth structures and in the upper zone of the ground above the water table. The main mechanisms of desaturation consist of evaporation from the surface and lowering of the water table. These mechanisms can conveniently be illustrated by considering systems of capillary tubes, which mimic the network of capillaries across the pore space in geomaterials. The evaporation of water from a capillary tube is shown in Figure 1.4. At *Stage 1*, let us assume that the air–water interface is flat and that the gauge water pressure is therefore zero in the tube. If evaporation occurs, water is initially removed without displacement of the gas–liquid–solid junction of the meniscus (as occurs to the drop on the tilting plate in Figure 1.3(b)). The meniscus curvature then increases and water pressure in the tube drops to values lower than atmospheric air pressure (*Stage 2*). At *Stage 3*, the water pressure caused by evaporation has decreased to such an extent that the contact angle is equal to the receding angle θ_r, and the negative pressure in the liquid is equal to the maximum negative pressure sustainable by the surface tension force. After this point, which is known as the air-entry pressure, any further evaporation causes a lowering of the water level in the capillary tube with the contact angle remaining equal to the receding angle and the negative water pressure at the meniscus always equal to the minimum sustainable value as governed by equation [1.1]. The relationship between the degree of saturation of the tube (the ratio between the water volume and the volume of the tube) and the water pressure is shown in Figure 1.4. Initially, water pressure decreases with very small decrease in the water volume. As the air-entry pressure is reached, water volume decreases at a constant water pressure.

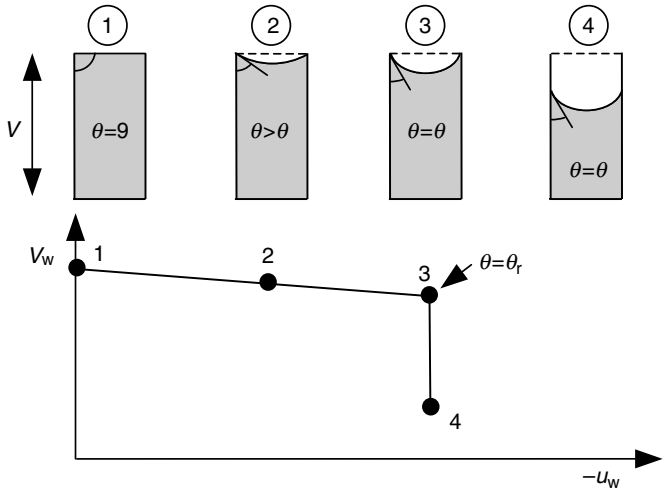

Figure 1.4. *Evaporation from a single capillary tube*

Let us now consider a system formed by three horizontal capillary tubes, A, B and C, respectively, as shown in Figure 1.5. For the sake of simplicity, let us assume that all tubes have the same length (L_A=L_B=L_C), the diameters of the tube are d_A=2d_B and d_B=2d_C, and θ_r=0.

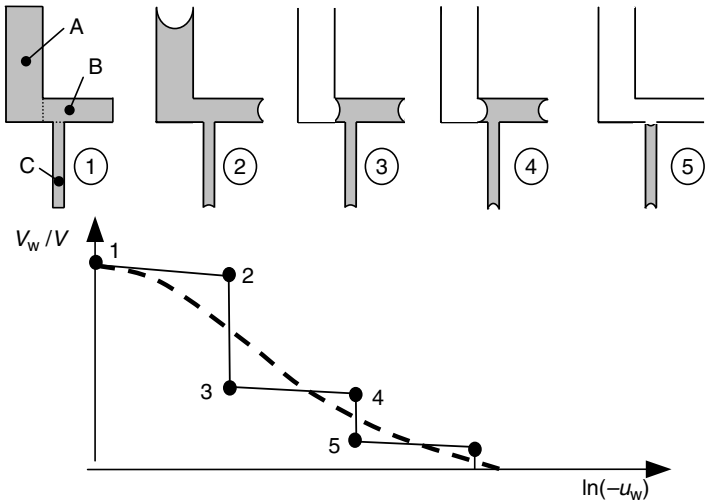

Figure 1.5. *Evaporation from a capillary system*

Initially, pressure is zero in the system and the contact angle is 90° (*Stage 1*). As evaporation occurs, menisci will initially curve without any displacement of the meniscus junction. Since water pressure u_w must be the same at the back of all menisci, equation [1.1] gives:

$$\frac{\cos\theta_A}{d_A} = \frac{\cos\theta_B}{d_B} = \frac{\cos\theta_C}{d_C} \qquad [1.2]$$

Since $d_A > d_B > d_C$, the contact angle will be lower in the larger tube (tube A) and the limit receding angle θ_r will be therefore reached in the larger tube first (*Stage 2*). At this stage, the larger tube will empty at constant pressure, which is the minimum pressure sustainable by the larger tube (*Stage 3*). As evaporation proceeds, the curvature of the menisci in the remaining water-filled tubes will further increase until the limit contact angle is reached in tube B (*Stage 4*). This tube will then empty at constant pressure (*Stage 5*). Further evaporation will eventually empty the smaller tube.

The relationship between the degree of saturation and water pressure in this capillary system is shown in Figure 1.5. If we imagine an infinite number of capillary tubes of different size, we might expect the relationship between the degree of saturation of the capillary system and water pressure to be given by the dashed curve in Figure 1.5.

1.2. Water retention behavior of geomaterials

The relationship between degree of saturation and (negative) water pressure for the capillary system shown in Figure 1.5 is essentially the same as observed experimentally in unsaturated geomaterials and is referred to as *water retention function* or *water retention curve*. This curve reveals the different states of saturation in a soil. If a saturated soil is exposed to evaporation, menisci at the surface will initially curve without any displacement of the meniscus junction (Figure 1.6(a)).

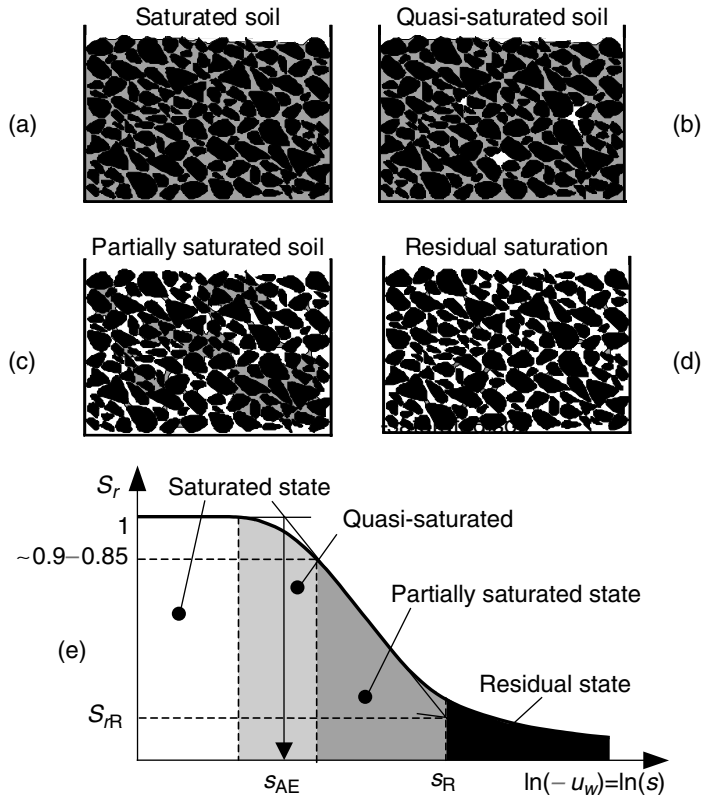

Figure 1.6. *States of saturation*

A negative pressure will be generated in the pore-water with the degree of saturation still remaining equal to 1 (*saturated state* in Figure 1.6(a)). As evaporation proceeds, meniscus curvature at the interface will increase and pore-water pressure will further decrease. The negative pore-water pressure will cause the expansion of air cavities in the larger pores within the soil and the degree of saturation will therefore decrease. However, the air phase is still discontinuous and not in direct contact with the surrounding air (*quasi-saturated state* in Figure 1.6(e)). At the stage where water menisci at the interface reach the limit curvature, menisci will recede into the soil and air will enter the soil. Water and air will both be continuous in the pore space and this state can be referred to as *partially saturated state*. A conventional value for the negative pressure (suction) corresponding to the entry of air into the pore space, s_{AE}, is obtained by intersecting the horizontal line at

degree of saturation equal to 1 with the line tangent to the curve at the inflection point (Figure 1.6(e)). Finally, a state is reached where water remains isolated at the particle contact and is no longer continuous in the pore space (*residual state* in Figure 1.6(e)). Equilibrium is then established through the vapor phase.

The relationship between degree of saturation, S_r, and suction, s, is hysteretic. The water retention behavior of a soil dried from saturated state ("*main drying*") differs from that of a soil wetted from dry state ("*main wetting*") as shown in Figure 1.7(a). The "main drying" and "main wetting" curves mark out the domain of possible attainable states (hysteresis domain). If a saturated soil is dried to an intermediate degree of saturation and is then wetted, the corresponding s–S_r curve scans the hysteresis domain, from the main drying toward the main wetting curve, and is therefore referred to as *scanning curve*. The behavior in the scanning region is often assumed to be reversible, whereas the water retention behavior is irreversible along the main drying and main wetting curves. The main reason for hysteresis is the so-called ink-bottle effect, which refers to the narrow point of contact between large cavities of adjoining pores. Consider the ink-bottle capillary tube connected to a water reservoir as shown in Figure 1.7. If the reservoir is lowered from the top of the tube, the capillary tube will remain saturated because the negative pressure can be sustained by the curvature of the meniscus at the top of the tube (Figure 1.7(b)). However, if the water reservoir is lowered to the bottom of the tube and then raised again, the capillary rise will be limited by the larger pore (Figure 1.7(c)). As a result, the capillary tube will show different degrees of saturation at the same water reservoir level and, hence, water pressure as occurs in geomaterials (Figure 1.7(a)).

1.3. Water retention mechanisms in geomaterials and the concept of suction

Figure 1.6 shows that unsaturated soils are characterized by negative pore-water pressures. If the soil is put in contact with a pool of water at atmospheric pressure, it will suck out water from the pool, i.e. the soil will show suction (Figure 1.8). However, the concept of suction in unsaturated geomaterials is more complex. Capillarity is not the only mechanism responsible for suction and water transfer does not solely occur via the liquid phase.

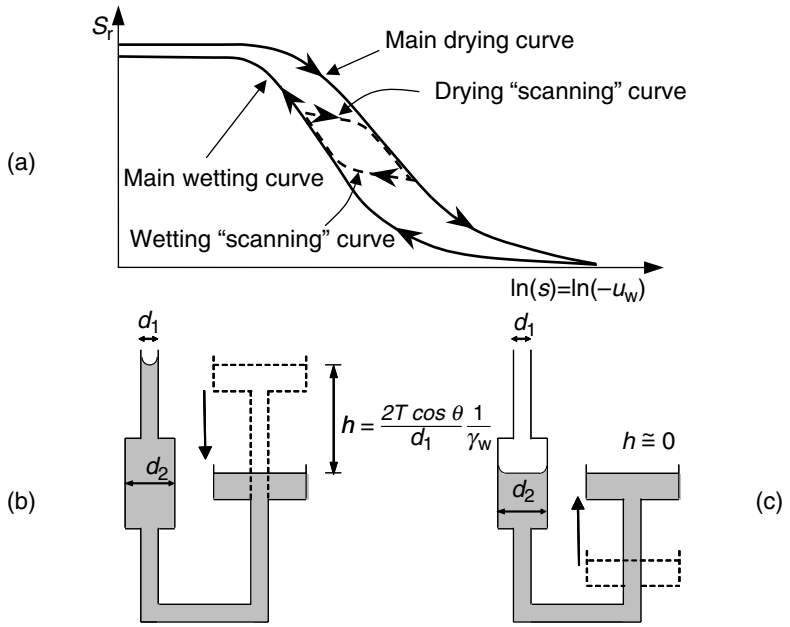

Figure 1.7. *Hysteresis of water retention behavior*

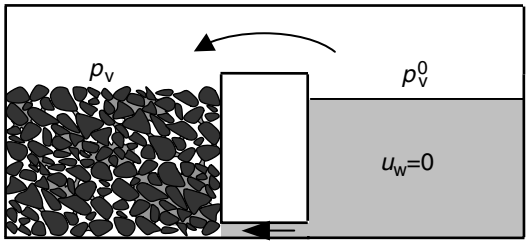

Figure 1.8. *Unsaturated geomaterials draw out water from a pool via liquid and vapor phase*

1.3.1. *Water equilibrium through the liquid phase and the matric suction*

Consider two clay particles in "contact" via the overlapping of their diffused double layers. The concentration of cations is higher in the interlayer compared with that in the solution (Figure 1.9(b)) due to the negatively charged surfaces of the clay particles. Because of this concentration difference, water molecules tend to diffuse toward the

interlayer in an attempt to equalize concentration. This mechanism of water retention in clayey geomaterials is referred to as an osmotic mechanism.

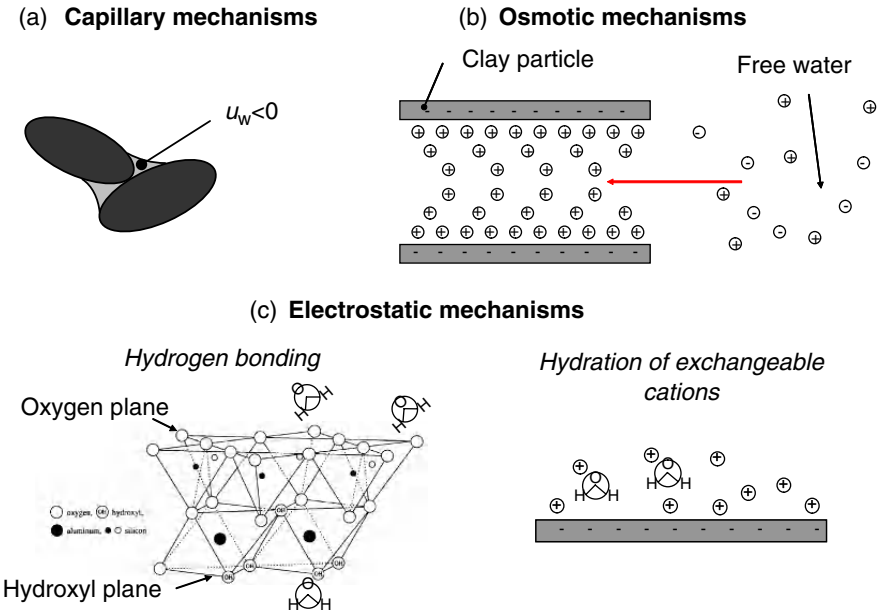

Figure 1.9. *Mechanisms of water retention associated with the soil matrix*

Another mechanism of water retention in clayey geomaterials is associated with electrostatic forces at the clay particle surface (Figure 1.9(c)). Water molecules form hydrogen bonding with the oxygen and hydroxyl outer plane in tetrahedron and octahedral sheets, respectively (clay particles consists of several layers which are in turn formed by tetrahedron and octahedral sheets). Water molecules are also retained by hydration of exchangeable cations in turn attracted by the negatively charged particle surface. As a very first approximation, capillary mechanisms play a role at high degrees of saturation, whereas osmotic and electrostatic mechanisms become relevant at medium to low degrees of saturation. Capillary, osmotic, and electrostatic mechanisms of water retention are directly or indirectly generated by the solid phase and are therefore associated with the soil "matrix". This is the reason why suction generated by these mechanisms is referred to as "matrix suction" or "*matric suction*".

1.3.2. *Water equilibrium through the vapor phase and the total suction*

Water can also be drawn out of the water pool via the vapor phase. This is because the pressure of vapor in equilibrium with soil water, p_v, is lower than the pressure of water vapor in equilibrium with pure water across a flat surface, p_v^0 (Figure 1.8). Two mechanisms contribute to the depression of water vapor, the negative pressure of soil water and the concentration of soil water. To understand these effects, let us examine the equilibrium of water (the chemical constituent H_2O) in liquid and vapor phase. Irrespective of whether the liquid–gas interface is flat or curved, the liquid phase consists of pure water or aqueous solution, or the gas phase consists of water vapor or a mixture of water vapor and air (Figure 1.10), equilibrium is attained when the chemical potential of water in the liquid, μ_w, equals the chemical potential of water in the gas phase, μ_v [BER 80]:

$$u_w = u_v. \qquad [1.3]$$

Assume to bring the system, reversibly and isothermally, from the state in Figure 1.10(a) (reference State 0) to the state in Figure 1.10(b) (liquid under negative pressure, State 1). For the entire process:

$$\int_0^1 \mathrm{d}\mu_w = \int_0^1 \mathrm{d}\mu_v. \qquad [1.4]$$

By definition, the chemical potential is equal to:

$$\mu \equiv h - Ts = u + pv - Ts, \qquad [1.5]$$

where h is the molar enthalpy (enthalpy per unit mole), u the molar internal energy, p the pressure, v the molar volume, T the temperature, and s the molar entropy. The first and second principle of thermodynamics, under the assumption that the work performed on the system is exclusively due to expansion work, can be written as:

$$\mathrm{d}u = \delta q - p\mathrm{d}v \ (\text{First principle}) \quad \delta q = T\mathrm{d}s \ (\text{Second principle}), \qquad [1.6]$$

where δq is the amount of heat transferred to the system. By combining equation [1.5] with [1.6], the increment of chemical potential $\mathrm{d}\mu$ can be written as follows:

$$\mathrm{d}\mu = v\mathrm{d}p - s\mathrm{d}T. \qquad [1.7]$$

By substituting equation [1.7] in [1.4], under the assumption that water vapor follows the ideal gas law and isothermal transformation ($\mathrm{d}T = 0$), we have:

$$\int_0^1 v_\mathrm{w}\mathrm{d}p_\mathrm{w} = \int_0^1 \frac{RT}{p_v}\mathrm{d}p_v, \qquad [1.8]$$

where the subscripts w and v refer to liquid water and vapor water, respectively; T is the absolute temperature; and R the universal gas constant. If the molar volume of liquid water v_w is assumed to be constant, integration of equation [1.8] leads to:

$$p_\mathrm{v} = p_\mathrm{v}^0 \exp\left[\frac{v_\mathrm{w}}{RT}\left(p_\mathrm{w} - p_\mathrm{w}^0\right)\right]. \qquad [1.9]$$

Equation [1.9] shows that the pressure of vapor in equilibrium with its own liquid, p_v, reduces as the liquid pressure decreases. This effect is known as Poynting effect [CHU 77].

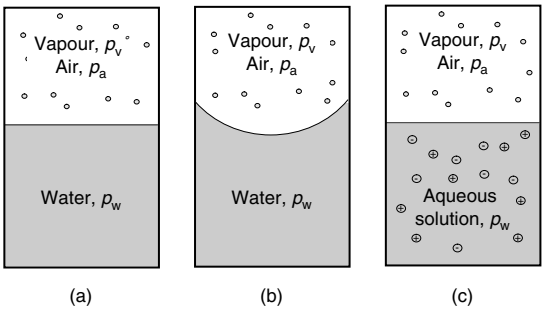

Figure 1.10. *Water vapor pressure in equilibrium with water under negative pressure or aqueous solution*

To analyze the effect of solute concentration on vapor pressure (Figure 1.10(c)), let us write the chemical potential of water in ideal solution, μ_w, and the chemical potential of ideal water vapor, μ_v, as follows [BER 80]:

$$\mu_\mathrm{w} = \mu_\mathrm{w}^0(p_\mathrm{w}, T) + RT\ln(1 - x_\mathrm{s}), \qquad [1.10]$$

$$\mu_{\mathrm{v}}(p_{\mathrm{v}},T)=\mu_{\mathrm{v}}\left(p_{\mathrm{v}}^{0},T\right)+RT\ln\left(\frac{p_{\mathrm{v}}}{p_{\mathrm{v}}^{0}}\right), \qquad [1.11]$$

where $\mu_{\mathrm{w}}^{0}(p_{\mathrm{w}},T)$ is the chemical potential of pure water at the same pressure p_{w} and temperature T, and x_{s} is the molar fraction of solute in the ideal solution. For the case of pure liquid having a flat interface (Figure 1.10(a)), $p_{\mathrm{w}}=p_{\mathrm{v}}^{0}+p_{\mathrm{a}}$ (p_{a} being the air pressure). Since,

$$\mu_{\mathrm{w}}^{0}(p_{\mathrm{w}},T)=\mu_{\mathrm{w}}^{0}\left(p_{\mathrm{a}}+p_{\mathrm{v}}^{0},T\right)\cong\mu_{\mathrm{w}}^{0}\left(p_{\mathrm{v}}^{0},T\right)=\mu_{\mathrm{v}}(p_{\mathrm{v}}^{0},T) \qquad [1.12]$$

subtracting equations [1.10] and [1.11] leads to:

$$p_{\mathrm{v}}=p_{\mathrm{v}}^{0}(1-x_{\mathrm{s}}). \qquad [1.13]$$

Equation [1.13] is known as Raoult's law and shows that the pressure of vapor in equilibrium with the aqueous solution decreases as the solute concentration x_{s} increases. The mechanisms of water retention through the vapor phase are therefore associated with solute concentration (equation [1.13]) and soil water negative pressure (equation [1.9]), the latter in turn generated by the solid phase. Accordingly, suction generated by the vapor phase is referred to as "*total suction*" to point out that suction is generated by both the solid phase (*matric suction*) and the solute concentration (*solute suction*). The solute suction is often referred to as "osmotic suction" which should not be mistaken, however, for the osmotic mechanism generating the matric suction (Figure 1.9).

1.3.3. *Measurement of matric and total suction*

Matric and total suction can be quantified by measuring the pressure that needs to be applied to water in a measurement system to establish equilibrium through liquid and vapor phase, respectively. If the measurement system is connected to the soil water through the liquid phase (left-hand side in Figure 1.11), solutes will rapidly diffuse toward the measurement system [TAR 04]. As the solute concentration is the same in the soil and measurement system, suction is only generated by the action of the solid matrix, and the negative pressure measured by the instrument is therefore referred to as "*matric suction*", s_{m}.

If the measurement system is connected to the soil water through the vapor phase (right-hand side in Figure 1.11), solutes cannot diffuse toward the measurement system. As a result, suction is also generated by the action of solutes in the soil water, and the negative pressure measured by the measurement system is therefore referred to as "*total suction*", s_t. The difference between total and matric suctions depends on the solute concentration and is referred to as "*solute suction*", s_s. As shown in Figure 1.11, total suction is defined as the (negative) pressure that needs to be applied to liquid water in the measurement system to establish equilibrium through the vapor phase. However, this pressure is never measured directly and total suction measurement is based on the measurement of pressure of water vapor in equilibrium with the soil water, which is then converted to total suction by inverting equation [1.9]:

$$s_t = -\frac{RT}{v_w} \ln \frac{p_v}{p_v^0}. \qquad [1.14]$$

In conclusion, the factor discriminating between the measurement of total and matric suction is the presence of solutes in the measurement system (at the same concentration as the soil water). Matric suction is measured when solutes are allowed to diffuse toward the measurement system whereas total suction is measured when pure water is present in the measurement system (typically in the vapor phase).

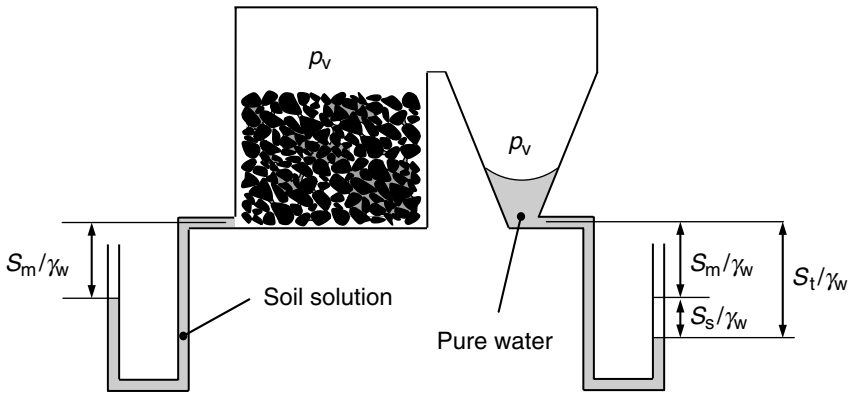

Figure 1.11. *Definition of total and matric suctions*

1.4. Water flow in capillary systems

To introduce the hydraulic conductivity of unsaturated geomaterials, it may be convenient to consider water flow in capillary tubes. Figure 1.12(a) shows water flow in a saturated capillary tube having diameter d. Under the assumption of laminar flow, the relationship between the flow actual velocity, v_{act}, and the hydraulic gradient, i, can be determined by solving the Navier–Stokes equations (Poiseuille's law):

$$v_{act} = \left[\frac{g}{2\eta} R_H^2\right] \bullet i = \left[\frac{g}{2\eta}\left(\frac{A_w}{P_w}\right)^2\right] \bullet i, \qquad [1.15]$$

where g is the acceleration of gravity, η the kinematic viscosity, and R_H the hydraulic radius, i.e. the ratio between the wetted area, A_w, and the wetted perimeter, P_w ($R_H=d/4$ for the tube in Figure 1.12(a)). Equation [1.15] points out that the relationship between flow velocity and hydraulic gradient is linear and this is exactly what occurs in saturated geomaterials. Equation [1.15] also appears to capture well the hydraulic response of saturated geomaterials from a quantitative standpoint. The term in square brackets represents the hydraulic conductivity, which depends on the fluid characteristics and on the tube geometry. The order of magnitude of the hydraulic conductivity in sands, silts, and clays can be calculated by considering characteristic pore sizes for these geomaterials ($d=d_{pore}\sim d_{grain}/10$). As shown in Table 1.1, the order of magnitude of hydraulic conductivity is captured well by equation [1.15] proving that the capillary tube may adequately serve as a basis to discuss water flow in unsaturated geomaterials.

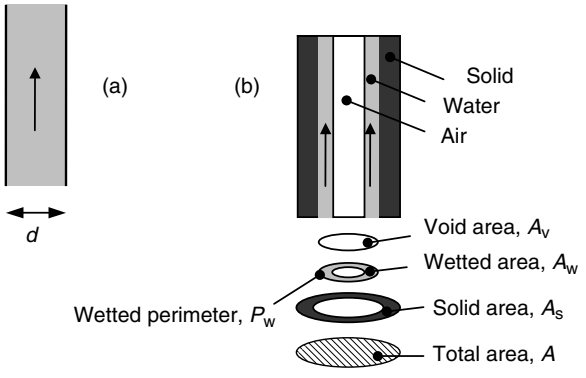

Figure 1.12. *Saturated and unsaturated flow in capillary tube*

Let us consider the case of water flow in an unsaturated capillary tube (Figure 1.12(b)). The flow average velocity v (water flow per unit total area A) is given by:

$$v = \frac{v_{act} \bullet A_w}{A}, \qquad [1.16]$$

where A_w is the wetted area. The wetted area, A_w, and the wetted perimeter, P_w, can be expressed in terms of void ratio, e, degree of saturation, S_r, and specific surface, S_0, as follows (assuming that areal and volumetric porosities are equal):

$$A_w = S_r \frac{e}{1+e} A \quad P_w = A_s S_0 = \frac{1}{1+e} A S_0. \qquad [1.17]$$

By combining equations [1.15–1.17], the following equation is obtained for unsaturated flow:

$$v = \left[\frac{g}{2\eta} \frac{1}{S_0^2} \frac{e^3}{1+e} S_r^3 \right] \bullet i. \qquad [1.18]$$

This equation is known as the Kozeny–Carman equation [MIT 93]. The unsaturated hydraulic conductivity can, therefore, be written as:

$$k = \left[\frac{g}{2\eta} \frac{1}{S_0^2} \frac{e^3}{1+e} \right] S_r^3 = k_{sat} \bullet S_r^3. \qquad [1.19]$$

The unsaturated hydraulic conductivity, therefore, depends on the degree of saturation through a power law in the simple model shown in Figure 1.12. In geomaterials, it is also found that the hydraulic conductivity essentially depends on degree of saturation even though the function $k=k(S_r)$ may differ from a power law. It is also generally observed that the relationship $k=k(S_r)$ does not show hysteresis in contrast to the relationship $S_r=S_r(s)$. It is instructive to compare the hydraulic conductivity function of sand and silt calculated using equation [1.19], assuming a saturated hydraulic conductivity of 10^{-3} and 10^{-6} m/s for the sand and silt, respectively, and an air-entry suction of 1 and 40 kPa for the sand and silt, respectively. As shown in Figure 1.13, the hydraulic conductivity of the silt is clearly lower than that of sand at saturation and low suctions. However, the hydraulic

conductivity may become greater than that of sand as suction increases, i.e. the sand can be found to be less permeable than silt under unsaturated conditions. This is the basis for capillary barriers made of coarse-grained materials.

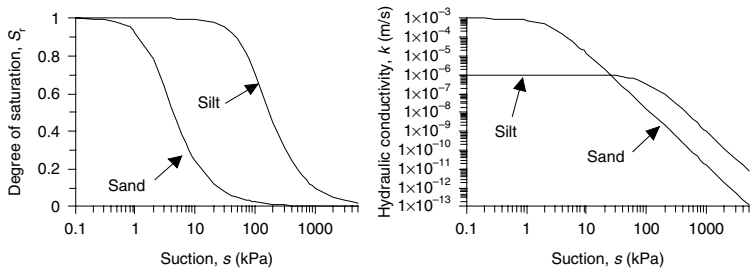

Figure 1.13. *Unsaturated hydraulic conductivity for sand and silt*

1.5. Mechanical interactions at the microscale

In unsaturated geomaterials, water exists at the inter-particle contacts around air-filled voids (*meniscus* water) and at the saturated sub-regions of the pore space (*bulk* water) (Figure 1.6(c)). Inter-particle contacts can therefore be divided into "*saturated*" contacts (bulk water) and "*meniscus*" contacts (meniscus water). In the saturated sub-regions, slippage at the "saturated" contacts is controlled by the *tangential* and *normal* components of the contact forces. As in saturated soil, these contact forces are influenced by externally applied total stresses and by the pore-water pressure in the surrounding voids. In contrast, menisci at the inter-particle contacts provide a stabilizing effect through an additional component of normal force at the contact with no addition to the tangential force [GAL 03, WHE 03]. Meniscus and bulk water, therefore, control the mechanical response of unsaturated geomaterials by different mechanisms.

Consider the meniscus formed at the contact between two rigid spherical particles (Figure 1.14(a)). The pressure difference across the liquid interface, u_a–u_w, is given by the Young–Laplace equation:

$$u_a - u_w = T\left(\frac{1}{r_1} - \frac{1}{r_2}\right) \cong T\left(\frac{1}{c} - \frac{1}{b}\right), \qquad [1.20]$$

where T is the surface tension and r_1 and r_2 are the principal radii of curvature.

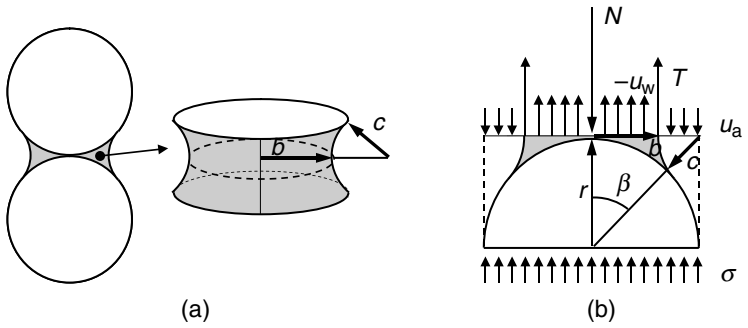

Figure 1.14. *Equilibrium at the meniscus contact*

If the contact angle is θ=0, the meniscus surface derived by solving equation [1.20] is a Plateau nodoid. However, little error is introduced if the meridian curve is assumed to be circular with radius c [FIS 26]. The radii b and c of the meniscus depend on the angle β defining the position of the meniscus junction and the particle radius r:

$$c = r\left(\frac{1}{\cos\beta} - 1\right) \quad b = r\left(1 + \tan\beta - \frac{1}{\cos\beta}\right). \qquad [1.21]$$

It is worth noting that u_a–u_w=0 for β=53° and is greater than zero for β<53°. Force equilibrium across the horizontal plane passing through the inter-particle contact leads to (Figure 1.14(b)):

$$\frac{N}{A} = (\sigma - u_a) + \left[\frac{1}{A}\left(A_w + P_w \frac{cb}{b-c}\right)\right](u_a - u_w), \qquad [1.22]$$

where N/A is the intergranular normal stress; σ is the total stress; A_w and P_w are the wetted area and perimeter, respectively; and A is the total area. Since the term in square brackets on the right-hand side of equation [1.22] is a function of β through equation [1.21] and suction u_a–u_w is also a function of β through equations [1.20] and [1.21], the intergranular stress generated by the meniscus (second term on the right-hand side of equation [1.22]) can be plotted against suction for different values of the particle radius r as shown

in Figure 1.15(a) (it is assumed that $u_a = 0$ and $\sigma = 0$). It is observed that the compressive intergranular stress generated by the meniscus, $(N/A)_m$, mainly depends on particle size and remains nearly constant for the given particle size. In other words, the value of suction within a meniscus water lens has very little effect on the stability of that contact. To a first approximation, the additional stabilizing intergranular stress can therefore be assumed to be constant whenever the meniscus water lens is present, but it disappears when the surrounding voids are water filled [WHE 03].

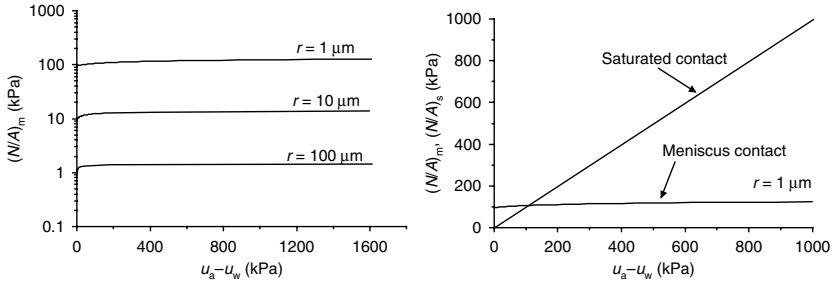

Figure 1.15. *(a) Intergranular stress generated by suction and (b) comparison of intergranular force at meniscus and saturated contact*

For the case of a saturated contact in a saturated "bulk water" sub-region, the intergranular stress is given by:

$$\frac{N}{A} = \sigma - u_w = \sigma + s. \qquad [1.23]$$

The intergranular stress for the case of point-like contact (zero contact area) is apparently equal to the effective stress. However, the intergranular stress for the case of zero or very small contact area should not be mistaken by the effective stress. Skempton [SKE 60] demonstrated that effective stress still controls the mechanical behavior of saturated porous media even if the contact area is very large. The intergranular stress can therefore be associated with the effective stress only in qualitative terms.

The compressive intergranular stresses generated by suction at a saturated contact, $(N/A)_s$, and at the meniscus contact, $(N/A)_m$, are compared in Figure 1.15(b). It can be observed that the suction has negligible effects on "meniscus" intergranular compressive stress as compared with the "saturated" compressive intergranular stress. This confirms once again that

the stabilizing effect of the menisci may be regarded as an on–off effect. Menisci "bond" particles together almost independent of the level of suction and their effect vanish as air-filled voids surrounding the menisci are flooded. It is also interesting to observe that the intergranular stress at zero suction is nil for the case of saturated contact (Figure 1.16) whereas it is greater than zero for the meniscus contract. Even if suction is zero ($b = c$ for $\beta = 53°$), the surface tension still acts as a compressive force along the wetted perimeter, which results in a compressive intergranular stress (Figure 1.14).

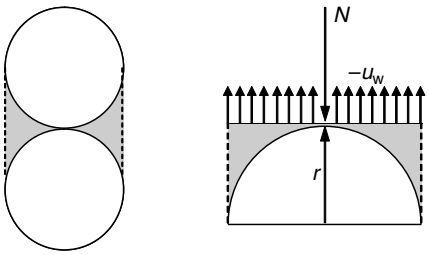

Figure 1.16. *Equilibrium at the saturated contact*

1.6. Microscopic interpretation of volumetric "collapse" and shear strength

Let us consider the case of an unsaturated geomaterial having an open structure, which is typically the case of soils compacted on the dry side of optimum or granular materials prepared by "wet tamping". If the material is wetted under constant total stress, σ, two distinct volumetric responses may be observed depending on the stress level. At low stresses, the material will swell, whereas at high stresses, the material will show an initial swelling followed by a significant volume decrease, which is referred to as "volumetric collapse" (Figure 1.17). This peculiar response of an open (unsaturated) structure can be explained from a microstructural standpoint. Let us consider the unsaturated material initially loaded by an external stress. This stress causes an increment in both the shear and normal forces at the particle contact. At some of the contact points, the ratio between shear and normal forces may exceed the inter-particle friction angle and slip will occur at these points. This results in a compression of the unsaturated geomaterial. However, at some meniscus inter-particle contacts, particle slip will be prevented by the additional normal forces generated by the menisci (see, for

example, the meniscus in black in Figure 1.18(a)). The "stabilizing" effect of menisci at the meniscus contacts will limit the decrease in volume while loading and the soil structure may therefore remain relatively "open".

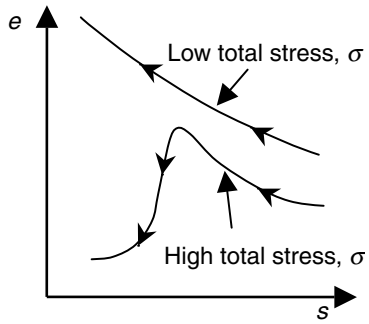

Figure 1.17. *Volumetric behavior while wetting of loose assemblage of particles or aggregates*

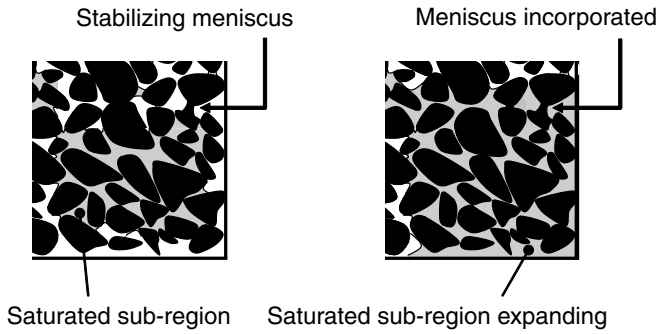

Figure 1.18. *Microscopic interpretation of volumetric collapse*

A subsequent decrease in suction (increase in pore-water pressure) will modify the intergranular stresses in the saturated sub-regions causing, as in saturated soils, the saturated sub-regions to swell. This will result in an overall volume increase as shown in Figure 1.17. At the same time, the saturated sub-regions will enlarge and will incorporate some menisci (Figure 1.18(b)). The progressive disappearance of menisci is associated with a loss in the normal forces at the particle contacts. Eventually, this can cause

particles to slip and an overall decrease in volume (volumetric collapse) can be observed as in Figure 1.17. For the particles to slip, the external stress should be relatively high to produce high shear forces at the inter-particle contact. If the external stress is low, shear stresses at the inter-particle contact will also be low and no slips will occur even if the stabilizing effect of menisci is lost as a result of flooding. This is the reason why no volume decrease may be observed while wetting at low stresses (Figure 1.17).

Intergranular stresses at the saturated and meniscus contacts can also explain the contribution of suction to shear strength, $\Delta\tau$, as illustrated in Figure 1.19. This additional contribution is given by the difference between the shear strength τ and the shear strength at zero suction, $\sigma \tan \phi'$, σ being the total stress. The geomaterial initially remains saturated (S_r~1) as suction increases. As Terzaghi's principle of effective stress holds in this range, the increase in shear strength is proportional to $\tan \phi'$, ϕ' being the effective angle of friction (continuous curve in Figure 1.19(b)). As suction increases beyond the air-entry suction, s_b, the soil desaturates and the shear strength $\Delta\tau$ is lower than the shear strength the specimen would have shown if it had remained saturated under any suction. In some cases, it is observed that at suctions close to the air-entry suction, the shear strength of the unsaturated geomaterial is higher than the shear strength under saturated conditions (dashed line in Figure 1.19(b)).

To provide a microscopic interpretation of this response, let us compare the same ideal packing under saturated and unsaturated conditions (Figure 1.20). Let us also assume that the contribution of suction to shear strength, $\Delta\tau$, is proportional to the intergranular stress, σ_i, generated by the suction s (again this assumption is acceptable only from a qualitative point of view):

$$\tau = \sigma_i \tan \phi'. \qquad [1.24]$$

The intergranular stress under saturated and unsaturated condition can be written as follows (by taking into account equations [1.22] and [1.23] and assuming σ=u_a=0):

$$\sigma_{i|saturated} = s\frac{a_m}{a} + s\frac{a_b}{a} \quad \sigma_{i|unsaturated} = (\sigma_i)_m \frac{a_m}{a} + (\sigma_i)_b \frac{a_b}{a} = (\sigma_i)_m \frac{a_m}{a} + s\frac{a_b}{a}, \qquad [1.25]$$

where a_m and a_b are the areas occupied by the meniscus and bulk water, respectively; a is the total area; and $(\sigma_i)_m$ and $(\sigma_i)_b$ are the intergranualar stresses at meniscus and saturated contacts, respectively.

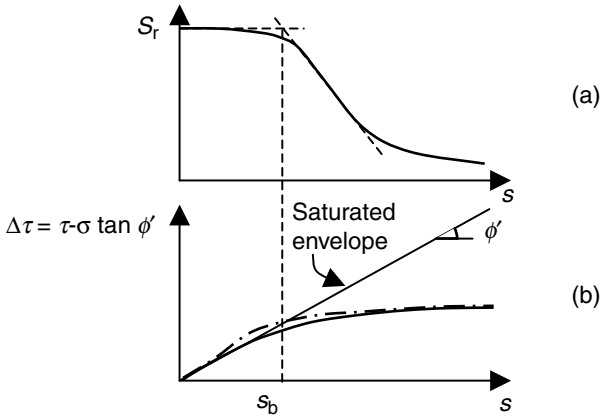

Figure 1.19. *Contribution of suction to shear strength*

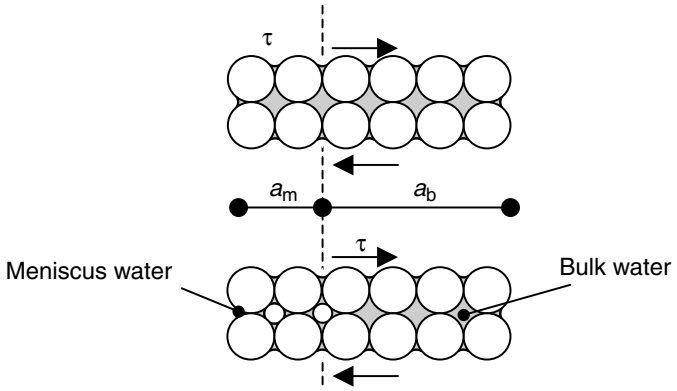

Figure 1.20. *Microscopic interpretation of shear strength*

Equation [1.25] shows that the difference between the intergranular stress under saturated and unsaturated is therefore associated with the difference in the saturated and meniscus intergranular stress across the area a_m. As shown in Figure 1.15, the meniscus intergranular stress can be higher than saturated intergranular stress at low suction and is lower at high suction. This qualitatively explains why the contribution of suction to shear strength, $\Delta\tau$,

may be higher than saturated shear strength at low suction and becomes lower than saturated shear strength as suction increases (dashed line in Figure 1.19). The increase in unsaturated shear strength around the air-entry suction may not be observed, whereas the decrease of the rate of change $d(\Delta\tau)/ds$ to a zero value is almost always observed in unsaturated geomaterials.

1.7. Bibliography

[BER 80] BERRY R.S., RICE S.A., ROSS J., *Physical Chemistry*, John Wiley & Sons, 1980.

[BER 50] BERTHELOT M., "Sur quelques phénomènes de dilatation forcée des liquides", *Annales de Chimie et de Physique*, vol. 30, p. 232-237, 1850.

[CHU 77] CHUE S.H., *Thermodynamics – A Rigorous Postulatory Approach*, John Wiley & Sons, 1977.

[FIS 26] FISHER R.A., "On the capillary forces in an ideal soil: correction of formulae given by W. B. Haines", *Journal of Agricultural Science*, vol. 16, no. 3, p. 492-505, 1926.

[GAL 03] GALLIPOLI D., GENS A., SHARMA R., VAUNAT J., "An elasto-plastic model for unsaturated soil incorporating the effects of suction and degree of saturation on mechanical behaviour", *Géotechnique*, vol. 53, no. 1, p. 123-136, 2003.

[GIB 48] GIBBS J.W., *The Collected Works of J. Willard Gibbs – Volume 1: Thermodynamics*, Yale University Press, 1948.

[JOH 69] JOHNSON R.E., DETTRE R.H., "Wettability and contact angles", in MATIJEVIC E. and EIRICH F.R. (eds.), *Surface and Colloid Science*, vol. 2, John Wiley & Sons, p. 85-152, 1969.

[MAR 95] MARINHO F.A.M., CHANDLER R.J., "Cavitation and the direct measurement of soil suction", in ALONSO E.E. and DELAGE P. (eds.), *Proc. 1st Int. Conf. Unsaturated Soils*, Paris, Balkema, Rotterdam, vol. 2, p. 623-630, 1995.

[MAR 08] MARINHO F.A.M., TAKE A., TARANTINO A., "Tensiometeric and axis translation techniques for suction measurement", *Geotechnical and Geological Engineering*, vol. 26, no. 6, p. 615-631, 2008.

[MIT 93] MITCHELL J.K., *Fundamentals of Soil Behavior*, Wiley Inter-Science, New York, 1993.

[SKE 60] SKEMPTON A.W., "Effective stress in soils, concrete and rocks", *Proc. Conf. Pore Pressure*, Butterworths, London, p. 4-16, 1960.

[TAR 04] TARANTINO A., "Panel lecture: direct measurement of soil water tension", *Proc. 3rd Int. Conf. on Unsaturated Soils*, Recife, Brazil, vol. 3, p. 1005-1017, 2004.

[WHE 03] WHEELER S.J., SHARMA R.S., BUISSON M.S.R, "Coupling of hydraulic hysteresis and stress-strain behaviour in unsaturated soils", *Géotechnique*, vol. 53, no. 1, p. 41-54, 2003.

Chapter 2

Mechanics of Unsaturated Soils

2.1. Introduction

Unsaturated soils play a major role in the construction of embankments and tunnels, road foundations (compaction effects), near the ground surface (infiltration and evaporation phenomena in the surface layer above the water table), and numerous geoenvironmental engineering applications (i.e. nuclear and domestic waste storage). A thorough understanding and modeling of the behavior of unsaturated soils is therefore important for the design and analysis of geostructures.

In general, soil is a mixture of a solid matrix (composed of all soil grains and aggregates) containing voids filled with a liquid and/or a gas, as well as other possible constituents; the voids may be considered as empty space if the mass of the liquid and/or air is not significant. We use the term "soil" to denote the mixture and not its solid components. Soil is defined as saturated when all the voids are filled with one fluid (usually water), and when the fluid pressure in the pores is compressive. This is generally the case of soil under the water table. The compressive fluid pressure in the pores plays a "neutral role", as it does not affect the strength and stiffness of the material [TER 36].

Chapter written by Lyesse LALOUI, Mathieu NUTH and Bertrand FRANÇOIS.

For all the other cases, the soil should be described as an unsaturated material. This covers a broad range of states [HUT 99] including:

– voids filled with a liquid containing a dissolved gas or whose pressure is in tension;

– voids filled with two immiscible fluids (i.e. water and gas).

Unsaturated materials distinguish themselves by the fact that the pore pressure affects the mechanical behavior by means of surface tension. Thus, the fluids are not "neutral" anymore like the saturated soils. This effect is associated with the capillary phenomena inside the pores and is manifested as a suction phenomenon in the entire material. Indeed, the total suction effect generated in the unsaturated soil is the sum of two contributions: the matric suction that is directly related to the capillary phenomena on the macroscopic behavior, and the osmotic suction that is due to the presence of dissolved salts in the pore water. If the changes in osmotic suction are less significant than those in matric suction, we can approximate the variations in the total suction as being only related to the changes in the matric suction.

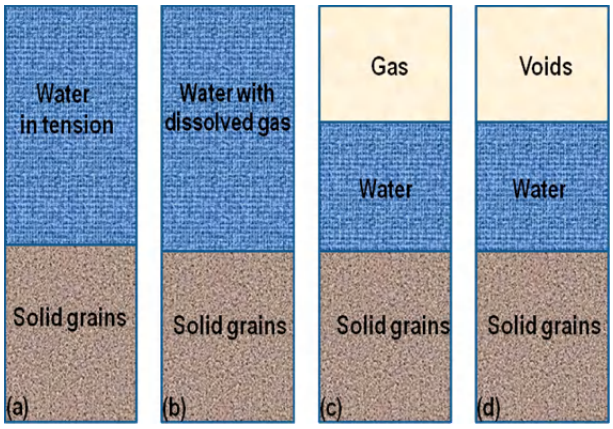

Figure 2.1. *Various states of unsaturated soils*

2.2. Stress states

The general description of an unsaturated soil, as depicted in Figure 2.1(c), shows that three stress variables should be considered: the external (or total) mechanical stress, σ, the pore-water stress, u_w, and the pore-air stress, u_a. The knowledge of only two of the three possible state variables

(σ, u_w, and u_a) suffices to define the stress state [FRE 77], which leads to the following possible controlling experimental stresses:

$$\begin{aligned} &(1)\ (\sigma - u_a) \text{ and } (u_a - u_w), \\ &(2)\ (\sigma - u_w) \text{ and } (u_a - u_w), \\ &(3)\ (\sigma - u_a) \text{ and } (\sigma - u_w). \end{aligned} \quad [2.1]$$

2.3. Thermo-hydro-mechanical behavior of unsaturated soils

A complete description of the rheological behavior of unsaturated soils is twofold. On the one hand, the soil water retention behavior (often called the "soil water retention curve", SWRC) needs to be quantified. On the other hand, the stress–strain behavior, or the mechanical response, must be described. Modern unsaturated soil mechanics offers a unified – or coupled – understanding of these two behaviors, which used to be described independently. This implies that the controlling experimental stresses defined in equation [2.1] will have a direct influence on both the void ratio and the degree of saturation. These variables will be used in the following section to describe the response of unsaturated soils using their mechanical and retention behaviors.

2.3.1. *Effects of suction on the stress–strain behavior of unsaturated soils*

Matric suction has been previously described as a controlling stress variable (equation [2.1]). This variable serves to quantify the effect of partial saturation on the mechanical stress–strain behavior of soils. A comparison of the unsaturated response with a saturated reference is of particular interest. Most of the results show that capillarity can have both stiffening and hardening effects, as reviewed in the following section.

In isotropic compression tests, the volumetric response depends on the level of suction. For example, the results from [SIV 93], plotted in Figure 2.2, allow us to draw the following conclusions (where $\sigma_{net}=\sigma-u_a$ is the net stress and $s=u_a-u_w$ is the matric suction):

– The stress–strain response is decomposed into an elastic part and an elastoplastic part, as carried out for conventional saturated compression tests.

– In the elastic region, the stiffness (or slope κ) is not significantly affected by suction.

– The mechanical compressibility (or slope λ) in the plastic region decreases (or more generally changes) with increasing suction.

– The plasticity limit is suction dependent.

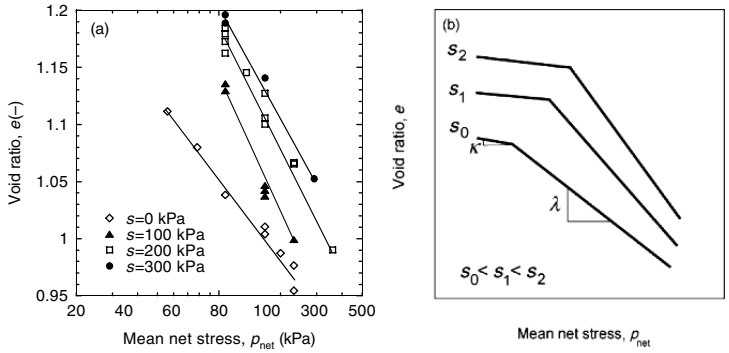

Figure 2.2. *Void ratio changes under isotropic mechanical load at several constant levels of suction. (a) Results for kaolin [SIV 93]. (b) Qualitative synthetic interpretation*

The plasticity limit is also called the preconsolidation pressure p'_c using Cam-Clay terminology [SCH 68]. As the preconsolidation pressure is an indicator of the overconsolidation ratio, it measures the degree of apparent hardening shown by the soil in drier conditions than the reference saturated state. It also shows that the elastic domain generally becomes larger with increasing suction, as demonstrated, for instance, by Kane [KAN 73], and shown in Figure 2.3.

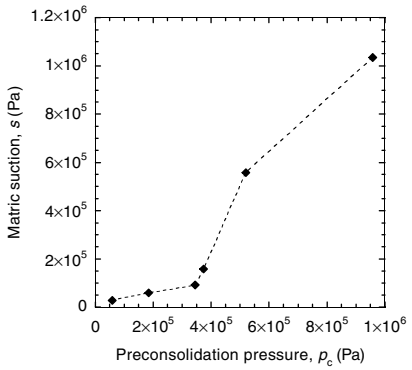

Figure 2.3. *Evolution of the preconsolidation pressure as a function of suction for loess. From Kane [KAN 73]*

In addition, the response to shearing of unsaturated samples using a triaxial apparatus, or a direct shear box, shows that the apparent shear resistance is higher in drier conditions (e.g. Figure 2.4). In a conventional deviatoric stress versus mean net stress plane (q–p_{net}), in which the critical state line (CSL) can be drawn, the angle of friction remains fairly constant with respect to the saturated friction angle, whereas the apparent cohesion is clearly suction dependent (see also equations [2.5] and [2.6]).

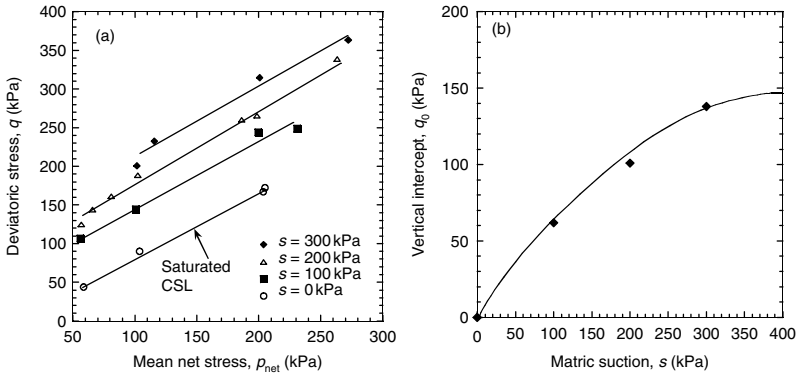

Figure 2.4. *Evolution of CSL with suction for compacted kaolin. Data from [WHE 95]*

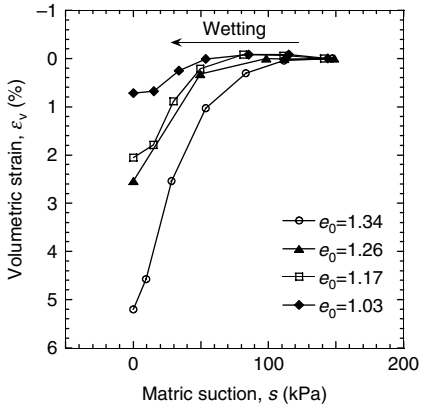

Figure 2.5. *Wetting collapse phenomenon in Pearl clay (experimental data from [SUN 07]). The constant e_0 represents the initial void ratio before wetting*

The relationship between the apparent cohesion and suction is not linear and tends to reach an asymptotic value at large matric suctions.

In addition, the pore wetting collapse is another typical signature of the mechanical behavior of unsaturated soils. It refers to the ability of partially saturated soils to undergo large volumetric compression under humidification and at a sufficiently large level of mechanical stress (Figure 2.5). The wetting collapse is a plastic phenomenon.

2.3.2. *Soil water retention behavior*

The relationship between the degree of saturation, S_r, and matric suction, s, enables us to describe the water retention behavior of the soil. The retention aspects are essential to properly describe the response of unsaturated soils, as they indicate the proportion of water within the voids. The water retention behavior is mainly characterized by capillary hysteresis and dependency on the void ratio.

The hysteretic property of the SWRC has been demonstrated in numerous research studies. The dependence of the degree of saturation on matric suction, as shown in Figure 2.6, signifies that the path of drying is located above the wetting path. Consequently, the processes of drying and wetting cause irreversible changes in the degree of saturation. The capillary hysteresis is attributed to the variable pore size distribution within the soil as well as to the wetting and drying contact angles of water with respect to the solid phase.

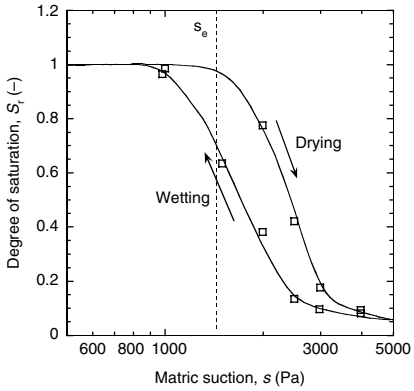

Figure 2.6. *Capillary hysteresis in sand. Data from [ENG 03]*

A new parameter is also defined in Figure 2.6. The air entry value s_e represents the suction above which the degree of saturation becomes lower than 1.

The (S_r–s) relationship is not unique and is actually related to the deformation of the soil skeleton. Small variations in the void ratio, for instance, due to mechanical compression, can have a pronounced effect on the soil water retention behavior.

Figure 2.7 shows an example of the alteration of the shape of the (S_r–s) curves as a function of the void ratio. The curves seem to be shifted toward higher levels of suction for denser states. This pattern indicates an increase in the degree of saturation when the pores (void space) become smaller. Nuth and Laloui [NUT 08a] tried to quantify the change in the air entry value with the void ratio (Figure 2.8).

This analysis showed that s_e can be used as a parameter controlling the coupling between the retention behavior and mechanical deformations.

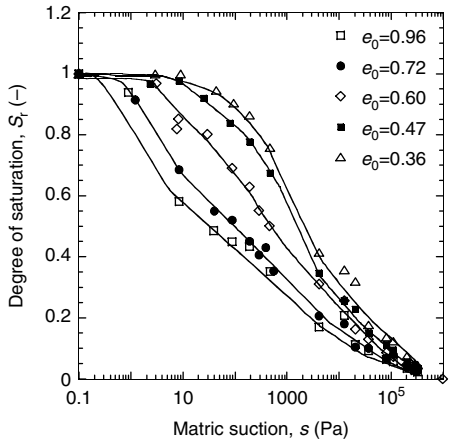

Figure 2.7. *Effect of the initial void ratio e_0 on the shape of the SWRC of sandy clayey silt, drying paths only (from [SAL 07])*

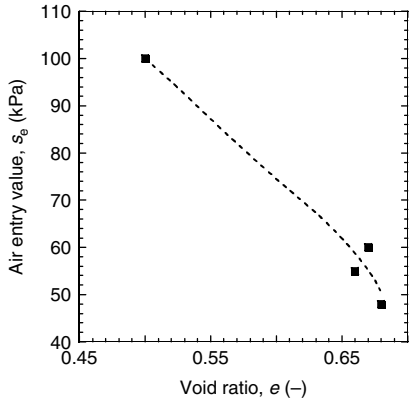

Figure 2.8. *Evolution of the air entry value as a function of the void ratio for Sion silt [NUT 08a]*

2.3.3. *Non-isothermal conditions*

The thermomechanical behavior of unsaturated soils must be considered as a coupled process, in which the water retention and mechanical response are closely related in a unified temperature-dependent response. The key intrinsic temperature-dependent soil variable is the preconsolidation pressure that decreases when the temperature increases. This observation can be made from different experimental tests, where various stress-suction-temperature paths are followed. Each type of test shows that plasticity occurs at lower isotropic stress levels when the temperature is increased. Thus, the thermoplasticity of soils is mainly governed by the evolution of the isotropic part of the yield limit as a function of temperature.

The combined effects of temperature and suction on preconsolidation pressure are shown in Figure 2.9 in terms of isotropic yield limit. The influence of temperature on the evolution of preconsolidation pressure is usually less significant than that of suction. However, the results confirm the decrease in preconsolidation stress p'_c with increasing temperature, and the increase in p'_c with increasing suction, which are consistent with the results obtained from other studies where the thermal and suction effects on the compression behavior of soils were investigated separately [ROM 03, TAN 08]. Based on the experiments studying the combined effects of temperature and suction on the preconsolidation pressure of sandy silt (Figure 2.10), Salager *et al.* [SAL 08] proposed to adopt a logarithmic function to model

these two phenomena using a combination of two separate laws, which were developed for non-isothermal saturated conditions [LAL 03] and isothermal unsaturated conditions [NUT 07], respectively.

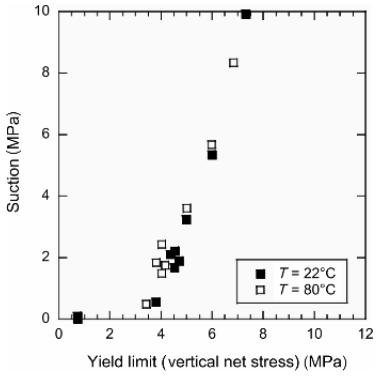

Figure 2.9. *Combined effect of temperature T and suction on the evolution of the yield limit in the net stress reference for compacted Boom clay [ROM 99]*

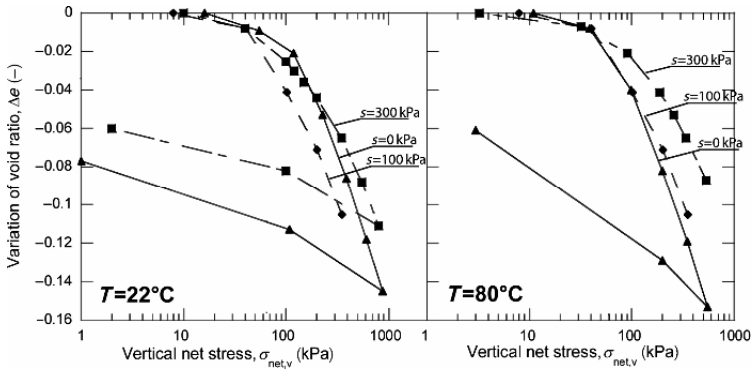

Figure 2.10. *Oedometric compression tests on sandy silt at different temperatures and suction levels [SAL 2008]*

When a soil is subjected to various heating–cooling cycles, under normally consolidated (NC) conditions, the clay contracts upon heating and a significant part of this deformation becomes irreversible upon cooling. This thermal contraction is an unusual behavior for many materials. This behavior over the whole cycle shows the irreversibility of the strain due to thermal loading, which is a characteristic of thermal hardening. In contrast to

the NC soil, the highly overconsolidated (OC) soils mostly exhibit reversible dilation upon heating. The effect of stress level on the volumetric thermomechanical response has been largely investigated under saturated conditions for various soils (in particular, see [BAL 91, CEK 04]). Under unsaturated conditions, a soil suction variation may lead to a change in the thermal volumetric strain during a heating–cooling cycle. At constant external stress, suction induces an overconsolidation of the soil due to an increase in the preconsolidation pressure with suction, which reduces the thermoplastic effect on the soil. A soil that behaves as a lightly OC soil under low suction (thermoplastic contraction upon heating) may respond as an apparently highly OC material under high suction (thermoelastic dilation upon heating) (Figure 2.11).

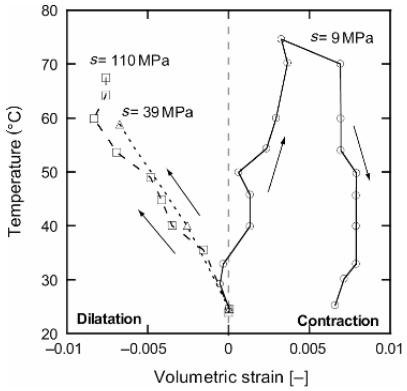

Figure 2.11. *Effect of suction on the volumetric response of MX80 bentonite subjected to thermal cycle under an external stress of 0.1 MPa [TAN 08]*

As far as wetting–drying paths are concerned, the temperature effects on the shrinkage and swelling/collapse of the soil with the changes in suction have been almost exclusively investigated on compacted materials. The influence of thermal effects on swelling/collapse behaviors seems to depend on the considered materials. The swelling potential of high-density compacted Boom clay increases with increase in temperature [ROM 03], while the swelling capacity of FEBEX bentonite seems to decrease with the increase in temperature [VIL 04]. In case of the collapse propensity of low-density Boom clay, the contraction strain upon wetting has been shown not to be significantly affected by the temperature [ROM 03]. On the contrary, when compacted Boom clay is wetted under strain constrains, the swelling

pressure is reduced due to the enhanced hardening process at elevated temperatures.

The temperature has an effect on the (S_r–s) relationship, and several factors contribute to the decrease in the water retention capability of the soils as the temperature is increased (change in the water surface tension, reduction in the layer thickness of the adsorbed water, and release of the dissolved air). Thus, at constant suction, the degree of saturation of a given soil is lower at elevated temperatures when compared with room temperature (Figure 2.12). On the contrary, for a given amount of water in the soil, the suction is reduced when the temperature is increased. The influence of the temperature on the water retention curve can be quantified in a constitutive model using the evolution of the air entry suction with temperature [FRA 08].

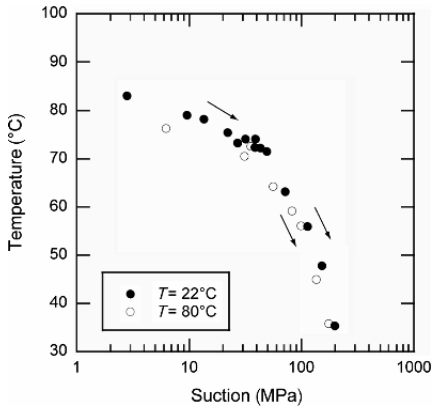

Figure 2.12. *Water retention curve of FoCa clay at 22 and 80°C. From [IMB 05]*

2.4. Effective stress in unsaturated soils

The constitutive modeling of multiphase porous media requires the determination of the effective stress of the solid skeleton. The effective stress allows us to model a multiphase porous medium as a mechanically equivalent, single-phase, single-stress state continuum. The skeleton deformation is then directly related to the effective stress by the constitutive equations. Each of the constituents of the medium is likely to react internally to a global external load. Thus, a general definition of the effective stress σ'_{ij} in a porous medium saturated with k fluids is given by:

$$\sigma'_{ij} = \sigma_{ij} + \sum_{k=1}^{n} \alpha_k u_k \delta_{ij}, \qquad [2.2]$$

where σ_{ij} is the exterior stress, δ_{ij} the Kroenecker's delta (δ_{ij}=1, if i=j, 0 otherwise), u_k the pressure of the fluid phase k, and α_k the corresponding weighting coefficient. For saturated soils, equation [2.2] becomes Terzaghi's effective stress [TER 36]. In unsaturated soils, the considered fluids are liquid water and gaseous air. A possible formulation of the effective stress is the generalized effective stress σ'_{ij}:

$$\sigma'_{ij} = (\sigma_{ij} - u_{\mathrm{a}}\delta_{ij}) + S_{\mathrm{r}}(u_{\mathrm{a}} - u_{\mathrm{w}})\delta_{ij}. \qquad [2.3]$$

In equation [2.3], the degree of saturation S_{r} is a weighting coefficient for the contribution of the fluid pressure. From a constitutive point of view and under given assumptions [LAL 09], thermodynamic [HUT 99] as well as energetic [HOU 97] approaches can help identify the appropriate form of the effective stress that must be associated with a work-conjugate strain variable. The complete stress–strain framework for the constitutive modeling of unsaturated soils can be found in [NUT 08b]:

$$\begin{pmatrix} \sigma' = \sigma_{\mathrm{net}} + S_{\mathrm{r}} \times s \\ s \end{pmatrix} \quad \text{and} \quad \begin{pmatrix} \varepsilon \\ S_{\mathrm{r}} \end{pmatrix}, \qquad [2.4]$$

where the effective stress σ' and suction s are the stress variables, and the skeleton deformation ε and degree of saturation S_{r} are the work-conjugate strain variables.

The use of unsaturated effective stress has a number of implications on the constitutive modeling of unsaturated soils. Some of the characteristics of unsaturated soils previously presented in this chapter can now be re-evaluated in terms of constitutive stress and strain variables (equation [2.4]). The conventional triaxial stresses are used for representations. The deviatoric stress q and mean stress p are defined as follows:

$$q = \hat{\sigma}_{11} - \hat{\sigma}_{33}, \qquad [2.5]$$

$$p = \frac{\hat{\sigma}_{11} + \hat{\sigma}_{22} + \hat{\sigma}_{33}}{3}, \qquad [2.6]$$

where $\hat{\sigma}_{ij}$ represents the stress-state variable, which is either the experimental stress or effective stress depending on the considered framework.

As the shear strength depends on the level of suction, the investigation of the CSL in terms of an effective stress must be addressed. In Figure 2.13, we compare the CSL obtained from experimental stresses with a reinterpretation in terms of effective stress. Using the experimental mean net stress for the *X*-coordinates, we show in Figure 2.13(a) that the CSL evolves with changing suction.

If the transformation from a net stress conception to an effective stress representation does not affect the deviatoric stress level (equations [2.3] and [2.5]), then the isotropic effect of suction normalized by the saturation degree is added to the net mean stress. The CSLs at different suctions are uniformly horizontally translated by this amount of extra stress. The immediate consequence is a reduction in the apparent cohesion (see Figure 2.13(b)). By using an effective stress representation, it appears that the CSL remains unique and does not depend on the suction level.

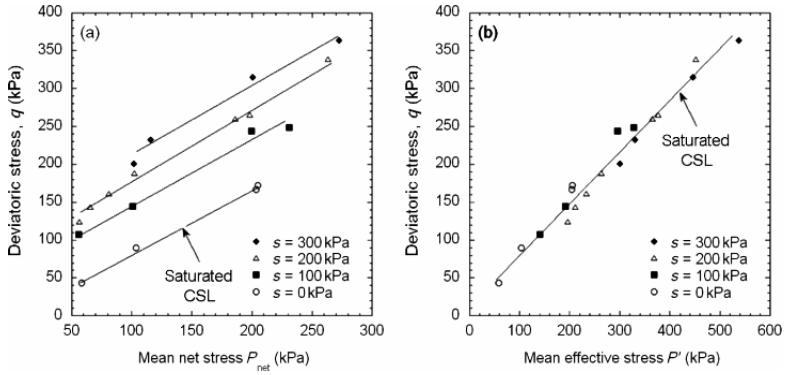

Figure 2.13. *CSLs for Kaolin at different suctions (data from [SIV 93])*

In addition, the effective stress is by definition the stress that induces the mechanical (elastic) strain of the solid skeleton. By introducing the constitutive matrix C^e_{ijkl}, the constitutive equation for the mechanical behavior can thus be simply written as:

$$\varepsilon_{ij}^{e} = C_{ijkl}^{e}\sigma'_{kl}. \qquad [2.7]$$

Equation [2.7] is particularly relevant for the formulation of a constitutive model, because the suction does not have to be explicitly expressed in the mechanical constitutive equation. The effective stress formulation given in equation [2.3] indicates that the effect of suction (and the degree of saturation) on the state of stress will be naturally accounted for in the effective stress formulation. Implicitly, temperature effects on the (S_r–s) relationship are also included in the effective stress formulation.

A constitutive model for unsaturated soils can thus be formulated in a unified manner between the saturated and unsaturated behaviors, while retaining the same stress and strain variables. Moreover, the defined stress framework enables a direct correspondence of the capillary hysteresis observed in the (S_r–s) plane into the (s–p') representation, as shown in Figure 2.14. As previously discussed, in Figure 2.14(a), the drying curve is not recovered after wetting due to dissipation. The consequence of capillary hysteresis is that, for a same level of suction, two different states of saturation can be obtained. The stress state and skeleton deformations are likely to be influenced by capillary irreversibility. Figure 2.14(b) shows the complete drying–wetting path in the (s–p') stress plane. Owing to the presence of the product of suction and the degree of saturation in the effective stress formulation, hysteresis is naturally taken into account. As a consequence, the retention behavior influences soil deformations.

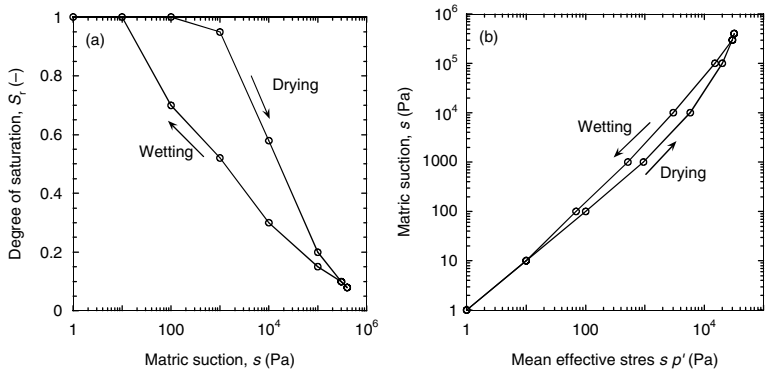

Figure 2.14. *(a) SWRC of Jossigny loam (from [FLE 93]). (b) Corresponding stress paths in the (s–p′) plane*

2.5. A coupled THM constitutive framework for unsaturated soils

This section presents the theoretical framework for the modeling of the thermo-hydro-mechanical (THM) behavior of unsaturated soils. The basic steps for the formulation of a non-isothermal unsaturated constitutive model are as follows:

– formulation of a saturated stress–strain model for the mechanical behavior;

– generalization of the stress and strain framework to partial saturation;

– formulation of a model for the water retention behavior;

– definition of the interdependencies between each parts;

– addition of thermal effects.

The proposed modeling framework is that of the Advanced Constitutive Model for Environmental Geomechanics (ACMEG) with unsaturated (S) and thermal (T) extensions, developed by Laloui *et al.* [FRA 08, NUT 07]. In the following, the stress and strain variables are those previously defined in equation [2.4].

2.5.1. *Mechanical model*

The formulation of the stress–strain (mechanical) model is based on the monotonic part of the Hujeux's elastoplastic model [HUJ 85]. The increment of strain $\mathrm{d}\varepsilon_{ij}$ is decomposed into:

$$\mathrm{d}\varepsilon_{ij} = \mathrm{d}\varepsilon_{ij}^{e} + \mathrm{d}\varepsilon_{ij}^{p}, \qquad [2.8]$$

where $d\varepsilon_{ij}^{e}$ is the elastic strain increment and $d\varepsilon_{ij}^{p}$ the plastic strain increment.

The volumetric and deviatoric increments of the elastic strain can be written as:

$$\mathrm{d}\varepsilon_{\mathrm{V}}^{e} = \frac{\mathrm{d}p'}{K_{\mathrm{ref}}\left(\dfrac{p'}{p'_{\mathrm{ref}}}\right)}, \qquad [2.9]$$

$$\mathrm{d}\varepsilon_{\mathrm{d}}^{e} = \frac{\mathrm{d}q}{3G_{\mathrm{ref}}\left(\dfrac{p'}{p'_{\mathrm{ref}}}\right)^{n^e}}. \qquad [2.10]$$

The material parameters K_{ref}, G_{ref}, and n^e are the bulk elastic modulus at a reference mean stress p'_{ref}, the reference shear elastic modulus at p'_{ref}, and the nonlinearity exponent, $n^e \in [0,1]$, respectively.

Under non-isothermal conditions, the elastic deformation can be expressed as:

$$\mathrm{d}\varepsilon_{ij}^{e} = C_{ijkl}\mathrm{d}\sigma'_{kl} - \frac{1}{3}\beta'_{\mathrm{s}}\mathrm{d}T\delta_{ij}, \qquad [2.11]$$

where the compression is assumed to be positive. The tensor C_{ijkl} is the mechanical elastic tensor and is composed of the nonlinear hypo-elastic moduli defined earlier. β'_{s} represents the volumetric thermal expansion coefficient of the solid skeleton. The elastic strain may be induced by total stress, suction, variations in the saturation degree (first term in equation [2.11]), or by temperature changes (second term in equation [2.11]).

Using the concept of multi-mechanism plasticity [MAN 65], the total irreversible strain increment $\mathrm{d}\varepsilon_{ij}^{p}$ is induced by two coupled dissipative processes: an isotropic and a deviatoric plastic mechanism. These processes lead to the plastic strain increments $\mathrm{d}\varepsilon_{ij}^{p,\mathrm{iso}}$ and $\mathrm{d}\varepsilon_{ij}^{p,\mathrm{dev}}$, respectively.

The yield limits of each mechanism, bounding the elastic domain in the effective stress space, can be written as (see Figure 2.15):

$$\tilde{f}_{\mathrm{iso}}(p', \varepsilon_{\mathrm{v}}^{p}, r_{\mathrm{iso}}) = p' - r_{\mathrm{iso}} \cdot d \cdot p'_{\mathrm{CR}}, \qquad [2.12]$$

$$\tilde{f}_{\mathrm{dev}}(p', q, r_{\mathrm{dev}}, \varepsilon_{\mathrm{v}}^{p}, \varepsilon_{\mathrm{d}}^{p}) = q - Mp'\left(1 - b\ln\frac{p'}{p'_{\mathrm{CR}}}\right)r_{\mathrm{dev}}, \qquad [2.13]$$

where p'_{CR} is the critical state pressure and d and b are the material parameters. The parameter M corresponds to the slope of the CSL in the (q–p') plane, which is assumed to be unique and independent of the level of

suction [NUT 08b]. The parameters r_{iso} and r_{dev} represent the degrees of mobilization of the isotropic and deviatoric mechanisms, respectively. They enable a progressive evolution of the isotropic and deviatoric yield limits [HUJ 85].

Upon hardening, a volumetric plastic strain ε_v^p is generated following the normal compression line in the plane $\left(\varepsilon_v^p - \ln p'\right)$, whose slope is equal to that of the CSL:

$$\ln \frac{p'_{CR}}{p'_{CR0}} = \beta \varepsilon_v^p, \qquad [2.14]$$

where p'_{CR0} and β are the initial critical state pressure and the coefficient of plastic compressibility, respectively. Starting from a saturated reference value β_0 at zero suction, the coefficient β is a function of suction, where Ω is a material parameter:

$$\beta = \tilde{\beta}(s) = \beta_0 + \Omega \cdot s. \qquad [2.15]$$

The critical state pressure in equation [2.14] can be related to the preconsolidation pressure p'_c using the material parameter d and is expressed as:

$$p'_c = d \cdot p'_{CR}. \qquad [2.16]$$

So far, a first level of coupling between the (S_r–s) relationship and mechanical stress–strain model is automatically created. Indeed, the effective stress varies with suction as shown in equation [2.3], so that the global state of stress depends on the SWRC. It is thus possible to generate volumetric changes by modifying only the suction (e.g. equation [2.9]).

Another contribution of the capillary effects still needs to be introduced into the mechanical model to account for the increase in the preconsolidation pressure with suction (see Figure 2.3). The size of the elastic domain in the (p',q,s) space, as shown in Figure 2.15, depends on the level of suction. In addition, the elastic domain can also be expressed in the (p',q,T) space, which shows a dependence of the preconsolidation pressure on the

temperature. This double dependence of p'_c on the variables s and T can be expressed by:

$$p'_c = \begin{cases} p'_{c0}\{1-\gamma_T \log[T/T_0]\} & \text{if } s \le s_e \\ p'_{c0}\{1-\gamma_T \log[T/T_0]\}\{1+\gamma_s \log[s/s_e]\} & \text{if } s \ge s_e \end{cases}, \qquad [2.17]$$

where p'_{c0} is the initial preconsolidation pressure at zero suction and at reference temperature T_0, γ_s and γ_T are material parameters, and s_e is the air entry suction beyond which the degree of saturation becomes less than 1. Equation [2.17] defines the loading collapse (LC) curve in the planes (s–p') and (T–p'). Equations [2.15] and [2.17] thus reflect the second level of coupling between the retention curve and the mechanical model.

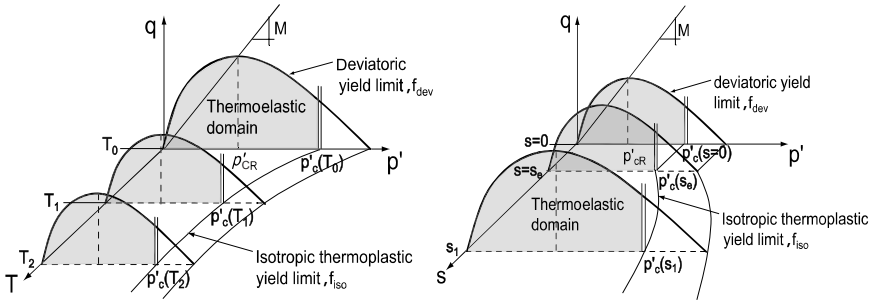

Figure 2.15. *Yield limits for the THM elastoplastic framework*

2.5.2. *Water retention model*

In parallel to the stress–strain module, the ACMEG-TS (temperature and suction) features an elastoplastic model for the SWRC, whose main characteristics are reviewed hereafter [NUT 08a]. Figure 2.16 shows the outline of the model in the plane (S_r–s) as well as the decomposition of the increment of the saturation degree dS_r into an elastic part dS_r^e and a plastic part dS_r^p:

$$dS_r = dS_r^e + dS_r^p . \qquad [2.18]$$

The elastic increment of the saturation degree can be written as:

$$\mathrm{d}S_{\mathrm{r}}^{\mathrm{e}} = \frac{\mathrm{d}s}{K_H \times (s / s_{\mathrm{e}})}, \qquad [2.19]$$

where s_{e} represents the "updated air entry value" and K_H denotes an elastic modulus. The elastic slope enables us to describe the scanning lines [NUT 08a]. If the suction remains lower than the updated air entry value, namely $s<s_{\mathrm{e}}$, then the degree of saturation equals 1 and there is no elastic increment. If the residual state is reached ($S_{\mathrm{r}}=S_{\mathrm{res}}$, where S_{res} is the residual degree of saturation), then the elastic increment also becomes null.

The elastic domain is delimited by the following yield limit:

$$f = \left\| \ln(s) - \ln(s_{\mathrm{D}}) + \frac{1}{2}[\ln(s_{\mathrm{D0}}) - \ln(s_{\mathrm{e}})] \right\| - \frac{1}{2}[\ln(s_{\mathrm{D0}}) - \ln(s_{\mathrm{e}})], \qquad [2.20]$$

where s_{D} is the actual "drying yield suction" and s_{D0} is the reference yield suction. The "drying yield suction" is the equivalent threshold of the preconsolidation pressure in the mechanical stress–strain model. It represents the maximum suction ever experienced by the material along a monotonic drying path. A similar threshold exists for the wetting path (capillary hysteresis). Equation [2.20] defines a yield surface evolving with kinematic hardening, i.e. either after a suction increase or decrease.

β_H is the slope of the plastic part of the degree of saturation $S_{\mathrm{r}}^{\mathrm{p}}$ and is defined as:

$$\ln\left(\frac{s_{\mathrm{D}}}{s_{\mathrm{D0}}}\right) = \beta_H S_{\mathrm{r}}^{\mathrm{p}}. \qquad [2.21]$$

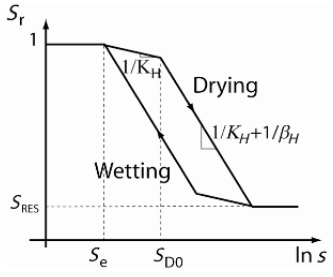

Figure 2.16. *The model for the SWRC*

The coupling between the mechanical model and the SWRC is introduced by the means of the air entry value s_e. This variable is continuously updated as a linear function of the volumetric strain ε_v that is calculated from the stress–strain model:

$$s_e = s_{e0} + \pi_H \cdot \varepsilon_v, \qquad [2.22]$$

where s_{e0} is the reference air entry value and π_H is a material parameter. Equation [2.22] has been derived in [NUT 08a] by collecting a number of retention curves in deformable soils from the literature. The hysteresis shown in Figure 2.16 is imposed to keep the same aperture (on a logarithmic scale) irrespective of the level of air entry, and we have:

$$s_{D0} = \frac{s_{DI} \times s_e}{s_{e0}}. \qquad [2.23]$$

Finally, the suction of the air entry is a function of the temperature [FRA 08] and can be given as:

$$s_e = s_e(T_0)\left\{1 - \theta_T \log\left\{\frac{T}{T_0}\right\}\right\}, \qquad [2.24]$$

where θ_T is a material parameter that describes the logarithmic evolution of the suction of the air entry as a function of temperature.

2.5.3. *Numerical simulations*

The swelling collapse behavior upon soaking is a built-in characteristic of the model. It has been widely observed experimentally (see Figure 2.17(b)) during the wetting of a material under a large initial net stress. This behavior justifies the use of the LC curve in the constitutive framework, even though the stress path is nonlinear in the (s–p') plane. Starting from an experimental initial state A (Figure 2.17(a)), p'_c decreases faster than the mean effective stress upon wetting (equation [2.17]). As point A is within the elastic domain but still close enough to the yield locus, two volumetric responses are predicted: (i) a fully reversible swelling upon effective stress relief along the paths AB and CD and (ii) a plastic compression accompanied with yielding on the LC curve along the path BC. The comparison of the numerical and

experimental results for kaolin shows some discrepancy between the suction levels for the activation of plasticity, most certainly due to some inaccuracy in the determination of the LC curve. However, the volumetric variations are fairly well predicted and the qualitative trends for the alternative swelling and collapsing are satisfactory.

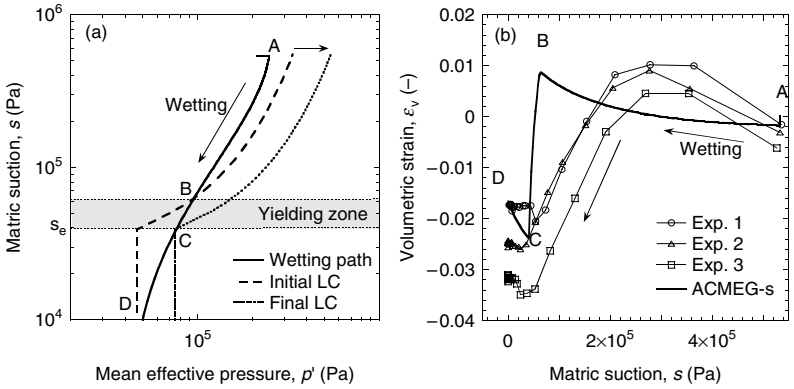

Figure 2.17. *Simulation of the wetting collapse. Experimental data from Kaolin [SIV 93]*

The following simulation focuses more on the soil water retention behavior. The air entry value s_e is considered as a variable describing the dependence of the shape of the SWRC on the void ratio (equation [2.22]). This dependence can be expressed in terms of a volumetric strain to normalize the calibration process.

An example of fitting of the parameter π_H to the volumetric strain data is shown in Figure 2.18(a). The predicted SWRCs upon drying are shown in Figure 2.18(b).

For a given initial void ratio e_0=0.51, the experimental SWRC is used to calibrate the model. The model shows that if the drying process is carried out under lower void ratios (0.47 and 0.44), then the water retention curves will be shifted to the right. This prediction is in good agreement with the experimental results due to the fact that denser soils are more difficult to dry out.

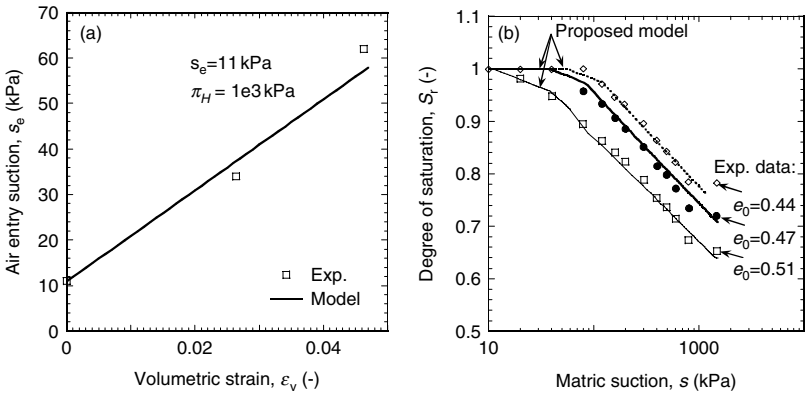

Figure 2.18. *Simulations of the retention of a glacial till (experimental data from [VAN 99]): (a) parameter calibration for the air entry value and (b) SWRCs for different initial volumes (from [NUT 08a])*

The ability of the model to predict the thermomechanical response of the unsaturated soils has been validated with the experimental results corresponding to different non-isothermal experiments done on various soils [FRA 08]. Among them, compression tests on FEBEX bentonite have been simulated.

Figure 2.19(a) compares the numerical simulations with oedometric compression tests at different suctions (T = 22°C). The initial strain observed at 0.1 MPa of net stress is due to the suction path from 127 MPa to the suction applied during compression. The subsequent compression paths clearly show an enlargement of the elastic domain when the suction is increased.

In Figure 2.19(b), we show the numerical predictions for oedometric compression tests done at two different temperatures under 127 MPa of suction. The initial strain observed for the path at 50°C is due to the temperature increase. In addition, a small reduction in the preconsolidation pressure due to a temperature increase from 20 to 50°C can also be observed.

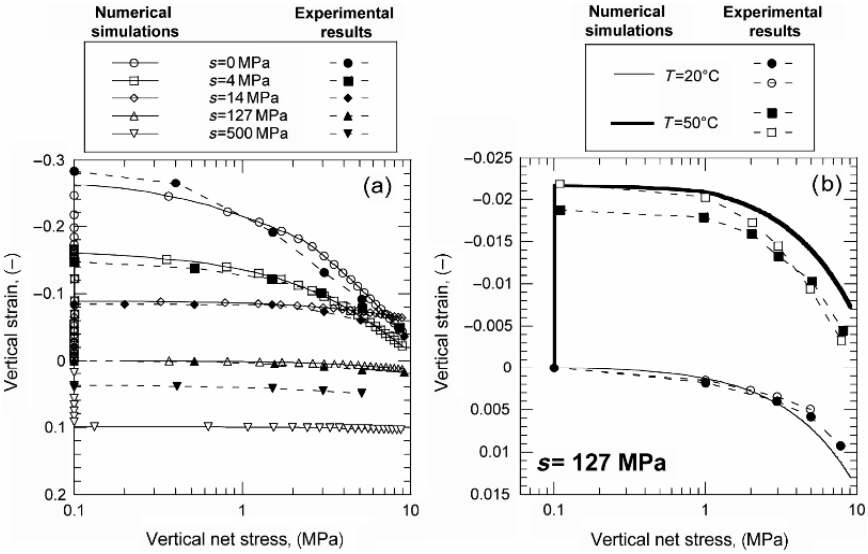

Figure 2.19. *Numerical prediction for oedometric compression tests using FEBEX bentonite at (a) different suctions and (b) different temperatures; from [FRA 08]*

2.6. Conclusion

An introduction to the mechanics of unsaturated soils in non-isothermal conditions was presented. It was shown that a consistent stress framework is an essential prerequisite for the constitutive modeling of unsaturated soils. Furthermore, it was also demonstrated how the material behavior strongly depends on the interaction between the mechanical stress–strain response and water retention aspect. The temperature variations were found to affect both these responses. The last part of this chapter presented some numerical simulations that allow us to assess the performance of an advanced constitutive model.

2.7. Bibliography

[BAL 91] BALDI G., HUECKEL T., PEANO A., PELLEGRINI R., *Developments in Modelling of Thermo-Hydro-Mechanical Behaviour of Boom Clay and Clay-Based Buffer Materials*, vols 1 and 2, O.f.O.P.o.E. Communities, Luxembourg, 1991.

[CEK 04] CEKEREVAC C., LALOUI L., "Experimental study of thermal effects on the mechanical behaviour of clays", *International Journal for Numerical and Analytical Methods in Geomechanics*, vol. 28, p. 209-228, 2004.

[ENG 03] ENGEL J., SCHANZ T., LAUER C., "State parameters for unsaturated soils, basic empirical concepts". *Unsaturated Soils: Numerical and Theoretical Approaches*, Weimar, p. 125-138, 2003.

[FLE 93] FLEUREAU J.M., KHEIRBEKSAOUD S., SOEMITRO R., TAIBI S., "Behavior of clayey soils on drying wetting paths", *Canadian Geotechnical Journal*, vol. 30, no. 2, p. 287-296, 1993.

[FRA 08] FRANCOIS B., LALOUI L., "ACMEG-TS: a constitutive model for unsaturated soils under non-isothermal conditions", *International Journal of Numerical and Analytical Methods in Geomechanics*, vol. 32, p. 1955-1988, 2008.

[FRE 77] FREDLUND D.G., MORGENSTERN N.R., "Stress state variables for unsaturated soils", *Journal of the Geotechnical Engineering Division, ASCE*, vol. 103, GT5, p. 447-466, 1977.

[HOU 97] HOULSBY G.T. "The work input to an unsaturated granular material", *Géotechnique*, vol. 47, no. 1, p. 193-196, 1997.

[HUJ 85] HUJEUX J., "Une loi de comportement pour le chargement cyclique des sols", *Génie Parasismique*, Les éditions de l'E.N.P.C, Paris, p. 287-353, 1985.

[HUT 99] HUTTER K., LALOUI L., VULLIET L., "Thermodynamically based mixture models of saturated and unsaturated soils", *Mechanics of Cohesive-Frictional Materials*, vol. 4, p. 295-338, 1999.

[IMB 05] IMBERT C., OLCHITZKY E., LABASSATERE T., DANGLA P., COURTOIS A., "Evaluation of a thermal criterion for an engineered barrier system", *Engineering Geology*, vol. 81, p. 269-283, 2005.

[KAN 73] KANE H. "Confined compression of loess", *7th ICSMFE*, Moscow, p. 155-122, 1973.

[LAL 03] LALOUI L., CEKEREVAC C., "Thermo-plasticity of clays: an isotropic yield mechanism", *Computers and Geotechnics*, vol. 30/8, p. 649-660, 2003.

[LAL 09] LALOUI L., NUTH M., "On the use of generalised effective stress in the constitutive modelling of unsaturated soils", *Computer and Geotechnics*, vol. 36, p. 20-23, 2009.

[MAN 65] MANDEL W., "Généralisation de la théorie de Koiter", *International Journal of Solids and Structures*, vol. 1, p. 273-295, 1965.

[NUT 07] NUTH M., LALOUI L., "New insight into the unified hydro-mechanical constitutive modelling of unsaturated soils", *Unsat Asia*, Nanjing, p. 109-125, 2007.

[NUT 08a] NUTH M., LALOUI L., "Advances in modelling hysteretic water retention curve in deformable soils", *Computers and Geotechnics*, vol. 35, no. 6, p. 835-844, 2008.

[NUT 08b] NUTH M., LALOUI L., "Effective stress concept in unsaturated soils: Clarification and validation of a unified framework", *International Journal for Numerical and Analytical Methods in Geomechanics*, vol. 32, p. 771-801, 2008.

[ROM 99] ROMERO E., Characterisation and thermo-mechanical behaviour of unsaturated Boom clay: an experimental study, PhD thesis, UPC, Barcelona, 1999.

[ROM 03] ROMERO E., GENS A., LLORET A., "Suction effects on a compacted clay under non-isothermal conditions", *Geotechnique*, vol. 53, no. 1, p. 65-81, 2003.

[SAL 07] SALAGER S., Etude de la rétention d'eau et de la consolidation de sols dans un cadre thermo-hydro-mécanique, PhD thesis, University of Montpellier 2, Montpellier, 2007.

[SAL 08] SALAGER S., FRANCOIS B., EL YOUSSOUFI S., LALOUI L., SAIX C., "Experimental investigations of temperature and suction effects on compressibility and pre-consolidation pressure of a sandy silt", *Soils and Foundations*, vol. 48, no. 4, p. 453-466, 2008.

[SCH 68] SCHOFIELD A.N., WROTH C.P., *Critical State Soil Mechanics*, McGraw-Hill, 1968.

[SIV 93] SIVAKUMAR V., A critical state framework for unsaturated soils, PhD thesis, University of Sheffield, Sheffield, 1993.

[SUN 07] SUN D.A., SHENG D., XU Y., "Collapse behaviour of unsaturated compacted soil with different initial densities", *Canadian Geotechnical Journal*, vol. 44, no. 6, p. 673-686, 2007.

[TAN 08] TANG A.M., Effet de la température sur le comportement des barrières de confinement, PhD thesis, Ecole Nationale des Ponts et Chaussées, Paris, 2005.

[TER 36] TERZAGHI K., "The shearing resistance of saturated soils and the angle between the planes of shear", *International Conference on Soil Mechanics and Foundation Engineering*, Harvard University Press, p. 54-56, 1936.

[VAN 99] VANAPALLI S.K., FREDLUND D., PUFAHL D.E., "The influence of soil structure and stress history on the soil-water characteristics of a compacted till", *Geotechnique*, vol. 49, no. 2, p. 143-159, 1999.

[VIL 04] VILLAR M., LLORET A., "Influence of temperature on the hydro-mechanical behaviour of a compacted bentonite", *Applied Clay Science*, vol. 26, p. 337-350, 2004.

[WHE 95] WHEELER S.J., SIVAKUMAR V., "An elasto-plastic critical state framework for unsaturated soil", *Géotechnique*, vol. 45, no. 1, p. 35-53, 1995.

Chapter 3

Desiccation Cracking of Soils

3.1. Introduction

Cracking of drying soils is a crucial issue in geoenvironmental engineering. Drying fractures strongly affect permeability and may compromise the integrity of structures, such as clay buffers and backfill for nuclear waste isolation liners of landfills. In addition, cracking may be a cause of substantial damage in foundation-supported structures. Compressibility increases substantially, while the rate of consolidation decreases with the appearance of desiccation cracks [MOR 92]. Drying cracks are also a possible precursor for the inception of a failure surface at the top of dams and embankments. Assessment of the potential for such damage is difficult, as the mechanisms and principal variables in the process are not fully understood, despite decades of research and substantial progress, e.g. [ABU 93, COR 60, KON 97].

The primary scope of this chapter is to present the mechanisms of desiccation, including shrinkage and cracking. For this purpose, experimental evidence as well as some of the substantial advances made in recent years in understanding the hydromechanics of unsaturated soils are reviewed. In addition, a possible scenario of processes that lead to cracking and that stem from drying shrinkage is also presented.

Chapter written by Hervé PERON, Lyesse LALOUI, Liang-Bo HU and Tomasz HUECKEL.

The chapter first reviews the basic processes underlying the term "desiccation". Then, the results of an experimental study of desiccation are presented, in which strains, suction, water content, degree of saturation, and crack geometry are investigated. The conditions of cracking initiation are discussed, especially with respect to the degree of saturation and suction. An insight into the microscale is proposed, taking into account that computationally viable variables are those at the macroscale, whereas the control variables of the underlying mechanisms are those at the microscale. A set of processes and thresholds leading to crack initiation is established. Lastly, desiccation crack pattern formation is discussed.

3.2. Physical processes involved in desiccation cracking of soils

3.2.1. *Drying*

Drying is a set of processes resulting from an initial thermodynamic imbalance between the soil moisture and its surroundings, which causes evaporation, transfer of fluids within the soil, shrinkage, and possible cracking. In a general case, the fluid movement is accomplished through both liquid and gaseous phases. According to equilibrium thermodynamics laws, the phase change between pore liquid and vapor occurs instantaneously at the interface between the phases, so that the specific vapor and liquid Gibbs potentials remain equal [COU 98, MAI 01]. This generates liquid pressure reduction (i.e. suction increase) in the interface neighborhood according to Kelvin's law, and as a result, a gradient of suction within the body. Thus, the liquid movement develops in response to this gradient. External pressures, high temperatures, and shrinkage deformations may also contribute to the pore fluid pressure generation and subsequent fluid movement.

An initial state refers to a porous material in a saturated state at equilibrium (no evaporation), i.e. with the boundary surface (or external to the body) humidity equal (macroscopically) to the saturation vapor concentration in ambient air. To avoid ambiguity, let us assume that the medium is initially covered with a thin film of liquid, so that no menisci are formed at this stage. Subsequently, if a (negative) vapor concentration gradient is applied to the ambient (external) air, vapor transport occurs in a boundary layer, and vapor pressure at the boundary surface falls below the saturated vapor concentration. This gives rise to the water molecule flux

across the boundary, which can only (for a 1D problem, air flow eddies are excluded) be accommodated by water/vapor phase transition, under water molar amount continuity.

The mass rate of evaporation per unit area, not far from equilibrium states, is postulated via vapor mass exchange, J_{v} following two main alternative constitutive laws (flux driven by temperature difference is discussed by [RAM 08]). Evaporation in the first law is driven by a vapor pressure difference, while in the second, it is driven by a difference in the chemical potential between the phases; in both the cases, these are local differences (not gradients). The former law is known as the Hertz–Knudsen equation [KNU 15] and the latter takes on an Onsager format [VAN 63], i.e.

$$J_{\mathrm{v}} = L_{p_{\mathrm{v}}}(w,T)\ln\left(\frac{p_{\mathrm{v}}}{p_{\mathrm{vs}}}\right) \quad \text{or} \quad J_{\mathrm{v}} = L_{\mu_{\mathrm{v}}}(w,T)\left(\frac{\mu_{\mathrm{l}}-\mu_{\mathrm{v}}}{T}\right), \qquad [3.1]$$

where w is the water content, T is the temperature, $L_{p_{\mathrm{v}}}$ and $L_{\mu_{\mathrm{v}}}$ are the evaporation rate coefficients, p_{vs} and p_{v} are the pressures of saturated vapor and vapor above the free surface of the liquid being vaporized, respectively, and μ_{l} and μ_{v} are the chemical potentials of the liquid and its vapor, respectively. In the latter form, the difference is understood locally, as occurring between the different mixture components at a point. When simulated via molecular dynamics, the resulting rate coefficient is overestimated by several orders of magnitude [JON 92]. Hence, practically, the formula's coefficient is found (often highly variable, see e.g. [BEN 82, CAM 05]) via solutions of boundary value problems of a diffusive near-surface layer moisture transport, which are calibrated against the experimental results ([HU 08a, HU 08b, HU 10, LOZ 08]).

The evaporation mass flux in the case of a generic liquid/vapor interface away from any solid walls is theoretically independent of the surface tension coefficient and the contact angle of the fluid against the solid at the air interface, which are the properties defining the capillary phenomena developing at a grain (micro) scale.

Drying is intrinsically a non-adiabatic process, because it requires energy (needed for evaporation). If the heat needed for evaporation (i.e. the latent heat of evaporation) is only supplied by the soil itself, a straightforward calculation (also carried out by [BAG 97]), tells us that for a water-saturated

clay with a specific heat of 1.3 kJ kg^{-1} K^{-1} and a porosity of 0.3, the temperature decrease would be about 346 K. However, in general, the heat source is the gas (air) environment, where the soil dries. In this situation, isothermal drying can be assumed if the phase change rate is limited by the mass transfer, and is therefore not controlled by the heat transfer. This situation is encountered in many types of soil [PER 08].

Macroscopic mass balance equations for both the phases provide additional constraints for the overall system of the governing equations (see e.g. [LOZ 08]).

The liquid/solid relative velocity is related to the gradient of the water head via Darcy's law. The Darcean flux of liquid $\mathbf{q}_\mathrm{l}$ [M L^{-2} T^{-1}] is given by:

$$\mathbf{q}_\mathrm{l} = \rho_\mathrm{l} n S_\mathrm{r} (\mathbf{v}_\mathrm{l} - \mathbf{v}_\mathrm{s}) = -\left(\frac{k}{g}\right)(-\nabla p_\mathrm{l} + \rho_\mathrm{l}\mathbf{g}), \qquad [3.2]$$

where the velocities of the liquid and solid are denoted by $\mathbf{v}_\mathrm{l}$ and $\mathbf{v}_\mathrm{s}$, respectively, n is the porosity, S_r is the degree of saturation, k is the hydraulic conductivity of the medium, $\mathbf{g}$ is the gravity vector, and ρ_l and p_l are the intrinsic density and pressure of the liquid, respectively.

When a continuous gaseous phase is present within the body, the gaseous phase movement can also be described by Darcy's law, as the consequence of a gradient of gas (fluid) head.

We should also consider transport of vapor associated with evaporation phenomenon. Even in the absence of a gas pressure gradient, vapor diffusion due to a difference in vapor concentration (or mole fraction) occurs and is expressed according to Fick's law, whose applicability to a gaseous mixture has been proven with the kinetic theory of gases. Here, vapor and dry air are assumed to form an ideal mixture. Fick's law for vapor diffusion is expressed as:

$$\mathbf{q}_\mathrm{v}^\mathrm{d} = \rho_\mathrm{v} n(1 - S_\mathrm{r})(\mathbf{v}_\mathrm{v} - \mathbf{v}_\mathrm{g}) = -\rho_\mathrm{g}\mathbf{D}_\mathrm{v}\nabla\left(\frac{\rho_\mathrm{v}}{\rho_\mathrm{g}}\right), \qquad [3.3]$$

where $\mathbf{q}_\mathrm{v}^\mathrm{d}$ is the diffusive vapor flux with respect to the gaseous mixture, $\mathbf{v}_\mathrm{v}$ is the velocity of the vapor, ρ_v is its density, ρ_g is the density of the gaseous

mixture, and $\mathbf{D}_v$ is a molecular diffusion tensor representative of vapor diffusion through dry air inside the porous medium. $\mathbf{D}_v$ is different from the molecular diffusion coefficient in a purely gaseous medium because it takes into account the tortuosity of the medium [PHI 57].

In certain situations, other phenomena can take place. Effusion of vapor (Knudsen model) occurs when the mean free path of the vapor molecule is in the same order as the diameter of the pores. Stefan's flux can occur when intensive vapor production creates a significant vapor pressure gradient [KOW 03]. The liquid phase may contain dissolved air. In this case, we would have to consider air dissolution into the liquid phase, which is governed by Henry's law, plus subsequent transport of the dissolved air into the liquid, which is mainly governed by Fick's law.

Under non-isothermal conditions, additional mechanisms of moisture transfer have to be considered during drying. The Soret effect (or thermodiffusion) refers to an additional diffusion-like process of vapor in dry air, occurring when a temperature gradient exists [PLA 06]. In addition, the evaporation–condensation mechanism might also act: liquid particles evaporate faster from the meniscus surface located in the warmer zone than they do from the surface located in the cooler zone. Then, capillary uplift of the liquid bridge or liquid pocket takes place towards the warmer zone because of the difference in the surface tensions between the menisci [KOW 03].

3.2.2. *Shrinkage*

At the microscale, it may be considered that the basic process behind the shrinkage of soil is a decrease in the liquid pressure and, more generally, an increase in suction s, caused by the evaporation at the location of interphase menisci, and which acts as an attractive force between the components of the matrix. At the initial saturated stage of the process, the menisci are located only at the external boundary of the soil body. At the macroscale, this translates into application of suction at the boundary and a resulting change in the pore pressure throughout the soil mass, eventually producing an increase in the effective (compression) stress of the matrix and the ensuing shrinking. For fine soils with no swelling minerals, it is reasonable to assume, following [MIT 05], that the mechanisms related to the adsorbed

water are not prevalent (i.e. capillary processes predominate), at least for a large range of water content and associated shrinkage strains.

Shrinkage strain then can be seen as the consequence of an effective stress increase. The effective stress embeds the contributions of externally applied stresses and internal pore fluid pressures. Bishop's generalized effective stress is a standard and broadly recognized effective stress for partially saturated soils [NUT 08] whose component σ'_{ij} is expressed as follows:

$$\sigma'_{ij} = \sigma^{\text{net}}_{ij} + S_{\text{r}} s \delta_{ij}, \qquad [3.4]$$

where σ^{net}_{ij} is the net stress component (difference between the total stress component and air pressure), s the matric suction, and δ_{ij} the Kronecker symbol.

3.2.3. *Air entry*

Most of the shrinkage induced by drying occurs during the stage of the process when the soil is still saturated. During that stage, the volume of water loss is equal to the reduction in the volume of the body. All the liquid that is evaporated is delivered from the inside of the pore vessels via Darcy flow or diffusion assisted by a squeezing action of the converging pore walls subjected to the internal negative liquid pressure. There are no interphase interfaces and no vapor within the body. All menisci coincide with the body perimeter through the entire duration of this stage.

Scherer [SCH 90] explains the persistence of the meniscus at the boundary by the fact that a meniscus displacement would expose the solid walls, and hence, a solid/liquid interface would be replaced by a solid/vapor interface, which is more energetic than the solid/liquid one. To counteract such an increase in the energy of the system, "liquid tends to spread from the interior of the body" to cover the solid/vapor interface. [SCH 90] suggests that the energy freed in that process constitutes a driving force for the deformation (shrinkage) of solids. Though the specific mechanism of that "spreading" remains unclear, it is definitely clear that deformation of the pore vessels contributes to that counteraction. In other words, the enthalpy of

the covered liquid/solid interface of a shrunk vessel should be compared with that of the exposed vapor/solid interface of a much less shrunk tube.

However at some point, the excess of energy of the system with the exposed walls is insufficient to deform the porous material, and hence, the energetic advantage of the fully saturated material disappears, leading to the invasion of gas into the interior of the porous body.

In another interpretation, the mechanism of the air entry is classically linked to the evolution of meniscus at the surface pore entry. [ZSI 11], [TER 27], [SCH 90] and [FRE 93] suggest that air entry occurs when a meniscus undergoing shrinkage due to the increase in suction becomes small enough to fit a throat of the largest external pore of the porous medium. This concept implies that the meniscus has (and maintains) its spherical shape and that its radius shrinks faster than that of the pore vessel. Its relationship to the liquid/external gas pressure difference (p_l–p_g) is controlled by the surface tension via Young–Laplace equation:

$$p_l - p_g = -\frac{2\tau_s}{a}, \qquad [3.5]$$

where a is the pore size at the sample surface and τ_s is the liquid surface tension.

On the other hand, the relationship between the radius of the pore vessel at any point and the water pressure is controlled by the pore vessel wall compressibility and fluid viscosity.

The above-mentioned interpretation of air entry is yet to be corroborated experimentally for soils. Moreover, it implies that either the contact angle at the moment of entry is zero for any mineral and any liquid, or that the pore exit is covered with a thin water film (see e.g. [KRO 99]), which is not seen in experiments with (non-clayey) soils.

An alternative macroscale interpretation of air entry into a pore vessel filled with evaporating water is possible, based on *water tensile fracture* at the pore system exits [WIN 71]. Because of the locking nature of the volumetric strain-stress law, it is easy to anticipate that in a porous medium subjected to evaporation fluxes applied at its boundaries, a very high suction may develop at the boundaries at an advanced stage of pore dewatering.

Water tensile fracture in pure conditions is estimated from a p, V, T equation of state to be as high as at p=–230 MPa [PIC 81, YAY 70]. However, water in capillaries is widely believed to reach tensile failure at a much lower suction via cavitation. Cavitation is understood as the existence of microscopic air bubbles at the solid walls, or attached to solid impurities suspended in the liquid, or nucleation of the new ones via evaporation (see e.g. [OER 71]). These gas bubbles can grow without limit if they first overcome an energy barrier of the bubble surface tension after reaching a critical size via temperature increase or liquid pressure decrease. The critical size, r_c^b, above which the bubble growth is unstable, can be given as [OER 71]:

$$r_c^b = \frac{2\tau_s}{p_v - p_l}. \qquad [3.6]$$

Isothermal changes in the vapor pressure affect the radius below 0.1 μm. However, when the water tension increases in the vessel, the bubble's critical size for the onset of growth is reduced. Upon tension reaching a value corresponding to the bubble critical size "equal or smaller than the pore size," $r_c^b = a$, "a bubble of water vapor could grow without being suppressed by pore walls" [OR 02]. In the case of drying, such a situation is most likely reached where the tension is the highest, which is near a pore vessel exit. Note that at such location, the cavitating bubble, which is filled with pressurized vapor instantly reaches the free surface of the water vessel and as its pressure is sufficient to break the surface tension it dissolves in the external gas. Equation [3.6] indicates that nuclei of about 1.45 μm are sufficient to initiate cavitation within water mass at a negative pressure of about 100 kPa.

The above-mentioned two alternative mechanisms of air entry suffer from the same fundamental shortcoming: lack of direct experimental evidence. Each of them is based on some ancillary hypotheses that may be questioned. The common trait of both the mechanisms is that each of them takes place initially at the external boundary of the drying body, and that in both the cases, the direct driving variable is the negative water pressure, which attains a threshold value. Most interestingly, numerically, the threshold values for the two mechanisms are expressed through the same equation (equation [3.5] or [3.6]) at $r_c^b = a$. Indeed, they relate to a surface tension controlled radius

of curvature of a liquid–vapor interface. This coincidence did not escape the attention of [SCH 95], in the context of Scherer's comprehensive study of drying of silica gels. However, they underline that "cavitation… within the (drying) front… would be undistinguishable from regular emptying of pores". Needless to say, these phenomena still represent different events. In the meniscus hypothesis, the interface is between the liquid and an open, even if bound by a curved surface vapor, and moves inward, relative to its previous position. In the water tensile strength hypothesis, the interface is between water and its vapor enclosed by the bubble, which moves outward. However, the specific dynamics of the bubble depends on many factors, such as bubble flattening and effect of latent heat (see e.g. [YAN 08]), and when a bubble eventually bursts, the interface does move inward, over a finite distance of the current bubble diameter. Reports of drying front advancement via abrupt jumps (Haines jumps, see e.g. [HAI 25, RAN 78, RAM 08, SHA 86]) and recent molecular dynamics simulations make the latter interpretation even more plausible. In what follows, we have discussed the air entry criterion as a phenomenological one, also invoking the fact that it has been corroborated to hold true for many soils tested by independent operators [FRE 93].

Based on the actual porosimetry data for Bioley clayey silt and Sion silt [PER 08], a microscale hydromechanical model has been proposed to simulate the shrinkage deformation and subsequent air entry occurring at different moments in the cylindrical pore vessels (see [HU 08a, HU 08b, HU 10]). The model exploits the idea of [OR 02], according to which the size of a cavitation-created bubble is equal to the size of the soil pore vessel. For the bimodal pore model, it was found that water in larger pores cavitates much earlier than in smaller pores. An averaged suction-saturation-deformation pattern seen in macroscopic experiments has been reproduced by the two-pore system [HU 08a, HU 08b, HU 07, HU 10a, HU 10b].

3.2.4. *Cracking*

Desiccation macro-cracks are likely to occur if the drying shrinkage is constrained [COR 60]. Typically, these constraints can arise from different causes [HUE 92]: (i) a frictional or any other traction or displacement boundary conditions, (ii) any eigen-stress concentrations within the soil sample, and (iii) intrinsic soil inhomogeneity factors, such as soil texture and soil structure, or simply, mineral inhomogeneities. In the field, cause (i) can

arise from any restraining structure, whereas cause (ii) occurs due to soil moisture gradients, which do not fulfill the strain compatibility conditions (see e.g. [KOW 03]). In this contribution, causes (i) and (ii) are focused. Irrespective of the soil internal structure, any soil element that is allowed to dry and its shrinkage is not constrained in its movement by the adjacent elements or boundary conditions, would not crack. In early studies, stress generation and subsequent cracking was related to the change in the rheological properties of soil during drying. Because of the liquid loss, the tensile forces generated by the constraint mechanisms explained earlier build up, and finally, are relieved by tensile failure and cracking [LAC 61].

As with most of the real materials under a generic load, the approach to soil drying failure criteria may either be macroscopic or microscopic. When the shrinkage deformations at a macroscale are expressed through a phenomenological approach, i.e. directly relating the development of shrinkage deformations to a non-mechanical variable such as water content, or a fluid variable such as suction, it is convenient to split the total strain increment $d\boldsymbol{\varepsilon}$ into a mechanical solid strain increment $d\boldsymbol{\varepsilon}^m$ and a shrinkage strain increment $d\boldsymbol{\varepsilon}^h$ as follows:

$$d\boldsymbol{\varepsilon} = d\boldsymbol{\varepsilon}^m + d\boldsymbol{\varepsilon}^h. \qquad [3.7]$$

In this way, desiccation-induced stress could be dealt with using an approach that is analogous to that used for thermal stress calculation. Many studies aimed at explaining the origin of tensile stress generation during desiccation have eventually used such an approach [KOW 03]. In reaction to any restraint in its shrinkage deformation, a total stress increment $d\boldsymbol{\sigma}$ arises in the considered element of soil. Such a stress increment could be expressed by:

$$d\boldsymbol{\sigma} = \mathbf{D}d\boldsymbol{\varepsilon}^m = \mathbf{D}(d\boldsymbol{\varepsilon} - d\boldsymbol{\varepsilon}^h), \qquad [3.8]$$

where $\mathbf{D}$ is the stiffness matrix.

Experimental evidence clearly shows that desiccation cracking mainly occurs in Mode I (i.e. opening mode), indicating that cracking is the result of soil tensile strength mobilization, as commonly acknowledged. Prediction of desiccation cracking thus necessitates determination of tensile strength.

Most of the existing yield and failure criteria for soils relate to compression behavior involving shear resistance. This is not surprising because the tensile strength of soils is usually very small [MIT 05].

Morris *et al.* [MOR 92] have suggested a criterion for cracking initiation based on a modification of the Mohr-Coulomb criterion in the tensile range. It is assumed that the soil tensile strength and apparent cohesion (denoted as c_{app}) increase linearly with the increase in suction. An arbitrary value of a coefficient α_t is set such that $\sigma_t=\alpha_t c_{app}\cot\phi$, where σ_t is the absolute value of tensile strength and ϕ the friction angle. The authors have suggested that $\sigma_t=c_{app}/2$. For the usual friction angles, we can realize that such a value is close to a "corrected" tensile strength deduced from Mohr-Coulomb criterion, for which the tensile stresses normal to the shearing plane are not allowed [PER 08]: $\sigma_t=c_{app}\cos\phi/(1+\sin\phi)$.

However, in order to effectively account for desiccation cracking, a more specific tensile failure mechanism must be addressed. In this sense, micro- or meso-scale considerations are often resorted to. In the first place, Griffith's criterion deserves consideration. Griffith [GRI 24], working on elastic materials, considered the numerous minute cracks and defects in the materials that were "naturally" present at all times, and derived the value of the minor principal stress at failure, defined as the tensile strength. Griffith's criterion is routinely used in rock mechanics to interpret tensile failure. In soil mechanics, it has also been invoked to interpret several macroscopic traction test results [BIS 69].

As soil undergoes drying, it exhibits suction change, which, in turn, causes the inter-particle forces to increase. An apparent cohesion is thus generated, and consequently, a tensile strength. There is thus a coupling between suction and tensile strength, which was recognized early in the study of this field. Some authors, e.g. [SCH 82] and [KIM 03], have attempted to directly relate tensile strength to the normal inter-particle force, calculated from microscale considerations. Considering Griffith theory of tensile failure, it is believed that such approaches give only a partial view of the real mechanisms related to macroscopic tensile failure and the way in which tensile strength evolves during drying. Thus, these mechanisms remain poorly understood.

By adopting a total (or net) stress interpretation of the processes leading to cracking, [SNY 85] combined an expression of intergranular stress for

unsaturated soil with the notions from Griffith's theory of fracture of flawed elastic solids, leading to an expression for the tensile strength:

$$\sigma_t = \frac{\chi}{f_{flaw}} s, \qquad [3.9]$$

where f_{flaw} accounts for the shape and size of the so-called flaw and χ depends on the degree of saturation. The ratio χ/f_{flaw} decreases with the saturation degree; it is almost 1 when the pores are small, and can reach very low values if pores are big. For a saturated soil, $\sigma_t=s$. In the case of uniformly packed particles (no flaws), $f_{flaw}=1$, and $\sigma_t=\chi s$. The criterion expresses the fact that tensile strength depends on the degree of saturation and suction, and is also related to the most critical flaw in the sense of Griffith's theory. A large air-filled pore can play the role of a crack inceptor.

A specifically drying-oriented fracture mechanism has been proposed for silica gels by [SCH 92]. Similar to high water content soils, silica gels show shrinkage limit, air entry, and cracking in a very quick succession. Scherer envisions failure as an activation (growth) of a pre-existing crack-like flaw in a silica gel body, extending from its surface to certain depth, at least one order of magnitude larger than a typical pore size. Such micro-flaws are most likely to be present at the silica gel surfaces, and also at the soil body surfaces. A pre-requisite of the activation is the prior air entry, such as to generate a meniscus located near the crack tip.

In the stress analysis of drying porous medium, it is important to strictly distinguish between the total stress analysis (the one adopted up to this point in the present section) and effective stress analysis. In the former case, similar to thermal cooling, a near-surface soil layer is likely to be under tensile total stress due to reaction forces to the constraint of any of the above-listed sources. Scherer [SCH 92] explicitly addresses the case of the constraints induced through inhomogeneity due to non-uniform water withdrawal during transient water loss. In such a case, the surface will be under tensile total stress, with a compressed center. However, when analyzing the effective stress, we need to consider evaporation-driven suction in water, which is the largest at the body surface. This suction is usually larger than the total tensile stress, producing the largest effective stress compression at the surface. However, contrary to a straightforward expectation, tensile cracks propagate from the flaws in the compressive zone. Scherer proposes this apparent

paradox to be deconstructed by employing a local fracture condition at the tip of a pre-existing flaw.

The main postulate of this condition is that a flaw becomes activated when it is drained from almost all water, and filled only at a tip with water under a meniscus (). Therefore, a crack-face becomes a part of the "external" boundary, at which the conditions for the air entry are the same as described in section 2.3. This certainly must occur after the menisci in pores have shrunk to the size of the pores, and the suction (negative pore pressure) is the highest within the body. The surroundings of the crack are subjected to self-equilibrating tensile total stress, which is a function of the pore water suction (as this is an externally unconstrained body; see also [BRI 90]). We take advantage of one of the principal findings of fracture mechanics that the remotely acting tensile stress becomes dramatically amplified at the crack tip. Consequently, we find a much higher total tensile stress locally at the tip, than the external one. By assuming the plastic field near the tip to be very small and using the effective stress definition, following [SCH 92], the maximum effective stress at the crack tip can be given as:

$$\sigma_{\mathrm{c}}'^{\max} = 2B\sigma_x\sqrt{\frac{c}{r_{\mathrm{c}}}} + np_{\mathrm{l}}, \qquad [3.10]$$

where B=1.12 is a constant, n is the porosity, c the flaw depth, r_{c} the finite curvature radius of the flaw tip, and σ_x the total (tensile) stress induced by suction at the boundaries of a representative elementary volume (see [BRI 90]),

$$\sigma_x = \frac{1-2\nu}{1-\nu}(p_{\mathrm{l}} - \langle p_{\mathrm{l}}\rangle), \qquad [3.11]$$

where $\langle p_{\mathrm{l}}\rangle$ is an average partial liquid stress. This is a self-equilibrated stress for the no-external constraint case, considered by [SCH 90]. For the externally kinematically constrained bodies, the total stress is enhanced by the tensile contribution from the reaction forces.

The most important conclusion from equation [3.10] is that for sufficiently large ratio c/r_{c}, the effective stress at the tip *is tensile*, and may reach Mode I critical stress intensity factor of the solid, $K_{\mathrm{Ic}}^{\mathrm{s}}$, giving rise to crack propagation and failure.

Hence, the criterion for drying cracking (or crack propagation) is:

$$B\sigma_{\mathrm{c}}'^{\max}\sqrt{\pi c'} \geq K_{\mathrm{Ic}}^{\mathrm{s}}, \qquad [3.12]$$

where c' is the depth of the crack of a failing element of the microstructure. As σ_x in the right-hand side of equation [3.10] is a function of water pressure, the criterion given by equation [3.12] eventually provides a limiting suction against tensile cracking, while the effective stress throughout most of the body is compressive. Two parameters, the radius of the tip, r_{c} and the depth c' are hardly material characteristics. For silica gels, [SCH 92] has managed to express equation [3.12] in terms of measurable quantities,

$$\sigma_x \geq \frac{1}{B\sqrt{\pi}} K_{\mathrm{Ic}}, \qquad [3.13]$$

where K_{IC} is the critical stress intensity factor in terms of total stresses, measured in perfectly drained conditions.

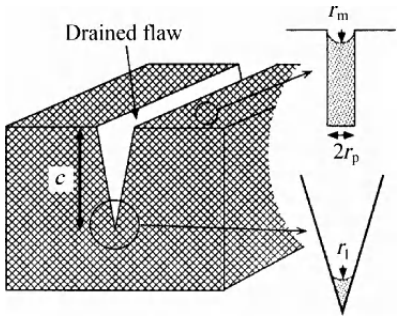

Figure 3.1. *Simplified model for surface flaw of length c at the inception of cracking in a gel, following modification by [SCH 92]. r_m is the radius of the meniscus in a pore of radius r_p located in the bulk of the gel. r_l is the radius of curvature of the liquid in the flaw*

While it may be questionable that desiccation shrinkage is considered as elastic, as it is mainly irreversible, nevertheless, the use of linear elastic fracture mechanics may be considered, just as a convenient numerical expedient.

3.3. Experimental characterization of desiccation process in soils and its controlling variables

It is intended here to quantify the processes of drying shrinkage leading to desiccation cracking in soils, by establishing experimental relationships between drying and cracking on the one hand, and physical variables at the macroscale on the other hand. The variables investigated are water content, suction, saturation degree, strains, stresses, and crack geometry. Konrad and Ayad [KON 97] performed field desiccation experiments on intact clay, while [MIL 98] carried out a small-scale desiccation test on landfill liners. Both the studies mainly focused on suction evolution during drying and crack pattern geometry, without addressing shrinkage mechanisms and mechanical conditions of crack initiation. [KLE 85, DAN 93, and ALB 01] conducted desiccation tests on compacted soils used for clay liners and covers. Their main aim was to estimate the hydraulic conductivity decay of such cracked soil specimens. Only a few empirical relationships between cracking potential, shrinkage strains, and compaction conditions have been proposed.

A paramount question that arises during an investigation of desiccation in an initially saturated soil is whether cracking occurs when the soil is still saturated. Related to this topic, cavitation is invocated as a fundamental mechanism of cracking initiation in material such as gels ([SCH 90, SCH 92]; see section 2.4), but this requires clarifications when dealing with soils. Some insights into the relationship between cracking and pore water cavitation onset have been provided by [HU 08a, HU 08b]. Finally, it has been repeatedly noted that desiccation crack patterns show remarkable periodicity, both in nature and in the laboratory, and their quantification remains elusive for soils.

3.3.1. *Desiccation tests*

3.3.1.1. *Desiccation tests on 1D bars*

Clayey silt from Bioley (Switzerland) was prepared as a saturated slurry (gravimetric water content w=49%) and shaped into rectangular bars (length 300 mm, width 50 mm, thickness 12 mm). Details of the experiments can be found in [PER 09a, PER 09b] and in [HU 06]. Two types of tests were carried out: free desiccation tests and constrained desiccation tests. Free desiccation tests consisted of drying a bar at a fixed temperature (18°C) and relative humidity (40%) on a Teflon substrate (which minimizes the boundary constraint). Strain/water content data were obtained by calliper measurements

and weighing. Water content repartition throughout the sample was also monitored. For constrained desiccation tests, a constraint was created at the bottom surface in the axial direction only, by using a substrate with thin parallel lateral notches. In both the cases, horizontal strains were measured at mid thickness, while vertical strain was measured at the center of the bar.

In all the free desiccation tests, none of the bars experienced cracking. The strain/water content evolution from w=32% (liquid limit value) to 20% (shrinkage limit) was quasi-linear and isotropic. Above the liquid limit, the bar was in a quasi-liquid state, and its behavior is not considered here. Local water content measurements revealed small heterogeneities between the bar center and extremities, which disappeared below w=25%.

In all the constrained desiccation tests, due to the parallel notches, the value of axial strains was 0.5% at the onset of cracking, and hence, much lower than those obtained in the free desiccation tests at comparable water content. Strains in the transversal direction were also lower (due to a slight friction). In turn, vertical strains were larger. Cracks appeared successively in the bar at an average water content range between 24 and 22%. They formed a parallel set normal to the axial constraint (see Figure 3.2). Several cracks often formed simultaneously; more commonly, they would cut the bar into two pieces, and then the formed pieces were again cut into two pieces. Just before the appearance of the main cracks, small, localized cracks were observed at the bar's bottom corner, causing a slight detachment of the bar extremities from the support.

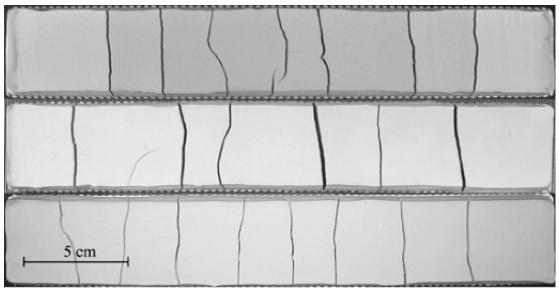

Figure 3.2. *Examples of desiccation crack 1D patterns*

3.3.1.2. *Desiccation tests on 2D slabs*

Desiccation tests were performed, for which a bottom substrate was devised with 2D constraints, instead of the 1D constraint considered so far.

Slabs with two different thicknesses (4 and 12 mm) were tested. All the tested samples cracked, leading to the formation of a 2D net of cracks (see Figure 3.3). Marked differences were observed between samples that were 4 mm high and those that were 12 mm high. The former experienced a large number (from 160 to 352) of relatively thin cracks; the latter experienced a small number of relatively wide cracks (from 16 to 31). Corte and Higashi [COR 60] observed the same trend in drying square-shaped slabs.

Crack intersecting angles were also measured. Generally, cracks intersect at about 90°, up to about 150°, and angles above and beyond this range are rare. During tests with 4 mm high slabs, it was observed that some groups of three cracks intersecting at 120° had the tendency to appear simultaneously, especially at the beginning of the cracking stage (Figure 3.3(c), circled cracks). Upon further desiccation, the crack pattern changed, and cracks tended to meet other existing cracks that formed an angle of about 90° (Figure 3.3(d), photograph taken 4 h later when all the cracks were formed). It appears that a 2D constraint tends to originate two limiting kinds of crack patterns: 90° intersecting and 120° intersecting cracks. It can be deduced that the geometry of the crack pattern strongly depends on the nature of the boundary constraint and the sample geometry.

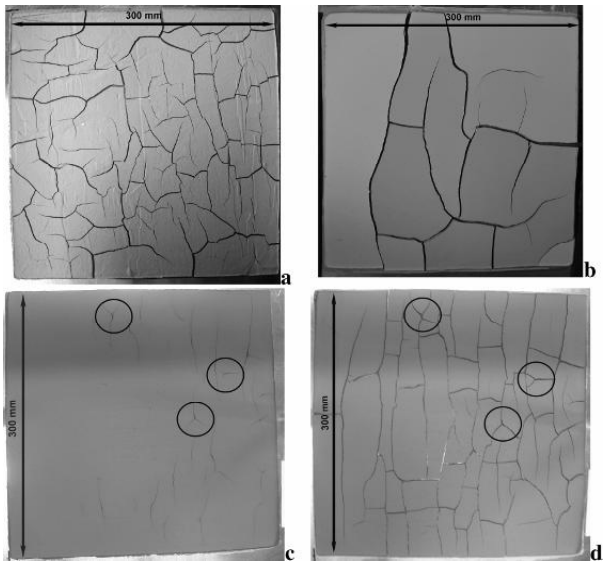

Figure 3.3. *Examples of desiccation crack 2D patterns; (a) 4 mm high slab; (b) 12 mm high slab; (c) initial stage of cracking: 120° intercepting cracks circled; and (d) final stage of cracking: 120° intercepting cracks circled (4 mm high slab)*

3.3.2. *Drying shrinkage*

Apart from the desiccation tests, a water retention curve (WRC) was determined for Bioley clayey silt (i.e. the soil used for desiccation tests, see the previous section) as well as two other soils, namely, Sion silt and La Frasse clay. The strains and the degree of saturation at different stages of drying and rewetting were determined [PER 07a, PER 07b] for the above-mentioned soils. Figure 3.4 features the obtained WRC. It appears that [PER 09a, PER 09b]:

– Air entry value and shrinkage limit are very close to each other.

– Strains experienced during desiccation up to the air entry value (as long as S_r remains close to 100%) are mainly irreversible; this stage is followed by a domain with lower and mostly reversible deformations at decreasing S_r.

– Cracking does not take place in unconstrained specimens. In the constrained specimens, it occurs very closely after the end of shrinkage and very soon after (and very close to) the air entry. This observation is confirmed by tests on other materials (a silt and a silty clay). This behavior is highlighted in Figure 3.5, in which the evolution of the degree of saturation is reported as drying proceeds, as well as the moment of cracking initiation, for the three soils. Cracking initiates at degree of saturation values close to 95%.

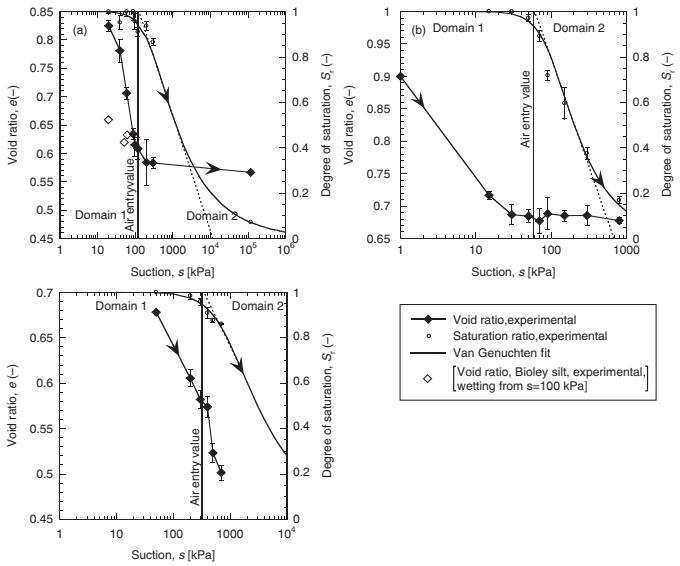

Figure 3.4. *WRC for three soils: (a) Bioley silt, (b) Sion silt and (c) La Frasse clay*

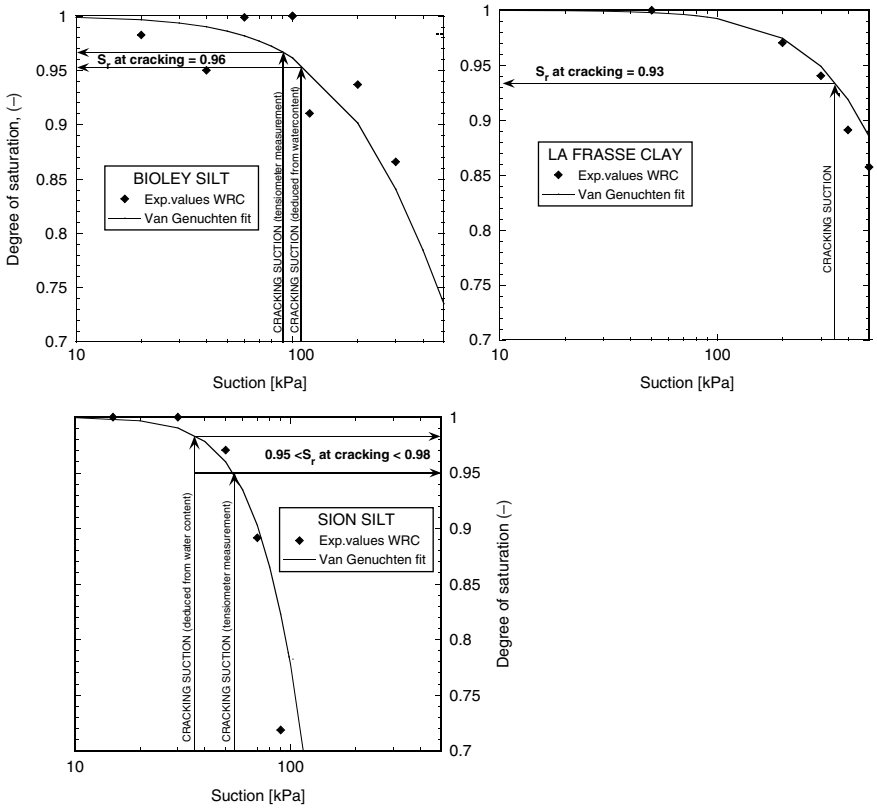

Figure 3.5. *Degree of saturation at the time of cracking Bioley clayey silt, La Frasse clay and Sion silt*

3.3.3. *Desiccation cracking initiation conditions in soils*

Some prior results [AVI 04, AYA 97, COR 60, NAH 04] are close to the present findings that desiccation cracking of initially saturated and remolded soils occurs when the overall degree of saturation is 100%. In an attempt to shed light on the role of the air entry in crack initiation in saturation conditions, it may be useful to address the phenomena arising during drying at the soil pore scale. Some earlier studies have proposed that defects and air-filled pores may act as crack initiators in soils [FRY 67, MOR 92, SNY 85].

By resuming our parallel with gels, it is of great interest that drying gel cracking has a tendency to occur because the material degree of saturation is still very close to 100% (within the measurement error range), and its water content is not far from air entry and shrinkage limit [DWI 86, SIM 89] in laboratory tests. Cracking near the air entry value has been linked to the formation of a drying front in the gel at the moment of air entry. Drained zones with a certain extension, shape, and orientation with respect to the stress field could be considered as defects controlling the conditions for crack inception [SCH 90, SCH 92].

It appears that for soils as well, the air entry is a precursor event for cracking. In none of the tests, it took place after the formation of cracks. And it certainly is not a sufficient condition for cracking, which never happened in the unconstrained tests. Nevertheless, the actual mechanism of air entry is poorly understood and in need of thorough investigations.

3.4. Scenarios of soil desiccation crack pattern formation

3.4.1. *Interpretation of desiccation of bars (1D case)*

To further quantify the desiccation process in soils, a stress field arising from the desiccation experiments of the bar (section 3.1.1) has been modeled using finite elements. Strains are here viewed as a combination of a drying shrinkage-induced (volumetric) part, ε^{h}, proportional to water content change, Δw, and a mechanical part generated to satisfy strain compatibility (which induces stresses). Subsequently, the analogy between the equation describing moisture transport and the elastic response to changes in water content, on the one hand, and the thermoelasticity of the heat-diffusing elastic medium, on the other hand, has been used. It should be noted again that this is a single-phase (hence, total stress) approach. No pore water pressure and/or effective stress effects have been addressed. The elastic formulation that is used here produces a valid stress field [PER 09a, PER 09b], but we must be aware that most of the deformations produced during the first drying of a soil mass are irreversible, as presented in section 3.2.

The field and constitutive equations of the numerical model are hereafter summarized. The linear momentum conservation law is given as:

$$\nabla \boldsymbol{\sigma} + \rho \mathbf{g} = 0, \qquad [3.14]$$

where $\boldsymbol{\sigma}$ is the total (Cauchy) stress tensor with tensile stresses taken as positive and ρ the total mass density of the medium.

In what follows, we have limited our considerations to the linear, small strain theories. The mechanical behavior of the whole medium is assumed to be governed by the total stress, which is related to a mechanical elastic strain $\boldsymbol{\varepsilon}^{\mathrm{me}}$ through:

$$\boldsymbol{\sigma} = \mathbf{D} : \boldsymbol{\varepsilon}^{\mathrm{me}}, \qquad [3.15]$$

where $\mathbf{D}$ is the linear elastic constitutive tensor.

By assuming that drying-induced water mass transfer through the body is solely governed by a diffusion law and neglecting the deformation influence on water mass transfer [PER 08], mass conservation of water states:

$$\partial_{\mathrm{t}} w - \nabla[\lambda \nabla w] = 0, \qquad [3.16]$$

where λ is a diffusivity coefficient [$\mathrm{m}^2\ \mathrm{s}^{-1}$] and w the gravimetric water content.

The total strain (positive in compression) is divided into two parts, the drying-induced part due to water mass removal and the mechanical part due to total stress variation. The mechanical strain rate is assumed to be purely elastic and the drying-induced strain rate is assumed to be proportional and opposite in sign to water content increment dw. These assumptions lead to:

$$\mathrm{d}\varepsilon_{\mathrm{v}} = \frac{\mathrm{d}p}{K} + \alpha\, \mathrm{d}w; \quad \mathrm{d}\varepsilon_{\mathrm{d}} = \frac{\mathrm{d}q}{3G}, \qquad [3.17]$$

where K and G are the bulk and shear elastic moduli, respectively; $\mathrm{d}\varepsilon_{\mathrm{v}}$ and $\mathrm{d}\varepsilon_{\mathrm{d}}$ are the volumetric and deviatoric strain rate invariants, respectively; p and q are the mean and deviatoric stress invariants, respectively; and α is a hydric shrinkage coefficient.

By considering the boundary conditions, the weak form of the governing equations may be obtained through a variational approach. The governing equations written in matrix form become:

$$\begin{bmatrix} \mathbf{K} & 0 \\ 0 & \mathbf{H_1} \end{bmatrix} \begin{Bmatrix} \bar{\mathbf{u}} \\ \bar{w} \end{Bmatrix} + \begin{bmatrix} 0 & 0 \\ 0 & \mathbf{H_2} \end{bmatrix} \begin{Bmatrix} 0 \\ \partial_t \bar{w} \end{Bmatrix} = \begin{Bmatrix} \mathbf{f_u} \\ \mathbf{f_w} \end{Bmatrix}, \quad [3.18]$$

where $\bar{\mathbf{u}}$ and $\bar{w}$ are the nodal unknowns, $\mathbf{K}$ is the stiffness matrix, $\mathbf{H_1}$ is a "water diffusivity" matrix, $\mathbf{H_2}$ is a time dependence matrix, and $\mathbf{f_u}$ and $\mathbf{f_w}$ are the nodal flux vectors.

The formulation of the problem is analogous to thermal diffusion in an elastic body. It can be solved as follows. First, a strain-independent water content field is determined. Then, the water content field intervenes as a solicitation for the determination of the displacement field. Eventually, in equation [3.18], the term f_u includes a nodal force term due to the drying-induced strain, deduced from the water content.

A 2D model of the bar used in the desiccation tests has been examined. The bar (under plain strain hypothesis) has been subjected to a condition of zero displacement at the bottom. Drying boundary conditions consist of imposing decreasing water content values on the surfaces of the top and side extremities of the bar, with a constant rate of 1.2% per hour (as recorded during the experiments). The simulation has been performed with the finite element code GefDyn [AUB 95, MOD 91]. Linear elements are used for the calculation of water content, and quadratic elements are employed for the displacements calculation. An implicit time integration scheme is adopted. The extensive results can be found in [HU 06] and [PER 08]; only the main results regarding the crack initiation location are summarized here.

The results (Figure 3.6) show that the maximum tensile total stress of 5.18 kPa (in absolute value) in the horizontal direction is reached at the bar top along the central vertical section (although the minor stress is almost constant in a large central part of the bar), indicating that the first vertical crack would initiate at this location. This is under the assumption that a tension cutoff yield criterion was used. Under the conditions of simulation, fracture mechanics theory shows that such a crack is unstable [BAI 00], and

should fully propagate through the specimen thickness, splitting the bar into two halves and entailing a complete (or partial) axial stress relief. A subsequent shrinkage and cracking process would resume independently in the newly formed half-bars resulting from the first vertical cracking, leading to the formation of a regular crack spacing. As a deviation from this scheme, it is noted here that many times, cracks appeared simultaneously within the bar.

The slight detachment experimentally observed near the bottom extremity is explained by the shear effect. It induces large but concentrated tensile stresses, generating conditions for early crack formation. The complex stress field in this zone certainly prevents from larger crack extension.

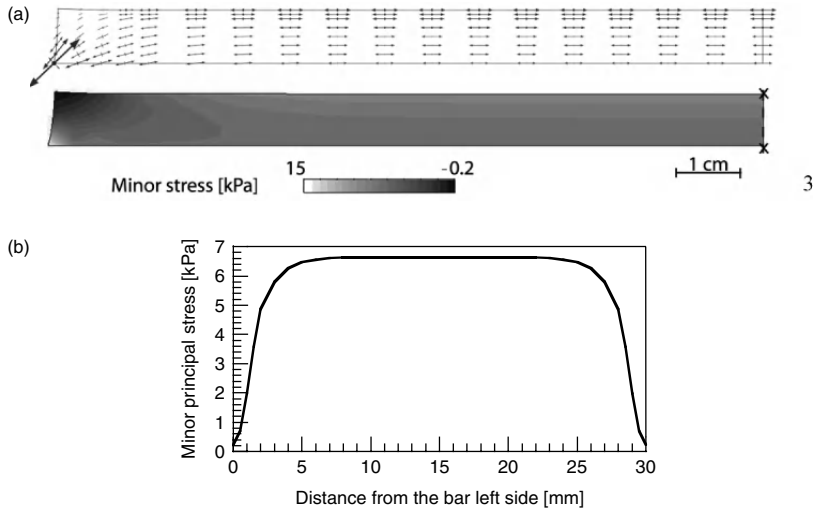

Figure 3.6. *Simulation of constrained desiccation tests (tensile stresses positive): (a) minor principal stress field (half bar), onset of cracking and (b) minor principal stress evolution along the bar top surface*

The above-mentioned analysis results are obtained under the assumption that failure is controlled by total stress. This is certainly one possible representation. As presented in section 2.4, an alternative effective stress approach is quite promising. However, the criterion for crack propagation and ensuing failure needs to be expressed via a local condition for effective stress at the vicinity of a pre-existing flaw, where tensile-effective stress may

arise in the strictly localized neighborhood of the flaw tip. This approach is pursued in a separate forthcoming publication.

3.4.2. *Interpretation of desiccation of slabs (2D case)*

The formation of the 2D crack patterns observed in section 3.1.2 is now addressed. The interpretation of the 90° crack intersection angle is straightforward. Once a crack has formed, tensile stresses perpendicular to the crack axis are released near the crack. A propagating crack, when approaching the vicinity of another existing crack, tends to orientate in the direction perpendicular to the local maximum tensile stress, i.e. parallel to the existing crack.

The case of 120° intersection angles results from an energy minimization process, as demonstrated earlier for soils and reported by [COR 60]. First, cracking, by creating new solid surfaces, is an energy-consuming process. Consider an infinite slab subjected to a horizontal 2D constraint while it dries. If the tensile stress at a given point is isotropic, then the sample tends to crack along several planes of failure. Of the infinite theoretical possibilities, failure will occur in three planes oriented at 120°, because this geometry produces the lowest crack area enclosing the maximum soil volume and thus enables the consumption of a minimum surface energy per unit volume. This reflects the tendency of any physical process to do the most with the least.

The interpretation provided in section 5.1 for 1D crack patterns can be extended to the 2D case in order to interpret the ensuing patterns with regular crack spacing also observed in this case.

3.4.3. *Further considerations*

With the interpretation similar to that of section 5.1, Groisman and Kaplan [GRO 94] proposed to relate crack spacing to dried slab thickness. Desiccation of circular slabs was considered, whose shrinkage was restrained in the horizontal plane because of friction between the soil and its bottom support. The process of fragmentation of the specimen consists of a successive cracking of individual cells between adjacent cracks, where the total stress reaches the tensile strength. The process must stop when the dimension of the cells drops below a critical value, as the bottom friction

ceases to supply the stress needed for cracking. Such a critical value directly depends on the thickness of the cell.

In conclusion, if we assume that cracks form successively in locations well defined by the total stress field and boundary conditions, it is relatively easy to interpret the formation of the crack pattern. Final crack spacing should be the consequence of changes in the tensile strength or other material properties. When the crack pattern emerges from a homogeneous stress field, it is less straightforward to quantify the observed process. Therefore, fracture mechanics should be invoked, i.e. global energy considerations. Derivation of crack spacing using such an approach can be found in [PER 09a, PER 09b], as well as in [BAZ 91].

3.5. Conclusion

Desiccation can be seen as a set of processes that include surface evaporation, shrinkage, possible air-entry, and cracking. For a relatively high saturation ratio and continuous liquid phase, the basic process behind the shrinkage of a soil is a liquid pressure decrease/suction increase, caused by evaporation flux at the level of menisci, which acts as an attractive force between the components of the matrix. Therefore, the matrix suffers an increasing internal compression and the sample shrinks. Experimental evidence clearly shows that desiccation cracking occurs in Mode I (i.e. opening mode), indicating that cracking initiation is the result of soil tensile strength mobilization. The factors controlling shrinkage and cracking were examined. Based on this analysis, the following conclusion can be drawn:

– Free desiccation tests on initially saturated slurries confirm the general characteristics well known from WRC studies, i.e. the existence of two distinct domains for drying shrinkage (Domain 1 at a degree of saturation close to 1, with mostly irreversible deformation, and Domain 2 at a decreasing degree of saturation, with a much smaller deformation, mainly reversible).

– The experimental results presented in this chapter show that desiccation cracking occurs in Domain 1 at non-zero suction and at a degree of saturation almost equal to 100%, close to the onset of air entry. The increase in suction in the drying body alters the liquid-phase repartition (degree of

saturation) and occupation of the porous space; this modifies the conditions for desiccation-crack initiation during drying.

– The stress states that lead to desiccation cracking clearly result from the presence of restraining boundary conditions and/or moisture gradients. During this stage, a large part of deformation is irreversible. Stress builds up until a critical point at which the tensile strength is met. The crack patterns may be interpreted by examining the total stress field at that time. Regular crack pattern geometry then stems from a recursive process of reaching tensile strength, which ends once the conditions for crack initiation (or propagation) can no longer be reached.

– An alternative effective stress approach to failure requires a localized (or microscopic) failure condition to be met at a site of a strict vicinity of a tip of a random flaw, where tensile effective stress can develop within the otherwise compressive macroscale effective stress field.

– The role of desiccation cracking in the behavior of unsaturated soils is equally important, as it is poorly understood. In general conditions, cracking depends on both stress and strain history, in addition to the history of kinematic constraints, and finally, the history of water content.

– In the cases investigated, we realized that the initial cracking during the drying of initially saturated soil takes place very soon after the degree of saturation starts to decrease. Thus, any further desaturation occurs in the presence of and concomitant with further development of cracking. Their presence and evolution may hardly be without any fundamental effect on both mechanical and permeability properties.

3.6. Bibliography

[ABU 93] ABU HEJLEH A., Desiccation theory for soft cohesive soils, PhD Thesis, University of Colorado, Boulder, 1993.

[ALB 01] ALBRECHT B.A, BENSON C.H., “Effect of desiccation on compacted natural clay”, *Journal of Geotechnical and Geoenvironmental Engineering*, vol. 127, no. 1, p. 67-75, 2001.

[AUB 95] AUBRY D., CHOUVET D., MODARESSI A., MODARESSI, H., Gefdyn: logiciel d’analyse du comportement mécanique des sols par éléments finis avec prise en compte du couplage sol-eau-air, Report, Ecole Centrale Paris, 1995.

[AVI 04] AVILÁ G., Estudio de la retracción y el agritamiento de arcillas – Aplicación a la arcilla de Bogota, PhD Thesis, Universitat Politecnica de Catalunya, Barcelona, 2004.

[AYA 97] AYAD R., KONRAD J.M., SOULIÉ M., "Desiccation of a sensitive clay: application of the model CRACK", *Canadian Geotechnical Journal*, vol. 34, p. 942-951, 1997.

[BAG 97] BAGGIO P., BONACINA C., SCHREFLER, B.A., "Some considerations on modelling heat and mass transfer in porous media", *Transport Porous Med.*, vol. 8, p. 233-251, 1997.

[BAI 00] BAI T., POLLARD D.D., GAO H., "Explanation for fracture spacing in layered materials", *Nature*, vol. 403, p. 753-756, 2000.

[BAZ 91] BAZANT Z.P., CEDOLIN L., *Stability of Structures – Elastic, Inelastic, Fracture, and Damage Theories*, Oxford University Press, 1991.

[BEN 82] BÉNET JC, JOUANNA P., "Phenomenological relation of phase change of water in a porous medium: experimental verification and measurement of the phenomenological coefficient", *International Journal of Heat and Mass Transfer*, vol. 25, p. 1747-1754, 1982.

[BIS 69] BISHOP A., GARGA, V., "Drained tension tests on London Clay", *Géotechnique*, vol. 19, p. 309-313, 1969.

[BRI 90] BRINKER C.J., SCHERER G.W. *Sol-Gel Science: The Physics and Chemistry of Sol-Gel Processing*, Academic Press, New York/London, 1990.

[CAM 05] CAMASSEL B., SGHAIER N., PRATA M., BEN NASRALLAHAND S., "Evaporation in a capillary tube of square cross section: application to ion transport", *Chemical Engineering Science*, vol. 60, no. 3, p. 815-826, 2005.

[COR 60] CORTE A., HIGASHI A., Experimental Research on Desiccation Cracks in Soil, Research report 66, US Army Snow and Ice and Permafrost Research Establishment, 1960.

[COU 98] COUSSY O., EYMARD R., LASSABATÈRE T., "Constitutive modelling of unsaturated drying deformable media", *Journal of Engineering Mechanics, ASCE*, vol. 124, no. 6, p. 658-667, 1998.

[DAN 93] DANIEL D., WU, Y., "Compacted clay liners and covers for arid sites", *Journal of Geotechnical Engineering, ASCE*, vol. 119, no. 2, p. 223-237, 1993.

[DWI 86] DWIVEDI K., "Drying behaviour of alumina gels", *Journal of Materials Science Letters*, vol. 5, p. 373-376, 1986.

[FRE 93] FREDLUND D.G., RAHARDJO H., *Soil Mechanics for Unsaturated Soils*, John Wiley & Sons, 1993.

[FRY 67] FRYDMAN S., "Triaxial and tensile strength tests on stabilized soil", *Proceedings of the third Asian Regional Conference on Soil Mechanics and Foundation Engineering*, Haifa, p. 269-275, 1967.

[GRI 24] GRIFFITH A.A., "Theory of rupture", Proceedings of the First International Conference on Applied Mechanics, Delft, p. 55-63, 1924.

[GRO 94] GROISMAN A., KAPLAN, E., "An experimental study of cracking induced by desiccation", *Europhysics Letters*, vol. 25, no. 6, p. 415-420, 1994.

[HAI 25] HAINES W.B., "Studies in the physical properties of soils II A note on the cohesion developed by capillary forces in an ideal soil", *Journal of Agricultural Science*, vol. 15, p 529-535, 1925.

[HU 06] HU L., PERON H., HUECKEL T., LALOUI L., "Numerical and phenomenological study of desiccation of soil", *Advances in Unsaturated Soil, Seepage, and Environmental Geotechnics*, ASCE Geotechnical Special Publication 148, p. 166-173, 2006.

[HU 07] HU L.B., PERON H., HUECKEL T., LALOUI L., "Drying shrinkage of deformable porous media: mechanisms included by the fluid removal", *Computer Applications in Geotechnical Engineering*, in Geotechnical Special Publication No. 154, SIEGEL T., LUNA R., HUECKEL T., LALOUI L. (eds.), Washington, DC, ASCE, 2007.

[HU 08a] HU L.B., Physico-chemo-mechanical coupling mechanisms in soil behaviour, PhD Dissertation, Duke University, North Carolina, USA, 2008.

[HU 08b] HU L., HUECKEL T., PERON H., LALOUI L., "Modeling evaporation, shrinkage and cracking of desiccating soils", *12th International Conference of International Association for Computer Methods and Advances in Geomechanics (IACMAG)*, p. 1083-1090, 2008.

[HU 10a] HU L.B., PERON H., HUECKEL T., LALOUI L., "Desiccation Shrinkage of Silts and Sands. Part 1: Concepts and a Microstructural Model", *Computers and Geotechnics*, submitted, 2010.

[HU 10b] HU L.B., PERON H., HUECKEL T., LALOUI L., "Desiccation Shrinkage of Silts and Sands. Part 2: A Numerical Study", *Computers and Geotechnics*, submitted, 2010.

[HUE 92] HUECKEL T., "On effective stress concept and deformation in clays subjected to environmental loads: discussion", *Canadian Geotechnical Journal*, vol. 29, p. 1120-1125, 1992.

[JON 92] JONES F.E., *Evaporation of Water*, Lewis Publishers, 1992.

[KIM 03] KIM T., HWANG C., "Modelling of tensile strength on moist granular earth material at low water content", *Engineering Geology*, vol. 69, p. 233-244, 2003.

[KLE 85] KLEPPE J.H., OLSON, R.E., "Desiccation cracking of soil barrier", *Hydraulic Barrier in Soil and Rock*, ASTM STP 874, p. 263-275, 1985.

[KNU 15] KNUDSEN M., "Maximum rate of evaporation of mercury", *Annalen der Physik*, vol. 47, p. 697–708, 1915.

[KON 97] KONRAD J.M., AYAD R., "An idealized framework for the analysis of cohesive soils undergoing desiccation", *Canadian Geotechnical Journal*, vol. 34, p. 477-488, 1997.

[KOW 03] KOWALSKI S.J., *Thermomechanics of Drying Processes*, Springer Verlag, 2003.

[KRO 99] KROTOV V.V., RUSANOV A.I., *Physicochemical Hydrodynamics of Capillary Systems*, Imperial College Press, London, 1999.

[LAC 61] LACHENBRUCH A.H., "Depth and spacing of tension cracks", *Journal of Geophysical Research*, vol. 66, no. 12, p. 4273-4292, 1961.

[LOZ 08] LOZANO A.L., CHERBLANC F., COUSIN B., BÉNET J.C., "Experimental study and modelling of the water phase change kinetics in soils", *European Journal of Soil Science*, vol. 59, no. 5, p. 939-949, 2008.

[MAI 01] MAINGUY M., COUSSY O., BAROGHEL-BOUNY, V., "Role of air pressure in drying of weakly permeable materials", *Journal of Engineering Mechanics, ASCE*, vol. 127, no. 6, p. 582-592, 2001.

[MIL 98] MILLER C.J., MI H., YESILLER N., "Experimental analysis of desiccation crack propagation in clay liners", *Water Resources Bulletin*, vol. 34, no. 3, p. 677-686, 1998.

[MIT 05] MITCHELL J.K., SOGA K., *Fundamentals of Soil Behaviour*, John Wiley & Sons, 2005.

[MOD 91] MODARESSI H., LALOUI L., AUBRY D., "Numerical modelling of thermal consolidation", *Second European Conference in Numerical Methods in Geotechnical Engineering*, Santander 90, p. 280-292, 1991.

[MOR 92] MORRIS P.H., GRAHAM J., WILLIAMS D.J., "Cracking in drying soils", *Canadian Geotechnical Journal*, vol. 29, p. 262-277, 1992.

[NAH 04] NAHLAWI H., Behaviour of a reactive soil during desiccation, Master Thesis, Monash University, Clayton, Australia, 2004.

[NUT 08] NUTH M, LALOUI L., "Effective stress concept in unsaturated soils: Clarification and validation of a unified framework", *International Journal for Numerical and Analytical Methods in Geomechanics*, vol. 32, p. 771-801, 2008.

[OER 71] OERTLI J.J. "The stability of water under tension in the xylem", *Zeitschrift für Pflanzenphysiologie*, vol 65, no. 3, p 195-209, 1971.

[OR 02] OR D., TULLER M., "Cavitation during desaturation of porous media under tension", *Water Resources Research*, vol. 38, no. 5, p. 19-1-19-4, 2002.

[PER 07a] PERON H., HU L., LALOUI L., HUECKEL T., "Mechanisms of desiccation cracking of soil: validation", *International Symposium on Numerical Models in Geomechanics* – NUMOG X, Taylor & Francis Group, p. 277-282, 2007.

[PER 07b] PERON H., HUECKEL T., LALOUI L., "An improved volume measurement for determining soil water retention curve", *Geotechnical Testing Journal*, vol. 30, no. 1, p. 1-8, 2007.

[PER 08] PERON H., Desiccation cracking of soils, PhD Thesis, Ecole Polytechnique Fédérale de Lausanne, 2008.

[PER 09a] PERON H., DELENNE J.Y., LALOUI L., EL YOUSSOUFI M.S., "Discrete element modelling of drying shrinkage and cracking of soils", *Computers and Geotechnics*, vol. 36, p. 61-69, 2009.

[PER 09b] PERON H., HUECKEL T., LALOUI L., HU L., "Fundamentals of desiccation cracking of fine-grained soils: experimental characterisation and mechanisms identification", *Canadian Geotechnical Journal*, vol. 46, 1177-1201, 2009.

[PHI 57] PHILIP J.R., DE VRIES D.A., "Moisture movement in porous materials under temperature gradients", *Transactions of the American Geophysical Union*, vol. 38, p. 222-232, 1957.

[PIC 81] PICKARD W.F., "The ascent of sap in plants", *Progress in Biophysics and Molecular Biology*, vol. 37, p. 181-229, 1981.

[PLA 06] PLATTEN J.K., "The Soret effect: a review of recent experimental results", *Journal of Applied Mechanics, ASME*, vol. 73, p. 5-15, 2006.

[RAM 08] RAMON G., ORON, A., "Capillary rise of a meniscus with phase change", *Journal of Colloid and Interface Science*, vol. 327,145-151, 2008.

[RAN 78] RAND R.H., "The dynamics of an evaporating meniscus", *Acta Mechanica*, vol. 29, p. 135-146, 1978.

[SCH 90] SCHERER G.W., "Theory of drying", *Journal of the American Ceramic Society*, vol. 73, no. 1, p. 3-14, 1990.

[SCH 82] SCHUBERT K., *Kapillarität in porösen Feststoffsystemen*, Springer Verlag, 1982.

[SCH 92] SCHERER G.W., "Crack-tip stress in gels", *Journal of Non-Crystalline Solids*, vol. 44, p. 210-216, 1992.

[SCH 95] SCHERER G.W., SMITH D.M., "Cavitation during drying of a gel", *Journal of Non-Crystalline Solids*, vol. 189, p. 197-211, 1995.

[SHA 86] SHAW, T.M., "Movement of a drying front in a porous material", *Materials Research Society Symposia Proceedings*, vol. 73, p. 215-223, 1986.

[SNY 85] SNYDER V.A., MILLER R.D., "Tensile strength of unsaturated soils", *Soil Science Society of America Journal*, vol. 49, p. 58-65, 1985.

[SIM 89] SIMPKINS G., JOHNSON JR. D.W., FLEMING D.A., "Drying behaviour of colloidal silica gels", *Journal of the American Ceramic Society*, vol. 72, no. 10, p. 1816-1821, 1989.

[TER 27] TERZAGHI, K., "Concrete roads – a problem in foundation engineering", *Boston Society of Civil Engineers*, vol. 14, no. 5, p. 265-282, 1927.

[VAN 63] VAN RYSSELBERGH P., *Thermodynamics of Irreversible Processes*, Blaisdell Publishing Company, Paris, 1963.

[WIN 71] WINNICK, J. AND CHO, S.J., "PVT behaviour of water at negative pressures", *Journal of Chemical Physics*, vol. 55, p. 2092-2097, 1971.

[YAN 08] YANG B., PROSPERETTI A., "Vapour bubble collapse in isothermal and non-isothermal liquids", *Journal of Fluid Mechanics*, vol. 601, pp 253-279, 2008.

[YAY 70] YAYANOS, A.A., "Equation of state for P-V isotherms of water and NaCl solutions", *Journal of Applied Physics*, vol. 41, p. 2259-2260, 1970.

[ZSI 11] ZSIGMONDY, R., "Über die Struktur Des gels der Kieselsäure", *Theorie der Entwässerung, Zeitschriften für Anorganische Chemie*, vol. 71, 356-377, 1911

PART II

Experimental Characterization

Chapter 4

Experimental Techniques for Unsaturated Geomaterials

4.1. Introduction

Research on unsaturated geomaterials is primarily concerned with unsaturated soils, i.e. soils not fully saturated with water, with quite significant early experimental contributions devoted to water-retention properties coming from soil science and geotechnical engineering [CRO 52]. Unsaturated soil testing using the triaxial apparatus is also based on the controlled suction device designed by Bishop and Donald [BIS 61]. The system of suction control used was the so-called axis translation system in which suction was achieved by imposing a positive air back pressure u_a into the sample, while keeping null the water pressure u_w, based on Richards [RIC 41] pressure plate apparatus. Applications to other multiphase geomaterials, including chalks [DEL 96, DEG 03] and hydrocarbon contaminated soils [CUI 03], will not be further commented here owing to space constraint.

Starting from this point, this chapter presents a short survey on how the suction control and measurement techniques in unsaturated soils developed, with and without simultaneously applied stress conditions. Owing to space constraint, experimental investigations on water transfers will not be commented on here and readers can refer to [BEN 97] and [MAS 08],

Chapter written by Pierre DELAGE.

among others. Note that more detailed descriptions can be found in the proceedings of various international and local conferences on unsaturated soils (Paris 1995, Beijing 1998, Recife 2002, Arizona 2006, Barcelona 2010). Among other conferences, interesting recent information can also be found in the state-of-the-art lectures of the EXPERUS 2005 Conference [TAR 08b] and in the Proceedings of the 1st E-UNSAT 08 Conference in Durham. Besides unsaturated soils, some recent extensions to other multiphase geomaterials such as chalk will also be introduced.

4.2. Techniques for controlling suction

4.2.1. *Axis translation technique*

The axis translation technique is applied by using Richards' apparatus, presented in Figure 4.1. As seen in the figure, the air backpressure is applied inside an airtight cell, the base of which comprises a water-saturated low porosity disk called "high air entry value (HAEV) porous disk". Most often, these disks are made up of ceramic with pores of sufficiently small diameters to remain saturated due to capillarity, even when air pressure is applied into the cell. Typically, HAEV porous disks are defined by the pressure they are able to resist, for example, 500 of 1500 kPa.

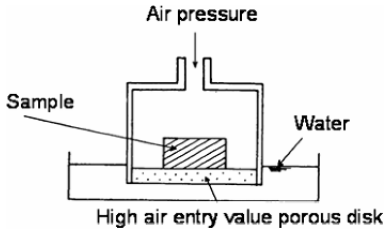

Figure 4.1. *Richards's pressure plate apparatus*

To obtain the water retention curve of a sample starting from a saturated state, the air pressure u_a is increased step-by-step, resulting in a corresponding increase in suction, given that suction s is equal to:

$$s = u_a - u_w \qquad [4.1]$$

with u_w=0 kPa, given that the saturated porous disk is placed into water at atmospheric pressure. When air pressure is increased, air penetrates the sample

and water is expelled into the porous disk, giving rise to a decrease in both water content and degree of saturation. Note that as water transfer occurs in the liquid phase, the axis translation technique controls the matrix suction.

Equilibrium is achieved at each suction step (around 1 week) and the sample is quickly withdrawn from the cell and weighted so as to determine its water content. Figure 4.2 presents the water retention curve of clayey sand by [CRO 52] with distinct drying and wetting paths and the typical hysteresis effect, according to which the drying curve is located above the wetting curve. The air entry in a low deformable material can also be derived from the shape of the curve starting from the saturated state as described in the figure.

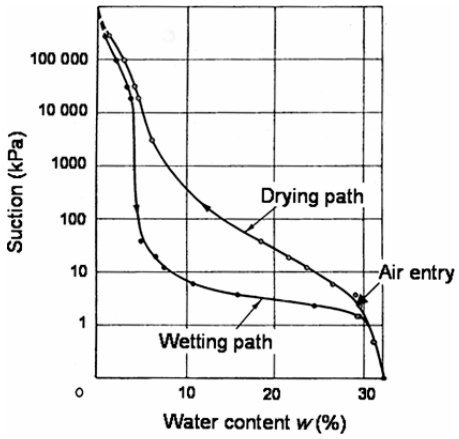

Figure 4.2. *Water retention curve of a clayey sand [CRO 52]*

The axis translation technique is the most widely used technique for controlling suction, most often between 0 and 1500 kPa. Extension at higher suctions (12 MPa) have been conducted by [ESC 89] by designing systems able to withstand high air pressure, with special attention paid to safety issues given the high level of energy stored. Its advantages and drawbacks have been discussed in [FRE 93] and in various papers including [VAN 08] and [DEL 08a]. The main concern is related to the progressive dissolution of air under pressure into water [DEG 03, FRE 93, VAN 08] and the transfer of air through membranes when the technique is used in triaxial testing. Some concerns at high degrees of saturation when the air phase is no longer continuous with occluded air bubbles have also been noted by [BOC 80].

4.2.2. *The osmotic technique*

An alternative technique for controlling suction is the osmotic technique [KAS 71, ZUR 66] in which samples are placed in contact with a semipermeable membrane (most often dialysis cellulotic membranes), behind which an aqueous solution of large-sized polyethyleneglycol (PEG) molecules is circulated. As the water molecules can cross the membrane while the PEG molecules cannot, an osmotic suction is applied to the soil through the membrane, and the higher the concentration of the PEG solution, the higher is the suction. Owing to liquid water exchanges, the osmotic technique controls the matrix suction of the soil, similar to the axis translation method. The system is easy to adapt for the determination of the WRC by placing the sample in a tube-shaped semipermeable membrane and by plunging it in a PEG solution stirred by a magnetic stirrer [CUI 96], as shown in Figure 4.3. In terms of calibration, Williams and Shaykewich [WIL 69] found a good agreement between independent calibrations performed by vapor control or relative humidity measurements for total suctions between 0 and 1.5 Mpa, while [DEL 98] extended this calibration up to 10 MPa.

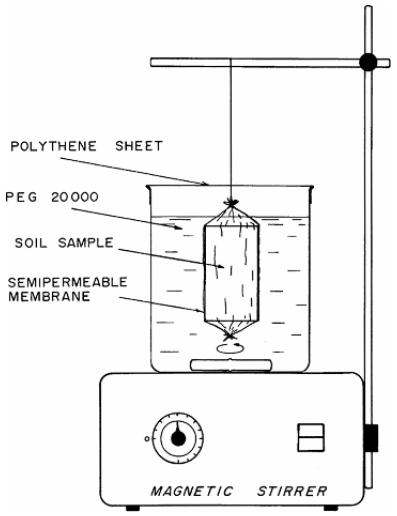

Figure 4.3. *An application of the osmotic technique for controlling suction [CUI 96]*

Further calibrations were carried out by [DIN 95, TAR 00, and MON 07], who made direct suction measurements in osmotically controlled conditions by using high-capacity tensiometers (HCT) [RID 93], which are presented in Figure 4.4. The figure shows that for a given concentration, the suction applied is dependent on the couple membrane/PEG used. Note that the Williams and Shaykewich calibration curve is similar to that obtained by [MON 07] with PEG 3500.

The main advantage of the osmotic method is that the status of water is similar to the real one with no artificial air backpressure imposed to the sample (particularly interesting at high degrees of saturation when the air phase becomes occluded). In addition, matrix suctions as high as 10 MPa can easily be achieved. However, the main drawback is related to the fragility and vulnerability of cellulotic membranes to bacteria attack (which can be overcome by using antibiotics in the solution). The use of more resistant polyether sulfonated membranes [MON 07, SLA 00] seems to be an interesting alternative. A more detailed description of the technique is given in [BLA 08], and its advantages and drawbacks are discussed in detail in [DEL 08b].

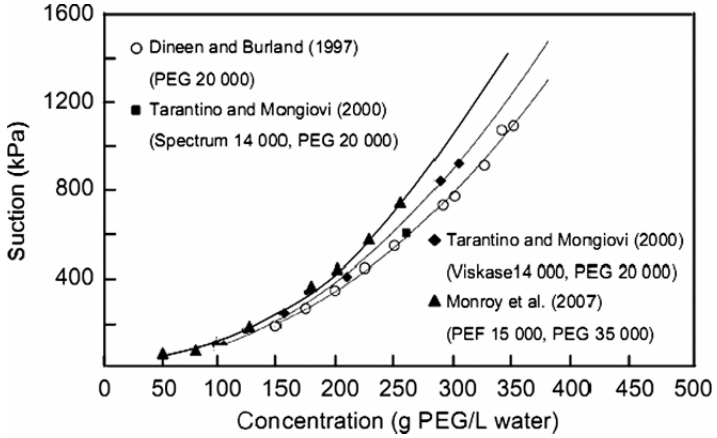

Figure 4.4. *Calibration of the osmotic technique (after [DEL 08b])*

4.2.3. *Suction control through vapor equilibrium*

The vapor equilibrium technique is implemented by controlling the relative humidity of a closed system (desiccator) based on the relation existing at equilibrium between suction and the relative humidity given by Kelvin's law [FRE 93]. The relative humidity can be controlled by using saturated saline

solutions [DEL 98, TAN 05]. This technique is easy to use and can reach very high suction values, as shown in Table 4.1.

Saturated saline solution	Relative humidity (%)	Suction (MPa)
K_2SO_4	97	4.2
K_2NO_3	93.7	9.0
$ZnSO_4$	91.3	12.6
NaCl	76	37.8
$Mg(NO_3)_2$	55	82.4
K_2CO_3	44	137.8
KCH_3CO_2	20	182.1

Table 4.1. *Suctions corresponding to several saturated salt solutions at 20°C (after [DEL 98])*

As water exchanges occur by vapor transfer, this technique controls the total suction. Its main drawback is that equilibration time can be long (several weeks) because of vapor transfer. However, this time can be reduced by circulating the air with controlled relative humidity inside the closed system [DEL 08a, PIN 09].

4.3. Techniques for measuring suction

Techniques for measuring suction appear to be more delicate than those for controlling suction. Again, a variety of pioneering direct and indirect techniques have been described in [CRO 52]. In this chapter, only the most frequently used recent techniques will be mentioned. Other techniques and further details can be found, for instance, in [RID 96], [MAR 08] and [BUL 08].

4.3.1. *Tensiometers*

The direct method of measuring suction is based on the use of tensiometers. Electronic tensiometers provide the measurement of the negative pore pressure, similar to that of the pore pressure gauges in the positive range. For a long time, tensiometer measurements have been limited to maximum suctions of 70–80 kPa because of water cavitation. An important contribution has been provided by the invention of HCT by [RID 93]. HCTs are able to measure suction as high as 1500 kPa.

The principle of HCT (see Figure 4.5) is based on the use of a very thin water chamber (less than 1 mm thick) in the gauge.

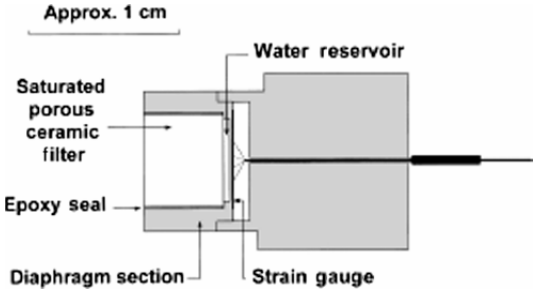

Figure 4.5. *High capacity tensiometer [RID 95]*

The soil suction is transmitted to the water chamber through a HAEV ceramic porous disk, and the negative water pressure in the chamber is monitored by a deformable thin metal membrane on which a strain gauge is stuck. Various authors have developed HCTs based on Ridley and Burland's principle and more detailed descriptions of the system and the precautions to be followed when carrying out HCT measurements (careful saturation of the porous disk, application of cycles of high pressure, etc.) can be found in [RID 95], [TAR 01], [MAR 08] and [DEL 08a] among the others).

4.3.2. *The filter paper method*

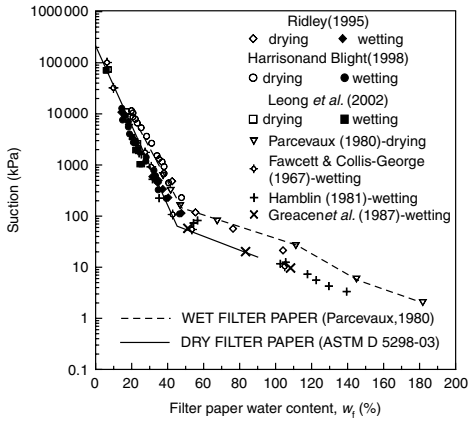

Figure 4.6. *Water retention curves of filter paper Whatman 42*

The filter paper method was initially proposed by Gardner [GAR 37] and further developed by [FAW 67], [PAR 80], [HAM 81], [CHA 86], [GRE 87], [RID 95], [HAR 98] and [LEO 02] among others. The method has been standardized by American Society for Testing and Materials (ASTM) [AST 03]. It is an indirect method based on the water-retention properties of a calibrated filter paper (Whatman No. 42 or Schleicher and Schuell). The method consists of placing a filter paper in contact with the sample so as to reach suction equilibration between the sample and the filter paper (1-week duration). Afterwards, the paper is carefully weighed and the water content obtained provides the suction through the use of the calibrated water retention curve of the paper. While ASTM recommends using an initially dry paper filter (using its main wetting path), some authors have also used an initially wet filter paper (using the main drying paths). Figure 4.6 presents the calibrated main drying and wetting paths of a Whatman 42 filter paper obtained by various authors. This relatively simple but destructive technique appears to provide quite satisfactory results. Note that some attempts to measure the total suction with no contact between the sample and the paper have been made [BUL 02].

Other indirect methods are described in [BUL 08], including methods based on the measurement of the relative humidity of the sample pore water through Peltier-type thermocouple psychrometers [VER 78, ZER 95], transistor psychrometers [CAR 07, TRU 95, WOO 93], or hygrometers of different kinds (capacitive or resistive). Thermocouple psychrometers appear to have a delicate use because of temperature effects, whereas hygrometers provide satisfactory measurements at suctions higher than several MPa.

A technique that was recently developed is the chilled-mirror dew-point psychrometer ([AGU 05, LEO 03, TAN 05, THA 05]) that precisely measures the temperature at which the condensation of water vapor at a given relative humidity first appears (dew-point temperature). A soil sample in equilibrium with the surrounding air is placed in a housing chamber containing a mirror and a photoelectric detector of condensation on the mirror. The temperature of the mirror is precisely controlled by a thermoelectric (Peltier) cooler. The relative humidity is calculated from the difference between the dew-point temperature and the temperature of the soil sample, which is measured with an infrared thermometer. The measuring time is around 5 min (General Eastern or Decagon Devices). Figure 4.7 presents the comparison of the measurements conducted with transistor

psychrometers (soil mechanics instrumentation, SMI) and dew-point psychrometer (WP4) along the drying path of a compacted destructured argillite ([CAR 07, DEL 08]).

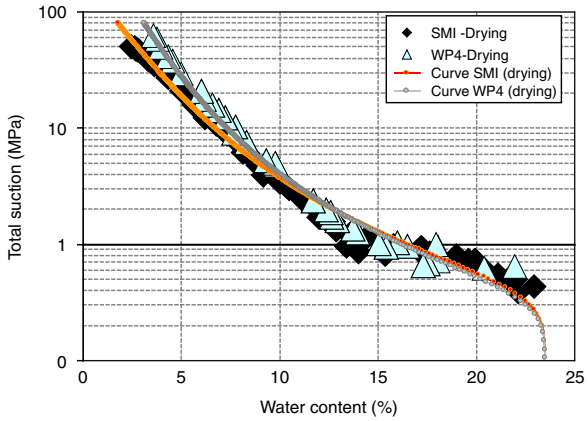

Figure 4.7. *Comparison between SMI and WP4 psychrometer data. Drying paths on a compacted destructured argillite [CAR 07]*

4.4. Mechanical testing devices

4.4.1. *Introduction*

In triaxial testing, the state of an unsaturated soil has to be fully characterized by the following data:

– net mean stress (p–u_a);

– deviatoric stress q;

– suction (u_a–u_w);

– specific volume v=1+e;

– degree of saturation S_r=V_w/eV_s (where V_w, e, and V_s are the water volume, void ratio, and volume of the solid of the sample, respectively).

The total sample characterization is more complex than in saturated soils because the changes in the water content are no longer linked to the sample volume changes. It is also necessary to know the changes in the degree of saturation. For this reason, special attention has been paid to a careful monitoring of the changes in the volume and water content during shear.

Figure 4.8 presents the first suction-controlled triaxial apparatus, developed by Bishop and Donald [BIS 61].

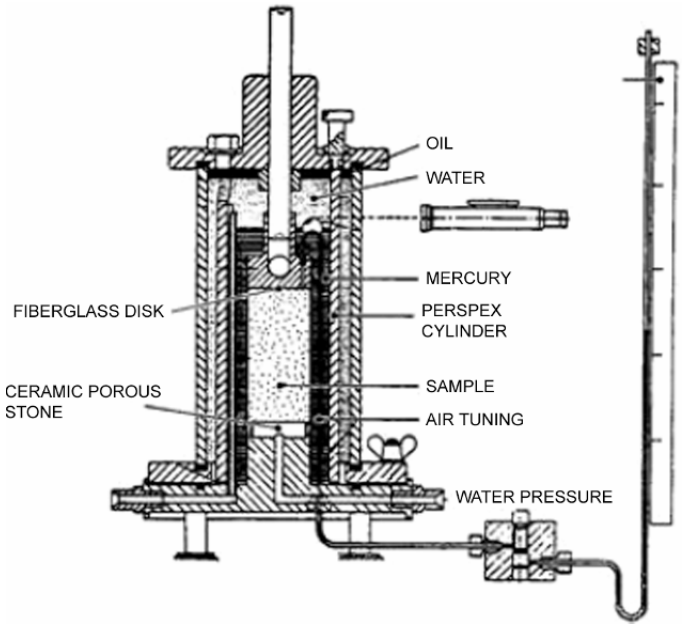

Figure 4.8. *Bishop and Donald's suction-controlled apparatus [BIS 61]*

Suction is controlled by using the axis translation method. The porous disk at the base of the sample is replaced by a HAEV ceramic disk, whereas air pressure is applied through the porous disk at the top of the sample. Volume changes are monitored by immersing the sample in a tube full of mercury and by optically monitoring the mercury level. Actually, most of the recently developed triaxial systems are based on the same principle.

In fact, most of the innovative developments of suction-controlled soil mechanics apparatuses developed after Bishop and Donald's triaxial were made in the oedometer and direct shear box. Stress conditions in these devices are less satisfactory than in the triaxial apparatus, but tests are easier to carry out, which is a probable reason for their development.

4.4.2. *Control suction oedometers and direct shear boxes*

The applications of the axis translation method to the oedometer and direct shear box were initially presented by [ESC 69], [ESC 80] and [ESC 86]. The principle of the systems was to isolate the device (oedometer cell or shear box) in an airtight chamber capable of sustaining air pressure. For safety reasons, particular attention has to be paid to the mechanical resistance of the cells, as can be seen in Figure 4.9. Air tightness must be cautiously ensured at the joints around the pistons used to apply vertical stresses, because friction can affect the value of the stress applied on the sample. Friction may also affect the rod that allows for the mutual displacement of the two half-boxes of the shear box. The confining cell of the shear box has to be large enough to allow for shear displacement. These systems have been extended to suctions as high as 12 MPa [ESC 89]. Suction-controlled shear boxes were also developed by [GAN 88].

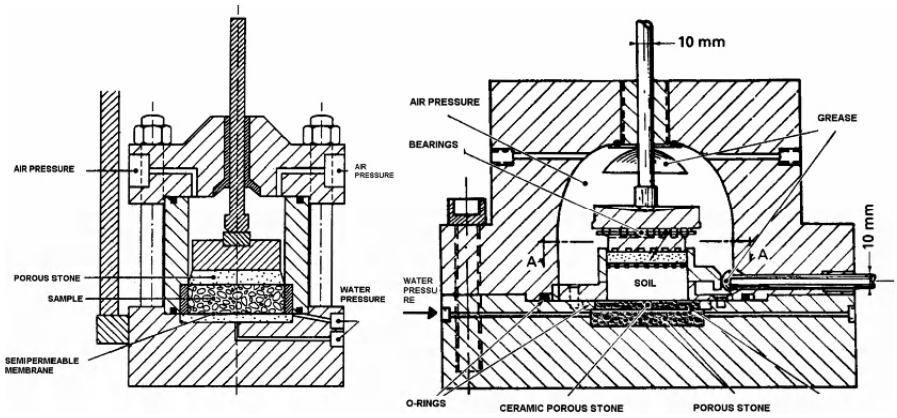

Figure 4.9. *Controlled suction oedometer and shear box, axis translation method [ESC 69, ESC 86]*

Recent developments in axis translation oedometers include the Universitat Politécnica de Catalunya (UPC) oedometer [HOF 05] shown in Figure 4.10. This device can also be used for controlling suction by using the vapor equilibrium technique. Note the special device of the porous disks placed on both the bottom and top of the sample, in which both HAEV water-saturated ceramic disk and coarse air-saturated porous disk are placed. This optimizes the drainage length, equal to half the height of the sample.

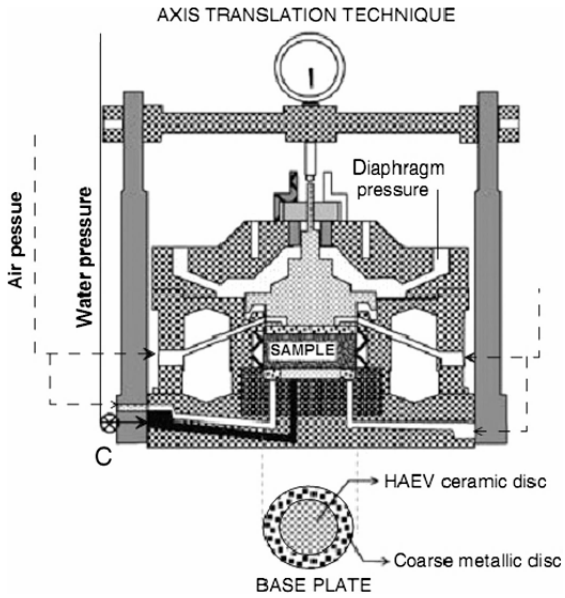

Figure 4.10. *UPC oedometer axis translation cell [HOF 05]*

The osmotic technique has been adapted to the oedometer by [KAS 71]. Two semipermeable membranes were placed on both the top and bottom faces of the sample, and the PEG solution was circulated behind the membrane by using two bottles placed at different levels.

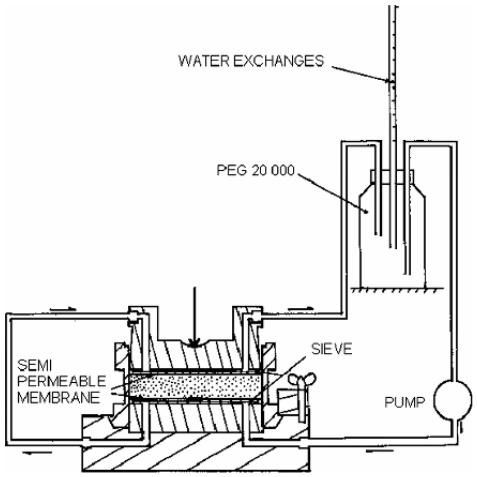

Figure 4.11. *The Kassiff and Benshalom osmotic oedometer modified by [DEL 92]*

Suction was controlled due to the water exchanges occurring through the membrane between the PEG and the sample. The system has been subsequently completed by [DEL 92] by adding a system allowing PEG circulation inside a closed circuit including a 1 liter closed bottle full of PEG, to allow constant PEG concentration in the circuit in spite of the water exchanges with the sample (Figure 4.11). A capillary tube placed in the bottle allowed monitoring of the water exchanges. An alternative method of controlling water exchanges by placing the bottle on a balance has been proposed by [DIN 95]. As seen previously, the maximum possible suction attainable with the osmotic technique has been extended up to 10 MPa, a suction value rarely attained when using the axis translation technique [DEL 98]. An osmotic direct shear box based on the same principles has been proposed by [BOS 05].

4.4.3. *Controlled suction triaxial devices*

Most of the researches carried out on the mechanical behavior of unsaturated soils are now carried out in controlled suction triaxial devices, and many recent developments have been carried out accordingly ([BLA 08, HOY 08]).

4.4.3.1. *Testing rates*

Controlled suction triaxial tests in unsaturated soils are comparable to drained saturated triaxial tests. At any time, the system that controls suction should provide or extract the amount of water necessary to counterbalance the effects of the triaxial compression. Experience [RAM 99] shows that water exchanges at control suction are controlled by volume changes with water extraction during shear contraction and water infiltration during shear dilatancy. As in saturated drained tests, the shearing rate depends on the suction changes induced by the volume changes, the drainage length of the sample, and the water permeability of the sample. A further condition is imposed in unsaturated soils testing by low permeability and thickness (i.e. the impedance) of the HAEV porous stone or semipermeable membrane used. This problem has been discussed by [HO 82] based on the calculations made by [GIB 54] for saturated soils. In a saturated sample, the pore-pressure generation induced by the volume changes during shearing is easy to estimate, which is not the case of suction changes during shearing in unsaturated samples. [HO 82] provided an estimation of the strain rate close to the rate of thee saturated drained tests, i.e. close to 1 μm/minute. A similar value was

obtained with the osmotic technique, considering the impedance of a semipermeable membrane [DEL 87]. Some improvements have been provided so as to reduce the drainage length by applying air pressure through the membrane at the middle height of the sample [MAÂ 96] or by controlling both air and water pressure at both the ends of the triaxial sample by using a special porous disk similar to that presented in Figure 4.10 [ROM 97, BAR 02]. Table 4.2 provides some published data giving both shearing rates and drainage lengths.

Author	**Soil**	**Drainage length**	**Shearing rate (µm/mn)**
Bishop and Donald (1961)	Brahead silt	*H*	2.13
Gulhati and Satija (1981)	Dhanauri clay I_p=24	*H*	6
Ho and Fredlund (1982)	Silty sand, sandy silt	*H*	1.43
Delage *et al.* (1987)	Jossigny LP silt I_p=19	*H*/2	1
Romero *et al.* (1997), Barrera *et al.* (2002)	Barcelona LP silt I_p=16	*H*/2	1
Wheeler and Sivakumar (1995)	Speswhite Kaolin I_p=	*H*	1.4
Maâtouk *et al.* (1995)	LP loess I_p=7	*H*/2	
Rampino *et al.* (1999)	Silty sand I_p=13	*H*	1.26
Laloui *et al.* (1997), Geiser (1999)	Sion sandy silt I_p=8	*H*	1.5
Rampino (constant rate of strain, CRS)	Silty sand I_p=13	*H*	5

Table 4.2. *Shearing rates used in some unsaturated testing devices (from [DEL 02])*

4.4.3.2. *Volume-change monitoring*

For obvious safety reasons, mercury is no longer used and various alternative methods of volume-change monitoring have been developed. [CUI 96] adapted the system of Figure 4.8 by replacing mercury with water, and using water and air as confining fluids. [RAM 99] and [AVE 02] also used air pressure, developed a specially designed cylinder to improve the precision (Figure 4.12), and monitored the change in the water level with a differential pressure transducer, like [NG 02].

Another option is based on the use of double-cell systems [WHE 88]. In such systems, as the inner cell does not experience any stress changes during increases in the confining pressures, volume changes can satisfactorily be derived from the water exchanges of the inner cell.

It seems that the recent trends in monitoring volume changes in unsaturated soils are based on the precise monitoring of sample deformation, by local measurement (linear variable differential transformer (LVDT) of Hall effect gauges) [CAB 06], laser monitoring along the whole sample [BAR 02], or image analysis [RIF 02]. A summary of the techniques for monitoring volume changes in unsaturated soils has been provided by [GEI 00] and [LAL 06].

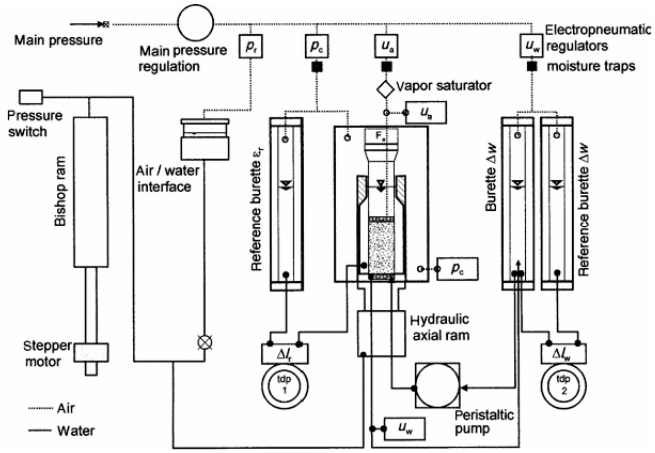

Figure 4.12. *Volume-change monitoring [AVE 02]*

4.4.3.3. *Other controlled suction triaxial devices*

The alternative methods of controlling suction described earlier (osmotic and vapor control) have been applied to triaxial devices.

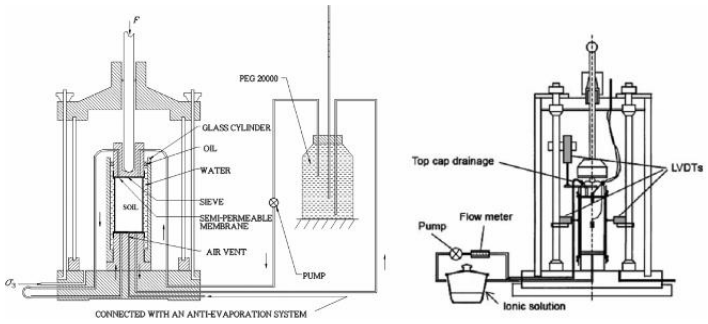

Figure 4.13. *Osmotic- and vapor-controlled suction triaxial devices [DEL 87, CUI 96, BLA 00]*

Following the osmotic-controlled suction oedometer of [KAS 71], [DEL 87] and [CUI 96] developed an osmotic-controlled triaxial apparatus in which suction was controlled through two semipermeable membranes placed on top and bottom of the sample, resulting in a $H/2$ drainage length, as seen in Figure 4.13. The figure also shows the vapor-controlled triaxial apparatus of [BLA 00] in which a controlled relative humidity is circulated along the external face of the sample through a geosynthetic membrane.

4.4.4. *Other suction-controlled devices*

Various other sophisticated devices that cannot be described here have been developed (see [HOY 08] for more detail), including true suction controlled apparatuses [HOY 01, MAT 02]. In addition, to investigate small strain parameters, a resonant column torsional shear system [VAS 07] and systems with bender elements [CAB 06] have also been developed.

4.5. Concluding remarks

Since the pioneering contributions made in the 1950s–1960s, considerable developments have been made in experimental unsaturated soil mechanics in the recent decades, with many new devices that now allow for a complete description of the changes in the state of unsaturated samples under various loading conditions, including true triaxial conditions and behavior at small strains. A particular effort has been made in terms of volume-change measurements and reduction in the drainage path to properly ensure constant suction conditions during shearing. However, due to the various parameters that have to be controlled/measured, testing of unsaturated soils remains a delicate task that requires particular attention.

Some new and promising developments that could not be described here owing to lack of space are linked to the measurement of suction changes during loading by using HCT, either in the oedometer [TAR 08a] or the triaxial apparatus [COL 02, MEI 02]. By detecting suction changes during compression or shearing, these kinds of test open up new research perspectives in unsaturated soil mechanics.

4.6. Bibliography

[AGU 05] AGUS S.S., SCHANZ T., "Comparison of four methods for measuring total suction", *Vadose Zone Journal*, vol. 4, no. 4, p. 1087-1095, 2005.

[AST 03] ASTM International., Standard Test Method for Measurement of Soil Potential (Suction) Using Filter Paper, D 5298-03, 2003.

[AVE 02] AVERSA S., NICOTERA M.V., "A triaxial and oedometer apparatus for testing unsaturated soils", *Geotechnical Testing Journal*, vol. 25, no. 1, p. 3-15, 2002.

[BAR 02] BARRERA M., ROMERO E., LLORET A., VAUNAT J., "Hydro-mechanical behaviour of a clayey silt during controlled-suction shearing". *Proc. 3rd Int. Conf. on Unsaturated Soils, UNSAT'2002*, Recife, Brazil, Balkema, p. 485-490, 2002.

[BEN 97] BENSON C.H., GRIBB M.M., "Measuring hydraulic conductivity in the laboratory and in the field", *Unsaturated Soil Engineering Practice*. ASCE Geotechnical Special Publication No. 68, p. 113-168, 1997.

[BIS 61] BISHOP A.W., DONALD I.B., "The experimental study of party saturated soil in the triaxial apparatus". *Proc. 5th Conf. on Soil Mechanics and Found Eng*., vol. 1, p. 13-21, 1961.

[BLA 00] BLATZ J., GRAHAM J., "A system for controlled suction in triaxial tests", *Géotechnique*, vol. 50, no. 4, p. 465-478, 2000.

[BLA 08] BLATZ J., CUI Y.J., OLDECOP L., "Vapour equilibrium and osmotic technique for suction control", *Geotechnical and Geological Engineering*, vol. 26, no. 6, p. 661–673, 2008.

[BUL 02] BULUT R., HINEIDI S.M., BAILEY B., "Suction measurements-filter paper and chilled-mirror psychrometer". *Proc. of the Texas Section of the American Society of Civil Engineers Fall 2002 Meeting*, Waco, TX, October 2-5, 2002.

[BUL 08] BULUT R., LEONG E.C., "Indirect measurement of suction", *Geotechnical and Geological Engineering*, vol. 26, no. 6, p. 633-644, 2008.

[BOC 80] BOCKING K.A., FREDLUND D.G., "Limitations of the axis translation technique". *Proc. 4th Int. Conf. on Expansive Soils*, p. 117-135, 1980.

[BOS 05] BOSO M., TARANTINO A., MONGIOVÌ L., "A direct shear box improved with the osmotic technique". *Proc. Int. Symp. on Advanced Experimental Unsaturated Soil Mechanics*, p. 85-91, 2005.

[CAB 06] CABARKAPA Z., CUCCOVILLO T., "Automated triaxial apparatus for testing unsaturated soils", *ASTM Geotechnical Testing Journal*, vol. 29, no. 1, p. 21-29, 2006.

[CAR 07] CARDOSO R., ROMERO E., LIMA A., FERRARI A., "A comparative study of soil suction measurement using two different high-range psychrometers". *Proc. 2nd Int. Conf. Mechanics of Unsaturated Soils*, T. SCHANZ (ed.). Springer Proceedings in Physics, vol. 112, p. 79-93, 2007.

[CHA 86] CHANDLER R.J., GUTIERREZ C.I., "The filter-paper method of suction measurement", *Géotechnique*, vol. 36, no. 2, p. 265-268, 1986.

[COL 02] COLMENARES J.E., RIDLEY A.M., "Stress-strain and strength relationships for a reconstituted clayey silt". *Proc. 3rd Int. Conf. on Unsaturated Soils, UNSAT'2002*, (2), Recife, Brazil, Balkema, p. 481-484, 2002.

[CRO 52] CRONEY D., "The movement and distribution of water in soil", *Géotechnique*, vol. 3, no. 1, p. 1-16, 1952.

[CUI 96] CUI Y.J., DELAGE P., "Yielding and plastic behaviour of an unsaturated compacted silt", *Géotechnique*, vol. 46, no. 2, p. 291-311, 1996.

[CUI 03] CUI Y.J., DELAGE P., ALZOGHBI P., "Retention and transport of a hydrocarbon in a silt", *Géotechnique*,vol. 53, no. 1, p. 83-91, 2003.

[DEG 03] DE GENNARO V., DELAGE P., CUI Y.-J., SCHROEDER CH., COLLIN F., "Time-dependent behaviour of oil reservoir chalk: a multiphase approach", *Soils and Foundations*, vol. 43, no. 4, p. 131-147, 2003.

[DEL 87] DELAGE P., SURAJ DE SILVA G.P.R., DE LAURE E., "Un nouvel appareil triaxial pour les sols non saturés". *9e Eur. Conf. Soil Mechanics Found. Eng.*, 1, Dublin, p. 26-28, 1987.

[DEL 92] DELAGE P., SURAJ DE SILVA G.P.R., VICOL T., "Suction controlled testing of non saturated soils with an osmotic consolidometer". *7th International Conference on Expansive Soils*, Dallas, p. 206-211, 1992.

[DEL 96] DELAGE P., SCHROEDER C., CUI Y.J., "Subsidence and capillary effects in chalks". *EUROCK '96, Prediction and Performance in Rock Mechanics and Rock Engineering*, 2, Turin, Italy, September 2-5, p. 1291-1298, 1996.

[DEL 98] DELAGE P., HOWAT M., CUI Y.J., "The relationship between suction and swelling properties in a heavily compacted unsaturated clay", *Engineering Geology*, vol. 50, no. 12, p. 31-48, 1998.

[DEL 08a] DELAGE P., ROMERO E., TARANTINO S., "Recent developments in the techniques of controlling and measuring suction in unsaturated soils". Keynote Lecture, *Proc. 1st Eur. Conf. on Unsaturated Soils*, Durham, CRC Press, p. 33-52, 2008.

[DEL 08b] DELAGE P., CUI Y.J., "An evaluation of the osmotic method of controlling suction", *Geomechanics and Geoengineering: An International Journal*, vol. 3, no. 1, p. 1-11, 2008.

[DIN 95] DINEEN K., BURLAND J.B., "A new approach to osmotically controlled oedometer testing". *Proc. 1st Int. Conf on Unsaturated Soils UNSAT'95*, Paris 2, p. 459-465, 1995.

[ESC 69] ESCARIO V., "Swelling of soils in contact with water at a negative pressure". *Int. Conf. on Expansive Soils*, College Station, TX, p. 207-217, 1969.

[ESC 80] ESCARIO V., "Suction controlled penetration and shear tests". *Proc 4th Int. Conf. on Expansive Soils*, p. 1-17, 1980.

[ESC 86] ESCARIO V., SAEZ, J., "The shear strength of partly saturated soils", *Géotechnique*, vol. 36, p. 453-456, 1986.

[ESC 89] ESCARIO V., JUCA F., "Strength and deformation of partly saturated soils", *Proc. 12th Int. Conf. Soil Mech. and Found. Eng.*, 1, Rio de Janeiro, Balkema, p. 43-46, 1989.

[FAW 67] FAWCETT R., COLLIS-GEORGE N., "A filter paper method for determining the moisture characteristics of soil", *Australian Journal of Experimental Agriculture and Animal Husbandry*, vol. 7, p. 162-167, 1967.

[FRE 93] FREDLUND D.G., RAHARDJO H., *Soil Mechanics for Unsaturated Soils*, John Wiley, New York, 1993.

[GAN 88] GAN J.K.M., FREDLUND D.G., RAHARDJO H., "Determination of the shear strength parameters of an unsaturated soil using the direct shear test", *Canadian Geotechnical Journal*, vol. 25, no. 3, p. 500-510, 1988.

[GAR 37] GARDNER R., "A method of measuring the capillary tension of soil moisture over a wide moisture range", *Soil Science*, vol. 43, p. 227-283, 1937.

[GEI 00] GEISER F., LALOUI L., VULLIET L., "On the volume measurement in unsaturated triaxial test". *Proc. Asian Conf. on Unsaturated Soils*, Balkema, Rotterdam, p. 669-674, 2000.

[GIB 54] GIBSON R.E., HENKEL D.J., "Influence of duration of tests at constant rate of strain on measured drained strength", *Géotechnique*, vol. 4, p. 6-15, 1954.

[GRE 87] GREACEN E.L., WALKER G.R., COOK P.G., "Evaluation of the filter paper method for measuring soil water suction", *Int. Conf. on Measurement of Soil and Plan Water Status*, 137-143, 1987.

[HAM 81] HAMBLIN A.P., "Filter paper method for routine measurement of field water potential", *Journal of Hydrology*, vol. 53, p. 355-360, 1981.

[HAR 98] HARRISON B., BLIGHT G., "The effect of filter paper and psychrometer calibration techniques on soil suction measurements". *Proc. 2nd Int. Conf. on Unsaturated Soils*, 1, International Academic Publishers, Beijing, p. 362–367, 1998.

[HO 82] HO D.Y.F., FREDLUND D.G., "A multi-stage triaxial test for unsaturated soils", *ASTM Geotechnical Testing Journal*, vol. 5, no. 1-2, p. 18-25, 1982.

[HOF 05] HOFFMANN C., ROMERO E., ALONSO E.E., "Combining different controlled-suction techniques to study expansive clays". *Proc. Int. Symp. on Advanced Experimental Unsaturated Soil Mechanics*, Trento, Italy, June 27-29. A. TARANTINO, E. ROMERO and Y.J. CUI (eds.), A.A. Balkema, Leiden, p. 61-67, 2005.

[HOY 01] HOYOS L.R., MACARI E.J., "Development of stress/suction controlled true triaxial testing device for unsaturated soils", *Geotechnical Testing Journal*, vol. 24, no. 1, p. 5-13, 2001.

[HOY 08] HOYOS L., LALOUI L., VASSALLO R., "Mechanical testing in unsaturated soils", *Geological Engineering*, vol. 26, no. 6, p. 675-689, 2008.

[KAS 71] KASSIFF G., BEN SHALOM A., "Experimental relationship between swell pressure and suction", *Géotechnique*, vol. 21, p. 245-255, 1971.

[LAL 06] LALOUI L., GEISER F., PERON H., VULLIET L., "Advances in volume measurements in unsaturated triaxial tests", *Soils and Foundations*, vol. 46, no. 3, p. 441-449, 2006.

[LEO 02] LEONG E., HE L., RAHARDJO H., "Factors affecting the filter paper method for total and matric suction measurements", *Geotechnical Testing Journal*, vol. 25, no. 3, p. 322-333, 2002.

[LEO 03] LEONG E.C., TRIPATHY S., RAHARDJO H., "Total suction measurement of unsaturated soils with a device using the chilled-mirror dew-point technique", *Géotechnique*, vol. 53, no. 2, p. 173-182, 2003.

[MAÂ 96] MAÂTOUK A., LEROUEIL S., LA ROCHELLE P., "Yielding and critical state of a collapsible unsaturated silty soil", *Géotechnique*, vol. 45, no. 3, p. 465-477, 1995.

[MAR 08] MARINHO F.A.M., TAKE A., TARANTINO A., "Tensiometric and axis translation techniques for suction measurement", *Geotechnical and Geological Engineering*, vol. 26, no. 6, p. 615-631, 2008.

[MAS 08] MASROURI F., BICALHO K., KAWAI K., "Laboratoty hydraulic testing in unsaturated soils", *Geotechnical and Geological Engineering*, vol. 26, no. 6, p. 691-704, 2008.

[MAT 02] MATSUOKA H., SUN D., KOGANE A., FUKUZAWA N., ICHIHARA W., "Stress-strain behaviour of unsaturated soil in true triaxial tests", *Canadian Geotechnical Journal*, 39, 608-619, 2002.

[MEI 02] MEILANI I., RAHARDJO H., LEONG E.C., FREDLUND D.G., "Mini suction probe for matric suction measurements", *Canadian Geotechnical Journal*, 39, 1427-1432, 2002.

[MON 07] MONROY R., RIDLEY A. DINEEN K., ZDRAKOVIC L., "The suitability of osmotic technique for the long term testing of partly saturated soils", *Geotechnical Testing Journal*, vol. 30, no. 3, p. 220-226, 2007.

[NG 02] NG C.W.W., ZHAN L.T., CUI Y.J., "A new simple system for measuring volume changes in unsaturated soils", *Canadian Geotechnical Journal*, vol. 39, p. 757-764, 2002.

[PAR 80] PARCEVAUX P., "Étude microscopique et macroscopique du gonflement de sols argileux", PhD thesis, École Nationale Supérieure des Mines de Paris, 1980.

[PIN 09] PINTADO X., LLORET A., ROMERO E., "Assessment of the use of the vapour equilibrium technique in controlled-suction tests", *Canadian Geotechnical Journal*, vol. 46, no. 4, p. 411-423, 2009.

[RAM 99] RAMPINO C., MANCUSO C., VINALE F., "Laboratory testing on an unsaturated soil: equipement, procedures, and first experimental results", *Canadian Geotechnical Journal*, vol. 36, no. 1, p. 1-12, 1999.

[RIC 41] RICHARDS L.A., "A pressure – membrane extraction apparatus for soil solution", *Soil Science*, vol. 51, p. 377-386, 1941.

[RID 93] RIDLEY A.M., BURLAND J.B., "A new instrument for measurement of soil moisture suction", *Géotechnique*, vol. 43, no. 2, p. 321-324, 1993.

[RID 95] RIDLEY A.M., "Discussion on 'Laboratory Filter Paper Suction Measurements'" by S.L. HOUSTON, W.N. HOUSTON, and A.-M. WAGNER. *Geotechnical Testing Journal*, vol. 18, no. 3, p. 391-396, 1995.

[RID 96] RIDLEY A.M., WRAY W.K., "Suction measurement: a review of current theory and practices". *Proc. 1st Int. Conf on Unsaturated Soils UNSAT' 95*, 3, Paris, Balkema, Rotterdam, p. 1293-1322, 1996.

[RIF 02] RIFAÏ A., LALOUI L., VULLIET L., "Volume measurement in unsaturated triaxial test using liquid variation and image processing". *Proc. 3rd Int. Conf. on Unsaturated Soils, UNSAT'2002*, p. 441-445, 2002.

[ROM 97] ROMERO E., FACIO J.A., LLORET A., GENS A., ALONSO E.E., "A new suction and temperature controlled triaxial apparatus". *Proc. 14th Int. Conf. on Soil Mechanics and Geotech. Eng.*, Hamburg, Balkema, (1), p. 185-188, 1997.

[SLA 00] SLATTER E.E., JUNGNICKEL C.A., SMITH D.W., ALLMAN M.A., "Investigation of suction generation in apparatus employing osmotic methods". *Unsaturated Soils for Asia*, Balkema, Rotterdam, p. 297-302, 2000.

[TAN 05] TANG, A.M., CUI, Y.J., "Controlling suction by the vapour equilibrium technique at different temperatures and its application in determining the water retention properties of MX80 clay", *Canadian Geotechnical Journal*, vol. 42, p. 287-296, 2005.

[TAR 01] TARANTINO A., MONGIOVI L., "Experimental procedures and cavitation mechanisms in tensiometer measurements", *Geotechnical and Geological Engineering*, vol. 19, no. 34, p. 189-210, 2001.

[TAR 08a] TARANTINO A., DE COL E., "Compaction behaviour of clay", *Géotechnique*, vol. 58, no. 3, p. 199-213, 2008.

[TAR 08b] TARANTINO A., ROMERO E., CUI Y.J. (eds.), "Laboratory and field testing of unsaturated soils", *Geotechnical and Geological Engineering*, vol. 26, no. 6, Springer, 2008.

[TAR 00] TARANTINO A., MONGIOVI L., "A study of the efficiency of semi-permeable membranes in controlling soil matrix suction using the osmotic technique", *Unsaturated Soils for Asia*, Toll and Leong, eds, Balkema, p. 303-308, 2000.

[THA 05] THAKUR V.K.S., SINGH D.N., "Swelling and suction in clay minerals". *Proc. Int. Symp. on Advanced Experimental Unsaturated Soil Mechanics EXPERUS 2005*, Trento. A. TARANTINO, E. ROMERO and Y.J. CUI (eds.). A.A. Balkema Publishers, Leiden, p. 27-31, 2005.

[TRU 95] TRUONG H.V.P., HOLDEN J.C., "Soil suction measurement with transistor psychrometer". *Proc. 1st Int. Conf. on Unsaturated Soils, Paris. Unsaturated Soils*. E.E. ALONSO, P. DELAGE (eds.). A.A. Balkema/Presses des Ponts et Chaussées, Paris, vol. 2, p. 659-665, 1995.

[VAN 08] VANAPPALLI S., NICOTERA M.V, SHARMA R.S., "Axis translation and negative water column techniques for suction control", *Geotechnical and Geological Engineering*, vol. 26, no. 6, p. 645-660, 2008.

[VAS 07] VASSALLO R., MANCUSO C., VINALE F., "Effects of net stress and suction hystory on the small strain stiffness of a compacted clayey silt", *Canadian Geotechnical Journal*, vol. 44, no. 4, p. 447-462, 2007.

[VER 78] VERBRUGGE J.C., "Emploi d'une méthode psychrométrique dans des essais triaxiaux sur un limon remanié non saturé", *Revue Canadienne de Géotechnique*, vol. 15, p. 501-509, 1978.

[WHE 88] WHEELER S.J., "The undrained shear strength of soils containing large gas bubbles", *Géotechnique*, vol. 38, p. 399-413, 1988.

[WIL 69] WILLIAMS J., SHAYKEWICH C.F., "An evaluation of polyethylene glycol PEG 6000 and PEG 20000 in the osmotic control of soil water matric potential", *Canadian Journal of Soil Science*, vol. 102, no. 6, p. 394-398, 1969.

[WOO 93] WOODBURN J.A., HOLDEN J., PETER P., "The transistor psychrometer: a new instrument for measuring soil suction", *Unsaturated Soils*, Geotechnical Special Publication 39. S.L. HOUSTON and W.K. WRAY (eds.), ASCE, Dallas, p. 91-102, 1993.

[ZER 95] ZERHOUNI M.I., "Essais triaxiaux utilisant des psychromètres." *C.R. 1er Congrès Int. sur les Sols non saturés UNSAT'95*, Paris, vol. 2, p. 673-678, 1995.

[ZUR 66] ZUR B., "Osmotic control the matric soil water potential", *Soil Science*, vol. 102, p. 394-398, 1966.

Chapter 5

New Experimental Tools for the Characterization of Highly Overconsolidated Clayey Materials in Unsaturated Conditions

5.1. Introduction

Several geo-engineering applications, such as the design of nuclear waste repositories or petroleum exploitation, necessitate the study of highly overconsolidated clayey material behaviors. Stress history, diagenesis, and cementation may cause these materials to have a high preconsolidation pressure (usually greater than 10 MPa [FRA 08]). In addition, it is well known that the mechanical response of clayey materials depends on the thermal and hydraulic changes. Temperature changes affect the swelling pressure, volume variation, stiffness, yielding limit, and time-dependent behavior (e.g. [CEK 09, HUE 90, SUL 02, SAL 08]).

The effects of changes in the degree of saturation have also been analyzed, highlighting the influence on deformability, swelling, collapse, irreversible strain accumulation, and strength [LAL 09]. Void ratio variations induced by the mechanical loading can significantly modify the hydraulic properties of these materials [NUT 08, SAL 10]. Moreover, the effects of the temperature on the hydraulic response, such as changes in the water retention curves and permeability, have been identified

---

Chapter written by Simon SALAGER, Alessio FERRARI and Lyesse LALOUI.

[ROM 99, SAL 09]. It is evident that the behavioral features of highly consolidated clayey materials must be analyzed, and the mutual influences among the mechanical, thermal, and hydraulic responses should be considered. We refer to this mutual influence as the thermo-hydro-mechanical (THM) response of the material.

Proper experimental tools must consequently allow those aspects to be taken into account. At the same time, the stress state, temperature, and pore water potential must be controlled. Owing to the high preconsolidation pressure of the materials, the testing devices must be designed to study material behaviors under high stress levels, usually approximately dozens of mega pascals. Temperature is applied in the range of 20-90°C for most situations and up to 150°C for some specific cases. In addition, the pore water pressure has to be controlled in positive and negative ranges. To reproduce *in situ*-saturated conditions, the backpressure may reach several MPa. In unsaturated conditions, high suction values have to be applied to induce a significant reduction in the degree of saturation.

This chapter presents some of the experimental facilities that have recently been developed at the EPFL Soil Mechanics Group. Three apparatuses operating in non-isothermal conditions are described in detail: a sorption bench for determining water retention curves, an oedometric cell for analyzing volumetric responses under high vertical loads, and a triaxial cell designed for extreme loading conditions.

5.2. Sorption bench

The sorption bench was developed with the aim of standardizing and simplifying the process of identifying water retention curves for clayey soils. The layout of the apparatus is depicted in Figure 5.1. The device is composed of eight closed desiccators that are immersed in a heat-regulated bath. The temperature control allows the determination of retention curves at different temperatures and allows the proper control of imposed suction values.

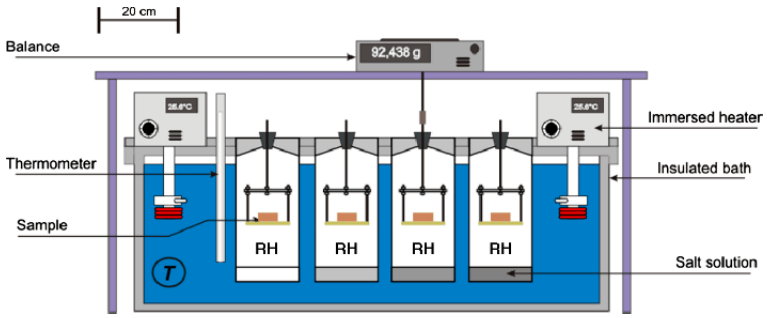

Figure 5.1. *Layout of the sorption bench*

5.2.1. *Suction control*

The vapor equilibrium technique is used to control suction within each container. The technique is implemented by controlling the relative humidity of the closed system in which the soil is placed. The soil water potential is applied by the migration of water molecules through the vapor phase, from a reference system to a known soil pore potential, until equilibrium is achieved ([BLA 08, TAN 05]). At the end of the equalization phase, the pore water and the vapor phase have the same chemical potential. Through this equality and by assuming that the water vapor follows the ideal gas law, it is possible to express the total suction of the porous media as a function of the relative humidity of the closed system, by means of the psychrometric (or Kelvin's) law [OBR 48, WIN 60]:

$$\psi = \frac{\rho_{\mathrm{w}} RT}{M_{\mathrm{w}}} \ln(\mathrm{RH}), \qquad [5.1]$$

where ψ is the total suction (Pa), ρ_{w} the density of water (kg m^{-3}), R the ideal gas constant (J mol^{-1} K^{-1}), T the temperature (K), M_{w} the liquid phase molar mass (kg mol^{-1}), and RH the relative humidity of the atmosphere expressed as a percentage.

The relative humidity within each container is fixed by means of a saturated saline solution, which is poured directly into the container (Figure 5.2). The relative humidity depends on the salt used and on the imposed temperature. This method allows a wide range of suction pressures, from 4 to 400 MPa. The use of saturated aqueous solutions prevents changes in the

salt concentration and, in turn, the relative humidity, which can derive from the exchange of water between the specimen and the solution. The use of different suction values in each container allows several samples to be tested simultaneously. In this way, it is possible to obtain a complete retention curve, at a given temperature, by a single test sequence.

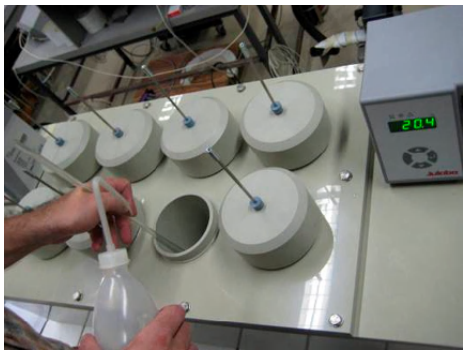

Figure 5.2. *Sorption bench: pouring the salt solution into the containers*

5.2.2. *Drying or wetting kinetics analysis*

The sorption bench allows the evolution of specimen weights to be measured. For this purpose, a precision balance is placed on an aluminum frame above the sorption bench (Figure 5.1). The balance is fixed on a truck that slides on a double guide-way system. This allows the truck to be easily moved in two orthogonal directions and to be precisely placed above each desiccator. Once the balance is in the right position, the specimen holder is coupled to the balance, and weighing can be recorded.

A special stopper system was developed that minimizes the interference of the weighting operation on the equalization process of the specimen to the imposed relative humidity. For certain soils, the vapor equilibrium technique takes a long time to equalize; consequently, disturbances in thermodynamic equilibrium, caused by handling the specimen or drying due to air exposure, have to be avoided. Measuring the weight of the specimen at different times allows the thermodynamic equilibrium and the evolution of the water content during the drying or wetting process to be monitored.

5.2.3. *Example test results*

In order to illustrate the use of the sorption bench, an experimental protocol carried out on Boom Clay samples is presented. Boom Clay is a polyphasic sediment that is composed of non-clay and clay minerals, fossil remains, and organic matter. The clay fraction is estimated to be about 55% and is dominated by illite (50%) and smectite (30%). Indicative values for the liquid and plastic limits are 55-80 and 23-29%, respectively [BAL 91, BER 97, HOR 87]. The aim of this study was to investigate the non-isothermal evolution of the retention properties of this material. The main drying path of the water retention curves was determined at two different temperatures (21 and 80°C). At the end of each equalization stage, the total volumes of the specimens were measured by immersion in a Kerdane bath [PER 07]. Figure 5.3 depicts the results in terms of water content and degree of saturation as a function of the imposed relative humidity.

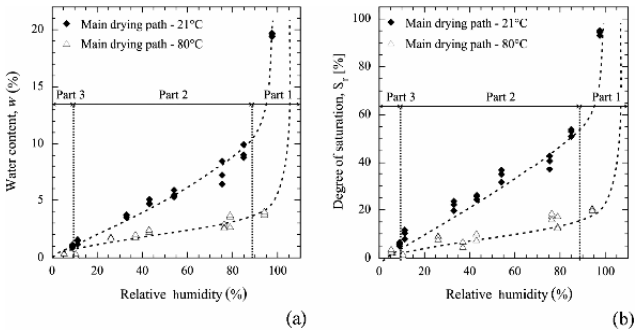

Figure 5.3. *Sorption isotherms of Boom Clay: (a) water content versus relative humidity and (b) degree of saturation versus relative humidity [RIZ 11]*

A general reduction of the water retention capability of the soil was observed when the temperature was increased. For a qualitative interpretation of obtained results, the curves are subdivided into three parts (Figure 5.3). In the first part, the water films around the solid phase are thick enough to allow the presence of capillary bonds. As the drying proceeds, the retention mechanism is characterized by multilayer adsorption (part 2) that appears to be strongly influenced by the temperature. The capillary water starts to disappear at approximately the same relative humidity for both temperatures, whereas both the water content and the degree of saturation corresponding to this limit decrease with temperature. The third part, which

corresponds to the adsorption of the first layer of water molecules, appears to be narrow and not affected by the variation of temperature.

5.3. High pressure THM oedometric cell

This section presents an oedometric cell that is devoted to the investigation of the volumetric response of highly overconsolidated clayey soils under non-isothermal conditions. Figure 5.4 shows an outline of the device. The apparatus allows independent control of vertical stress, total suction and temperature, and the measurement of water content variations and volumetric strains.

5.3.1. *Loading system*

The cell is designed to hold cylindrical samples (23 mm in height and 80 mm in diameter). The oedometer cell is fixed to a rigid stainless steel frame. The loading ram is positioned in the lower part of the system, while the upper base of the specimen is in contact with a fixed cylinder. This prevents the specimen from being loaded before the test starts. All the planar joints were precisely realized in an effort to keep a perfect contact between the specimen and the piston surfaces. A vertical load is applied by a hydraulic jack that is connected to a volume/pressure controller.

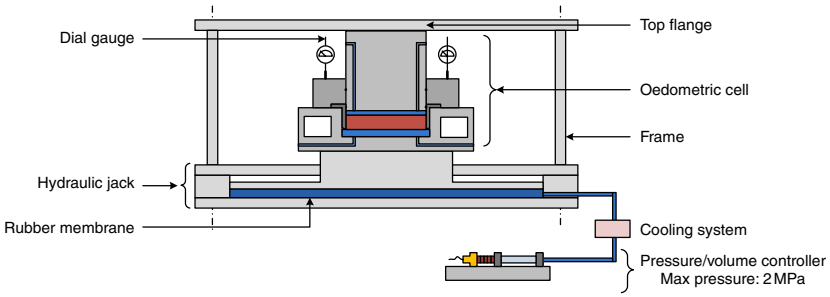

Figure 5.4. *High-pressure THM oedometric cell: loading system*

The relationship between the controller pressure and the vertical stress on the specimen has been assessed through calibration, taking into account frictions developing into the system. During calibration, the cell was filled with water and water pressure was monitored during cycles of loading and

unloading. The maximum pressure that can be attained by the controller (2 MPa) corresponds to a maximum vertical stress of approximately 24.6 MPa±20 kPa on the specimen. Volumetric strain is measured by three dial gauges that are fixed to the frame and are in contact with the loading ram, with a resolution of 0.001 mm.

5.3.2. *Suction control*

Total suction is controlled by means of the vapor equilibrium technique (see section 5.2.1). A salt solution fixes the relative humidity in a desiccator, equipped with a temperature/psychrometer sensor (Figure 5.5). The desiccator rests on a digital balance in order to measure the water exchange with the specimen. A convection system, regulated by a peristaltic air pump, transports the vapor from the desiccator to the specimen. Two sintered brass porous plates are in contact with the base of the specimen; they have been designed to have a high permeability, to facilitate vapor diffusion, and to work at high stresses.

By operating on the circuit valves, vapor can be forced to circulate through the sample or along its base. The first solution is used for samples with relatively low degree of saturation; this solution is preferable since it significantly reduces the equalization time. The second solution is used for nearly saturated specimens with low air permeability.

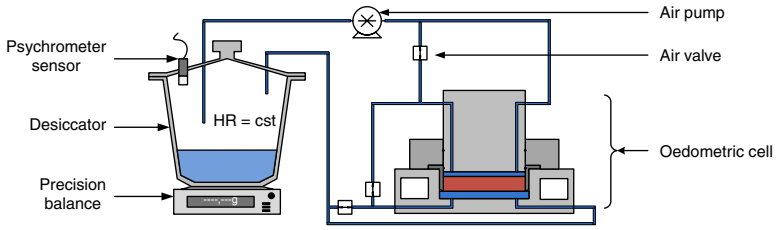

Figure 5.5. *High pressure THM oedometric cell: suction control system*

5.3.3. *Temperature control*

The heating system consists of a ring-shaped chamber that surrounds the specimen. Water is heated by a cryostat circulates through this chamber (Figure 5.6). The temperature can be controlled in the range of 5-90°C with

an accuracy of 0.1°C. The entire oedometer is located in an insulating box in order to reduce the ambient temperature influence and the heat dissipation.

Preliminary tests were run to assess the time needed for a complete thermal equalization of a specimen to an imposed temperature. For this purpose, a thermocouple was placed in the middle of a specimen and heating-cooling cycles were performed in steps of 10°C, lasting for 48 h. Test results showed that on average 12 h were required for the specimen to reach the imposed temperature. When equilibrium was attained, no significant differences between the temperature in the heating system and the temperature of the specimen were noted.

The hydraulic and pneumatic circuits pass through the cooling system to minimize the thermal interference on the loading system (Figure 5.4). Cooling is achieved by a radiator that is refrigerated by water at the laboratory temperature.

The combined effects of high vertical stresses and temperature on the deformability of the system were assessed by means of calibration tests. A high-rigidity cylinder in INVAR® (Fe-Ni36%) was positioned in the specimen chamber for these tests. Loading-unloading cycles at different temperatures and heating-cooling cycles at constant vertical load were performed while the displacements of the system were recorded (Figure 5.7). This facilitated the definition of a correction factor that could be applied to the displacement measurements (Δh^*) to obtain the real displacement of the specimen (Δh), taking into account the applied vertical stress (p_v, in kPa), and temperature variation (ΔT, in °C):

$$\Delta h = \Delta h^* - 2.2\, p_v^{0.52} - 0.0032 \Delta T^2 - 0.123 \Delta T. \qquad [5.2]$$

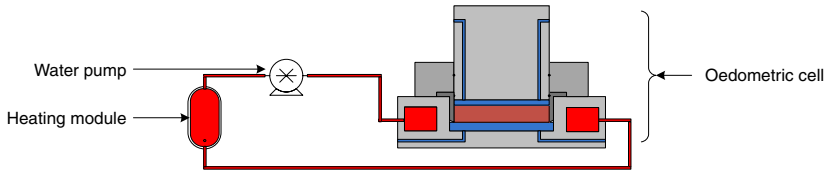

Figure 5.6. *High pressure THM oedometric cell: temperature control system*

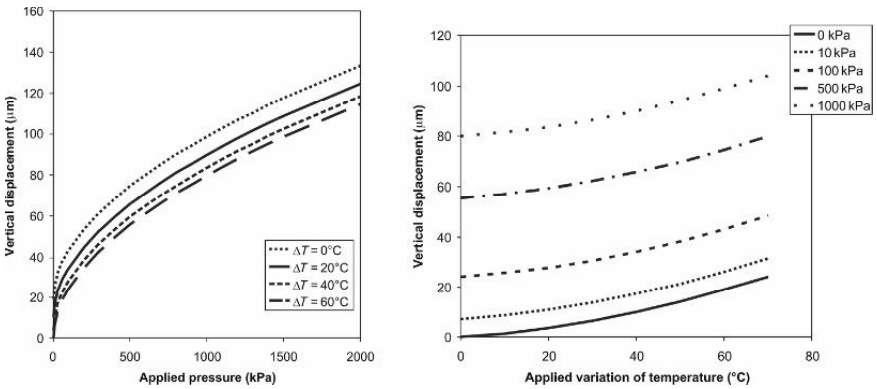

Figure 5.7. *High pressure THM oedometric cell: temperature control system calibration curves of the oedometric cell*

5.3.4. *Example test results*

Test results obtained on samples of Opalinus Clay are reported as an example of the use of the high pressure THM oedometric cell. Opalinus Clay has a clay fraction in the range 50–70%, consisting mostly kaolinite and illite [CHE 92], a liquid limit of 38% and a plastic limit of 23% [COR 07].

Three test results, demonstrating the effects of temperature and suction on the deformability of the material, are presented. Testing conditions were 22°C (15 MPa), 22°C (20.2 MPa), and 80°C (4 MPa). The samples, obtained from borehole cores, were first equalized to the imposed suction in a desiccator with controlled relative humidity. They were then placed into the oedometric cell and equilibrated at the testing temperature. The applied suction was kept constant by means of the convection system. Vertical stress was then applied in steps.

Void ratio variations versus applied vertical stresses are depicted in Figure 5.8. This highlights the suction- and temperature-dependent behavior of the material.

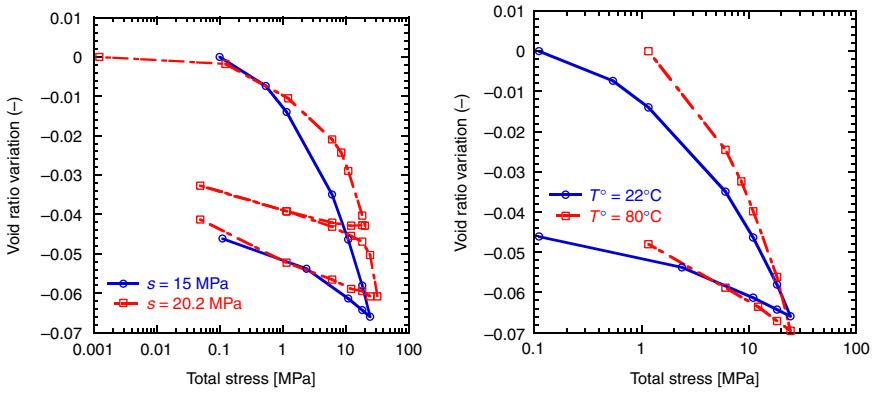

Figure 5.8. *Oedometric compression test on Opalinus Clay for two suctions and two temperatures*

5.4. High pressure and high temperature THM triaxial cell

A new multipurpose triaxial cell was developed to perform suction-controlled tests on unsaturated materials under wide ranges of temperature and cell pressure.

This section focuses on two primary innovative features of the apparatus, namely the double-wall system, which allows proper measurement of variations in the sample volume, and the hydraulic and pneumatic circuits, which allow several testing layouts to be applied for saturated and unsaturated conditions.

Figure 5.9 depicts a general layout of the cell and associated devices. The cell holds specimens that are 50 mm in diameter and 100 mm in height. Cell pressure is controlled in the range 0–30 MPa by means of a pressure/volume controller. The maximum attainable axial force is 450 kN. The temperature of the system can be controlled in the range 5–150°C. The vertical displacement is measured by two LVDTs positioned outside the cell.

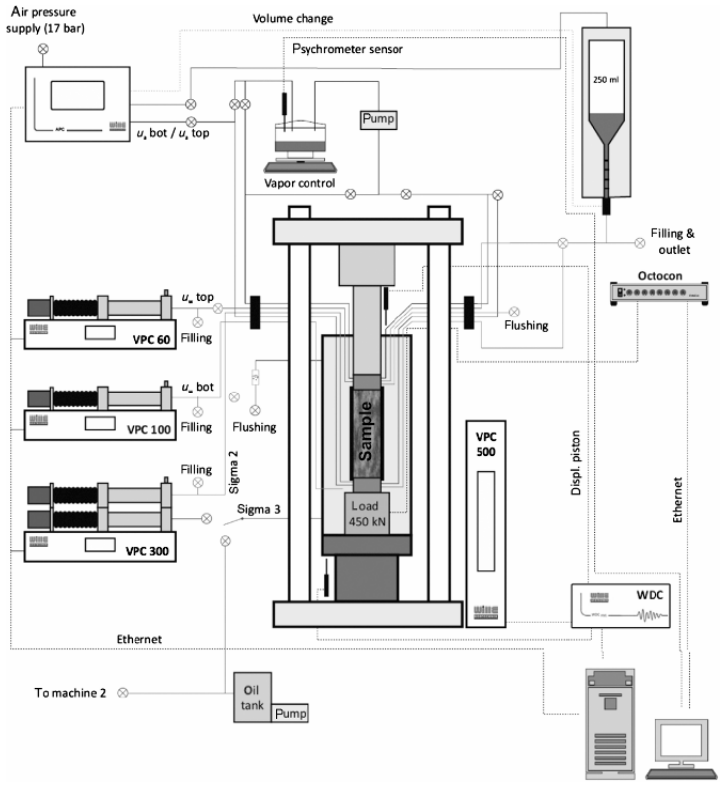

Figure 5.9. *High pressure and high temperature THM triaxial cell: general outline*

5.4.1. *The double wall system*

An independent measurement of sample volume variation is required when dealing with soils in partial saturation conditions [HOY 08]. Assessment of the sample's volumetric strain, based on cell fluid volume variations, can be inaccurate. This is particularly true under high confining pressure and due to the compressibility of the confining fluid and the deformability of the cell. This issue was solved by adopting the double cell concept described by [WHE 88] and [SIV 93]. Figure 5.10 shows the technical solution. The sample is placed between the top and bottom caps and is surrounded by a membrane that can work at high pressures and temperatures. An inner steel cylinder is sealed to both the top and the bottom base of the cell. The space between the membrane and the inner cylinder defines the inner chamber. The confining pressure is applied by a special

pressure/volume controller that has two separate outlets connected to the inner and the outer chambers. Each outlet is equipped with a device for measuring volume changes. The volumetric strain of the sample is then calculated by analyzing the measures from the inner chamber only.

Most of the sources of measurement error, related to the direct measurement of sample volume variations and discussed by [HEA 86], can be reduced with this system. In order to reduce the effects of the compressibility of the confining fluid, the distance between the membrane and the inner cylinder is limited; even at high pressures, the volume changes of the cell fluid are not significant when compared to the sample volumetric strains. The inner cylinder receives the same pressure from the inside and the outside; this limits the volume change of the cylinder even at very high pressures. Moreover, all the tubes of the hydraulic, pneumatic, and electric circuits go through the outer chamber. Consequently, their deformation does not influence the measurement accuracy.

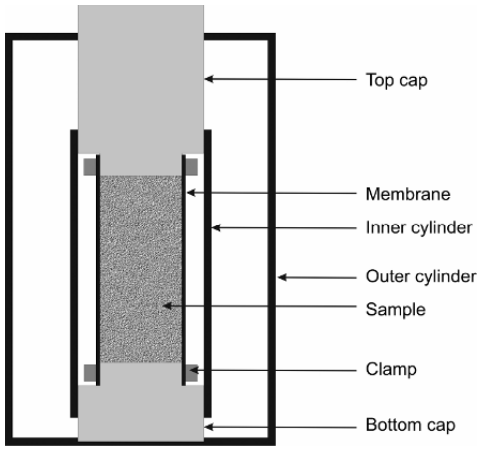

Figure 5.10. *High pressure and high temperature THM triaxial cell: outline of the double wall system*

5.4.2. *Possible experimental layouts*

Several experimental layouts can be used depending mainly on the degree of saturation of the specimen to be tested. The apparatus can be

adapted by simple modifications such as changing the positions of various components.

A traditional experimental layout for tests in saturated conditions was applied. Top and bottom caps were equipped with sintered steel porous plates, designed to work at high pressures. Two pressure/volume controllers were used to independently control the pore water pressure and to measure the water volume exchange at each base (top and bottom). The use of independent controllers allows the measurement of the pore water pressure developing in undrained tests in each base, and allows running permeability tests by applying a hydraulic gradient along the sample.

When dealing with high values of suction pressure, the vapor technique can be implemented to control the total suction in a similar way as described for the oedometric cell. In this case, air at a controlled relative humidity is forced to circulate by means of a pump, and water content variations can be inferred by the changes in weight of the salt solution in the desiccator (Figure 5.9).

The axis translation technique was used to control matrix suction in the range of 0-1.5 MPa. In this case, air and water pressure are regulated independently, and are applied to top and bottom caps. Custom four-hole caps (Figure 5.11) were designed to apply air and water pressure simultaneously at each base. High air entry value ceramic disks were used for the application of the pore water pressure, preventing the inlet of air pressure in the water circuit. Air pressure was provided by the laboratory-compressed air system. This pressure is regulated to the target value by an electronic air pressure regulator and is recorded before it enters the specimen. A “T-shape” connection allows the same pressure to be applied to the top and bottom bases of the specimen. Two pressure/volume controllers were used to apply water pressure independently at each base and to record water volume exchanges through the bases. A custom flushing system ensured that air bubbles moved away from the caps without altering the measures of exchanged water volumes and without lowering water pressures in the caps.

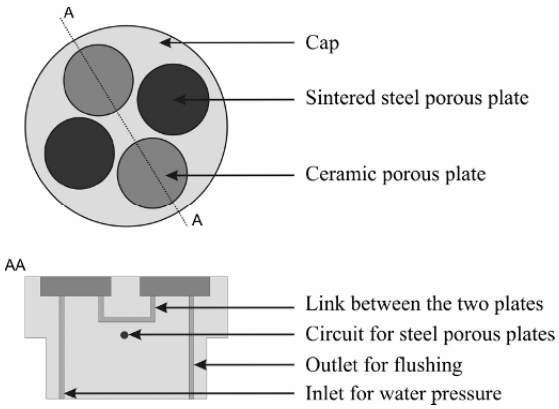

Figure 5.11. *High pressure and high temperature THM triaxial cell: special caps for the application of the axis translation technique*

5.5. Conclusions

Different experimental devices and techniques have been presented to study the THM behavior of highly overconsolidated clayey materials. The major issues in developing such experimental tools are the simultaneous control of the stress, strain rate, thermal and hydraulic states, and measurement of water content variations. The results provided were selected to demonstrate the potential applications of some novel technologies.

5.6. Bibliography

[BAL 91] BALDI G., HUECKEL T., PEANO A., PELLEGRINI R., Developments in modelling of thermo-hydro-geomechanical behaviour of Boom Clay and clay-based buffer materials, ISMES, Final Report, EUR 13365, vol. 1, 1991.

[BLA 08] BLATZ J.A., CUI Y.-J., OLDECOP L., "Vapour equilibrium and osmotic technique for suction control", *Geotechnical and Geological Engineering*, vol. 26, no. 6, p. 661-673, 2008.

[BER 97] BERNIER F., VOLCKAERT G., ALONSO E., VILLAR M., "Suction-controlled experiments on Boom Clay", *Engineering Geology*, vol. 47, p. 325-338, 1997.

[CEK 09] CEKEREVAC C., LALOUI L., "Experimental analysis of the cyclic behaviour of Kaolin at high temperature", *Géotechnique*, in press.

[CHE 92] CHERMAK J.A., "Low temperature experimental investigation of the effect of high pH NaOH solutions on the Opalinus shale", *Clays and Clay Minerals*, vol. 40, no. 6, p. 650-658, 1992.

[COR 07] CORKUM A.G., MARTIN C.D., "The mechanical behaviour of weak mudstone (Opalinus Clay) at low stresses", *International Journal of Rock Mechanics and Mining Sciences*, vol. 44, no. 2, p. 196-209, 2007.

[FRA 08] FRANCOIS B., Thermo-plasticity of fine-grained soils at various saturation states: application to nuclear waste disposal, PhD Thesis, EPFL, Lausanne, 2008.

[HEA 86] HEAD K.H., *Manual of Soil Laboratory Testing*, vol. 3, Pentech Press, London, 1986.

[HOR 87] HORSEMAN S.T., WINTER M.G., ENTWISTLE D.C., "Geotechnical characterizatio of Boom Clay in relation to the disposal od radioactive waste", *Geotechnical and Geological Engineering, ASCE*, vol. 26, no. 6, p. 675-698, 2008.

[HOY 08] HOYOS L.R., LALOUI L., VASSALO R., "Mechanical testing in unsaturated soils", *Commission of the European Communities*, EUR 10987, 1987.

[HUE 90] HUECKEL T., BALDI G., "Termoplastic behavior of saturated clays: an experimental constitutive study", *Journal of Geotechnical Engineering, ASCE*, vol. 116, no. 12, p. 1778-1796, 1990.

[LAL 09] LALOUI L., NUTH M., "On the use of the generalised effective stress in the constitutive modelling of unsaturated soils", *Computer and Geotechnics*, vol. 36, p. 20-23, 2009.

[NUT 08] NUTH M., LALOUI L., "Advances in modelling hysteretic water retention curve in deformable soils", *Computers and Geotechnics*, vol. 35, no. 6, p. 835-844, 2008.

[OBR 48] O'BRIEN F., "The control of humidity by saturated salt solutions", *Journal of Scientific Instruments*, vol 25, p. 73-76, 1948.

[PER 07] PERON H., HUECKEL T., LALOUI L., "An improved volume measurement for determining soil water retention curve", *Geotechnical Testing Journal*, vol. 30, no. 1, p. 1-8, 2007.

[RIZ 11] RIZZI, M., Characterization and constitutive modelling of the behaviour of granular bentonite during THM-processes, PhD Thesis, EPFL, In process.

[ROM 99] ROMERO E., Characterization and thermo-hydro-mechanical behaviour of unsaturated Boom Clay: an experimental study, PhD Thesis, Universitat Politècnica de Catalunya, Barcelona, Spain, 1999.

[SAL 08] SALAGER S., FRANCOIS B., EL YOUSSOUFI M. S., LALOUI L., SAIX C., "Experimental investigations on temperature and suction effects on mechanical behaviour of a sandy silt", *Soils and Foundations*, vol. 48, no. 4, p. 453-466, 2008.

[SAL 09] SALAGER S., EL YOUSSOUFI M. S., SAIX C., "Temperature effect on water retention phenomena in deformable soils – Theoretical and experimental aspects", *European Journal of Soil Science*, vol. 61, no. 1, p. 97-107, 2010.

[SAL 10] SALAGER S., EL YOUSSOUFI M. S., SAIX C., "Definition and experimental determination of a soil water retention surface", *Canadian Geotechnical Journal*, in press.

[SIV 93] SIVAKUMAR V., A critical state framework for unsaturated soils, PhD Thesis, University of Sheffield, Sheffield, 1993.

[SUL 02] SULTAN N., DELAGE P., CUI Y.J., "Temperature effects on the volume change behaviour of Boom Clay", *Engineering Geology*, vol. 64, p. 135-145, 2002.

[TAN 05] TANG A.M., CUI Y.-J., "Controlling suction by the vapour equilibrium technique at different temperatures and its application in determining the water retention properties of MX80 clay", *Canadian Geotechnical Journal*, vol. 42, p. 287-296, 2005.

[WHE 88] WHEELER S.J., "The undrained shear strength of soils containing large gas bubbles", *Géotechnique*, vol. 38, no. 3, p. 399-413, 1988.

[WIN 60] WINSTON P.W., BATES D.H., "Saturated solutions for the control of humidity in biological research", *Ecology*, vol. 41, no. 1, p. 232-237, 1960.

Chapter 6

Field Measurement of Suction, Water Content and Water Permeability

Suction and (volumetric) water content play a key role in the mechanical and hydraulic behavior of unsaturated geomaterials, and their field measurement is therefore a fundamental issue in engineering applications. Techniques for suction measurement in the laboratory and field have widely been reviewed in the literature [BUL 08, DUR 05, MAR 08, RID 96a, RID 98, SCA 02, TAR 08, YOU 02], in addition to techniques for water content measurements based on dielectric methods [GAR 01, JON 02, NOR 01, O'CO 99, ROB 03, TAR 08]. The reader may refer to these publications for a comprehensive discussion on these techniques. The aim of this chapter is to present the basic principles of field measurement of suction and water content to help new readers systematize the large information available in the literature. A brief overview of the methods to determine the hydraulic conductivity in the field is also presented at the end of the chapter.

6.1. Direct measurement of suction

Suction in the field is directly measured by tensiometers. The essential components of tensiometers are a high air entry porous ceramic, a reservoir of liquid (usually water), and a means of measuring stress (a strain-gauged diaphragm for the device shown in Figure 6.1). When the porous ceramic is

---

Chapter written by Alessandro TARANTINO.

placed in contact with the unsaturated geomaterial, water is drawn out of the water reservoir and a negative pressure develops in it. The negative pressure causes the diaphragm to bend towards the porous ceramic, and can thus be inferred from the change in the electrical resistance of the strain gauge attached onto the backside of the diaphragm. Water in the reservoir and the ceramic can remain under tension because of the menisci that form at the ceramic interface (Figure 6.1). These sustain the difference between the external air pressure (atmospheric) and the negative water pressure in the reservoir. The highest sustainable pressure differential depends on the maximum meniscus curvature, which in turn depends on the ceramic pore size. The maximum sustainable pressure differential is known as the *air entry value* of the ceramic, which limits the highest measurable water tension.

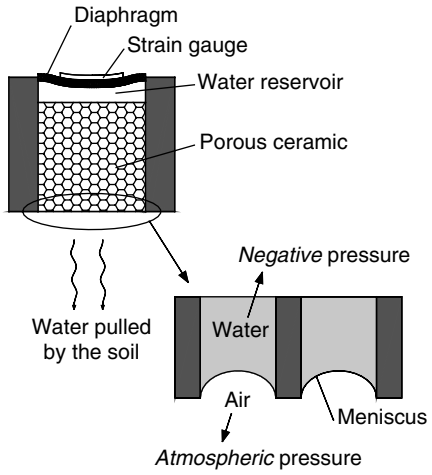

Figure 6.1. *Working principle of tensiometer*

Water tensions less than the ceramic air entry value can be sustained, but not indefinitely. Water tension tends to expand pre-existing air cavities trapped in the crevices in the water reservoir walls and in the ceramic filter causing the air pressure in these air cavities to drop to values lower than the atmospheric pressure. Because of the air pressure differential, air diffuses towards these cavities from outside the tensiometer and cavities will expand until occupying the entire cross-section of the water reservoir. This process is referred to as tensiometer *cavitation*.

The rate of growth of air cavities depends on the number and size of pre-existing cavities. When the number and size of air cavities is minimized by (i) adopting a water reservoir of reduced size; (ii) filling the tensiometer under vacuum with deaired water; and (iii) pre-pressuring the water in the ceramic filter and reservoir at high pressures, the rate of growth of air cavities can be significantly slowed down and even absolute negative water pressures (gauge pressures lower than –100 kPa) can be sustained for relatively long time (from hours to weeks), as first demonstrated by [RID 93]. Tensiometers capable of measuring negative absolute pore water pressures are referred to as high-capacity tensiometers. The process of cavitation can be easily detected when measuring the negative absolute pressures. As air occupies the entire cross-section of the water reservoir, absolute negative pressures can no longer be transmitted to the sensing device (gases cannot sustain negative absolute pressures). Pressure rapidly increases to around zero absolute pressure as the air cavity rapidly expands in the reservoir (–100 kPa in terms of gauge pressure), as shown in Figure 6.2.

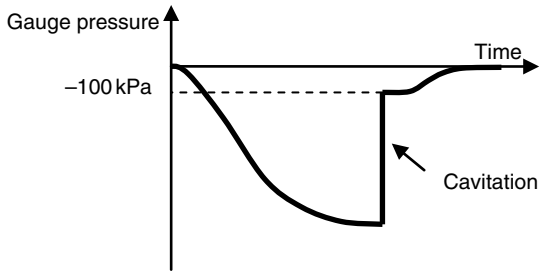

Figure 6.2. *Cavitation in high-capacity tensiometer*

For the case where tensiometers (i) have relatively large water reservoirs; (ii) are filled with ordinary tap water; and (iii) are not pre-conditioned by applying high pressurization pressures, air cavities rapidly grow as zero absolute pressure is approached. Measurement range is therefore limited to positive absolute pressures (from 0 to –100 kPa in terms of gauge pressures). Tensiometers capable of measuring only the positive absolute pore water pressures are referred to as *conventional tensiometers.* Cavitation in conventional tensiometer is difficult to detect because air is capable of transmitting positive absolute pressures.

6.1.1. *Conventional tensiometers (positive absolute pressure)*

Conventional tensiometers differ depending on the relative position between the porous filter and the sensing device, and the technique is used to resaturate the porous filter, and the procedure is adopted to ensure soil-tensiometer contact. A common design consists of a water reservoir tube, a differential pressure transducer connected to the top of the tube, and a porous ceramic cup at the bottom of the tube (Figure 6.3).

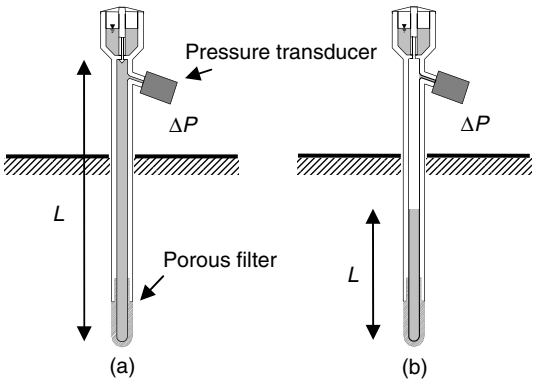

Figure 6.3. *Schematic layout of tensiometer with sensing device at the ground surface and manual refilling (jet-fill vacuum gauge tensiometer, Soilmoisture Equipment Corp., Santa Barbara, CA, USA)*

Suction measured at the tensiometer tip for the case of a fully saturated tube is given by:

$$s = \Delta P - L\gamma_{\mathrm{w}} \qquad [6.1]$$

where ΔP is the differential pressure reading, γ_{w} is the unit weight of water, and L is the tube length. Equation [6.1] shows that the useful range of the tensiometer is reduced by the term $L\gamma_{\mathrm{w}}$, i.e. the longer the tube, the lower is the measurement range. Theoretically, the minimum pressure that can be measured by a conventional tensiometer is –100 kPa. In practice, it is difficult to measure negative pressures lower than –60/–70 kPa, because air rapidly forms in the tube at these pressures. Ridley *et al.* [RID 98] showed that the useful range of these tensiometers was really only 0–50 kPa for an instrument that was 1.5 m in length, because at suctions greater than 50 kPa, the formation of air in the instrument became uncontrollable and too rapid to

be removed manually. Moreover, if the formation of air is not arrested, the tensiometer eventually becomes completely dry and the gauge indicates a tension of zero. This can easily be confused with a real measurement of zero, which would be indicative of "wet" conditions, and thus obviously grossly incorrect. When air forms in the upper portion of the tube (Figure 6.3(b)), suction is given by:

$$s = \Delta P - L_{\mathrm{w}} \gamma_{\mathrm{w}} \qquad [6.2]$$

where L_{w} is the height of the water column. Of course, if suction is inferred from equation [6.1] by assuming that the tube is fully saturated, then suction measurement will be affected by significant error. Frequent maintenance is therefore required to maintain the tube fully saturated. Saturation is generally achieved by injecting water from the reservoir at the top of the tube and letting water flowing out of the porous tip. Moisture content is temporarily increased around the tensiometer tip, and some time is required to re-establish moisture equilibrium conditions. Figure 6.4 shows a measurement where suction tends to decrease with time after installation, and in practice, it may be difficult to recognize whether suction is actually decreasing in the ground or the tensiometer is desaturating. If the tensiometer is refilled, two typical responses could be observed. If suction keeps decreasing following the same trend (continuous line in Figure 6.4), the tensiometer was fully saturated and readings before refilling were actually correct. If this was not the case (dashed line in Figure 6.4), then the actual suction was greater than the measured suction over the period preceding the refilling, and the decrease in suction observed over this period was therefore associated with cavitation.

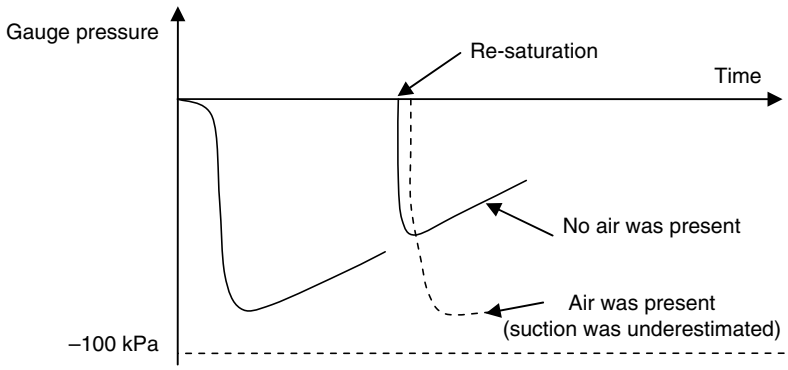

Figure 6.4. *Resaturation of conventional tensiometer*

To overcome the limitations of long water tube reservoir, tensiometers are manufactured by positioning the sensor device close to the porous filter to reduce the water reservoir length to some centimeters (Figure 6.5(a)).

In this case, air forming in the water reservoir will not affect measurement accuracy, provided the ceramic remains saturated and a negative pressure is still transmitted to the fluid in the water reservoir. However, the response time of the instrument will significantly increase, because air compressibility is much higher than water compressibility. To function correctly in the field, these tensiometers also require a means of removing air (if it forms) from the reservoir of liquid. Recently, a self-filling tensiometer has become commercially available (TS1, UMS, Munich, Germany). After drying periods, when the soil is rewetted by rain, an integrated micropump, controlled by an onboard controller, starts to suck the water from the soil into the tensiometer until the whole interior is filled with water again [DUR 05].

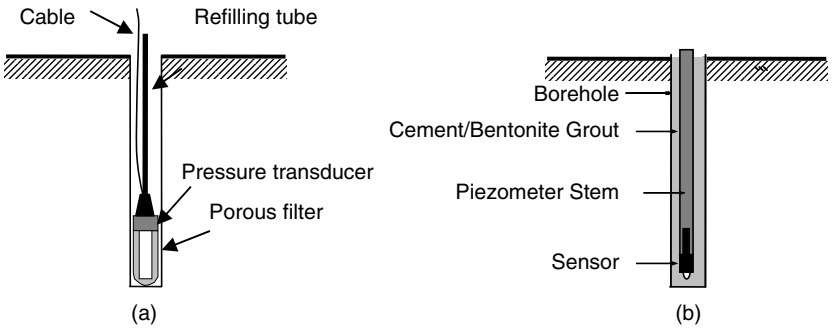

Figure 6.5. *Schematic layout of tensiometer with sensing device close to the porous tip (a) pressed in pre-drilled hole and (b) in borehole filled with cement-bentonite grout [RID 03]*

A hydraulic contact between the tensiometer cup and the soil is essential for proper operation. If the tensiometer cup is pressed in a predrilled hole that is slightly narrower than the diameter of the cup itself, this contact is generally sufficient. In coarse-grained soils, this practice might, however, not be feasible. In these cases, either a slurry of local sieved fine soil or a silty contact material can be used to provide contact in a predrilled access hole of larger diameter. To ensure soil-tensiometer contact, an alternative

method comprises installation of the tensiometer in boreholes, which are subsequently filled with a cement-bentonite grout. The grout acts as a secondary filter for transmitting the negative pore water pressures from the soil to the piezometer. If designed correctly, the grout will not desaturate until the suction is equal to or greater than 100 kPa, and therefore, it will not restrict the range of suctions that can be measured by the tensiometer [RID 03].

6.1.2. *High-capacity tensiometers (negative absolute pressure)*

Ridley and Burland [RID 93] introduced the concept of measuring suctions greater than 100 kPa. They [RID 96b] then presented an integral strain-gauged tensiometer, which could measure suctions up to 1500 kPa (the design of this tensiometer is essentially shown in Figure 6.1). This tensiometer uses a combination of fine porous filters (capable of remaining saturated to 1500 kPa) and a technique of preconditioning the instrument by pressurizing the water in the instrument to very high pressures (e.g. 4000 kPa). A technique was developed by [RID 96b] for placing the new tensiometers at depths up to 5 m (Figure 6.6). However, when cavitation occurs, it is necessary to remove the tensiometer from the ground to resaturate it using the pressurization technique, and this is the main limitation of high-capacity tensiometers for field measurements. Recently, [CUI 08] presented a device that could measure suction changes in the low range (20–160 kPa) at small depths (25 and 45 cm) along a period of 3 weeks. The installation system allowed simple replacement of the tensiometer when resaturation by pressurization is required following cavitation.

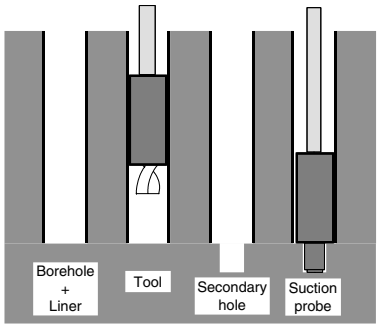

Figure 6.6. *Installation of high-capacity tensiometer [RID 96b]*

6.2. Indirect measurement of suction

To monitor suctions greater than 70–80 kPa in the field, i.e. beyond the measurement range of conventional tensiometers, devices have been developed that could measure suction in an indirect fashion. Instruments for indirect measurement are based on equilibrium through liquid or vapor phase.

6.2.1. *Equilibrium through liquid phase*

These devices are based on the measurement of water content-related properties in porous blocks that are in hydrostatic equilibrium with the surrounding soil. A porous block is a rigid porous medium with its own water retention behavior. This is characterized by a main drying and main wetting curve as well as scanning curves spanning the region between the two bounding curves (Figure 6.7). When the porous block is placed in contact with the soil, water flows in or out of the porous block until suction in the porous block equals suction in the surrounding soil. Water content at equilibrium is not uniquely related to suction because of water retention hysteresis. However, if the hysteresis domain is relatively narrow, then a relationship can be established between the porous block water content and suction with a given level of confidence (Figure 6.7). If water content or its related property is measured, then suction can be inferred from a suitable calibration curve with an inherent error associated with the water retention hysteresis of the porous block. Water content related properties include electrical resistance (electrical conductivity sensors), heat dissipation (thermal conductivity sensors), or dielectric permittivity (equitensiometers).

Electrical conductivity sensors have porous element made of gypsum or a granular matrix of silt size (Watermark™ sensors). Such devices are generally inexpensive, but are more suitable for trend measurement rather than accurate determination of suction. Electrical conductivity is affected by soil salinity ([AIT 51]), and hence, calibrations for these devices are needed to examine saline soils. Gypsum blocks have the advantage that they tend to buffer the soil salinity, thereby decreasing this effect. They do this by dissolution of gypsum, which means that gypsum block sensors have a limited life (up to 5 years in alkaline or neutral soils). *Thermal conductivity sensors* rely on the measurement of the water content of the block by measurement of the temperature rise induced by a heater embedded at the

center of the porous block. The *Equitensiometer* (dielectric permittivity sensors) is a new device that uses a "specially formulated porous matric material" ([DEL 05]) that is intended to eliminate hysteretic behavior between drying and wetting. A ThetaProbe sensor is used to measure the water content of the porous block (Figure 6.8).

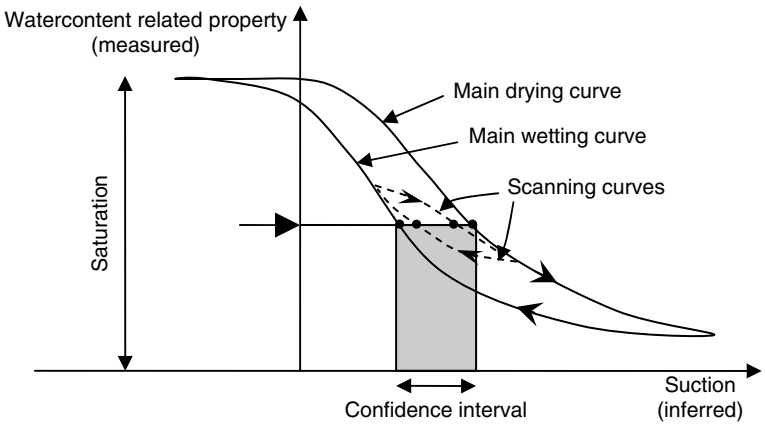

Figure 6.7. *Working principle of porous block sensors*

A common feature of all porous block devices is the relatively slow response. As suction in the surrounding soil changes, water has to flow in or out of the porous block until equilibrium is re-established. However, the porous block is unsaturated and is therefore characterized by relatively low hydraulic conductivity. As a result, equalization may take days, if not weeks. For example, [BER 02] showed that the response of Watermark electrical conductivity sensors is slow when compared with tensiometers (lags by about 2 days). [SHU 00] showed that full equalization time of thermal conductivity sensors can be about 2 weeks, although a dry sensor may only take 4 days. [NG 03] demonstrated that thermal conductivity sensors showed a slower response (2 days' lag) when compared with tensiometers.

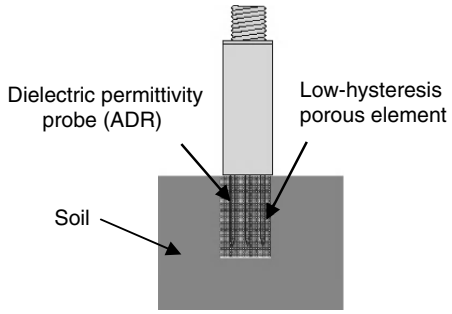

Figure 6.8. *Schematic layout of equitensiometer (Delta-T Devices Ltd, Cambridge, UK)*

6.2.2. *Equilibrium through vapor phase*

The total suction s_t can be inferred from the measurement of the relative humidity of air in equilibrium with soil water according to the "psychrometric law" (see Chapter 1):

$$s_t = -\frac{RT}{v_w} \ln \frac{p_v}{p_{v0}(T)} = -\frac{RT}{v_w} \ln \mathrm{RH} \qquad [6.3]$$

where T is the absolute temperature, R the universal gas constant, v_w the molar volume of liquid water, p_v the pressure of the vapor in equilibrium with the liquid, p_{v0} the saturated vapor pressure at the same temperature, and RH the relative humidity. In the field, relative humidity can be measured by using the thermocouple psychrometer. Psychrometers measure the difference between a dry- and wet-bulb temperature. The dry bulb records the temperature of the surrounding soils, whereas the wet bulb records the temperature of an evaporating surface. The lower the humidity, the higher will be the rate of evaporation from the wet bulb, and thus the temperature depression below the ambient level. As air is an effective diffusion barrier for most solutes, the suction inferred from the psychrometric law includes both the osmotic and matric component of suction. A thermocouple is a double junction of two dissimilar metals (Figure 6.9). When the two junctions are subject to different temperatures, they generate a voltage difference (Seebeck effect). Conversely, when an electrical current is applied, the junction is heated or cooled, depending on the direction of the current (Peltier effect) ([DUR 05]). For typical soil use, one junction of the thermocouple is suspended in a thin-walled porous ceramic or stainless

screen cup buried in the soil, while another is embedded in an insulated plug to measure the ambient temperature at the same location. Using electrical current, the suspended thermocouple is cooled below the dew point until water condenses on the junction. The cooling current then stops, and as water evaporates, it draws heat from the junction, depressing it below the temperature of the surrounding air until it attains wet-bulb temperature. The difference in the temperatures between the wet and dry bulb is related to the relative humidity measured via a calibration curve developed by suspending the thermocouple over salt solutions of known relative humidity.

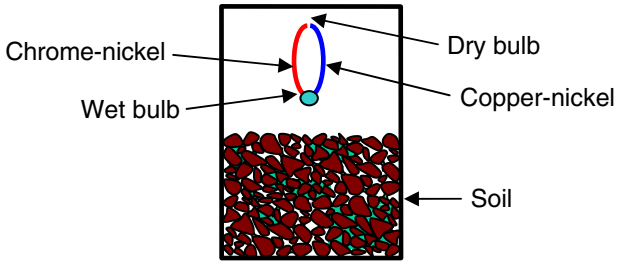

Figure 6.9. *Working principle of thermocouple psychrometer*

One of the limitations of the psychrometer is the necessity of equilibrium through the vapor phase, which causes a relatively slow response time. In addition, psychrometers are highly susceptible to thermal gradient effects and do not perform well at shallow soil depths. As a result, suctions lower than 1000–2000 kPa are difficult to measure, and psychrometer should therefore be used only to measure suction in the high range. To clarify this point, let us consider the effect of small temperature fluctuations on relative humidity. If temperature changes very rapidly, it can be assumed that water vapor pressure p_v remains constant, whereas saturated vapor pressure p_{v0} changes according to the change in the temperature. By deriving equation [6.3] and considering the Clausius–Clapeyron equation:

$$\frac{\mathrm{d}p_{v0}}{\mathrm{d}T} = \frac{M_w L p_{v0}}{RT^2}, \qquad [6.4]$$

where M_w is the molar weight of water (M_w=18.016 g/mol), R the universal gas constant (R=8.314 J/K/mol), L the latent heat of evaporation (L= 2 453 000 J/kg at 20°C), and T the absolute temperature, we obtain:

$$\frac{\partial s_{\mathrm{t}}}{\partial T} = (s_{\mathrm{t}} + \rho_{\mathrm{w}} L)\frac{1}{T} \cong \frac{\rho_{\mathrm{w}} L}{T}, \qquad [6.5]$$

where ρ_{w} is the water density. According to equation [6.5], a temperature fluctuation of only ±0.01°C produces a change in suction of about ±80 kPa at 20°C. This is the reason why it is difficult to accurately measure suction lower than 1000–2000 kPa, and the response may be highly inaccurate when the psychrometer is installed at shallow depths.

6.3. Measurement of water content

The dielectric permittivity of the soil "mixture" depends on the permittivity of the single soil components (solid, liquid, and gas) and their volumetric fraction. As the relative permittivity of air is 1, ranges from 3 to 5 in most soil mineral grains, and is approximately 80 for water (at 20°C), the permittivity of the soil mixture is essentially controlled by water, and hence, by its volumetric fraction. Soil dielectric permittivity can therefore be related to the volumetric water content (volume of water per total volume of soil) through suitable calibration, and this is the principle of dielectric methods for water content measurement. The soil dielectric permittivity is not measured in a static electric field, but in an alternate electric field that propagates in the form of waves. Under such conditions, the dielectric permittivity of water is frequency dependent, and has a real and an imaginary component. A better understanding of soil dielectric properties and wave propagation in transmission lines is therefore essential to discuss the dielectric methods. These two topics are not commonly covered in undergraduate and graduate courses, and will be introduced in this chapter. Dielectric methods examined in this chapter include broadband high-frequency methods (Time Domain Reflectometry, TDR) and single low-frequency methods (Amplitude Domain Reflectometry (ADR) and Capacitance).

6.3.1. *Soil dielectric permittivity*

The origin of high permittivity of water is the asymmetry of charge in the water molecule that produces a permanent dipole. Let us consider the capacitor shown in Figure 6.10, where the static electric field generated by the surface charge σ causes water molecules (permanent dipoles) to line up.

At the surface, there are unbalanced charges that produce an additional *surface polarization charge* σ_P that partly neutralizes the original charge. The electric field E resulting from this additional polarization charge is lower than the static electric field in vacuum E_0 by a factor ε_r, which is referred to as the *relative permittivity* ($E=E_0/\varepsilon_r$). The higher the polarization, the higher is the dielectric permittivity. When a time-harmonic field propagates as a wave through the material, the dipoles align with the field, oscillating and in turn establishing a polarization wave that propagates through the material superposing the driving field. This alignment manifests itself as the real (in-phase) part of the relative permittivity (ε_r'). As the frequency is increased, the molecules being aligned by the alternating field can no longer keep up with the speed of field alternation (*dipole relaxation*). This reduces the intensity of polarization and gives rise to a time lag between the applied field and the polarization wave. This phase shift manifests itself as the imaginary (out-of-phase) part of the relative permittivity (ε_r'') and causes dissipation of energy in the form of heat (as in microwave ovens).

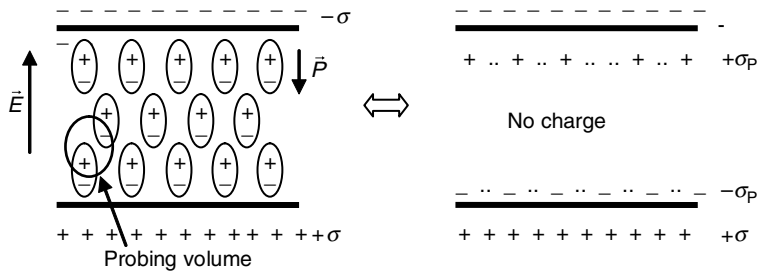

Figure 6.10. *Capacitor filled with dielectric material*

The real and imaginary part of dielectric permittivity of pure water, ε_r' and ε_r'', respectively, is plotted in Figure 6.11. The figure also reports the upper bound of the TDR bandwidth (~1.5 GHz) showing that the TDR frequencies are well below the relaxation frequency of free water (~17 GHz) and are therefore associated with negligible dielectric losses. Water in soils is rarely pure and usually contains charge carriers such as ions. Ionic conductivity causes a loss of energy (*conductive loss*) in addition to loss due to dipole relaxation (*relaxation loss).* Figure 6.11 shows the real and imaginary part of relative permittivity of aqueous solutions at different concentrations (tap, moderately saline, and sea water). The static

permittivity, ε_{rs}, decreases with increasing concentration of dissolved ions. The ions orient the water molecules around them, thereby reducing their ability to orient in the applied fields, and thus reducing the static dielectric permittivity. Figure 6.11 also shows that the effect of ionic loss on the imaginary part of dielectric permittivity is inversely proportional to the frequency and tends to become negligible at high frequencies. The equivalent complex permittivity of aqueous solution accounting for both dielectric and conductive losses can be expressed as follows:

$$\varepsilon_r^*(f) = \varepsilon_r'(f) - j\varepsilon_r''(f) - j\frac{\sigma_{dc}}{2\pi f \varepsilon_0}, \qquad [6.6]$$

where ε_0 is the permittivity in free space, σ_{dc} the direct current electric conductivity, and f the frequency.

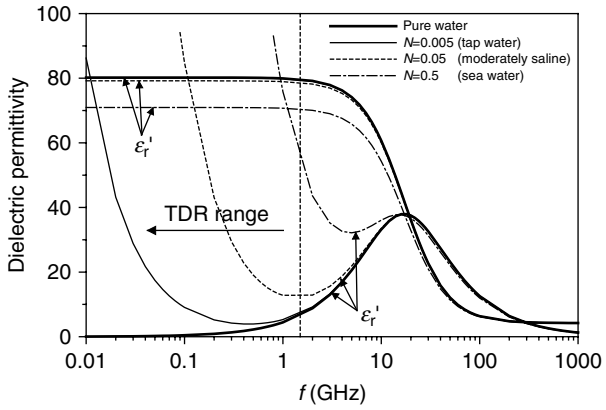

Figure 6.11. *Real and imaginary part of relative permittivity of pure water and aqueous solutions at different concentration (T=20°C)*

6.3.2. *Wave propagation in transmission lines*

Electromagnetic wave propagation inside a transmission line is described by the line current I and the voltage V between the conductors. If V and I are time-harmonic cosine functions with angular frequency ω and the symbolic representation of sinusoidal signal is adopted, the following transmission line equations can be obtained [KRA 99]:

$$\begin{cases} \vec{V}(t,z) = \vec{V}_0^{+} e^{-\gamma z + j\omega t} + \vec{V}_0^{-} e^{\gamma z + j\omega t} \\ \vec{I}(t,z) = \dfrac{\vec{V}_0^{+}}{\vec{Z}_c} e^{-\gamma z + j\omega t} - \dfrac{\vec{V}_0^{-}}{\vec{Z}_c} e^{\gamma z + j\omega t} \end{cases}, \quad [6.7]$$

where the two terms in each equation denotes the traveling waves in the positive and negative directions, respectively. The *propagation constant* γ and the *characteristic cable impedance* Z_c are the two parameters governing the propagation of electromagnetic waves along the transmission line, and can be expressed for the case of non-ferromagnetic materials as follows [KRA 99]:

$$\gamma = \frac{j\omega}{c}\sqrt{\varepsilon_r^*} = \alpha + j\beta; \quad \vec{Z}_c = \frac{Z_p}{\sqrt{\varepsilon_r^*}}, \quad [6.8]$$

where c is the speed of an electromagnetic wave in free space (c=3×10^8 m/s), ε_r* the equivalent permittivity, and Z_p the characteristic impedance in vacuum, which is only a function of the cross-sectional geometry of the transmission line and can be assumed, as a first approximation, to be equal to the characteristic impedance in air. The real part, α, of the propagation constant is called the attenuation constant, because it accounts for signal attenuation along the line given by exp(–αz). The imaginary part, β, is called the phase constant of the line and accounts for the propagation velocity of the wave through the transmission line. The propagation velocity V_p through the transmission line can be obtained from equations [6.6], [6.7] and [6.8]:

$$V_p = \frac{\omega}{\mathrm{Im}[\gamma]} = \frac{c}{\sqrt{\frac{\varepsilon_r'}{2}}\left[\sqrt{1+\left(\frac{\varepsilon_r'' + \sigma/2\pi f\varepsilon_0}{\varepsilon_r'}\right)^2}+1\right]^{1/2}}, \quad [6.9]$$

where f is the frequency (f=ω/2π). If the frequency is sufficiently lower than the relaxation frequency f_{rel}, so that the imaginary part of the dielectric permittivity ε'' is small and is sufficiently high such that the term $\sigma/2\pi f\varepsilon_0$ is also small, then the velocity of propagation reduces to:

$$V_p \approx \frac{c}{\sqrt{\varepsilon'_r}}. \qquad [6.10]$$

If this is not the case, then the velocity of propagation may be expressed in terms of apparent permittivity, K_a:

$$V_p = \frac{c}{\sqrt{K_a}} \quad \text{with} \quad K_a = \frac{\varepsilon'_r}{2}\left[\sqrt{1+\left(\frac{\varepsilon''_r + \sigma/2\pi f \varepsilon_0}{\varepsilon'_r}\right)^2} + 1\right]. \qquad [6.11]$$

In general, the apparent permittivity is a function of frequency and temperature because ε' and ε'' depend on frequency and temperature. As an example, Figure 6.12(a) shows the apparent permittivity of moderately saline water (σ~0.5 S/m) at different temperatures. It can be noticed that the apparent permittivity in the high-frequency range of TDR bandwidth is fairly constant and equal to the static permittivity of pure water.

Figure 6.12b shows the apparent permittivity for saline water having electrical conductivity of about 5 S/m (sea water) at different temperatures. In this case, the apparent permittivity in the high-frequency range of TDR bandwidth is significantly higher than the static permittivity of pure water due to the contribution of the term $\sigma/2\pi f\varepsilon_0$. In addition, the apparent permittivity increases with the temperature in contrast to the moderately saline water.

TDR measurement of water content is based on the measurement of wave propagation velocity. The TDR upper bandwidth is around 1.5 GHz and, as shown in Figure 6.12, this frequency falls in the range where the apparent permittivity K_a is not affected by both relaxation and conductive losses (with the exception of high-conductivity pore water or very active clays). On the other hand, single frequency methods (ADR and Capacitance methods) operate at lower frequencies (~100 MHz) and are therefore more sensitive to electrical conductivity of soils.

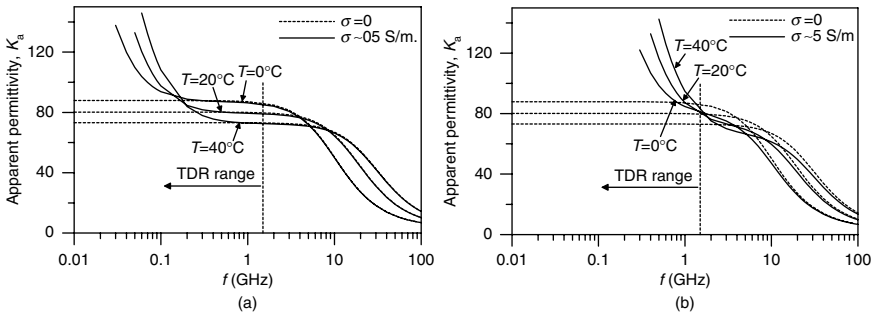

Figure 6.12. *Apparent permittivity, K_a, of aqueous solution water having $\sigma \sim 0.5$ S/m (moderately saline) and $\sigma \sim 5$ S/m (sea water)*

6.3.3. *TDR applied to volumetric water content measurement*

A TDR system consists of a step pulse generator, an oscilloscope, a coaxial cable, and a probe that comprises a head incorporating two or three rods (Figure 6.13). The step pulse generator launches a fast-rise time voltage step associated with a bandwidth of up to 1.5 GHz and the reflection waveform is recorded by an equivalent time sampling oscilloscope. The highest frequencies are sufficiently lower than the relaxation frequency of water (Figure 6.11), and fall in the range where the effect of electrical conductivity is often negligible (Figure 6.12).

TDR working principle can be illustrated following [NIS 95]. Let us assume that the impedance of segment AB, Z_C, is greater than that of segment BC, Z_P. This is the case of probe inserted in water or wet soil. At time t=0, the step pulse generator starts to launch electromagnetic waves to produce a voltage step, V_0. At time $t=t_A$, the front of the voltage step reaches the oscilloscope that records an instantaneously rise in voltage, V_0 (stage 1). At point B, a part of the voltage step is reflected back towards the sampler, $U_{r,1}$, and a part is transmitted further on, $U_{t,1}$. As $Z_C > Z_P$, the reflection coefficient ρ is negative ($\rho<0$) and a negative reflected step is observed (the reflected wave travels in counter phase with the wave transmitted by the pulse generator). The superposition of these two waves causes a drop in voltage amplitude with respect to the original wave (stage 2). At time $t=t_B$, the front of the reflected step reaches the oscilloscope that detects a drop in the voltage. On the other side, the transmitted voltage step $U_{t,1}$ is totally reflected in phase at the end of the transmission line (open-ended circuit), because $Z_L \to \infty$ and the reflection coefficient ρ=1 (stage 3). The reflection of

the transmitted voltage step $U_{t,1}$ reaches the back point B. Here, it is partly reflected in phase (ρ>0) towards point C, $U_{r,2}$, and partly transmitted in phase towards the sampler, $U_{t,2}$ (stage 4). The transmitted voltage step $U_{t,2}$ reaches the sampler at t=t_C. As the sampler is in phase with the waves transmitted by the pulse generator, it measures a rise in the voltage (stage 5). Multiple reflections will then take place in the system until a stable level is reached.

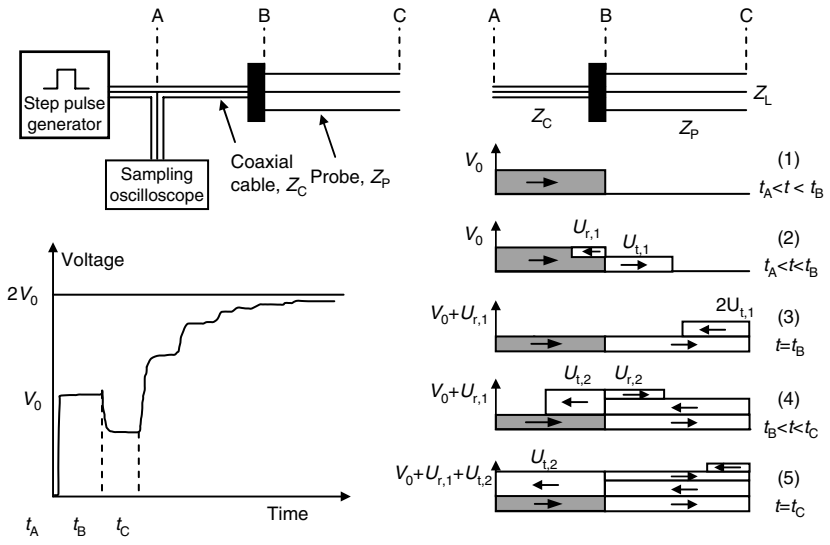

Figure 6.13. *Voltage step reflections in an open-ended transmission line having an impedance discontinuity (after [NIS 95])*

The apparent permittivity, K_a, of the medium in which the probe is inserted can be obtained from the propagation velocity of the pulse in the probe according to equation [6.11]:

$$K_a = \left(\frac{c}{V_p}\right)^2 = \left(c\frac{t_C - t_B}{2L_{BC}}\right)^2. \qquad [6.12]$$

The time t_B at which the signal enters the probe and the time t_C at which the signal is reflected at the end of the rods can be derived from the reflection waveform, as illustrated in Figure 6.14. In this figure, the time t_{head}

represents the time at which the signal enters the head of the probe and Δt is the time taken by the signal to travel along the head and reach the top of the rods (refer to [TAR 08] for a detailed discussion on the procedures to determine t_{head}, t_B, and t_C).

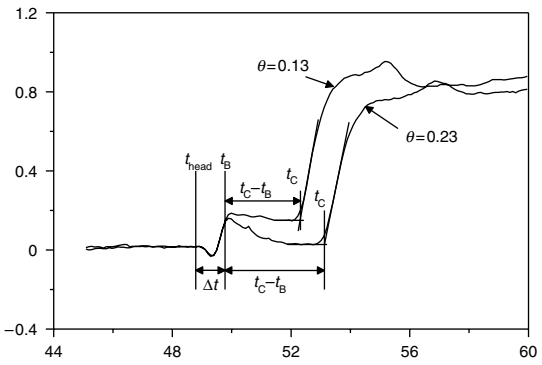

Figure 6.14. *Reflection waveforms in fine sand samples and travel time determination*

In their early work, [TOP 80] assumed that the apparent dielectric permittivity could be directly related to volumetric water content θ through a polynomial calibration curve (*Topp's equation*):

$$\theta = -5.3\times10^{-2} + 2.92\times10^{-2} K_a - 5.5\times10^{-4} K_a^2 + 4.3\times10^{-6} K_a^3. \quad [6.13]$$

They suggested that such a calibration curve was almost independent of soil density, texture, temperature, and salt content. Indeed, Topp's equation has been proven successful to infer soil water content, provided the soil does not contain substantial amount of bound water and does not have pores filled with saline water (K_a is affected by high electrical conductivity as shown in Figure 6.12(b)), and does not have high porosity (refer to [TAR 08] for a detailed discussion of limitations of Topp's equation).

6.3.4. *Water content measurement using capacitance*

Owing to installation difficulties, TDR systems are not always adapted for the determination of water content at relatively high depths. Depth capacitance probes have been designed to sense the soil from within an

access tube (Figure 6.15). These probes are relatively inexpensive and easy to operate, and are becoming a popular choice for routine monitoring purposes. Surface capacitance insertion probes have also been developed and may be an interesting alternative to TDR when measurements at few locations in the field have to be made. The depth capacitance installation probe consists of an electrode pair separated by a plastic dielectric. The upper and lower electrodes and the plastic separator are in the shape of a cylinder that fits closely inside the plastic access tube. The lines of force between the capacitor plates intersect the soil outside the tube (the length of the plates is of the same order of magnitude as the plate distance). A resonant *LC* circuit (*L* is the inductance and *C* the capacitance) in the probe includes the ensemble of the soil outside the access tube, the access tube itself, as well as the air space between the probe and the access tube, as one of the capacitive element. The LC circuit is included in the tuned circuit of an oscillator to measure the resonant frequency F_{res} of the *LC* circuit. The resonant frequency depends on the capacity of the soil-access tube system *C*, which in turn is linked to the soil apparent permittivity K_a. Water content measurements can be performed by directly relating the resonant frequency F_{res} to the water content ([PAL 97]) or by developing a calibration between the resonant frequency F_{res} and the apparent permittivity K_a, which, in turn, can be related to water content using the empirical TDR relationships ([ROB 98]). The major disadvantage of the single-step calibration is that one cannot separate errors due to the instrument from those due to the calibration between the capacitance and soil water content.

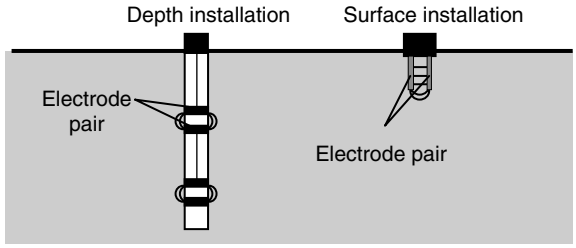

Figure 6.15. *Surface and depth installation capacitance probes and relative electric fields*

It should be noted that the operating frequency of the capacitance probe is in the range of 70–150 MHz. In this frequency range, the apparent permittivity is more sensitive to electrical conductivity with respect to TDR. For example, consider the aqueous solution shown in Figure 6.12(a) having

σ~0.5 S/m. In the high-frequency range of TDR bandwidth, the apparent permittivity is equal to the static permittivity in contrast to the capacitance probe range (~70-150 MHz), where the apparent permittivity is significantly affected by electrical conductivity. If this aqueous solution resided in the soil, then the bulk apparent permittivity would essentially depend on the water content in TDR measurement, and would be significantly affected by electrical conductivity when using the capacitance probe. In other words, "universal" calibration curves for capacitance probes relating resonant frequency to volumetric water content can be valid only for soils with low electrical conductivity (0.05–0.1 S/m according to [ROB 98]) and relatively low water content (θ<~0.30 according to [KEL 04]). For soils having relatively high bulk electrical conductivity (saline water or high cation exchange capacity), either a soil-specific calibration curve needs to be obtained or the electrical conductivity needs to be measured independently and used to correct apparent permittivity.

6.3.5. *Water content measurement using ADR*

This probe consists of a sinusoidal oscillator (typically 100 MHz), a fixed impedance section of a coaxial line, and a stainless steel wire sensing probe that behaves as an additional section of the transmission line with an impedance dependent on the dielectric permittivity of the soil surrounding the probe wires (Figure 6.16). If this impedance differs from that of the internal coaxial transmission line, then a proportion of the signal is reflected back from the junction between the probe rods and the coaxial transmission line. The difference between the peak voltage at its start and the peak voltage at the junction can be related to the impedance Z_L of the soil surrounding the probe wires, which can be in turn related to soil permittivity ([GAS 96]). The main limitation of this type of probe is, similar to the capacitance probes, the low operating frequency (100 MHz). As shown in Figure 6.12, the apparent permittivity of water at 100 MHz is no longer equal to static permittivity when the pore water bulk conductivity becomes relatively high (greater than around 0.5 S/m). Universal or manufacturer calibrations are therefore applicable as long as the soil does not contain saline water and/or clays having high cation exchange capacity. If this is not the case, then the apparent permittivity measured by the impedance probe at given water contents tends to be higher than that measured using TDR ([COS 05]), and a soil-specific calibration is highly recommended.

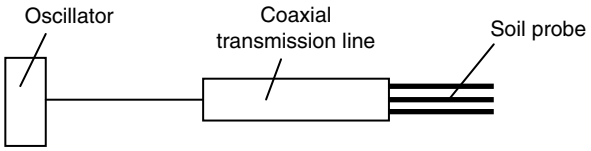

Figure 6.16. *ADR probe*

6.4. Field measurement of water permeability

Direct measurement of unsaturated permeability to water (hydraulic conductivity) in the field is a very difficult task. Normally, the permeability function relating unsaturated permeability to suction is estimated from the saturated permeability, k_{sat}, and the water retention curve. However, it is important to have methods for field determination of flow under a suction gradient. As pointed out by [BEN 97], there is little value in using small specimens in the laboratory to assess field hydraulic conductivity. The main methods for field determination of unsaturated permeability include Infiltrometers, Disc Permeameter, Guelph Permeameter, and Cone Permeameter. A more complete discussion on some of the equipment is given by [STE 95].

Infiltrometers are simple and widely used to estimate infiltration into a soil. They are usually used to estimate the permeability under field-saturated conditions by continuing flow until a steady state is observed. Double-ring infiltrometers are used to ensure one-dimensional vertical flow from the inner ring where measurements are made. Tensiometers can be used to observe the movement of the wetting front and to calculate hydraulic gradient (which otherwise have to be assumed).

Tension Disc Permeameter ([PER 88]) can be used to determine near-saturated permeability, but is limited to suctions of 3–5 kPa. A bubbling tower is used to create negative pressure. [REY 91] described the analysis to obtain the near-saturated permeability.

Guelph Permeameter ([REY 85]) can be fitted with a tension adapter that allows measurement under suction. Morii *et al.* [MOR 03] used TDR for moisture content measurement near the Guelph ring and used an unsaturated flow finite element code to back-analyze unsaturated permeability.

Cone Permeameter ([KOD 98]) has a porous filter close to the tip of a cone penetrometer with two tensiometer rings fitted 50 and 90 mm above the

filter. A constant head is applied to the filter for 5–10 min, and tensiometer readings are observed during water redistribution. Inverse analysis is used to determine the water retention curve parameters, saturated hydraulic conductivity, and ratio of horizontal/vertical permeability ([SIM 98]).

6.5. Bibliography

[AIT 51] AITCHISON G.D., BUTLER P.F., GURR C.G., "Techniques associated with the use of Gypsum Block Soil Moisture MetersQ", *Australian Journal of Applied Science*, vol. 2, p. 57-75, 1951.

[BEN 97] BENSON C.H., GUNTER J.A., BOUTWELL G.P., TRAUTWEIN S.J., BERZANSKIS P.H., "Comparison of four methods to assess hydraulic conductivity", *Journal of Geotechnical and Geoenvironmental Engineering*, vol. 123, no. 10, p. 929-937, 1997.

[BER 02] BERTOLINO A.V.F.A., SOUZA A.P., FERNANDES N.F., RANGEL, A.M., DE CAMPOS T.M.P., SHOCK C.C., "Monitoring the field soil matrix potential using mercury tensiometer and granular matrix sensors", in JUCÁ J.F.T, DE CAMPOS T.M.P., MARINHO F.A.M. (eds.), *Unsaturated Soils*, *Proc. 3rd Int. Conf. on Unsaturated Soils*, Balkema, Recife, Lisse, vol. 1, p. 335-338, 2002.

[BUL 08] BULUT R., LEONG E.C, "Indirect measurement of suction", *Geotechnical and Geological Engineering*, vol. 26, no. 6, p. 1573-1529, 2008.

[COS 05] COSH M.H., JACKSON T.J., BINDLISH R., FAMIGLIETTI J.S., RYU D., "Calibration of an impedance probe for estimation of surface soil water content over large regions", *Journal of Hydrology*, vol. 311, p. 49–58, 2005.

[CUI 08] CUI Y.J., TANG A.M., MANTHO A.T., DE LAURE E., "Monitoring field soil suction using a miniature tensiometer", *Geotechnical Testing Journal*, vol. 31, no. 1, p. 95-100, 2008.

[DEL 05] DELTA-T, *Delta T Devices – Soil Moisture Sensors*, http://www.delta-t.co.uk, 2005.

[DUR 05] DURNER W., OR D., "Soil water potential measurement", in ANDERSON M.G., MCDONNELL J.J. (eds.), *Encyclopedia of Hydrological Sciences*, John Wiley & Sons, p. 1089-1102, 2005.

[GAR 01] GARDNER C.M.K., ROBINSON D.A., BLYTH K., COOPER J.D., "Soil water content measurement", in SMITH K., MULLINS C. (eds.), *Soil and Environmental Analysis: Physical Methods*, Second edition, Marcel Dekker, Inc., New York, p. 1-64, 2001.

[GAS 96] GASKIN G.J., MILLER J.D., "Measurement of soil water content using a simplified impedance measuring technique", *Journal of Agricultural Research*, vol. 63, p. 153-160, 1996.

[JON 02] JONES S.B., WRAITH J.M., OR D., "Time domain reflectometry measurement principles and applications", *Hydological Processes*, vol. 16, p. 141-153, 2002.

[KEL 04] KELLENERS T.J., SOPPE R.W.O., AYARS J.E., SKAGGS T.H., "Calibration of capacitance probe sensors in a saline silty slay", *Soil Science Society of America Journal*, vol. 68, p. 770–778, 2004.

[KOD 98] KODEŠOVÁ R., GRIBB M.M., ŠIMŮNEK J., "A new CPT method for estimating soil hydraulic properties", ROBERTSON P.K., MAYNE P.W. (eds.), *Proc. 1st Int. Conf. on Site Characterization*, Balkema, Rotterdam, vol. 2, p. 1421-1425, 1998.

[KRA 99] KRAUS J.D., FLEISCH D.A. *Electromagnetics with Applications*, McGraw-Hill, 1999.

[MAR 08] MARINHO F.A.M., TAKE A., TARANTINO A., "Tensiometeric and axis translation techniques for suction measurement", *Geotechnical and Geological Engineering*, vol. 26, no. 6, p. 615-631, 2008.

[MOR 03] MORII T., TAKESHITA Y., INOUE M. "*In-situ* measurement and evaluation of soil permeability in sand sediment", KARUBE D., IIZUKA A., KATO S., KAWAI K., TATEYAMA K. (eds.), *Proc. 2nd Asian Conf. on Unsaturated Soils*, UNSAT-ASIA 2003, Kobe, p.107-112, 2003.

[NIS 95] NISSEN H.H., MOLDRUP P., "Theoretical background for the TDR methodology", *Proc. of the Symposium: Time Domain Reflectometry Applications in Soil Science*, 16 September 1994, Tjele, Denmark. SP Report, vol. 3, no. 11, p. 9-23, 1995.

[NOR 01] NOBORIO K., "Measurement of soil water content and electrical conductivity by TDR: a review", *Computers and Electronics in Agriculture*, vol. 31, p. 213-237, 2001.

[NG 03] NG C.W.W., ZHAN L.T., BAO C.G., FREDLUND D.G., GONG B.W., "Performance of an unsaturated expansive soil slope subjected to artificial rainfall infiltration", *Geotechnique*, vol. 53, no. 2, p. 143-157, 2003.

[O'CO 99] O' CONNOR K.M., DOWDING C.H, *Geomeasurements by Pulsing TDR Cables and Probes*, CRC Press, 1999.

[PAL 97] PALTINEANU I.C., STARR J.L., "Real-time soil water dynamics using multisensor capacitance probes: Laboratory calibration", *Soil Science Society of America Journal*, vol. 61, p. 1576-1585, 1997.

[PER 88] PERROUX K.M., WHITE I. "Designs for disc permeameters", *Soil Science Society of America Journal*, vol. 52, p. 1205-1215, 1988.

[REY 85] REYNOLDS W.D., ELRICK D.E. "*In situ* measurement of field-saturated hydraulic conductivity, sorptivity and the α-parameter using the Guelph Permeameter", *Soil Science*, vol. 140, p. 292-302, 1985.

[REY 91] REYNOLDS W.D., ELRICK D.E. "Determination of hydraulic conductivity using a tension Infiltrometer", *Soil Science Society of America Journal*, vol. 55, no. 3, p. 633-639, 1991.

[RID 93] RIDLEY A.M., BURLAND J.B., "A new instrument for the measurement of soil moisture suction", *Géotechnique*, vol. 43, no. 2, p. 321-324, 1993.

[RID 96a] RIDLEY A.M., WRAY W.K., "State of the art report – suction measurement: a review of current theory and practices", ALONSO and DELAGE (eds.), *Proc. 1st International Conference on Unsaturated Soils, Unsaturated Soils*, Paris, vol. 3, p. 1293-1322, 1996.

[RID 96b] RIDLEY A.M., BURLAND J.B. "A pore pressure probe for the *in situ* measurement of a wide range of soil suction", *Advances in Site Investigation Practice*, Thomas Telford, London, p 510-520, 1996.

[RID 98] RIDLEY A. M., PATEL A.R., MARSLAND F. "Tensiometers: their design and use for civil engineering purposes", *Geotechnical Site Characterisation*, Balkema, Rotterdam, p. 851-856, 1998.

[RID 03] RIDLEY A.M., DINEEN K., BURLAND J.B., VAUGHAN P.R., "Soil matrix suction: some examples of its measurement and application in geotechnical engineering", *Géotechnique*, vol. 53, no. 2, p. 241-253, 2003.

[ROB 98] ROBINSON D.A., GARDNER C.M.K., EVANS J., COOPER J.D., HODNETT M.J., BELL J.P., "The dielectric calibration of capacitance probes for soil hydrology using an oscillation frequency response model", *Hydrology and Earth System Sciences*, vol. 2, no. 1, p.111-120, 1998.

[ROB 03] ROBINSON D.A., JONES S.B., WRAITH J.M., OR D., FRIEDMAN S.P., "A review of advances in dielectric and electrical conductivity measurement in soils using TDR", *Vadose Zone Journal*, vol. 2, p. 444-475, 2003.

[SCA 02] SCANLON B.R. ANDRASKI B.J., BILSKIE J., "Miscellaneous methods for measuring matric or water potential", in DANE J.H., TOPP G.C. (eds.) *Methods of Soil Analysis, Part 4, Physical Methods*, SSSA Book Series No. 5, Soil Science Society of America, Madison, p. 643-670, 2002.

[SHU 00] SHUAI F., FREDLUND D.G., "Use of a new thermal conductivity sensor to measure soil suction", in SHACKLEFORD C.D., HOUSTON S.L., CHANG N.Y. (eds.), *Advances in Unsaturated Geotechnics*, Geotechnical Special Publication No. 99, American Society of Civil Engineers, Reston, p. 1-12, 2000.

[SIM 98] ŠIMŮNEK J., GRIBB M.M., HOPMANS J.W., VAN GENUCHTEN M.T., "Estimating soil hydraulic properties from field data via inverse modelling". *Proc. 2nd Int. Conf. Unsaturated Soils*, International Academic Publishers, Beijing, vol. 1, pp. 515-520, 1998.

[STE 95] STEVENS D.B., *Vadose Zone Hydrology*, CRC Press, Boca Raton, 347 pp, 1995.

[TAR 08] TARANTINO A., RIDLEY A.M., TOLL D.G., "Field measurement of suction, water content, and water permeability", *Geotechnical and Geological Engineering*, vol. 26, no. 6, p. 751-782, 2008.

[TOP 80] TOPP G.C., DAVIS J.L., ANNAN A.P., "Electromagnetic determination of soil water content: Measurements in coaxial transmission lines", *Water Resource Research*, vol. 16 p. 574-582, 1980.

[YOU 02] YOUNG M.H., SISSON J.B. "3.2.2 Tensiometry", in DANE J.H., TOPP G.C. (eds.) *Methods of Soil Analysis, Part 4, Physical Methods*, SSSA Book Series No. 5, Madison: Soil Science Society of America, p. 575–608, 2002.

PART III

Theoretical Developments

Chapter 7

Hydromechanical Coupling Theory in Unsaturated Geomaterials and Its Numerical Integration

7.1. Introduction – problems to be treated

Here, we are interested in a number of different physical phenomena, including:

– The nonlinear solid mechanics, and especially, the soil, rock, or concrete mechanics: we consider the relationships between displacements, strains, stresses, and forces within the solids. The material behavior is described by a constitutive model, which can take into account elastoplasticity or elastoviscoplasticity. On the other hand, large transformations and large strains may lead to geometrical nonlinearities.

– The fluid flow within the porous media: fluid can be in a single phase of various natures (water, air, gas, oil, etc.) or be an association of two fluids leading to unsaturated media (water and air, oil and gas, oil and water, etc.). In the second case, partial saturation leads to permeability and storage terms, depending on the saturation degree or suction level, involving nonlinear aspects.

– The thermal transfers within the porous media. Conduction is the leading process in solid mechanics (in the geomaterial matrix), but

Chapter written by Robert CHARLIER, Jean-Pol RADU, Pierre GERARD and Frédéric COLLIN.

convection can also occur in the porous volume as a consequence of fluid flow. Radiation transfer could also occur inside the pores, but will be neglected here. Conduction coefficients and latent heat may depend on the temperature.

– The pollutant transport or any spatial transfer of substance (including heat, dissolved gas, etc.) due to fluid flow. The pollutant concentration may be high enough to modify the densities, involving nonlinear effects.

All these problems are nonlinear, and can be formulated with sets of partial differential equations. Moreover, only three types of differential equations have to be considered concerning (i) solid mechanics, (ii) diffusion and (iii) advection-diffusion problems.

7.1.1. *Solid mechanics*

On the one hand, solid mechanics can be modeled on the following basis. The equilibrium equation is:

$$\partial_i \sigma_{ij} + P_j = 0, \qquad [7.1]$$

where $\underline{P}$ is the vector of the volume forces, $\underline{\sigma}$ the Cauchy's stress tensor, and $\underline{\partial}$ the spatial partial derivative operator:

$$\partial_i \equiv \frac{\partial}{\partial x_i}. \qquad [7.2]$$

The stress tensor is obtained as a result of the time integration of a constitutive equation (elastic, elastoplastic, damage, or elastoviscoplastic), possibly including the coupling terms [ALO 90, BER 08, COL 05, COU 95, COU 04]:

$$\overset{\circ}{\sigma}_{ij} = fct(\sigma, D, k), \qquad [7.3]$$

where $\underline{\overset{\circ}{\sigma}}$ is the stress rate, $\underline{D}$ the strain rate, and k a set of history parameters (state variables, e.g. the preconsolidation stress). In the most classical case of elastoplasticity, this equation reduces to:

$$\overset{\circ}{\sigma}_{ij} = C_{ijkl} D_{kl}. \qquad [7.4]$$

Most of the constitutive equations for geomaterials are nonlinear.

When modeling a solid mechanics problem with the finite element method, the most used formulation is based on displacements $\underline{u}$ or on actualized coordinates $\underline{x}$. If we consider only small strains and displacements, the strain rate reduces to the well-known Cauchy's strain rate:

$$D_{ij} = \dot{\varepsilon}_{ij} = \frac{1}{2}(\partial_i \dot{u}_j + \partial_j \dot{u}_i). \qquad [7.5]$$

However, if large strains are to be considered, then the preceding equations have to be reconsidered. The stress-strain rate couple has to be more precisely defined with respect to the configuration evolution. Among the multiple other choices (see Piola-Kirchoff stress-Green strain), we will only consider Cauchy's stress and Cauchy's strain rate. These tensors are defined in the global axis in the current configuration, which is continuously deforming. If we note $\underline{X}$, the coordinates in a reference state (an initial one; however, initial state in geomechanics is always arbitrary), and $\underline{x}$, the coordinates in the current configuration (Figure 7.1), we can define the Jacobian tensor of the transformation:

$$F_{ij} = \frac{\partial x_i}{\partial X_j}. \qquad [7.6]$$

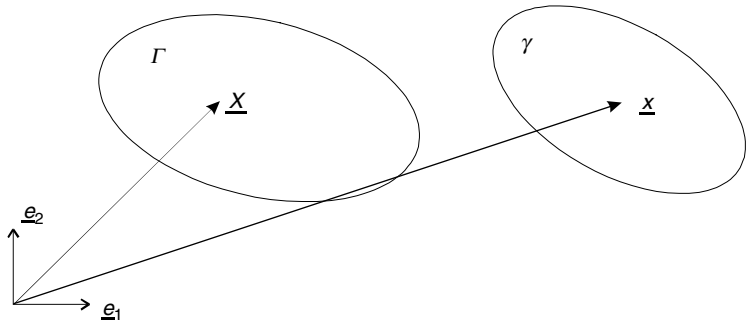

Figure 7.1. *Initial and current configurations*

The velocity gradient is defined as:

$$\underline{\underline{L}} = \frac{\partial \underline{\underline{u}}}{\partial \underline{\underline{X}}} = \dot{\underline{\underline{F}}}\underline{\underline{F}}^{-1}. \quad [7.7]$$

The symmetric part of the velocity gradient is the strain rate associated with Cauchy's stress:

$$\underline{\underline{D}} = \mathrm{sym}(\underline{\underline{L}}) = \frac{1}{2}(\underline{\underline{L}} + \underline{\underline{L}}^{\mathrm{T}}). \quad [7.8]$$

The material stress evolution must then be described as a function of the strain rate using a constitutive equation [7.3]. However, as Cauchy's stress tensor is defined in a global axis, the solid rotations may modify the tensor Cartesian components. This evolution is not linked to strains and hence is not described by the constitutive equation. Among other possibilities, Jaumann's objective derivative of stress is a good component update:

$$\dot{\underline{\underline{\sigma}}} = \frac{D\underline{\underline{\sigma}}}{\mathrm{d}t} = \breve{\underline{\underline{\sigma}}} + \underline{\underline{\omega}}\,\underline{\underline{\sigma}} + \underline{\underline{\sigma}}\,\underline{\underline{\omega}}^{\mathrm{T}}, \quad [7.9]$$

$$\underline{\underline{\omega}} = \mathrm{skw}(\underline{\underline{L}}) = \frac{1}{2}(\underline{\underline{L}} - \underline{\underline{L}}^{\mathrm{T}}). \quad [7.10]$$

Such a large strain model [7.6–7.10] is nonlinear.

The time dimension should not be addressed for solid mechanics problems, unless when viscous terms are considered in the constitutive model. Generally, the time that appears in the time derivatives in equations [7.3–7.5, 7.7–7.10] is only a formal one.

7.1.2. *Diffusion*

Fluid flow in porous media and thermal conduction exchanges in solids are modeled using similar diffusion equations.

The balance equation can be given as:

$$\partial_i f_i + Q = \dot{S}, \quad [7.11]$$

where $\underline{f}$ represents a flux of fluid or heat, Q a sink term, and S the storage of fluid or heat. When modeling a diffusion problem with the finite element method, the most used formulation is based on fluid pore pressure p or temperature T.

Subsequently, Darcy's law for fluid flow in porous media gives the fluid flux:

$$f_i = -\frac{k}{\mu}(\partial_i p + \partial_i \rho g z), \qquad [7.12]$$

with the intrinsic permeability k (possibly depending on the saturation degree), dynamic viscosity μ, density ρ, and gravity acceleration g. The fluid storage term depends on the saturation degree S_r and the fluid pressure:

$$\dot{S} = fct(p, S_r). \qquad [7.13]$$

For thermal conduction, we can obtain Fourier's law:

$$f_i = -\lambda \partial_i T, \qquad [7.14]$$

with the conductivity coefficient λ. The heat storage (enthalpy) term depends on the temperature:

$$\dot{S} = fct(T). \qquad [7.15]$$

The diffusion problem is nonlinear when:

– the permeability depends (directly or indirectly) on the fluid pore pressure;

– the fluid storage is a nonlinear function of the pore pressure;

– partial saturation occurs;

– the conductivity coefficient depends on the temperature;

– the enthalpy is a nonlinear function of the temperature.

When the storage term is considered, the time dimension of the problem has to be addressed.

7.1.3. *Advection–diffusion*

Transport of pollutant or heat in porous media is governed by a combination of advection and diffusion [CHA 01, COL 02, COL 03, GEN 01a, LI 97, LEW 00]. Advection phenomenon is related to the transport (noted as a flow $\underline{f}_{\text{adv}}$) of any substance by a fluid flow, described by its velocity $\underline{f}_{\text{diff}}^{\text{fluid}}$:

$$\underline{f}_{\text{adv}} = C\underline{f}_{\text{diff}}^{\text{fluid}}. \qquad [7.16]$$

The substance concentration C is generally supposed to be small enough not to influence the fluid flow. In porous media, due to the pores' network tortuosity and friction, advection is always associated with diffusion characterized by diffusion–dispersion tensor $\underline{D}$. Therefore, the total flux of the substance is:

$$f_{i,\text{adv-dif}f} = C\, f_{i,\text{diff}}^{\text{fluid}} - \lambda D_{ij}\partial_j C. \qquad [7.17]$$

Balance equation and storage equations may be written in a way similar to the one employed for diffusion problems [7.11, 7.13, 7.15].

When compared with the diffusion constitutive law [7.12, 7.14], it appears here that advection does not depend on the concentration gradient, but directly on the concentration. This completely modifies the nature of the equations to be solved. Problems dominated by advection are very difficult to solve numerically [CHA 01]. In order to evaluate the relative advection effect, it is useful to evaluate the Peclet's number, which is a ratio between diffusive and advective effects:

$$Pe = \frac{f_{\text{diff}}^{\text{fluid}} h}{2D}, \qquad [7.18]$$

where h is an element dimension.

7.1.4. *Boundary conditions*

In the preceding section, differential equations are given for three types of problems. To solve these equations, we need to define the boundary and

initial conditions. Classical boundary conditions may be considered: imposed displacements or forces for solid mechanics problems, imposed fluid pressures/temperatures/concentrations, or imposed fluxes for diffusion and advection–diffusion problems.

However, it may be useful to consider more complex boundary conditions. For example, in solid mechanics, unilateral contact with friction or interface behavior is often considered [CHA 90].

On the other hand, initial conditions are often difficult to determine in geomechanics, e.g. the problem of initial stress state.

7.2. Numerical tools: the finite element method

7.2.1. *Introduction*

An approximated solution to most of the problems described by a set of partial differential equations may be obtained using numerical methods, such as the finite element method (FEM), the discrete element method, the finite difference method (FDM), the finite volume method, or the boundary element method (BEM). For the problems concerned here, the most frequently used methods are the finite element one and the finite difference one.

Nonlinear solid mechanics is better solved using the FEM. BEMs have strong limitations in the nonlinear field, and FDMs are not easy to apply to tensorial equations (with the exception of the fast Lagrangian analysis of continua (FLAC) code developed by Itasca).

Diffusion and advection–diffusion problems are often solved by finite difference or FEM. Some finite difference codes are very popular for fluid flow, e.g. *MODFLOW* for aquifer modeling or *ECLIPSE* [ECL 00] for oil reservoir modeling. These codes have been developed for a number of years and possess a number of specific features that allow numerous effects to be considered. However, they suffer from some drawbacks that limit their potentialities for modeling-coupled phenomena. Therefore, we will only provide a little information about finite differences.

7.2.2. *Finite element method*

The basic idea of the FEM is to divide the field to be analyzed into sub-domains, the so-called finite elements, of simple shape: e.g. triangles, quadrilaterals with linear, parabolic, cubic sides for 2D analysis. In each finite element, an analytical simple equation is postulated for the variable to be determined, i.e. the coordinate or displacement for solid mechanics, and the fluid pressure, temperature, and concentration for diffusion problems. In order to obtain C_0 continuity, the unknown variable field has to be continuous at the limit between finite elements. This requirement is obtained using common values of the field at specific points, the so-called nodes, *linking* the finite elements together. The field values at nodal points are the discretized problem unknowns.

For most of the solid mechanics and diffusion problems, isoparametric finite elements seem to be optimal [ZIE 89]. The unknown field $\underline{x}$ may then be written for solid mechanics problems in 2D cases:

$$\underline{x} = N_L(\xi,\eta)\underline{x_L} \quad L = 1, \text{nnode}, \qquad [7.19]$$

which depends on the nodal unknowns $\underline{x_L}$ and the shape functions N_L, depending on the isoparametric coordinates ξ and η defined on a reference-normalized space. Subsequently, the strain rate and spin may be derived using equations [7.8] and [7.10], and the stress rate may be obtained using [7.3], [7.4], and [7.9] and time-integrated. Eventually, equilibrium [7.1] has to be checked (section 7.2.4).

For scalar diffusion or advection–diffusion problems, the unknown field p (hereafter, we will use the pore pressure notation; however, temperature T or concentration C could be also considered changing the notation) may then be written as:

$$p = N_L(\xi,\eta)p_L \quad L = 1, \text{nnode}, \qquad [7.20]$$

which depends on the nodal unknowns p_L and the shape functions N_L. Subsequently, Darcy's velocity of the fluid and storage evolution may be derived using equations [7.12] and [7.13] ([7.14–7.15] or [7.16–7.17]). However, no time integration is required here. Eventually, balance equation [7.11] has to be checked (section 7.2.4).

The FEM allows an accurate modeling of the boundary condition due to easily adapted finite element shape. Internal boundaries of any shape between different geological layers or different solids can be modeled. In addition, specific finite elements for interface behavior or for unilateral boundaries can also be developed [CHA 90]. Variations in the finite element size and density over the mesh are also easy to manage due to the present mesh generators.

7.2.3. *Finite difference method*

The FDM does not explicitly postulate any specific shape of the unknown field. As we are concerned with partial differential equations, exact derivatives are replaced by an approximation based on neighbor values of the unknown:

$$\left(\frac{\partial p}{\partial x}\right)_i = \frac{p_{i+1} - p_{i-1}}{2h}, \qquad [7.21]$$

where the subscript i denotes the cell number and h denotes the cell size. For an orthogonal mesh, such derivatives are easily generalized to variable cell dimensions. However, non-orthogonal meshes present problems that are highly difficult to solve and are generally not used. Subsequently, boundary conditions have to be modeled by the juxtaposition of the orthogonal cells, giving a kind of stairs for oblique or curved boundaries. Similarly, local refinement of the mesh induces irreducible global refinement. These aspects are the most prominent drawbacks of the FDM when compared with the finite element one. On the other hand, CPU time is generally much shorter with finite differences than with finite elements.

7.2.4. *Solving the nonlinear problem: the Newton–Raphson method*

Let us now concentrate on the FEM. The fundamental equation to be solved is the equilibrium equation [7.1] (the balance equation [7.11] for diffusion phenomena). As the numerical methods are giving an approximated solution, the equilibrium/balance equation has to be solved with the best compromise. This is obtained using a global weak form of the local equation. Using weighted residuals, we can obtain the following for solid mechanics:

$$\int_V [\sigma_{ij} \ \delta\varepsilon_{ij}]\mathrm{d}V = \int_V P_i \delta u_i \mathrm{d}V + \int_A \overline{p}\delta u_i \mathrm{d}A, \qquad [7.22]$$

and for diffusion phenomena:

$$\int_V [\dot{S}\delta p - f_i \partial_i(\delta p)]\mathrm{d}V = \int_V Q\delta p \,\mathrm{d}V + \int_A q\delta p \,\mathrm{d}A, \qquad [7.23]$$

where $\overline{p}$ and q are the surface terms of imposed loads/fluxes. The weighting functions are denoted as $\underline{\delta u}$ and δp, and $\underline{\delta\varepsilon}$ represents a derivative of the weighting function based on Cauchy's strain derivate operator. An equivalent equation could be obtained based on the virtual power principle. Subsequently, $\underline{\delta u}$ and δp can be interpreted as virtual arbitrary displacements and pressures, respectively. Within the FEM, these global equilibrium/balance equation can be verified for a number of fundamental cases equivalent to the degrees of freedom (dof) of the problem, i.e. the number of nodes times the number of freedom degrees per node, minus the imposed values. The corresponding weighting functions will have simple forms based on the element shape functions (for Galerkin's approximation; for advection-dominated problems, other weighting functions have to be used).

Given a field of stress or flux, using the weighting functions, we can obtain a value for each dof, which is equivalent to a nodal expression of the equilibrium/balance equation. More precisely, for solid mechanics problems, we can obtain internal forces equivalent to stresses:

$$F_{Li}^{\mathrm{int}} = \int_V \sigma_{ij} B_{Lj} \mathrm{d}V, \qquad [7.24]$$

where B is a matrix of derivatives of the shape functions N. If equilibrium is respected from the discretized point of view, these internal forces are equal to external forces (if external forces are distributed, a weighting is necessary):

$$F_{Li}^{\mathrm{int}} = F_{Li}^{\mathrm{ext}}. \qquad [7.25]$$

Similarly, for diffusion phenomena, the nodal internal fluxes are equivalent to the local fluxes:

$$F_L^{\text{int}} = \int_V \left[\dot{S} N_L - f_i \partial_i N_L \right] \mathrm{d}V. \qquad [7.26]$$

If the balance equation is respected from the discretized point of view, these internal fluxes are equal to the external ones:

$$F_{Li}^{\text{int}} = F_{Li}^{\text{ext}}. \qquad [7.27]$$

However, as we are considering nonlinear problems, equilibrium/balance cannot be obtained immediately, but needs to be iterated. This means that the equations [7.25, 7.27] are not fulfilled until the last iteration of each step.

Nonlinear problems have been solved for some decades, and different methods have been used. From our point of view, the Newton–Raphson is the reference method and probably the best one for a large number of problems. Let us describe this method. In equation [7.25], the internal forces F_L^{int} depend on the basic unknown of the problem, i.e. the displacement field. Similarly, in equation [7.27], the internal fluxes depend on the pressure (temperature, concentration, etc.) field.

If they do not equilibrate the external forces/fluxes, the question to be discussed can be formulated in the following form:

> How should we modify the displacement field (the pressure field) in order to improve the equilibrium (the balance) as stated by equations [7.25, 7.27]?

Following the Newton–Raphson method, we can develop the internal force as a first-order Taylor's series around the last approximation of the displacement field:

$$F_{Li}^{\text{int}} = F_{Li}^{\text{int}}(u_{(i)}) + \frac{\partial F_{Li}^{\text{int}}}{\partial u_{Kj}} \mathrm{d}u_{Kj} + O^2 = F_{Li}^{\text{ext}}. \qquad [7.28]$$

This is the linearization of the nonlinear equilibrium equation. It allows a correction of the displacement field to be obtained:

$$\Delta u_{Kj} = \left(\frac{\partial F_{Li}^{\text{int}}}{\partial u_{Kj}} \right)^{-1} \left(F_{Li}^{\text{int}}(u_{(i)}) - F_{Li}^{\text{ext}} \right) = K_{Li,Kj} \left(F_{Li}^{\text{int}}(u_{(i)}) - F_{Li}^{\text{ext}} \right). \quad [7.29]$$

The matrix, $K_{Li,Kj,}$ is the so-called stiffness matrix. With the corrected displacement field, we can evaluate new strain rates, new stress rates, and new improved internal forces. Subsequently, equilibrium should be improved.

The same explanation may be developed for diffusion problems: Taylor's development of the internal fluxes with respect to the pressure/temperature/ concentration nodal unknowns.

The iterative process may be summarized as shown in Figure 7.2 for a one-dof solid mechanics problem. Starting from a first approximation of the displacement field $u_{(1)}$, we can calculate the internal forces $F_{L(1)}^{\text{int}}$ (point $A^{(1)}$) that are lower than the imposed external forces F_L^{ext}. Equilibrium is then not fulfilled and a new approximation of the displacement field is sought. The tangent stiffness matrix is evaluated and an improved displacement $u_{(2)}$ is obtained (point $B^{(1)}$) [7.29]. We can again calculate the internal forces $F_{L(2)}^{\text{int}}$ (point $A^{(2)}$) that are again lower than the external forces F_L^{ext}. As equilibrium is not yet fulfilled, a new approximation of the displacement field $u_{(3)}$ is searched (point $B^{(2)}$). The procedure has to be repeated until the equilibrium/balance equation is fulfilled with a given accuracy (numerical convergence norm). The process has a quadratic convergence, which is generally considered as the optimum numerical solution.

However, the Newton–Raphson method has an important drawback: it needs important work to be developed as well as run on a computer. In particular, the stiffness matrix K is time-consuming for the analytical development and numerical inversion. Therefore, other methods have been proposed:

– approximate stiffness matrix, in which some nonlinear terms are neglected;

– successive use of the same stiffness matrix avoiding new calculation and inversion at each iteration.

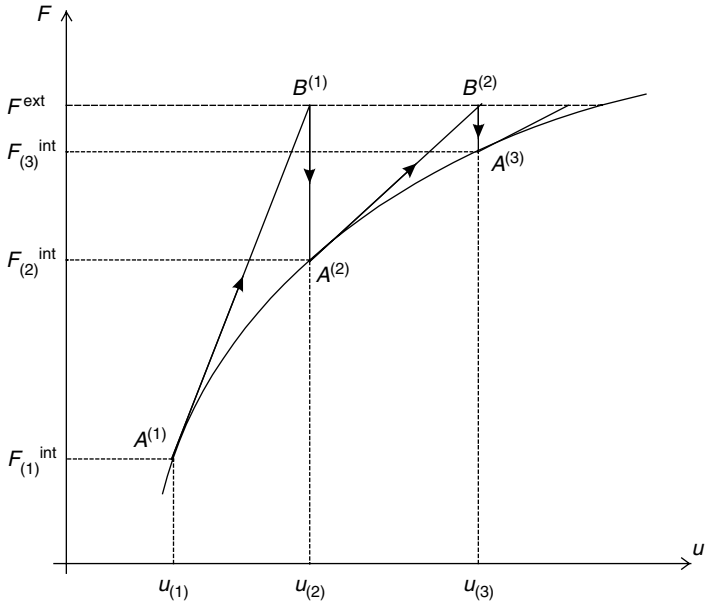

Figure 7.2. *Illustration of the Newton–Raphson process*

It should be noted that each alternative reduces the numerical convergence rate. For some highly nonlinear problems, the convergence may be lost, and subsequently no numerical solution may be obtained.

Some other authors, considering the properties and efficiency of explicit time schemes in rapid dynamics (like for shock modeling), add an artificial mass to the problem in order to solve it as a quick dynamic problem. It should be clear that such a technique might degrade the accuracy of the solution, as artificial inertial effects are added and the static equilibrium equation [7.1] is not checked.

7.2.5. *The stiffness matrix*

From equation [7.29], it appears that the stiffness matrix is a derivative of the internal forces:

$$K_{Li,Kj} = \frac{\partial F_{Li}^{\text{int}}}{\partial u_{Kj}} = \frac{\partial}{\partial u_{Kj}} \left(\int_V \sigma_{ij} B_{Lj} \mathrm{d}V \right). \qquad [7.30]$$

Two contributions will be obtained. On the one hand, we have to derive the stress state with respect to the strain field depending on the displacement field. On the other hand, the integral is performed on the volume and the $\underline{B}$ depends on the geometry. If we are concerned with large strains and if we are using Cauchy‘s stresses, then the geometry is defined in the current configuration, which changes from step to step, and even from one iteration to another. These two contributions, the material one, issued from the constitutive model, and the geometric one, have to be accurately calculated in order to guarantee the quadratic convergence rate.

A similar discussion may be given for diffusive problems. However, the geometry is not modified for pure diffusion problems, and hence, only the material term is to be considered.

7.2.6. *Transient effects: the time dimension*

The time dimension appears in first-order time derivatives in the constitutive mechanical model [7.3, 7.9] and diffusion problems through the storage term. Here, we will discuss the time integration procedure as well as the accuracy and stability problems that are involved.

7.2.6.1. *Time integration – diffusion problems*

The period to be considered is divided into time steps. Linear evolution of the basic variable with respect to the time is generally considered within a time step:

$$p = \frac{t - t_{\mathrm{A}}}{t_{\mathrm{B}} - t_{\mathrm{A}}} p_{\mathrm{B}} + \frac{t_{\mathrm{B}} - t}{t_{\mathrm{B}} - t_{\mathrm{A}}} p_{\mathrm{A}}, \qquad [7.31]$$

where the subscripts A and B denote the beginning and end of a time step, respectively. Then, the pressure rate can be given as:

$$\dot{p} = \frac{\mathrm{d}p}{\mathrm{d}t} = \frac{p_{\mathrm{B}} - p_{\mathrm{A}}}{t_{\mathrm{B}} - t_{\mathrm{A}}} = \frac{\Delta p}{\Delta t}. \qquad [7.32]$$

This time discretization is equivalent to a finite difference scheme. It allows us to evaluate any variable at any time within a time step.

The balance equation should ideally be fulfilled at any time during any time step. Of course, this is not possible for a discretized problem, and only a mean assessment of the balance equation can be obtained. Weighted residual formulations have been proposed in a similar way as that for finite elements [ZIE 89]. However, the implementation complexity is too high with respect to the accuracy. Therefore, the easiest solution is to assess only the balance equation at a given time noted as θ inside the time step:

$$\theta = \frac{t_\theta - t_\mathrm{A}}{t_\mathrm{B} - t_\mathrm{A}}. \qquad [7.33]$$

Subsequently, all the variables have to be evaluated at the reference time θ. Different classical schemes have been discussed for some decades:

– Fully explicit scheme – $\theta = 0$: all the variables and the balance are expressed at the beginning of the time step, where everything is known (solution of the preceding time step). The solution is therefore apparently very easy to be obtained.

– Crank–Nicholson scheme or mid-point scheme – $\theta = 1/2$.

– Galerkin's scheme – $\theta = 2/3$.

– Fully implicit scheme – $\theta = 1$.

The last three schemes are dependent on the pore pressure/temperature/concentration at the end of the time step, and may need to iterate if nonlinear problems are considered.

For some problems where rapid change in material properties occurs, difficulties in the modeling could appear. For instance, problems where phase changes occur, such as icing or vaporizing of water, are associated with latent heat consummation and abrupt change in specific heat and thermal conductivity. Such rapid change is not easy to model. The change in specific heat may be smoothened using an enthalpy formulation, because enthalpy H is an integral of the specific heat c. Subsequently, the finite difference of the enthalpy evaluated over the whole time step gives a mean value $\overline{c}$ and thus allows the accurate balance equation:

$$H = \int_T c \, \mathrm{d}T, \qquad [7.34]$$

$$\overline{c} = \frac{H_{\mathrm{B}} - H_{\mathrm{A}}}{t_{\mathrm{B}} - t_{\mathrm{A}}}. \qquad [7.35]$$

7.2.6.2. *Time integration – solid mechanics*

For solid mechanics problems, the constitutive law form [7.3, 7.4] is an incremental one at the difference with those for diffusion problems [7.12]. The knowledge of the stress tensor at any time implies to have time-integrated the constitutive law. The stress tensor is a state variable that is stored and transmitted from step-to-step based on its final/initial value, and this value plays a key role in the numerical algorithm.

Then, in almost all finite element code devoted to modeling, equilibrium is expressed at the end of the time steps, following a fully implicit scheme – θ=1, and using the end of step stress tensor value.

However, integrating the stress history with enough accuracy is crucial for the numerical process stability and global accuracy. Integrating the first-order differential equation:

$$\underline{\sigma}^{\mathrm{B}} = \underline{\sigma}^{\mathrm{A}} + \int_{t^{\mathrm{A}}}^{t^{\mathrm{B}}} \underline{\underline{C}}^{\mathrm{ep}} \underline{\dot{\varepsilon}} \, \mathrm{d}t \qquad [7.36]$$

can be based on similar concepts to those described in the preceding section. Various time schemes based on different θ values may be used. It can be noted that the stability and accuracy discussions (section 7.2.6.3) are similar.

When performing large time steps, obtaining enough accuracy may require using sub-stepping: within each global time step (as regulated by the global numerical convergence and accuracy problem), stress integration is performed at each finite element integration point after division of the step in a number a sub-steps, allowing high accuracy and stability.

7.2.6.3. *Scheme accuracy*

The theoretical analysis of a time integration scheme accuracy and stability is generally based on a simplified problem [ZIE 89]. Let us consider diffusion phenomena restricted to linear case. Introducing the discretized field [7.20] into the constitutive equations, Darcy's law can be rewritten as follows (neglecting here the gravity term for the sake of simplicity):

$$f_i = -\frac{k}{\mu}\partial_i p = -\frac{k}{\mu}(\partial_i N_L)p_L. \qquad [7.37]$$

Similarly, the storage law (linear case) gives:

$$\dot{S} = c\dot{p} = cN_L\dot{p}_L, \qquad [7.38]$$

where c is a storage parameter. By neglecting the source terms, the weak form of balance equation [7.23] can be given as:

$$\begin{aligned}&\int_V \left[\dot{S}\delta p - f_i\partial_i(\delta p)\right]\mathrm{d}V \\ &= \int_V c\ N_L\ \dot{p}_L N_K \delta p_K \mathrm{d}V - \int_V -\frac{k}{\mu}\partial_i N_L p_L \partial_i N_K \delta p_K \mathrm{d}V = 0.\end{aligned} \qquad [7.39]$$

Considering that nodal values are not concerned with the integration, the following can be obtained:

$$\begin{aligned}&\left(\int_V cN_L N_K \mathrm{d}V\right)\dot{p}_L\delta p_K + \left(\int_V \frac{k}{\mu}\partial_i N_L \partial_i N_K \mathrm{d}V\right)p_L\delta p_K \\ &= C_{KL}\dot{p}_L\delta p_K + K_{KL}p_L\delta p_K = 0,\end{aligned} \qquad [7.40]$$

which is valid for any arbitrary disturbance $\underline{\delta p}$. Then:

$$C_{KL}\dot{p}_L + K_{KL}p_L = 0, \qquad [7.41]$$

which is a simple system of linear equations with a time derivative, a storage matrix $\underline{\underline{C}}$, and a permeability matrix $\underline{\underline{K}}$. We can extract eigenvalues of this system and obtain a series of scalar independent equations of similar form:

$$\dot{p}_L + \alpha_L^2 p_L = 0 \quad (\text{no summation}), \qquad [7.42]$$

where L represents the number of the eigenmode with the eigenvalue α_L, and will not be noted in the following. The exact solution for equation [7.42] is a decreasing exponential:

$$p(t) = p(t_0)e^{-\alpha^2 t}. \qquad [7.43]$$

This problem represents the damping of a disturbance for a given eigenmode. Numerically, the modeling is approximated and numerical errors always appear. If equation [7.43] is well modeled, any numerical error will be rapidly damped if the error source is not maintained. Following this analysis, the whole accuracy and stability discussion may be given based on these last scalar equations [7.42, 7.43].

Introducing the time discretization [7.32, 7.33] in [7.42] gives:

$$\frac{p_B - p_A}{\Delta t} + \alpha^2 \left[(1-\theta)\, p_A + \theta p_B \right] = 0, \qquad [7.44]$$

which allows us to evaluate the end of step pressure as a function of the beginning of step 1:

$$p_B = A p_A, \qquad [7.45]$$

with the amplification factor:

$$A = \frac{1-(1-\theta)\alpha^2 \Delta t}{1+\theta \alpha^2 \Delta t}. \qquad [7.46]$$

To ensure the damping process of the numerical algorithm, which is the *stability condition*, it is strictly necessary that the amplification factor remains lower than 1:

$$-1 < A < 1. \qquad [7.47]$$

This condition is always verified if $\theta \geq 1/2$, and conditionally satisfied otherwise:

$$\Delta t \leq \frac{2}{(1-2\theta)\alpha^2} \text{ if } < 1/2. \qquad [7.48]$$

This last equation is not easy to verify, as it depends on the eigenvalues that are generally not calculated. Therefore, for the classical diffusion process considered in geomaterials, the condition $\theta \geq 1/2$ is generally used.

It should be noted that the amplification factor becomes negative for large time steps, unless for the fully implicit scheme. Then, the pertubated

pressure decreases monotonically in amplitude, but with changes in the sign. This may be questionable for some coupled phenomena, as it could induce oscillation of the coupled problem.

Let us now consider the accuracy of the numerical schemes. Developing the exact and numerical solution in Taylor's series allows their comparison:

$$\begin{aligned} A_{\text{exact}} &= 1 - x + \frac{1}{2}x^2 - \frac{1}{6}x^3 + \ldots \\ A_{\text{numerical}} &= 1 - x + \theta x^2 - \theta^2 x^3 + \ldots \\ x &= \alpha^2 \Delta t. \end{aligned} \qquad [7.49]$$

It appears that only the Crank–Nicholson scheme θ=1/2 has second-order accuracy properties. However, this conclusion is limited to infinitesimal time steps. For larger time steps, as in most numerical models, Galerkin's scheme θ=2/3 gives the optimal compromise and should be generally used.

The whole discussion related to the stability and accuracy of the proposed time numerical schemes is based on eigenmodes of a linear problem. Can we extrapolate them to general problems? The eigenvalue passage is only a mathematical tool for the consideration of scalar problems, and has no influence on our conclusions. In contrast, the nonlinear aspects could sometimes modify our conclusions. However, it is impossible to develop the analysis for a general nonlinear problem, and the preceding conclusions should be adopted as guidelines, as they appear to be fruitful in most cases.

7.2.7. *Advection diffusion processes*

Let us first consider a purely advective process. Then, the transport is governed by advection equation [7.16] and by balance equation [7.11]. By associating these two equations, we can obtain:

$$(\underline{\nabla}^{\mathrm{T}} C) \cdot \underline{f}_{\text{diff}}^{\text{fluid}} + \dot{C} = 0, \qquad [7.50]$$

which is a hyperbolic differential equation. It cannot be solved by the finite element or finite difference problem, but by characteristic methods. The idea is to follow the movement of a pollutant particle by simply integrating the fluid velocity field step-by-step. This integration has to be accurate enough, as errors are cumulated from one step to the next. On the other hand,

if advection is very small when compared with diffusion, then the finite element and FDMs are really efficient.

For most practical cases, an intermediate situation holds. It can be checked by the Peclet's number [7.18], which is high for mainly advective processes and low for mainly diffusive one. As diffusion has to be taken into account, the numerical solution must be based on the FEM (the finite difference one may also be used, but will not be discussed here). However, numerical experiments show that the classical Galerkin's formulation gives very poor results with high spatial oscillations and artificial dispersion. Therefore, new solutions have been proposed [CHA 01, ZIE 89]. A first solution is based on the use of weighting function that differs from the shape by an upwind term, in the weighted residual method, i.e. a term depending, in amplitude and direction, on the fluid velocity field. The main advantage of this method is to maintain the finite element code formalism. However, it is never possible to obtain a highly accurate procedure. Numerical dispersion will always occur.

Other solutions are based on the association of the characteristic method for the advection part of the process, and the FEM for the diffusive part [LI 97]. The characteristic method may be embedded in the finite element code, which has a strong influence on the finite element code structure. It is also possible to manage the two methods in separate codes, as in a staggered procedure (section 7.3.3).

7.3. Coupling various problems

7.3.1. *Finite element modeling: monolithical approach*

Modeling the coupling between different phenomena should imply modeling each of them, and simultaneously, all the interactions between them. A first approach consists of developing new finite elements and constitutive laws especially dedicated to the physically coupled problem to be modeled. This approach allows accurately taking all the coupling terms into account. However, there are some drawbacks that will be discussed in a later section.

The number of basic unknowns and therefore the number of dof per node are increased. This has a direct effect on the computer time used for solving the equation system (up to the third power of the total dof number). Coupled problems are highly time-consuming. Isoparametric finite elements will

often be considered. However, some specific difficulties may be encountered for specific problems. Nodal forces or fluxes are calculated in the same way as for decoupled problems (section 7.2.4). However, stiffness matrix evaluation is much more complex, as interactions between the different phenomena are to be taken into account. It must be noted that the stiffness or iteration matrix [7.29] is the derivative of internal nodal forces/fluxes with respect to the nodal unknowns (displacement/pressure/etc). The complexity is illustrated by the following scheme of the stiffness matrix, restricted to the coupling between two problems:

Derivative of problem 1 nodal forces with respect to problem 1 nodal unknowns	Derivative of problem 1 nodal forces with respect to problem 2 nodal unknowns
Derivative of problem 2 nodal forces with respect to problem 1 nodal unknowns	Derivative of problem 2 nodal forces with respect to problem 2 nodal unknowns

The part of the stiffness matrix in cells 1-1 and 2-2 are similar or simpler with regard to those involved in uncoupled problems. The two other cells 1-2 and 2-1 are new and may be of a certain complexity. It must also noted that the derivative considers internal nodal forces/fluxes as obtained numerically, i.e. taking into account all numerical integration/derivation procedures. On the other hand, large differences of orders of magnitude between different terms may cause troubles in solving the problem, and hence, need to be checked.

Numerical convergence of the Newton–Raphson process has to be evaluated carefully. It is generally based on some norms of the out-of-balance forces/fluxes. However, coupling often implies mixing of different kinds of dof, which may not be compared without precaution. Convergence has to be obtained for each basic problem modeled, not only for one, which would then predominate in the calculated indicator.

7.3.2. *Physical aspects: various terms of coupling*

A large number of different phenomena may be coupled. It is impossible to discuss all potential terms of coupling here, and we will restrict ourselves to some basic cases often implied in environmental geomaterial mechanics. In the following sections, some fundamental aspects of potential coupling are briefly described. More information can be found in the dedicated chapters of this book.

7.3.2.1. *Hydromechanical coupling*

Coupling mechanical deformation of soils or rock mass and water flow in pores is a frequent problem in geomechanics. Three dof per node are needed for 2D analysis (two displacements+one pore pressure) and four dof for 3D analysis (three displacements+one pore pressure).

The first coupling terms are related to the influence of pore pressure on mechanical equilibrium through Terzaghi's postulate:

$$\underline{\sigma} = \underline{\sigma'} + p\underline{I}, \qquad [7.51]$$

with the effective stress tensor $\underline{\sigma'}$ related to the strain rate tensor due to the constitutive equation [7.3], and the unity tensor $\underline{I}$. For unsaturated geomaterials, the effective stress concept has to be discussed [BIS 59, COU 95, COU 04, NUT 08], and generally, additional variables have to be considered [FRE 77].

The second type of coupling concerns the influence of the solid mechanics behavior on the flow process, which comes first through the storage term. Storage of water in saturated media is mainly due to pores strains, i.e. volumetric changes in soil/rock matrix:

$$\dot{S} = \dot{\varepsilon}_v. \qquad [7.52]$$

Another effect, which may be considered, is the permeability change related to the pore volume change, which may, for example, be modeled by the Kozeni–Carman law as a function of the porosity $k=k(n)$. In the excavation damaged zone around tunnels, the presence of micro- or macro-fractures has a much stronger effect and may change the permeability of several orders of magnitude [LEV 10, OLI 08].

Biot proposed an alternative formulation for rocks where contacts between grains are much more important than in soils. Following Biot, the coupling between flow and solid mechanics is found to be much more important [BIO 41, DET 91].

Other numerical problems could occur with the time dimension. First, implicit schemes are used for the solid mechanics equilibrium and various solutions are possible for the pore pressure diffusion process. Consistency would imply using fully explicit schemes for the two problems. Moreover, it

has been shown (section 7.2.6.2) that time oscillations of the pore pressure may occur for other time schemes. Associated with the Terzaghi's postulate, oscillations could also appear on the stress tensor, which can degrade the numerical convergence rate for elastoplastic or elastoviscoplastic constitutive laws.

Large strains and large displacements have been analyzed for solid mechanics. When solid mechanics is coupled with pore pressure diffusion, Darcy's fluid velocity and balance equations have to be calculated in the geometry of the current configuration, which changes from one iteration to the other. Thus, a geometric coupling term appears in the iteration matrix when deriving the nodal water fluxes with respect to the nodal displacements. On the other hand, the solid and fluid specific weights have to be actualized by taking into account the large strain process [BAR 98].

When using isoparametric finite elements, the shape functions for geometry and pore pressure are identical. For instance, let us consider a second-order finite element. As the displacement field is of the second order, the strain rate field is linear. For an elastic material, the effective stress tensor rate is also linear. However, the pore pressure field is quadratic. Subsequently, the Terzaghi's postulate mixes linear and quadratic field, which is not highly consistent. Some authors have proposed to mix the quadratic shape functions in one element for the geometry and linear shape functions for pore pressure. However, problems arise with the large strain geometry evolution and the choice of spatial integration points (1 or 4 Gauss points?).

Numerical locking problems may also appear for isoparametric finite element when the two-phase material (water+soil) is quite incompressible, i.e. for very short time steps with respect to the fluid diffusion time scale. Specific elements have to be developed for such problems.

7.3.2.2. *Thermo-hydro-mechanical coupling*

The phenomena considered here (e.g. for problems related to underground storage of nuclear waste disposals – [GEN 01b]) are much more complex as they associate multiphase fluid flow, hydromechanical coupling (section 7.3.2.1), and temperature effects. All the features described in the preceding section are to be considered here, along with some new points. 5 dof per node are needed for a 2D problem (two displacements, two

fluid pore pressures and the temperature) and six for a 3D problem (three displacements, two fluid pore pressures and the temperature).

Heat diffusion has to be modeled. Temperature variation affects fluid flow through modification of the fluid-specific weight or viscosity. Moreover, if the two fluids concerned are a liquid and a gas (e.g. water and air), then equilibrium between the phases has to be modeled: dry air–vapor equilibrium.

Heat transfer is governed not only by conduction, but also by advection through the liquid and gas movements. Similarly, transfers of vapor and dry air in the gas phase are governed by diffusion and gradient of species density, as well as by advection of the global gas movements. If the concerned geomaterials have a very low permeability (like clay for engineered barriers), then the diffusion effects will predominate and advection does not necessitate specific formulation (section 7.2.7) [COL 02].

7.3.3. *Finite element modeling: staggered approach*

Monolithical approach of coupled phenomena implies identical space and time meshes for each phenomenon. However, this is not always possible for various reasons. The coupled problems may have different numerical convergence properties, generally associated with different physical scales or nonlinearities. For example, a coupled hydromechanical problem may need large time steps for the fluid diffusion problem, to allow fluid diffusion along the distance of the order of magnitude of the finite elements in each step. At the same time, strong nonlinearities may occur in solid mechanics behavior (strong elastoplasticity changes, interface behavior, strain localization, etc.) and numerical convergence needs short time loading steps, which should be adapted automatically to the rate of convergence. Subsequently, it is quite impossible to obtain numerical convergence for identical time and space meshes.

Research teams of different physical and numerical cultures have progressively developed different modeling problems. For example, fluid flow has been largely developed using the FDM for hydrogeology problems, including pollutant transport, and for oil reservoir engineering (sections 7.2.1 and 7.2.3) considering multiphase fluid flow (oil, gas, condensate, water, etc.). Coupling such fluid flows with geomechanics in a monolithical

approach would imply implementation of all the physical features already developed in finite elements and finite differences codes, and the global human effort would be very significant.

Coupled problems generally present a higher nonlinearity level than uncoupled ones. Subsequently, inaccuracy in parameters or problem idealization may cause degradations of the convergence performance.

How can we solve such problems and obtain a convincing solution? First of all, a good strategy would be to start with the uncoupled modeling of the leading process, and try to obtain a first, and not too bad, solution. Then, we can add a first level of coupling and complexity, followed by a second one, until the full solution is obtained.

However, such a trick is not always sufficient. Staggered approaches may then give an interesting solution. In a staggered scheme, the different problems to be coupled are solved separately, with (depending on the case) different space or time mesh, or different numerical codes. However, coupling is ensured by the transfer of information between the separated models at regular meeting points. This concept is summarized in Figure 7.3, which allows theoretically coupling any models together.

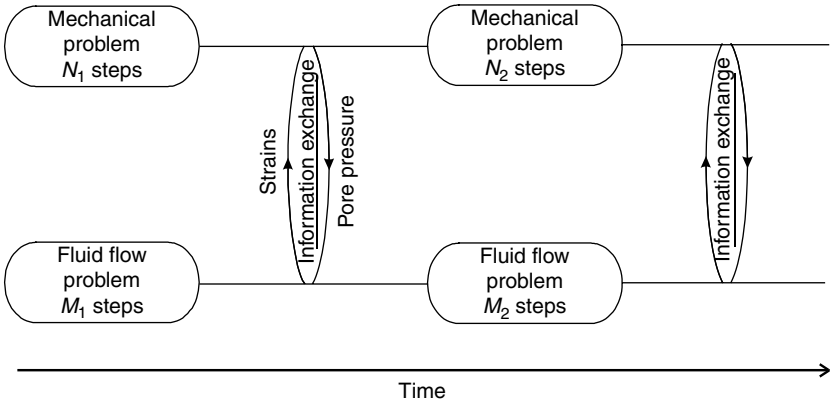

Figure 7.3. *Scheme of a staggered coupling*

When using different spatial meshes, or when coupling finite elements and finite differences codes, the transfer of information often needs an interpolation procedure, as the information to be exchanged is not defined at the points in the different meshes.

The accuracy of the coupling scheme will mainly depend on the frequency of information exchanges (which is limited by the lower time step that can be used) and on the type of information exchanged. The stability and accuracy of the process have been checked by different authors [RAD 94, TUR 93, ZIE 88], and it has been shown that a good choice of information exchange may highly improve the procedure efficiency.

7.4. Acknowledgment

The authors are grateful to FNRS, la Communauté Française de Belgique, and the European Commission for the financial help to carry out their research projects.

7.5. Bibliography

[ALO 90] ALONSO E.E., GENS A., JOSA A., "A constitutive model for partially saturated soils", *Géotechnique*, vol. 40, no. 3, p. 405-430, 1990.

[BAR 98] BARNICHON J.-D., Finite element modelling in structural and petroleum geology, PhD thesis, University of Liège, 1998.

[BER 08] FRANCOIS B., LALOUI L., "ACMEG-TS: a constitutive model for unsaturated soils under non-isothermal conditions", *International Journal of Numerical and Analytical Methods in Geomechanics*, vol. 32, p. 1955-1988, 2008.

[BIO 41] BIOT M.A., "General theory of three-dimensional consolidation", *Journal of Applied Physics*, vol. 12, p. 155-164, 1941.

[BIS 59] BISHOP A.W., "The principle of effective stress", *Tecnisk Ukeblad*, vol. 39, p. 859-863, 1959.

[CHA 90] CHARLIER R.,. HABRAKEN A.-M. "Numerical modelisation of contact with friction phenomena by the finite element method", *Computer and Geomechanics*, vol. 9, no. 1 and 2, p. 59-72, 1990.

[CHA 01] CHARLIER R., RADU J.-P., "Rétention et transfert des polluants chimiques solubles: mécanismes fondamentaux et modélisation numérique", *Traité de Mécanique et Ingénierie des Matériaux – MIM, Géomécanique environnementale*, Editions Hermes, Paris, 2001.

[COL 02] COLLIN F., LI X.L., RADU J.-P. CHARLIER R., "Thermo-hydro-mechanical coupling in clay barriers", *Engineering Geology*, vol. 64, p. 179-193, 2002.

[COL 03] COLLIN F., Couplages thermo-hydro-mécaniques dans les sols et les roches tendres partiellement saturés, PhD Thesis, University of Liège, 2003.

[COL 05] COLLIN F., LALOUI L., CHARLIER R., "Unified approach of coupled constitutive laws", ALERT autumn school 2005, *Revue Européenne de Génie Civil*, vol. 9, no. 5-6, p. 713-723, 2005.

[COU 95] COUSSY O., *Mechanics of Porous Continua*, Wiley, London, 1995.

[COU 04] COUSSY O., *Poromechanics*, Wiley, London, 2004.

[DET 91] DETOURNAY E., CHENG A.H.D., "Fundamental of poroelasticity", in J.A. HUDSON (ed.), *Comprehensive Rock Engineering, Practice and Projects*, vol. 2, Pergamon Press, 1991.

[ECL 00] ECLIPSE Technical Description, Schlumberger, 2000.

[FRE 77] FREDLUND D.G., MORGENSTERN N. R., "Stress state variables for unsaturated soils", *Journal of the Geotechnical Engineering Division, ASCE*, vol. 103(GT5), p. 447-466, 1977.

[GEN 01a] GENS A., OLIVELLA S., "THM phenomena in saturated and unsaturated materials. Fundamentals and formulation", *Revue Française de Génie Civil*, vol.5, no.6, p. 693-717, 2001.

[GEN 01b] GENS A., OLIVELLA S., "Clay barriers in radioactive waste disposal", *Revue Française de Génie Civil*, vol.5, no.6, p. 845-856, 2001.

[LEV 10] LEVASSEUR S., CHARLIER F., FRIEG B., COLLIN F., "Hydro-mechanical modelling of the excavation damaged zone around an underground excavation at Mont Terri Rock Laboratory", *International Journal of Rock Mechanics & Mining Sciences*, vol. 47, p. 414-425, 2010.

[LEW 00] LEWIS R.W., SCHREFLER B.A., *The Finite Element Method in the Static and Dynamic Deformation and Consolidation of Porous Media*, John Wiley & Sons, 2000.

[LI 97] LI X., RADU J.-P, CHARLIER R., "Numerical modeling of miscible pollutant transport by ground water in unsaturated zones", in YUAN (ed.), *Computer Methods and Advances in Geomechanics*, pp. 1255-1260, 1997.

[NUT 08] NUTH M., LALOUI L., "Effective stress concept in unsaturated soils: clarification and validation of a unified framework", *International Journal for Numerical and Analytical Method in Geomechanics*, vol. 32, p. 771-801, 2008.

[OLI 08] OLIVELLA S., ALONSO E.E., "Gas flow through clay barriers", *Géotechnique*, vol. 58, no. 3, p. 157–176, 2008.

[RAD 94] RADU J.-P., CHARLIER R., "Modelling of the hydromechanical coupling for non linear problems: fully coupled and staggered approaches", *Proceedings of the 8th Int. Conf. of the Int. Ass. for Computer Methods and Advances in Geomechanics*, West Virginia, USA, May, 1994.

[TUR 93] TURSKA E., SCHREFLER B.A., "On convergence conditions of partitioned solution procedures for consolidation problems", *Computational Methods in Applied Mechanics and Engineering*, vol. 106, p. 51-63, 1993.

[ZIE 88] ZIENCKIEWICZ O.C., PAUL D.K., CHAN A.H.C., "Unconditionally stable staggered solution procedure for soil-pore fluid interaction problems", *International Journal for Numerical Methods in Engineering*, vol. 26, p. 1039-1055, 1988.

[ZIE 89] ZIENCKIEWICZ O.C., TAYLOR R.L., *The Finite Element Method*, MacGraw-Hill Book Company, 4th ed., vol. 2, chapter 12, 1989.

Chapter 8

Conservation Laws for Coupled Hydro-Mechanical Processes in Unsaturated Porous Media: Theory and Implementation

8.1. Introduction

A portion of Earth's crust between the land surface and the phreatic zone consists of a three-phase solid–water–air system called the vadose, or unsaturated, zone [LU 04]. Water in the vadose zone has a pressure head less than atmospheric pressure and is retained by both capillary action and adhesion [LAM 69]. Movement of water within the vadose zone is governed by coupled hydro-mechanical conservation laws, as well as by a set of constitutive equations. The Richards equation [RIC 31] is often used to mathematically describe the flow of water, based partially on Darcy's law. However, this equation does not account for solid deformation that could impact, for instance, the stability of unsaturated slopes.

Coupling of hydro-mechanical processes may have a significant impact on the performance of civil infrastructures built on or within an unsaturated region. Collapse of the solid matrix could be triggered by the loss of capillary pressure due to increased saturation, as well as by frictional drag exerted by the

---

Chapter written by Ronaldo I. BORJA and Joshua A. WHITE.

fluid on the solid matrix in the presence of fluid flow. Conversely, deformation of the solid matrix, particularly when dominated by extreme volume changes, could induce significant changes in the fluid pressures and degree of saturation. In addition to coupled hydro-mechanical processes, constitutive responses in unsaturated porous materials are also known to be very complex. Deformation responses of the sediments are generally inelastic and hysteretic. Furthermore, the wetting and drying portions of the water retention curve are not the same, suggesting that a different form of hysteresis may have to be considered for modeling complex sequences of wetting and drying.

In this chapter, we review the conservation laws governing the coupled hydro-mechanical processes in unsaturated porous media, including the balance of mass and balance of momentum for all the constituent phases. There is no unique set of independent variables that one may choose for the formulation, and here, we select the displacement of the solid matrix and the pore water and pore air pressures as the preferred independent variables. We use the first and second laws of thermodynamics to infer an appropriate measure of effective stress for the solid deformation response, as well as identify other sets of energy-conjugate variables relevant for developing hydro-mechanical constitutive laws.

For the numerical implementation of the conservation laws, we employ a mixed finite element formulation utilizing stabilized low-order mixed finite elements in 2D and 3D [BOR 10, WHI 08]. The underlying rationale for choosing a low-order interpolation is to accommodate spatially varying material and geometric conditions. Sources of spatial heterogeneity include the irregular topography and spatially varying properties of the sediments, as well as the typically complex boundary conditions. However, low-order finite elements, particularly those employing equal-order interpolation of displacement and pressure fields, have a propensity to show pressure oscillation in the limit of full saturation and undrained loading. To circumvent the unstable behavior of these low-order mixed finite elements, we employ a polynomial pressure projection stabilization [BOC 06a, BOC 06b, DOH 04].

A numerical example is presented toward the end of this chapter illustrating how the developed conservation laws may be used for large-scale simulation of boundary-value problems in unsaturated porous materials. Coupling of the degrees of freedom is more intricate in the unsaturated case than in the fully saturated case. For example, the discrete gradient and discrete divergence

operators in the coupled system are strongly dependent on the degree of saturation, whereas they are constant in the fully saturated case. Thus, additional terms arise in the linearization of the coupled system. Furthermore, direct solvers may not be feasible for very large systems, and iterative solvers may need to be used. The numerical example aims to highlight the advances and challenges in solving coupled systems of equations in unsaturated porous mechanics.

8.2. Mass and momentum conservation laws

We consider a mixture consisting of a solid matrix with continuous voids filled with water and air. The total volume of the mixture is $V = V_{\rm s} + V_{\rm w} + V_{\rm a}$ and the total mass is $M = M_{\rm s} + M_{\rm w} + M_{\rm a}$, where $M_\alpha = \rho_\alpha V_\alpha$ for α = solid, water, and air; and ρ_α is the true mass density of the α constituent. The volume fraction occupied by the α constituent is given by $\phi^\alpha = V_\alpha / V$, which gives

$$\phi^{\rm s} + \phi^{\rm w} + \phi^{\rm a} = 1\,. \qquad [8.1]$$

The partial mass density of the α constituent is given by $\rho^\alpha = \phi^\alpha \rho_\alpha$, where ρ_α is the intrinsic mass density of the α constituent. This gives

$$\rho^{\rm s} + \rho^{\rm w} + \rho^{\rm a} = \rho\,, \qquad [8.2]$$

where $\rho = M/V$ is the total mass density of the mixture.

We denote the instantaneous intrinsic velocities of the solid, water, and air constituents by $\boldsymbol{v} \equiv \boldsymbol{v}_{\rm s}$, $\boldsymbol{v}_{\rm w}$, and $\boldsymbol{v}_{\rm a}$, respectively. The material time derivative following the solid motion is denoted by the symbol

$$\frac{{\rm d}(\cdot)}{{\rm d}t} = \frac{\partial(\cdot)}{\partial t} + \boldsymbol{\nabla}\cdot\boldsymbol{v}\,. \qquad [8.3]$$

In the absence of mass exchanges among the three constituents, the balance of mass for the solid, water, and air constituents, respectively, takes the form

$$\frac{{\rm d}\rho^{\rm s}}{{\rm d}t} + \rho^{\rm s}\boldsymbol{\nabla}\cdot\boldsymbol{v} = 0\,, \qquad [8.4]$$

$$\frac{{\rm d}\rho^{\rm w}}{{\rm d}t} + \rho^{\rm w}\boldsymbol{\nabla}\cdot\boldsymbol{v} = -\boldsymbol{\nabla}\cdot\boldsymbol{w}^{\rm w}\,, \qquad [8.5]$$

$$\frac{{\rm d}\rho^{\rm w}}{{\rm d}t} + \rho^{\rm a}\boldsymbol{\nabla}\cdot\boldsymbol{v} = -\boldsymbol{\nabla}\cdot\boldsymbol{w}^{\rm a}\,, \qquad [8.6]$$

where $\boldsymbol{w}^{\alpha}$ (for α = water, air) is the Eulerian relative flow vector of the α constituent with respect to the solid matrix and is given explicitly by the relations

$$\boldsymbol{w}^{\alpha} = \rho^{\alpha}\widetilde{\boldsymbol{v}}_{\alpha}\,, \qquad \widetilde{\boldsymbol{v}}_{\alpha} = \boldsymbol{v}_{\alpha} - \boldsymbol{v}\,, \qquad \alpha = \mathrm{w}, \mathrm{a}\,. \tag{8.7}$$

Barotropic flows satisfy functional relations of the form

$$f_{\alpha}(p_{\alpha}, \rho_{\alpha}) = 0\,, \qquad \alpha = \mathrm{s}, \mathrm{w}, \mathrm{a}\,, \tag{8.8}$$

where p_{α} denotes the intrinsic pressure equal to the actual force per unit actual area acting on the α constituent. The functional relations given earlier determine the intrinsic bulk modulus for the α constituent as

$$K_{\alpha} = \rho_{\alpha} p'_{\alpha}(\rho_{\alpha})\,, \qquad \alpha = \mathrm{s}, \mathrm{w}, \mathrm{a}\,. \tag{8.9}$$

In this case, the mass conservation laws specialize to form

$$\frac{\mathrm{d}\phi^{\mathrm{s}}}{\mathrm{d}t} + \frac{\phi^{\mathrm{s}}}{K_{\mathrm{s}}}\frac{\mathrm{d}p_{\mathrm{s}}}{\mathrm{d}t} + \phi^{\mathrm{s}}\boldsymbol{\nabla}\cdot\boldsymbol{v} = 0\,, \tag{8.10}$$

$$\frac{\mathrm{d}\phi^{\mathrm{w}}}{\mathrm{d}t} + \frac{\phi^{\mathrm{w}}}{K_{\mathrm{w}}}\frac{\mathrm{d}p_{\mathrm{w}}}{\mathrm{d}t} + \phi^{\mathrm{w}}\boldsymbol{\nabla}\cdot\boldsymbol{v} = -\frac{1}{\rho_{\mathrm{w}}}\boldsymbol{\nabla}\cdot\boldsymbol{w}^{\mathrm{w}}\,, \tag{8.11}$$

$$\frac{\mathrm{d}\phi^{\mathrm{a}}}{\mathrm{d}t} + \frac{\phi^{\mathrm{a}}}{K_{\mathrm{a}}}\frac{\mathrm{d}p_{\mathrm{a}}}{\mathrm{d}t} + \phi^{\mathrm{a}}\boldsymbol{\nabla}\cdot\boldsymbol{v} = -\frac{1}{\rho_{\mathrm{a}}}\boldsymbol{\nabla}\cdot\boldsymbol{w}^{\mathrm{a}}\,. \tag{8.12}$$

We introduce void fractions ψ^{w} and ψ^{a} representing the ratios between the volumes of water and air in the voids, respectively, to the total volume of the void itself. They are related to the volume fractions as

$$\psi^{\mathrm{w}} = \frac{\phi^{\mathrm{w}}}{1-\phi^{\mathrm{s}}}\,, \qquad \psi^{\mathrm{a}} = \frac{\phi^{\mathrm{a}}}{1-\phi^{\mathrm{s}}}\,, \qquad \psi^{\mathrm{w}} + \psi^{\mathrm{a}} = 1\,, \tag{8.13}$$

where ψ^{w} is the degree of saturation. Taking the derivatives and substituting them into equations [8.11] and [8.12] gives

$$(1-\phi^{\mathrm{s}})\frac{\mathrm{d}\psi^{\mathrm{w}}}{\mathrm{d}t} + \frac{\phi^{\mathrm{w}}}{K_{\mathrm{w}}}\frac{\mathrm{d}p_{\mathrm{w}}}{\mathrm{d}t} + \frac{\psi^{\mathrm{w}}\phi^{\mathrm{s}}}{K_{\mathrm{s}}}\frac{\mathrm{d}p_{\mathrm{s}}}{\mathrm{d}t} + \psi^{\mathrm{w}}\boldsymbol{\nabla}\cdot\boldsymbol{v} = -\frac{1}{\rho_{\mathrm{w}}}\boldsymbol{\nabla}\cdot\boldsymbol{w}^{\mathrm{w}}, \tag{8.14}$$

$$(1-\phi^{\mathrm{s}})\frac{\mathrm{d}\psi^{\mathrm{a}}}{\mathrm{d}t} + \frac{\phi^{\mathrm{a}}}{K_{\mathrm{a}}}\frac{\mathrm{d}p_{\mathrm{a}}}{\mathrm{d}t} + \frac{\psi^{\mathrm{a}}\phi^{\mathrm{s}}}{K_{\mathrm{s}}}\frac{\mathrm{d}p_{\mathrm{s}}}{\mathrm{d}t} + \psi^{\mathrm{a}}\boldsymbol{\nabla}\cdot\boldsymbol{v} = -\frac{1}{\rho_{\mathrm{a}}}\boldsymbol{\nabla}\cdot\boldsymbol{w}^{\mathrm{a}}\,. \tag{8.15}$$

Next, we consider a functional relationship for p_{s} of the form

$$p_{\mathrm{s}} = \widetilde{p}_{\mathrm{s}}(\rho^{\mathrm{s}}, \phi^{\mathrm{s}}) \neq \widetilde{p}_{\mathrm{s}}(\rho^{\mathrm{s}}/\phi^{\mathrm{s}})\,. \qquad [8.16]$$

The above-mentioned equation defines an elastic compressibility law for the solid matrix. Note that the functional relationship $p_{\mathrm{s}} = \widetilde{p}_{\mathrm{s}}(\rho^{\mathrm{s}}/\phi^{\mathrm{s}}) = \widetilde{p}_{\mathrm{s}}(\rho_{\mathrm{s}})$ defines the elastic compressibility law for the solid constituent and is a redundant expression. We thus assume in equation [8.16] that the functional relationship for p_{s} depends on ρ^{s} and ϕ^{s}, but not through $\rho^{\mathrm{s}}/\phi^{\mathrm{s}}$. Taking the material time derivative of equation [8.16] gives

$$\frac{\mathrm{d}p_{\mathrm{s}}}{\mathrm{d}t} = \frac{\partial \widetilde{p}_{\mathrm{s}}}{\partial \rho^{\mathrm{s}}}\frac{\mathrm{d}\rho^{\mathrm{s}}}{\mathrm{d}t} + \frac{\partial \widetilde{p}_{\mathrm{s}}}{\partial \phi^{\mathrm{s}}}\frac{\mathrm{d}\phi^{\mathrm{s}}}{\mathrm{d}t}\,. \qquad [8.17]$$

But

$$\frac{1}{\rho^{\mathrm{s}}}\frac{\mathrm{d}\rho^{\mathrm{s}}}{\mathrm{d}t} = \frac{\mathrm{d}}{\mathrm{d}t}\Big[\ln\Big(\frac{\rho^{\mathrm{s}}}{\rho_0^{\mathrm{s}}}\Big)\Big] = \frac{\mathrm{d}}{\mathrm{d}t}(\ln J^{-1}) = -\boldsymbol{\nabla}\cdot\boldsymbol{v}\,, \qquad [8.18]$$

where $\rho_0^{\mathrm{s}} = J\rho^{\mathrm{s}}$ is the partial mass density for solid in the reference configuration. Together with equation [8.10], equation [8.17] gives

$$\phi^{\mathrm{s}}\frac{\mathrm{d}p_{\mathrm{s}}}{\mathrm{d}t} = -K\boldsymbol{\nabla}\cdot\boldsymbol{v}\,, \qquad [8.19]$$

where

$$K = \phi^{\mathrm{s}}\Big(\rho^{\mathrm{s}}\frac{\partial \widetilde{p}_{\mathrm{s}}}{\partial \rho^{\mathrm{s}}} + \phi^{\mathrm{s}}\frac{\partial \widetilde{p}_{\mathrm{s}}}{\partial \phi^{\mathrm{s}}}\Big)\Big/\Big(1 + \frac{\partial \widetilde{p}_{\mathrm{s}}}{\partial \phi^{\mathrm{s}}}\frac{\phi^{\mathrm{s}}}{K_{\mathrm{s}}}\Big) \qquad [8.20]$$

is the elastic bulk modulus of the solid matrix. Substituting equation [8.19] into [8.10], [8.14], and [8.15] gives

$$\frac{\mathrm{d}\phi^{\mathrm{s}}}{\mathrm{d}t} + (B - 1 + \phi^{\mathrm{s}})\boldsymbol{\nabla}\cdot\boldsymbol{v} = 0\,, \qquad [8.21]$$

$$(1-\phi^{\mathrm{s}})\frac{\mathrm{d}\psi^{\mathrm{w}}}{\mathrm{d}t} + \frac{\phi^{\mathrm{w}}}{K_{\mathrm{w}}}\frac{\mathrm{d}p_{\mathrm{w}}}{\mathrm{d}t} + \psi^{\mathrm{w}}B\boldsymbol{\nabla}\cdot\boldsymbol{v} = -\frac{1}{\rho_{\mathrm{w}}}\boldsymbol{\nabla}\cdot\boldsymbol{w}^{\mathrm{w}}\,, \qquad [8.22]$$

$$(1-\phi^{\mathrm{s}})\frac{\mathrm{d}\psi^{\mathrm{a}}}{\mathrm{d}t} + \frac{\phi^{\mathrm{a}}}{K_{\mathrm{a}}}\frac{\mathrm{d}p_{\mathrm{a}}}{\mathrm{d}t} + \psi^{\mathrm{a}}B\boldsymbol{\nabla}\cdot\boldsymbol{v} = -\frac{1}{\rho_{\mathrm{a}}}\boldsymbol{\nabla}\cdot\boldsymbol{w}^{\mathrm{a}}\,, \qquad [8.23]$$

where

$$B = 1 - \frac{K}{K_{\mathrm{s}}} \qquad [8.24]$$

is the Biot coefficient.

The balance of linear momentum in the absence of inertia forces may be written for a solid–water–air mixture as

$$\boldsymbol{\nabla} \cdot \boldsymbol{\sigma}^{\mathrm{s}} + \rho^{\mathrm{s}} \boldsymbol{g} + \boldsymbol{h}^{\mathrm{s}} = \mathbf{0}\,, \qquad [8.25]$$

$$\boldsymbol{\nabla} \cdot \boldsymbol{\sigma}^{\mathrm{w}} + \rho^{\mathrm{w}} \boldsymbol{g} + \boldsymbol{h}^{\mathrm{w}} = \mathbf{0}\,, \qquad [8.26]$$

$$\boldsymbol{\nabla} \cdot \boldsymbol{\sigma}^{\mathrm{a}} + \rho^{\mathrm{a}} \boldsymbol{g} + \boldsymbol{h}^{\mathrm{a}} = \mathbf{0}\,, \qquad [8.27]$$

where $\boldsymbol{\sigma}^{\mathrm{s}}$, $\boldsymbol{\sigma}^{\mathrm{w}}$, and $\boldsymbol{\sigma}^{\mathrm{a}}$ are the partial Cauchy stress tensors defined as the ratio between the forces acting on solid, water, and air, respectively, per unit area of the mixture. The partial stresses satisfy the relation

$$\boldsymbol{\sigma}^{\mathrm{s}} + \boldsymbol{\sigma}^{\mathrm{w}} + \boldsymbol{\sigma}^{\mathrm{a}} = \boldsymbol{\sigma}\,, \qquad [8.28]$$

where $\boldsymbol{\sigma}$ is the total Cauchy stress tensor. The body force density vectors $\boldsymbol{h}^{\mathrm{s}}$, $\boldsymbol{h}^{\mathrm{w}}$, and $\boldsymbol{h}^{\mathrm{a}}$ act on the solid, water and air constituents, respectively, measured with respect to the total volume of the mixture and satisfy the closure condition

$$\boldsymbol{h}^{\mathrm{s}} + \boldsymbol{h}^{\mathrm{w}} + \boldsymbol{h}^{\mathrm{a}} = \mathbf{0}\,. \qquad [8.29]$$

Thus, the balance of linear momentum for the entire mixture takes the form

$$\boldsymbol{\nabla} \cdot \boldsymbol{\sigma} + \rho \boldsymbol{g} = \mathbf{0}\,, \qquad [8.30]$$

where $\boldsymbol{g}$ is the gravity acceleration vector.

8.3. Balance of energy and the effective stress

Imposing the first law of thermodynamics on a solid–water–air mixture yields the following expression for the material time derivative of internal energy [BOR 04, BOR 06, BOR 09]

$$\rho \dot{\overline{e}} = \boldsymbol{\sigma}^{\mathrm{s}} : \boldsymbol{d} + \boldsymbol{\sigma}^{\mathrm{w}} : \boldsymbol{d}_{\mathrm{w}} + \boldsymbol{\sigma}^{\mathrm{a}} : \boldsymbol{d}_{\mathrm{a}} + r - \boldsymbol{\nabla} \cdot \boldsymbol{q}\,, \qquad [8.31]$$

where $\boldsymbol{d}$, $\boldsymbol{d}_{\mathrm{w}}$, and $\boldsymbol{d}_{\mathrm{a}}$ are the rates of deformation for the solid, water, and air constituents, respectively, r is the heat supply per unit volume of the mixture, and $\boldsymbol{q}$ is the heat flux vector. If we assume that $\boldsymbol{\sigma}^{\mathrm{w}}$ and $\boldsymbol{\sigma}^{\mathrm{a}}$ are isotropic tensors of the form

$$\boldsymbol{\sigma}^{\mathrm{w}} = -\phi^{\mathrm{w}} p_{\mathrm{w}} \mathbf{1}\,, \qquad \boldsymbol{\sigma}^{\mathrm{a}} = -\phi^{\mathrm{a}} p_{\mathrm{a}} \mathbf{1}\,, \qquad [8.32]$$

where $\mathbf{1}$ is the second-order identity tensor (Kronecker delta), then we get

$$\rho\dot{\bar{e}} = \boldsymbol{\sigma}^{\mathrm{s}} : \boldsymbol{d} - \phi^{\mathrm{w}} p_{\mathrm{w}} \boldsymbol{\nabla} \cdot \boldsymbol{v}_{\mathrm{w}} - \phi^{\mathrm{a}} p_{\mathrm{a}} \boldsymbol{\nabla} \cdot \boldsymbol{v}_{\mathrm{a}} + r - \boldsymbol{\nabla} \cdot \boldsymbol{q}\,, \qquad [8.33]$$

where $\boldsymbol{v}_{\mathrm{w}}$ and $\boldsymbol{v}_{\mathrm{a}}$ are the velocities of water and air constituents, respectively. Adding the null scalar product $(\boldsymbol{\sigma} - \boldsymbol{\sigma}^{\mathrm{s}} - \boldsymbol{\sigma}^{\mathrm{w}} - \boldsymbol{\sigma}^{\mathrm{a}}) : \boldsymbol{d}$ to this expression gives

$$\rho\dot{\bar{e}} = \boldsymbol{\sigma} : \boldsymbol{d} - \phi^{\mathrm{w}} p_{\mathrm{w}} \boldsymbol{\nabla} \cdot \widetilde{\boldsymbol{v}}_{\mathrm{w}} - \phi^{\mathrm{a}} p_{\mathrm{a}} \boldsymbol{\nabla} \cdot \widetilde{\boldsymbol{v}}_{\mathrm{a}} + r - \boldsymbol{\nabla} \cdot \boldsymbol{q}\,, \qquad [8.34]$$

where $\widetilde{\boldsymbol{v}}_{\mathrm{w}}$ and $\widetilde{\boldsymbol{v}}_{\mathrm{a}}$ are the relative velocities of water and air constituents defined earlier in equation [8.7].

The divergence of the relative velocity $\widetilde{\boldsymbol{v}}_\alpha$ can be expressed in terms of the divergence of the Eulerian relative flow vector $\boldsymbol{w}^\alpha$ as

$$\boldsymbol{\nabla} \cdot \boldsymbol{w}^\alpha = \phi^\alpha \rho_\alpha \boldsymbol{\nabla} \cdot \widetilde{\boldsymbol{v}}_\alpha + \widetilde{\boldsymbol{v}}_\alpha \cdot \boldsymbol{\nabla}(\phi^\alpha \rho_\alpha)\,, \qquad \alpha = \mathrm{w}, \mathrm{a}\,. \qquad [8.35]$$

Solving for $\boldsymbol{\nabla} \cdot \widetilde{\boldsymbol{v}}_\alpha$ from the above-mentioned equation and using equations [8.22] and [8.23], we obtain the following alternative expression for the rate of change of internal energy

$$\rho\dot{\bar{e}} = \boldsymbol{\sigma}' : \boldsymbol{d} - s(1 - \phi^{\mathrm{s}}) \frac{\mathrm{d}\psi^{\mathrm{w}}}{\mathrm{d}t} + \mathcal{A} + \mathcal{G} + r - \boldsymbol{\nabla} \cdot \boldsymbol{q}\,, \qquad [8.36]$$

where

$$\boldsymbol{\sigma}' = \boldsymbol{\sigma} + B\overline{p}\mathbf{1}\,, \qquad [8.37]$$

$$\overline{p} = \psi^{\mathrm{w}} p_{\mathrm{w}} + \psi^{\mathrm{a}} p_{\mathrm{a}} = \psi^{\mathrm{w}} p_{\mathrm{w}} + (1 - \psi^{\mathrm{w}}) p_{\mathrm{a}}\,, \qquad [8.38]$$

$$s = p_{\mathrm{a}} - p_{\mathrm{w}}\,, \qquad [8.39]$$

and

$$\mathcal{A} = \sum_{\alpha = \mathrm{w},\mathrm{a}} \frac{\phi^\alpha}{K_\alpha} \frac{\mathrm{d}p_\alpha}{\mathrm{d}t} p_\alpha\,, \qquad [8.40]$$

$$\mathcal{G} = \sum_{\alpha = \mathrm{w},\mathrm{a}} \Big(\frac{1}{\rho_\alpha} \boldsymbol{\nabla} \cdot \boldsymbol{w}^\alpha - \phi^\alpha \boldsymbol{\nabla} \cdot \widetilde{\boldsymbol{v}}_\alpha \Big) p_\alpha\,. \qquad [8.41]$$

Equation [8.36] identifies $\boldsymbol{\sigma}'$ as the stress tensor, that is, energy conjugate to the rate of deformation of the solid matrix, $\boldsymbol{d}$, and the suction stress s as energy

conjugate to the rate of change of the degree of saturation, $\mathrm{d}\psi^{\mathrm{w}}/\mathrm{d}t$. The energy conjugacy between the intrinsic pressures in water and air and the rates of change of their respective intrinsic volumes are represented by the term $\mathcal{A}$. Finally, the term $\mathcal{G}$ represents the rate of energy expended by the fluid pressures in either injecting or expelling fluids relative to the solid matrix.

Equation [8.37] is the "effective stress equation" for the partially saturated porous material. It is very similar in form to Skempton's [SKE 61] equation except that he used Bishop's [BIS 59] parameter χ in lieu of degree of saturation ψ^{w} for the mean neutral stress $\overline{p}$. The ratio K/K_{s} is typically in the range 0.1–0.5 for saturated rocks and concrete [SKE 61], and so, Biot's coefficient B ranges from 0.9 to 0.5 for such materials. For soils, however, K/K_{s} is very small, and so it is customary to take $B = 1.0$ for such material, resulting in the following expression for the effective stress similar to that developed in [SCH 84]

$$\boldsymbol{\sigma}' = \boldsymbol{\sigma} + \left[\psi^{\mathrm{w}} p_{\mathrm{w}} + (1 - \psi^{\mathrm{w}}) p_{\mathrm{a}}\right] \mathbf{1} \,. \qquad [8.42]$$

However, if $\psi^{\mathrm{w}} = 1$ (fully saturated), the effective stress equation becomes

$$\boldsymbol{\sigma}' = \boldsymbol{\sigma} + B p_{\mathrm{w}} \mathbf{1} \,. \qquad [8.43]$$

This equation was shown by Nur and Byerlee [NUR 71] to be theoretically exact for saturated rocks. Finally, we recover Terzaghi's [TER 43] effective stress equation at full saturation and incompressible solids,

$$\boldsymbol{\sigma}' = \boldsymbol{\sigma} + p_{\mathrm{w}} \mathbf{1} \,. \qquad [8.44]$$

Thus, equation [8.37] is a complete effective stress equation for partially saturated porous materials capable of reproducing other well-known forms of the effective stress equation under special conditions.

That $\boldsymbol{\sigma}'$ is a complete effective stress tensor may be seen from equation [8.36], which contains the term $\boldsymbol{\sigma}' : \boldsymbol{d}$ plus other terms that are not related to the deformation of the solid phase. If, however, we define the "effective stress" as

$$\boldsymbol{\sigma}'' = \boldsymbol{\sigma} + \left[\psi^{\mathrm{w}} p_{\mathrm{w}} + (1 - \psi^{\mathrm{w}}) p_{\mathrm{a}}\right] \mathbf{1} \,, \qquad [8.45]$$

then we see that

$$\boldsymbol{\sigma}' : \boldsymbol{d} = \boldsymbol{\sigma}'' : \boldsymbol{d} - \frac{K}{K_{\mathrm{s}}} \overline{p} \mathbf{1} : \boldsymbol{d} \,. \qquad [8.46]$$

Therefore, $\boldsymbol{\sigma}''$ cannot represent the work done in compressing the solid constituent itself. Finally, if we consider the familiar net stress tensor

$$\boldsymbol{\sigma}_{\rm net} = \boldsymbol{\sigma} + p_{\rm a}\mathbf{1}\,, \qquad [8.47]$$

then

$$\boldsymbol{\sigma}' : \boldsymbol{d} = \boldsymbol{\sigma}_{\rm net} : \boldsymbol{d} - \Big(\psi^{\rm w} s + \frac{K}{K_{\rm s}}\overline{p}\Big)\mathbf{1} : \boldsymbol{d}\,. \qquad [8.48]$$

We see that $\boldsymbol{\sigma}_{\rm net}$ has one more term in the energy equation that it cannot represent, namely, the energy produced by the suction stress s which also depends on the rate of deformation of the solid matrix. On a related note, it is well known that the position of the critical state line for unsaturated soils generally varies with the suction stress when one uses the net stress in the constitutive description [NUT 08]. This is precisely due to the incomplete nature of the net stress as shown above, in that it cannot represent the energy produced by the suction stress in deforming the solid matrix.

8.4. Formulation of boundary-value problem

It is possible to formulate a complete boundary-value problem incorporating all of the elements presented in the previous section. However, we can simplify the formulation considerably by ignoring some terms that likely will not be relevant for the problem at hand. For example, for shallow, non-dynamic solid deformation we can set $p_{\rm a} = 0$ (i.e. atmospheric). Furthermore, $B = 1.0$ (incompressible solid) and $K_{\rm w} \to \infty$ (incompressible water constituent) are realistic assumptions for most geotechnical applications. We can also ignore the mass of air, so that balance of linear momentum in a given unsaturated porous domain $\mathcal{B}$ can be written simply as

$$\boldsymbol{\nabla}\cdot(\boldsymbol{\sigma}' - \psi^{\rm w} p\mathbf{1}) + \rho\boldsymbol{g} = \mathbf{0}\,, \qquad \rho = \phi^{\rm s}\rho_{\rm s} + \phi^{\rm w}\rho_{\rm w}\,, \qquad [8.49]$$

where $\boldsymbol{\sigma}'$ is the effective Cauchy stress tensor defined in equation [8.37], and $p \equiv p_{\rm w}$ for brevity. The balance of water mass in the subsurface takes the form

$$(1-\phi^{\rm s})\dot{\psi}^{\rm w} + \psi^{\rm w}\boldsymbol{\nabla}\cdot\boldsymbol{v} + \boldsymbol{\nabla}\cdot\boldsymbol{q} = 0\,, \qquad [8.50]$$

where $\boldsymbol{q} = \phi^{\rm w}\widetilde{\boldsymbol{v}}_{\rm w}$ is the relative discharge velocity and the superimposed dot is the material time derivative following the solid motion.

To complete the presentation of the governing equations, we need to make some constitutive assumptions. First, we assume that the relative discharge velocity is governed by the generalized Darcy's law of the form

$$\boldsymbol{q} = k_{\mathrm{rw}} \boldsymbol{K} \cdot \boldsymbol{\nabla} \Big(\frac{p}{\rho_{\mathrm{w}} \mathrm{g}} + z \Big) \,, \qquad [8.51]$$

where $\boldsymbol{K}$ is the hydraulic conductivity of the porous medium at complete saturation, k_{rw} the relative permeability that varies with degree of saturation ψ^{w}, g the gravity acceleration constant, and z the vertical coordinate. Furthermore, we assume two additional constitutive laws relating the Cauchy effective stress rate tensor $\dot{\boldsymbol{\sigma}}'$ with the strain rate tensor $\boldsymbol{\nabla}^{\mathrm{s}} \boldsymbol{v}$ for the solid matrix, and the suction stress $s = -p$ with degree of saturation ψ^{w}. The latter constitutive law may be determined experimentally from the soil water retention curve, which we express below using the Van Genuchten equation [VAN 80] as

$$\psi^{\mathrm{w}}(s) = \psi_1 + (\psi_2 - \psi_1) \Big[1 + \Big(\frac{s}{s_a} \Big)^n \Big]^{-m} . \qquad [8.52]$$

The above equation contains four parameters: ψ_1 is the residual water saturation, ψ_2 is the maximum water saturation, s_a is a scaling pressure, and n and m are empirical constants defining the shape of the saturation curve. The constants n and m are not independent, but are instead related to one another as

$$m = \frac{n-1}{n} \,. \qquad [8.53]$$

The water phase relative permeability is similarly defined as

$$k_{\mathrm{rw}}(\theta) = \theta^{1/2} \Big[1 - \Big(1 - \theta^{1/m} \Big)^m \Big]^2 , \qquad \theta = \frac{\psi^{\mathrm{w}} - \psi_1}{\psi_2 - \psi_1} . \qquad [8.54]$$

Finally, the material time derivative of degree of saturation can be expressed in terms of the material time derivative of suction as

$$\dot{\psi}^{\mathrm{w}} = \Psi \dot{s} = -\Psi \dot{p} \,, \qquad \Psi = \psi^{\mathrm{w}\prime}(s) \,. \qquad [8.55]$$

Thus, we see that the governing equations [8.49] and [8.50] can be expressed in terms of two independent variables alone, namely, the solid velocity $\boldsymbol{v} \equiv \dot{\boldsymbol{u}}$ and pore water pressure p. The solution is fully coupled in the sense that the independent variables are determined simultaneously.

We complete the statement of the problem by specifying appropriate boundary and initial conditions. To this end, we assume that the total boundary $\partial\mathcal{B}$ of domain $\mathcal{B}$ can be decomposed as follows

$$\partial\mathcal{B} = \overline{\partial\mathcal{B}_{\boldsymbol{u}} \cup \partial\mathcal{B}_{\boldsymbol{t}}} = \overline{\partial\mathcal{B}_p \cup \partial\mathcal{B}_q}\,, \qquad [8.56]$$

$$\varnothing = \partial\mathcal{B}_{\boldsymbol{u}} \cap \partial\mathcal{B}_{\boldsymbol{t}} = \partial\mathcal{B}_p \cap \partial\mathcal{B}_q\,, \qquad [8.57]$$

where $\partial\mathcal{B}_{\boldsymbol{u}}$ is the solid displacement boundary, $\partial\mathcal{B}_{\boldsymbol{t}}$ the solid traction boundary, $\partial\mathcal{B}_p$ the fluid pressure boundary and $\partial\mathcal{B}_q$ the fluid flux boundary. The boundary conditions are then given as

$$\boldsymbol{u} = \overline{\boldsymbol{u}} \quad \text{on } \partial\mathcal{B}_{\boldsymbol{u}}\,, \qquad [8.58]$$

$$\boldsymbol{n}\cdot\boldsymbol{\sigma} = \bar{\boldsymbol{t}} \quad \text{on } \partial\mathcal{B}_{\boldsymbol{t}}\,, \qquad [8.59]$$

$$p = \overline{p} \quad \text{on } \partial\mathcal{B}_p\,, \qquad [8.60]$$

$$-\boldsymbol{n}\cdot\boldsymbol{q} = \overline{q} \quad \text{on } \partial\mathcal{B}_q\,. \qquad [8.61]$$

The initial conditions are given as

$$\boldsymbol{u}(\boldsymbol{x}, t=0) = \boldsymbol{u}_0\,, \qquad p(\boldsymbol{x}, t=0) = p_0\,, \qquad [8.62]$$

for all $\boldsymbol{x} \in \mathcal{B}$.

Following standard lines, we consider two spaces of trial functions defined as

$$\mathcal{U} = \{\boldsymbol{u} : \mathcal{B} \to R^3 \,|\, u_i \in H^1, \boldsymbol{u} = \overline{\boldsymbol{u}} \text{ on } \partial\mathcal{B}_{\boldsymbol{u}}\}\,, \qquad [8.63]$$

$$\mathcal{P} = \{p : \mathcal{B} \to R^3 \,|\, p \in H^1, p = \overline{p} \text{ on } \partial\mathcal{B}_p\}\,, \qquad [8.64]$$

where H^1 denotes a Sobolev space of degree one. We also define the corresponding spaces of variations,

$$\mathcal{U}^* = \{\boldsymbol{\eta} : \mathcal{B} \to R^3 \,|\, \eta_i \in H^1, \boldsymbol{\eta} = \boldsymbol{0} \text{ on } \partial\mathcal{B}_{\boldsymbol{u}}\}\,, \qquad [8.65]$$

$$\mathcal{P}^* = \{\theta : \mathcal{B} \to R^3 \,|\, \theta \in H^1, \theta = 0 \text{ on } \partial\mathcal{B}_p\}\,. \qquad [8.66]$$

The weak form of the problem is then to find $\{\boldsymbol{u}, p\} \in \mathcal{U} \times \mathcal{P}$ such that for all $\{\boldsymbol{\eta}, \theta\} \in \mathcal{U}^* \times \mathcal{P}^*$, balance of momentum,

$$\int_{\mathcal{B}} \boldsymbol{\nabla}^{\mathrm{s}}\boldsymbol{\eta} : \boldsymbol{\sigma}' \,\mathrm{d}V - \int_{\mathcal{B}} \boldsymbol{\nabla}\cdot\boldsymbol{\eta}\psi^{\mathrm{w}} p \,\mathrm{d}V - \int_{\mathcal{B}} \boldsymbol{\eta}\cdot\rho\boldsymbol{g} \,\mathrm{d}V - \int_{\partial\mathcal{B}_{\boldsymbol{t}}} \boldsymbol{\eta}\cdot\bar{\boldsymbol{t}} \,\mathrm{d}A = 0, \quad [8.67]$$

and balance of mass,

$$-\int_{\mathcal{B}} \theta\psi^{\mathrm{w}} \boldsymbol{\nabla}\cdot\dot{\boldsymbol{u}} \,\mathrm{d}V - \int_{\mathcal{B}} \theta(1-\phi^{\mathrm{s}})\dot{\psi}^{\mathrm{w}} \,\mathrm{d}V + \int_{\mathcal{B}} \boldsymbol{\nabla}\theta\cdot\boldsymbol{q} \,\mathrm{d}V + \int_{\partial\mathcal{B}_q} \theta\overline{q} \,\mathrm{d}A = 0 \quad [8.68]$$

hold. Note in the above variational equation that we have left the term $\dot{\psi}^{\mathrm{w}}$ as is, instead of replacing it with $-\Psi\dot{p}$ as was done in equation [8.55]. In general, the saturation–suction relation is highly nonlinear, and using the tangent $\Psi = \psi^{\mathrm{w}\prime}(s)$ can lead to large mass balance errors in the time-discrete setting as pointed out in [CEL 90]. Instead of using the tangent Ψ, we have thus used a direct backward implicit time-integration on the saturation in the form $\dot{\psi}^{\mathrm{w}}_{n+1} \approx (\psi^{\mathrm{w}}_{n+1} - \psi^{\mathrm{w}}_n)/\Delta t$, which leads to more desirable stability properties [WHI 09].

The above equations show the tight coupling that exists between the two degrees of freedom $\boldsymbol{u}$ and p. In the fully saturated range, this tight coupling is somewhat alleviated by noting that the variational equation for the balance of mass simplifies to [AND 07]

$$-\int_{\mathcal{B}} \theta\boldsymbol{\nabla}\cdot\dot{\boldsymbol{u}} \,\mathrm{d}V + \int_{\mathcal{B}} \boldsymbol{\nabla}\theta\cdot\boldsymbol{q} \,\mathrm{d}V + \int_{\partial\mathcal{B}_q} \theta\overline{q} \,\mathrm{d}A = 0\,. \quad [8.69]$$

However, the two primary variables, $\boldsymbol{u}$ and p, are still linked together and must be determined simultaneously.

Mixed finite element (FE) equations may be readily developed from the above variational equations. The independent variables are the nodal displacement vector $\boldsymbol{d}$ and nodal pore water pressure vector $\boldsymbol{p}$. The coupled FE equations take the form

$$\boldsymbol{F}_{INT}(\boldsymbol{d}) + \boldsymbol{G}\boldsymbol{p} = \boldsymbol{F}_{EXT}\,, \quad [8.70]$$

$$\boldsymbol{G}^{\mathsf{T}}\dot{\boldsymbol{d}} + \boldsymbol{\Psi}(\boldsymbol{p}) + \boldsymbol{\Phi}\boldsymbol{p} = \boldsymbol{G}_{EXT}\,, \quad [8.71]$$

where $\boldsymbol{F}_{INT}(\boldsymbol{d})$ is the internal nodal force vector arising from the effective stress $\boldsymbol{\sigma}'$, $\boldsymbol{G}$ and $\boldsymbol{G}^{\mathsf{T}}$ are the discrete gradient and discrete divergence operators, respectively, which depend on $\boldsymbol{p}$ through the degree of saturation ψ^{w} in the unsaturated regime, $\boldsymbol{\Psi}(\boldsymbol{p})$ is a nonlinear vector function of the pressure resulting from direct time-integration of the rate of saturation (which vanishes at full saturation), $\boldsymbol{\Phi}$ is an effective conductivity matrix that also depends on the degree of saturation, and $\boldsymbol{F}_{EXT}$ and $\boldsymbol{G}_{EXT}$ are prescribed vectors of momentum and fluid supplies. The degree of coupling implied by the above equations is more intricate than in the fully saturated case because of the presence of ψ^{w} in many places, which produces additional terms in the derivatives relevant for Newton iteration.

As noted in section 8.1, we shall focus specifically on low-order mixed finite elements, such as the 2D quadrilateral and 3D hexahedral elements shown in Figure 8.1. Higher-order elements could be prohibitively expensive and may not be so useful for problems dominated by spatially varying material properties and irregular geometric conditions [EHL 02]. The mixed finite elements shown in Figure 8.1 employ equal-order interpolation for displacement and pressure fields (bilinear for 2D and trilinear for 3D), which work well under normal drainage loading conditions, but they could produce problematic pressure oscillations in the limit of full saturation and undrained loading. This numerical instability is well known and can be attributed to the failure of the equal-order pair to satisfy the discrete LBB condition [BRE 90]. A technique based on polynomial pressure projection has been shown to work for Stokes and Darcy equations [BOC 06a, BOC 06b, DOH 04], as well as for coupled solid deformation-fluid diffusion problems involving full and partial

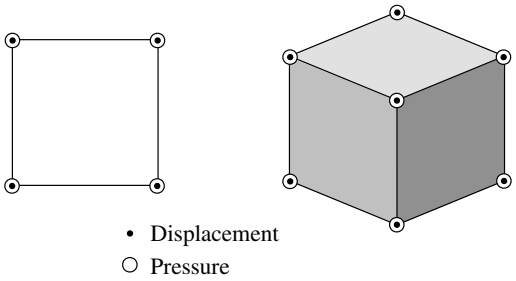

Figure 8.1. *Stabilized low-order mixed finite elements for coupled solid-deformation/fluid-diffusion: four-node quadrilateral for 2D (left) and eight-node hexahedral for 3D (right). After [BOR 10, WHI 08]*

saturation [BOR 10, WHI 08]. The stabilized hexahedral mixed element shown in Figure 8.1 is used in the 3D simulations described in the next section.

8.5. Numerical example

We consider an earthen embankment loaded by an upstream reservoir (Figures 8.2 and 8.3). The embankment has a somewhat complicated 3D structure due to its siting in a shallow valley. Parallel to the y-axis, the embankment spans the valley with a 4H:1V slope. Parallel to the x-axis, the upstream and downstream faces of the embankment have a 3H:2V slope. At its deepest point, the embankment is 6 m tall. We remark that in this case it would likely be insufficient to model just a 2D slice through the centerline of the structure. The geometry implies that both the fluid flow and deformation may deviate significantly from any sort of plane-flow, plane-strain assumptions.

The structure is founded on rigid, impermeable bedrock, and therefore, no-slip, no-flux boundary conditions are assigned at these faces. From the inherent symmetry in the problem, it is only necessary to model half of the domain. On the symmetry plane, we assign no-normal-displacement and no-flux boundary conditions. A convenient consequence of modeling only half the domain is that we can immediately view a cross-section of the solution through the centerline of the embankment. For the grid, we use low-order Lagrangian hexahedra. Note that for clarity Figure 8.3 only presents a rough version of the gridding, while the actual computations were run on a more refined grid.

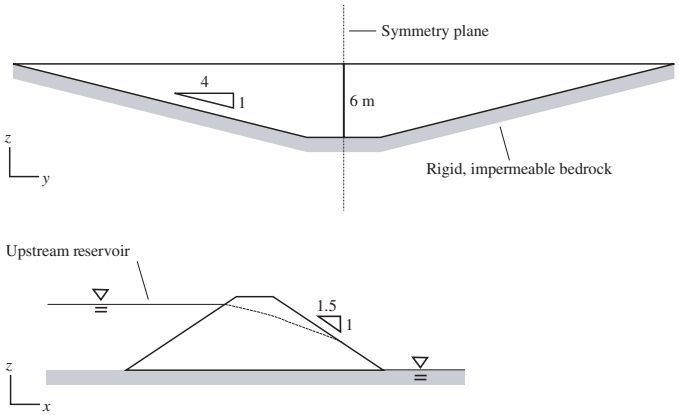

Figure 8.2. *Geometry and boundary conditions for a 3D embankment analysis*

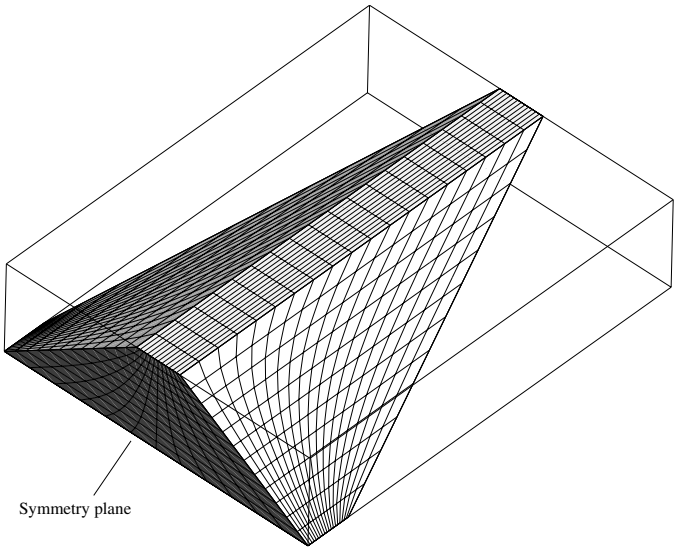

Figure 8.3. *Grid used for the embankment analysis. From symmetry, only half the domain is discretized. For clarity, only a rough version of the grid is shown*

The actual grid has 54,000 elements and 234,484 total degrees of freedom (175,863 displacement degrees and 58,621 pressure degrees). The grid has a structured topology, though of course more general unstructured grids could also be considered.

The soil in the embankment is modeled using a non-associative Drucker–Prager elastoplasticity model. The Drucker–Prager model uses a two-invariant, pressure-dependent yield surface that can be thought of as a smoothed version of the classic Mohr–Coulomb model. To calibrate the yield surface and plastic potential, three parameters are required: the soil cohesion, friction angle, and dilatancy angle. All three may be determined from standard laboratory tests. For simplicity we ignore any hardening or softening behavior in the cohesive or frictional behavior. Inside the yield surface, linear elastic behavior is defined using a bulk modulus and Poisson's ratio for the soil. We remark that while the Drucker–Prager model is simple to calibrate and is sufficient for our purposes here, it ignores many features of typical soil behavior that can be captured by more sophisticated models. For example, a cap model limiting the elastic region on the compression side could lead to a yield stress that depends on the suction stress [ALO 90, GAL 03, KHA 04, NUT 08]. Drucker–Prager

plasticity, however, is appropriate for yielding on the dilative side where the influence of suction on the yield stress may not be as apparent. Still, even though the yield stress for such material does not depend directly on suction, the constitutive model itself is expressed in terms of the proposed effective stress that depends on the capillary pressure.

We refer the interested reader to the extensive literature on soil constitutive modeling, including several valuable contributions on unsaturated soils in this book. For the flow response, the model requires relative-permeability and saturation relationships, for which we use a Van Genuchten [VAN 80] model. These relationships are plotted in Figure 8.4. For ease of reference, all of the model parameters are collected in Table 8.1.

We now consider the water table behavior on either side of the embankment. On the downstream side, the water table is fixed at $z = 0$ m,

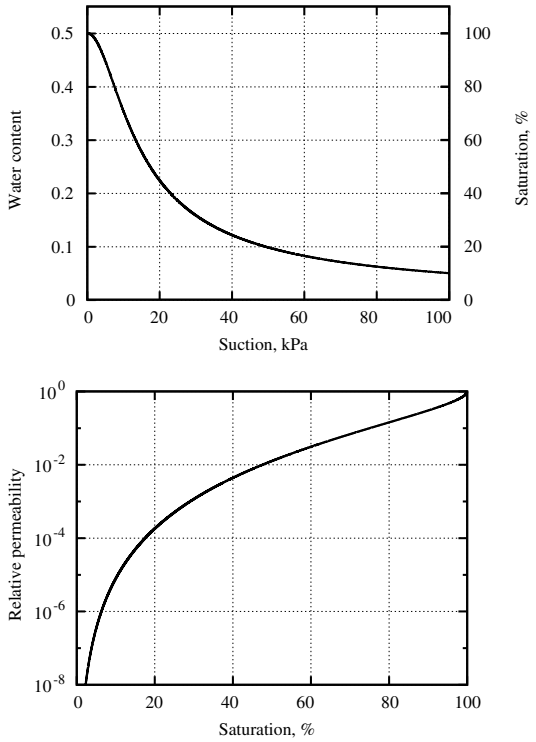

Figure 8.4. *Suction/saturation and saturation/relative permeability relationships for the embankment soil*

Porosity	$1 - \phi^{\mathrm{s}}$	0.5	—
Solid density	ρ_{s}	2.0	Mg/m^3
Fluid density	ρ_{w}	1.0	Mg/m^3
Bulk modulus	K	10.0	MPa
Poisson ratio	ν	0.2	—
Cohesion	c	2.0	kPa
Friction angle	ϕ	28.0	deg.
Dilatancy angle	ψ	10.0	deg.
Intrinsic permeability	k	10^{-12}	m^2
Dynamic viscosity	μ	10^{-6}	kPa·s
Residual saturation	ψ_1	0	—
Maximum saturation	ψ_2	1.0	—
Scaling suction	s_a	10.0	kPa
vG parameter	n	2.0	—
vG parameter	m	0.5	—

Table 8.1. *Model parameters used for the embankment example*

while on the upstream side the reservoir level $h(t)$ is allowed to vary with time. In particular, we assume the following variation of water elevation on the upstream side of the embankment:

$$h(t) = \begin{cases} 0 & t \leq 0 \\ 0.1t & 0 < t \leq 50 \\ 5.0 & 50 < t \leq 100 \\ 5.0 - 0.1(t - 100) & 100 < t \leq 150 \\ 0 & t > 150, \end{cases} \qquad [8.72]$$

where h is in meters and t is in hours. That is, the reservoir is initially empty, but is slowly raised to 5 m over 50 h, after which it is held constant for another 50 h before being drained again. The changing reservoir conditions will lead to complicated infiltration and exfiltration conditions on both upstream and downstream faces of the structure, as well as changing traction conditions on the upstream face.

At the beginning of the simulation, the embankment is assigned a hydrostatic pressure profile, consistent with water table level on either side. The entire embankment is therefore unsaturated, with a capillary fringe determined by the suction/saturation model. To determine the initial geostatic stress state, the soil is first allowed to consolidate under its own self-weight during a gravity-loading phase. With the initial stress state computed, the displacements are then reset to zero and the coupled hydromechanical portion

of the simulation begins. All time-integration calculations were carried out using the backward implicit scheme.

First, we examine the hydrologic response. Figure 8.5 shows snapshots of the saturation profile within the embankment at several timesteps. As the water level in the reservoir rises over the first 50 h, the upstream face of the embankment saturates and a wetting front gradually moves toward the downstream toe. Because the water table on the downstream side is held fixed, a seepage face eventually forms to accommodate the flux through the dam. The time-scale of loading is too short, however, for a steady-state profile to develop. At 100 h, the reservoir is drawn down and we observe a lowering of the phreatic surface. The drawdown is too rapid, however, for the phreatic surface to remain in equilibrium with the upstream reservoir level, and we observe the formation of a second seepage face on the upstream side of the dam. Over the course of the drawing, the height of the downstream seepage face also continues to grow. This simulation illustrates the complicated boundary conditions that may be encountered in a typical application, with exterior faces switching back and forth between fixed pressure and fixed flux depending on the external loading and internal pressure state. Also note that the saturation contours are fully 3D, due to interaction with the sloping valley floor. Indeed, there is significant flow convergence due to this geometry.

We now consider the solid response. Note that the upstream reservoir has a variety of effects on the soil in the embankment. As just noted, the hydrostatic pressure of the reservoir determines the fluid pressure condition at the upstream interface. This leads to increasing positive pressures in the embankment, which in turn reduce the effective stress in the soil skeleton. Also, recall that the effective density of the soil changes with saturation, as the skeleton begins to experience buoyant forces. These effects combine to lower the shear resistance of the soil. However, the weight of the reservoir exerts a normal (total) traction on the upstream face, which ensures that the soil remains stable. The importance of this normal traction is seen as soon as the reservoir is drawn down. When the reservoir level drops, the weakened soil in the dam is no longer properly confined and we observe the initiation of a slope failure. Figure 8.6(a) illustrates contours of equivalent plastic strain at 133 h, in which we see the beginning of shear localization at the base, which gradually grows upward. The potential for shear localization is also seen when plotting the scaled localization function [RUD 75] (Figure 8.6(b)). In the vicinity of

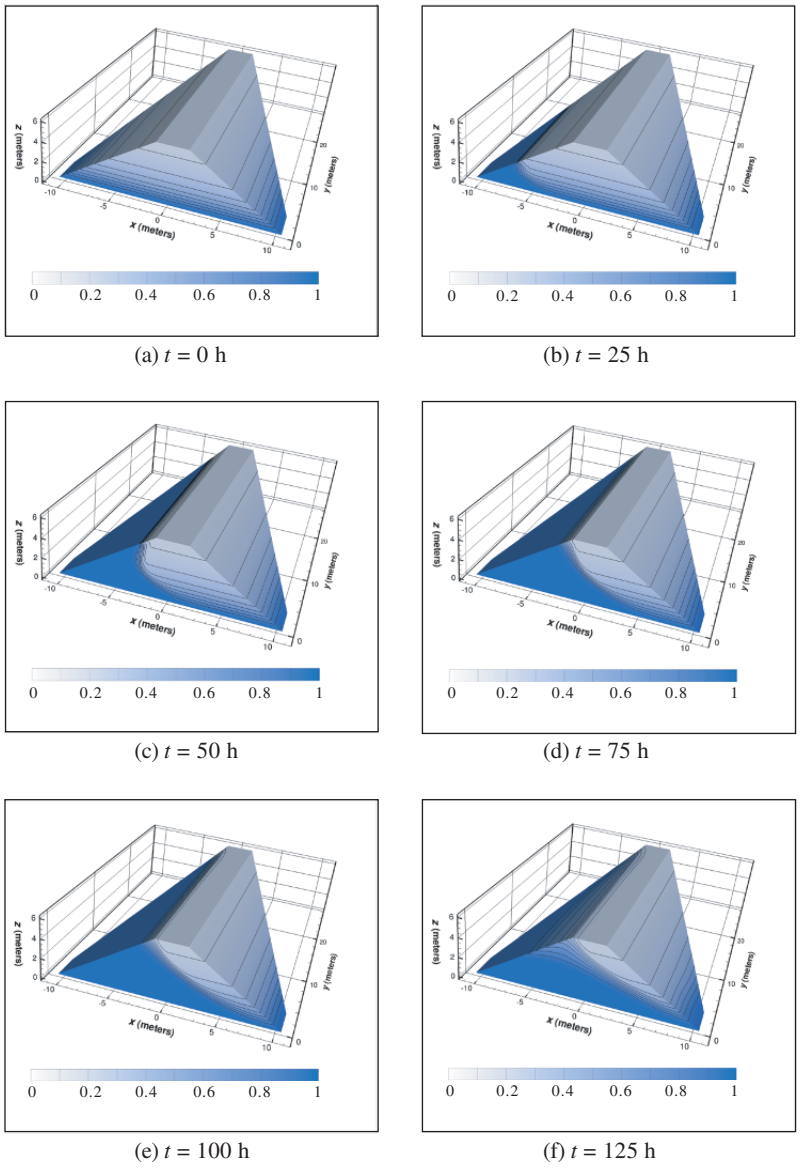

(a) $t = 0$ h (b) $t = 25$ h

(c) $t = 50$ h (d) $t = 75$ h

(e) $t = 100$ h (f) $t = 125$ h

Figure 8.5. *Snapshots of saturation contours in the embankment over the course of the simulation. Grayscale bar is the degree of saturation in decimals*

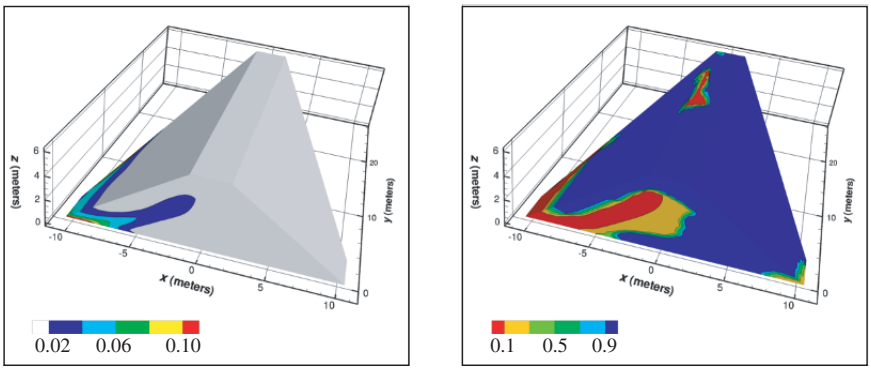

(a) Equivalent plastic strain (b) Scaled localization function

Figure 8.6. *Contours of: (a) equivalent plastic strain in percent and (b) scaled localization function at $t = 133$ h, showing the formation of an incipient failure surface on the upstream face due to the reservoir drawdown*

the shear band the localization function approaches the zero-threshold value for bifurcation and loss of stability. The use of the localization function is also interesting because it reveals other zones of weakness that are not immediately apparent from the plastic strain contours. Indeed, we observe the potential for shear localization at the downstream toe and near the far edge of the valley. Immediately after the 133-h mark, a complete slip surface formed and a global collapse occurred. Note that the soil at the shallower edges of the valley is not subject to the same level of forcing as the deeper central portion and remains stable. As a result, the failure surface has a complicated 3D structure.

Although we have not considered this case here, it is also important to consider what might happen if the reservoir was kept at full height and the growth of the seepage face at the toe was allowed to continue. The downstream face is always unconfined and we might eventually observe a slope failure on this face instead. The current embankment design does not contain any toe drains or a central core that might mitigate this effect.

It is interesting to compare the current analysis with more traditional slope stability methods. Perhaps the most obvious advantage is that it is fully 3D, while many simplified approaches require us to examine a representative 2D slice. Second, it rigorously accounts for unsaturated flow and effective stress behavior. The scaling of the suction/saturation relationship used

in this example is such that the embankment possesses a relatively large capillary fringe above the zero-pressure contour, and this vadose zone plays an important role in mechanics of the problem. Third, the simulation accounts for a tight-coupling between solid and fluid response. In principle, however, we could adopt an uncoupled analysis approach – first using a seepage simulation to predict a phreatic contour, and then a stress-deformation or method-of-slices analysis to examine the slope stability subject to the (now-fixed) pressure field. While we might be able to obtain a conservative estimate of the slope stability using this approach, it would ignore much of the time-dependent nature of the problem and any feedback effect of the solid deformation on the fluid flow. By necessity, such an uncoupled analysis must also make a variety of simplifying assumptions about the effective stress response, whereas the coupled model can accomodate much more sophisticated constitutive assumptions about the unsaturated soil behavior. Of course, there are disadvantages to the fully-coupled approach. The simulations are computationally more expensive, though growing computer power and intelligent solver design can mitigate much of this concern. Also, a more sophisticated model generally requires more material parameters that must be calibrated from experiments. Finally, it is difficult to assign a single metric of performance like factor-of-safety to such an analysis, which is an appealing concept from a design and practice point of view. Nevertheless, none of these disadvantages is severe, and they are perhaps the price of a more meaningful representation of the underlying physics.

8.6. Summary and conclusions

We have presented conservation laws governing the hydro-mechanical processes in unsaturated porous media using continuum mixture theory. From the first law of thermodynamics, we have identified a complete effective stress measure appropriate for constitutive modeling of the solid matrix. We have used this effective stress measure for stating the initial boundary-value problem for coupled solid deformation-fluid diffusion in unsaturated porous media, and for numerical implementation of the conservation laws based on mixed finite element formulation. We have investigated the low-order quadrilateral elements in 2D and hexahedral elements in 3D employing equal order interpolation of displacement and pore pressure fields, identified their stability (or lack of it) properties in the regime of full saturation and undrained loading, and introduced stabilization schemes so that these elements may be used effectively for the simulation of boundary-value problems for the entire

range of drainage and saturation conditions. The 3D numerical example presented in this chapter illustrates well the advances in large-scale simulation of coupled solid deformation-fluid diffusion analysis employing the proposed mixed finite element technique, as well as illustrates the potential challenges for accommodating more complex conditions including large deformation and more elaborate constitutive models for application to unsaturated porous media problems.

8.7. Acknowledgements

This work is supported by the US National Science Foundation under Contract Numbers CMMI-0824440 and CMMI-0936421 to Stanford University. Portions of this work were performed under the auspices of the U.S. Department of Energy by Lawrence Livermore National Laboratory under Contract DE-AC52-07NA27344. The second author is grateful for the support of the Lawrence Postdoctoral Fellowship Program.

8.8. Bibliography

[ALO 90] ALONSO E.E., GENS A., JOSA A., "A constitutive model for partially saturated soils", *Géotechnique*, vol. 40, p. 405–430, 1990.

[AND 07] ANDRADE J.E., BORJA R.I., "Modeling deformation banding in dense and loose fluid-saturated sands", *Finite Elements in Analysis and Design*, vol. 43, p. 361–383, 2007.

[BIS 59] BISHOP A.W., "The principle of effective stress", *Teknisk Ukeblad*, vol. 39, p. 859–863, 1959.

[BOC 06a] BOCHEV P.B., DOHRMANN C.R., GUNZBURGER M.D., "Stabilization of low-order mixed finite elements for the Stokes equations", *SIAM Journal for Numerical Analysis*, vol. 44, p. 82–101, 2006.

[BOC 06b] BOCHEV P.B., DOHRMANN C.R., "A computational study of stabilized, low-order C^0 finite element approximations of Darcy equations", *Computational Mechanics*, vol.38, p. 323–333, 2006.

[BOR 04] BORJA R.I., "Cam-Clay plasticity, Part V: A mathematical framework for three-phase deformation and strain localization analyses of partially saturated porous media", *Computer Methods in Applied Mechanics and Engineering*, vol. 193, p. 5301–5338, 2004.

[BOR 06] BORJA R.I., "On the mechanical energy and effective stress in saturated and unsaturated porous continua", *International Journal of Solids and Structures*, vol. 43, p. 1764–1786, 2006.

[BOR 09] BORJA R.I., KOLIJI A., "On the effective stress in unsaturated porous continua with double porosity", *Journal of the Mechanics and Physics of Solids*, vol. 57, p. 1182–1193, 2009.

[BOR 10] BORJA R.I., WHITE J.A., "Continuum deformation and stability analyses of a steep hillside slope under rainfall infiltration", *Acta Geotechnica*, vol. 5, p. 1–14, 2010.

[BRE 90] BREZZI F., "A discourse on the stability conditions for mixed finite element formulations", *Computer Methods in Applied Mechanics and Engineering*, vol. 82, p. 27–57, 1990.

[CEL 90] CELIA M., BOULOUTAS E., ZARBA R., "A general mass-conservative numerical solution for the unsaturated flow equation", *Water Resources Research*, vol. 26, p. 1483–1496, 1990.

[DOH 04] DOHRMANN C.R., BOCHEV P.B. "A stabilized finite element method for the Stokes problem based on polynomial pressure projections", *International Journal for Numerical Methods in Fluids*, vol. 46, p. 183–201, 2004.

[EHL 02] EHLERS W., AMMANN M., DIEBELS S., "h-Adaptive FE methods applied to single-and multiphase problems", *International Journal of Numerical Methods and Engineering*, vol. 54, p. 219–239, 2002.

[GAL 03] GALLIPOLI G., GENS A., SHARMA R., VAUNAT J., "An elasto-plastic model for unsaturated soil incorporating the effects of suction and degree of saturation on mechanical behavior", *Géotechnique*, vol. 53, p. 123–135, 2003.

[HOO 97] HOULSBY G.T. "The work input to an unsaturated granular material", *Géotechnique*, vol. 47, p. 193–196, 1997.

[KHA 04] KHALILI N., GEISER F., BLIGHT G.E., "Effective stress in unsaturated soils: review with new evidence", *International Journal of Geomechanics*, vol. 4, p. 115–126, 2004.

[LAM 69] LAMBE T.W., WHITMAN R.V., *Soil Mechanics*, New York, John Wiley, 1969.

[LU 04] LU N., LIKOS W.J., *Unsaturated Soil Mechanics*, Hoboken, NJ, John Wiley, 2004.

[NUR 71] NUR A., BYERLEE J.D., "An exact effective stress law for elastic deformation of rock with fluids", *Journal of Geophysical Research*, vol. 76, p. 6414–6419, 1971.

[NUT 08] NUTH M., LALOUI L., "Effective stress concept in unsaturated soils: Clarification and validation of a unified framework", *International Journal for Numerical and Analytical Methods in Geomechanics*, vol. 32, p. 771–801, 2008.

[RIC 31] RICHARDS L.A., "Capillary conduction of liquids in porous mediums", *Physics*, vol. 1, p. 318–333, 1931.

[RUD 75] RUDNICKI J.W., RICE J.R., "Conditions for the localization of deformation in pressure-sensitive dilatant materials", *Journal of the Mechanics and Physics of Solids*, vol. 23, p. 371–394, 1975.

[SCH 84] SCHREFLER B.A., The finite element method in soil consolidation (with applications to surface subsidence), PhD Thesis, University College of Swansea, C/Ph/76/84, 1984.

[SKE 61] SKEMPTON A.W., "Effective stress in soils, concrete and rocks", *Pore Pressure and Suction in Soils*, London, Butterworths, pp. 4–16, 1961.

[TER 43] TERZAGHI K., *Theoretical Soil Mechanics*, New York, NY, John Wiley, 1943.

[VAN 80] VAN GENUCHTEN M.T., "A closed-form equation for predicting the hydraulic conductivity of unsaturated soils", *Soil Science Society of America Journal*, vol. 44, p. 892–898, 1980.

[WHI 08] WHITE J.A., BORJA R.I., "Stabilized low-order finite elements for coupled solid-deformation/fluid-diffusion and their application to fault zone transients", *Computer Methods in Applied Mechanics and Engineering*, vol. 197, p. 4353–4366, 2008.

[WHI 09] WHITE J.A., Stabilized Finite Element Methods for Coupled Flow and Geomechanics, PhD Thesis, Stanford University, Stanford, California, 2009.

Chapter 9

Strain Localization Modeling in Coupled Transient Phenomena

9.1. Introduction

In many civil engineering problems (in a broad sense), the rupture of the foundation soil may be the relevant phenomenon for the global stability of a structure. For geomaterials, experimental observations clearly show localized ruptures [DES 96]. Some authors [KHO 06] also refer to diffuse mode of failure (which means homogenous failure in laboratory tests). In the first case, the phenomenon is preceded by progressive strain localization within thin bands, finally leading to rupture lines. It is thus very important to be able to numerically model the post-localization behavior of geomaterials for applications such as the evaluation of bearing capacity, slope stability, or damage zone around a tunnel. Furthermore, soils and rocks are porous materials, where the porous volume is filled with one or several fluids (water, gas, oil, etc.). The general behavior of the medium not only depends on the skeleton response (solid phase) to a given loading path, but also on the interactions occurring between the different phases of the medium. Capillary effects, temperature variations, and chemical reactions induce specific behaviors, which have to be modeled by multiphysical constitutive laws. It has been shown that these latter laws share a similar structure [COL 05]. The numerical tools for the modeling of post-failure problems

---

Chapter written by Frédéric COLLIN, Yannick SIEFFERT and René CHAMBON.

must thus be extended to this multiphysical context, to deal with the applications related to nuclear waste disposal and concrete behavior under severe loading. Then, new questions arise concerning the interactions between localization process and physical process (e.g. liquid diffusion). The answer to these new questions can only be given by experimental evidences. Section 9.2 of this chapter will summarize the main observations on localization phenomenon, from the experimental results. Section 9.3 is related to the theoretical tools devoted to localization process. Section 9.4 presents the description of the coupled second gradient model, which is the regularization technique used for the application described in section 9.5. Lastly, some conclusions are presented in section 9.6.

9.2. Experimental evidence

During the last 20 years, numerous experimental works have been devoted to the study of strain localization in soils and rocks. These studies performed by Vardoulakis *et al.* [HAN 91, VAR 78], Finno *et al.* [FIN 96, FIN 97], Desrues *et al.* [DES 84, DES 04], among the others, have mainly focused on the purely mechanical problem (dry sample or globally drained at low strain rate) or the hydromechanical problem (undrained or globally drained at fast strain rate). The study of the evolution of strain localization processes during the experiment needs special techniques, such as stereophotogrammetry, 3D digital image correlation, or X-ray micro tomography [LEN 07]. Thus, as in triaxial experiment (and more generally, in axisymmetric tests), the localization zone may remain more or less hidden inside the sample, and most of the experimental campaigns on localization have been performed in biaxial apparatus, where this latter process is "clearly" evidenced.

The main conclusions of the experimental works can be summarized as follows [DES 05]:

– Strain localization in shear band mode can be observed in most of the laboratory tests leading to rupture in geomaterials.

– Complex localization patterns may be the result of specific geometrical or loading conditions.

– Well-marked stress peaks in stress-strain curves can be considered as the signature of an established shear band system over the specimens (Figure 9.1).

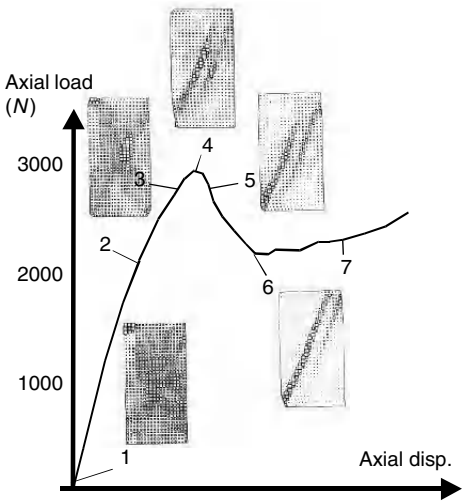

Figure 9.1. *Drained biaxial test on Hostun sand (after [MOK 99])*

When compared with pure mechanical experiments (on dry sample), hydromechanical experiments introduce another physical phenomenon (i.e. the fluid diffusion) that can influence the localization processes. This latter potential interaction depends, of course, on the (mechanical and diffusive) material properties, as well as on the boundary conditions of the problem. For drained conditions (if the value of the permeability is sufficiently low with respect to the velocity of the loading), the interactions are non-existent as long as no overpressures are generated, and the experimental observations are equivalent to those corresponding to dry conditions. For undrained conditions, overpressures are generated and some interactions exist between the two processes. It should be pointed out that in the laboratory, the boundary conditions that can be prescribed correspond to globally undrained conditions and not to locally undrained ones. This means that even in undrained conditions, some fluid flows can be created. The undrained experiments performed in Grenoble ([MOK 99, ROG 98]), among the others, have shown some common features and have led to the following observations:

– Plane strain undrained tests performed on loose and dense Hostun sand exhibit localization pattern.

– For dense (dilatant) sand specimen, localization is possible only when cavitation occurs in the pore fluid.

This last observation clearly shows evidence of the interaction between the localization and fluid diffusion, as long as the diffusion processes inhibit localization before cavitation within the pore volumes. Such phenomenon should thus be addressed both theoretically and numerically in a robust modeling of the rupture.

Experimental studies on strain localization in other multiphysical context (unsaturated conditions, thermomechanical, chemomechanical, etc.) are rather poor, and there is clearly a need for further investigations. It is indeed important to know whether the temperature or suction influence the occurrence of localization and the size of the process zone.

9.3. Regularization techniques

The experimental results show that shear band formation can occur in geomaterials for many loading conditions. The constitutive laws devoted to the modeling of their behavior must be able to reproduce such phenomenon. The principal questions are thus the following: how could we know if the constitutive model can predict a strain localization mode, and if this bifurcation occurs, how could we model it properly?

Following the previous works by [HAD 03], [HIL 58] and [MAN 66], Rice *et al.* [RIC 76, RUD 75] proposed the so-called Rice criterion, which analyzes the stress state and investigates the possibility of a bifurcation by the formation of a shear band in the stress and strain paths, for incrementally linear behavior. This criterion can be given as:

$$\det(nCn) \leq 0. \qquad [9.1]$$

In the case of a classical single-mechanism elastoplastic model, it has been proved that the previous criterion holds, provided C is chosen as the constitutive tensor corresponding to plastic loading [CHA 86].

These developments are valid for pure mechanical analysis. In a multiphysical context, Loret *et al.* [LOR 91] showed that for hydromechanical problems, the condition of localization depends only on the drained properties of the medium. Nevertheless, it should be emphasized that in coupled problems, much more complex localization pattern can be obtained, at least theoretically (Figure 9.2; [VAR 96] assumed an incrementally linear constitutive equation).

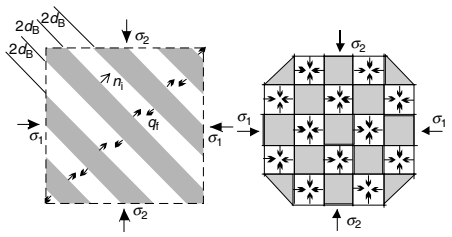

Figure 9.2. *Shear banding mode in water-saturated sand ("Dark" strips contract and "light" strips dilate) [VAR 96]*

Rupture in localized mode is observed experimentally; theoretical tools make it possible to characterize it when the conditions of occurrence of such phenomenon are met. A further step is to define a correct and robust modeling of strain localization, finally leading to rupture. However, it is well known that classical finite element models suffer from a pathological problem of mesh dependency for strain localization modeling. This is due to the properties of the underlying mathematical problem. In order to put this deficiency of classical tools in evidence, let us consider a very simple 1D problem of a constant section bar under uniaxial tension (Figure 9.3), made of a material with a very simple constitutive law (Figure 9.4(a)). This law may be the result of an elastic damage model or a strain softening elastoplastic model. It should be pointed out that the following discussion is also valid for a material layer under shear (replacing normal stress by shear stress).

When submitted to an axial displacement, the load-displacement curve remains linear up to the stress state reaching the yield stress f_y. After this point, the axial stress decreases, but according the static equilibrium condition, should remain homogenous all along the bar. For each point of the bar, two options exist: either the softening loading or the elastic unloading. Let us define α as the ratio of the length L_s (where we have softening loading) over L. For α=1, the load will decrease linearly down to zero for $\Delta=L\varepsilon_r$. For a limit case (α=0), the load will decrease linearly down to zero at the origin without energy consummation (Figure 9.4(b)). *A priori*, with classical numerical model, the length L_s is undetermined, and as far as the problem is ill-posed, we observe a mesh dependency of the response of the model. For an algorithm finding the most localized solution, L_s will be equal to the size of the smallest element: if the number of elements is increasing, the ratio α will tend to be zero! The situation is even worse

when considering the complete initial boundary value problem (see [KOT 08]).

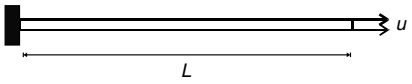

Figure 9.3. *Constant section bar under uniaxial tension*

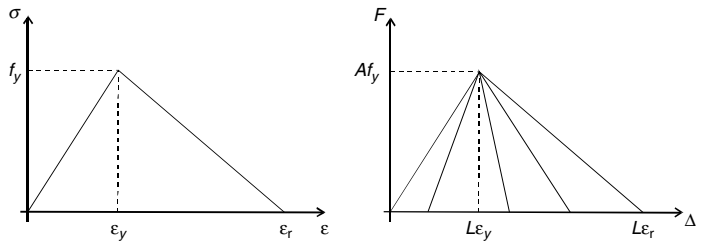

Figure 9.4. *Local and global behavior of the bar*

This simple example proves the need for an internal length scale for the correct modeling of the post-peak behavior. Several approaches have been proposed to introduce such an internal length scale in the problem. We can distinguish two categories of regularization techniques:

(1) Enrichment of the constitutive law

The theory introduces an internal length scale at the level of the constitutive model. The advanced analysis of the localization phenomena has shown that constitutive equations with internal length are necessary to properly model the experimental results involving some localized patterns: see, for instance, the pioneering works of Aifantis [AIF 84], which introduced gradient of internal variables, or the works of Bazant, Pijaudier-Cabot *et al.* [BAZ 84, PIJ 87], which proposed a family of constitutive models derived from non-local damage theory in which a non-local internal variable was used instead of the local one. This latter theory has also generated the implicit gradient models [PEE 96], where the non-local internal variable is an additional unknown and a solution of the Helmoltz differential equation.

(2) Enrichment of the kinematics

The theories based on an enhancement of the kinematics can be traced back to the pioneering works of [TOU 62], [MIN 64] and [GER 73]. Here, we consider the materials with microstructure as defined by [MIN 64] and [GER 73]. Adding some mathematical constraints to the more general materials with microstructure yields a large set of models. Among all these models, the more ancient and famous one is the Cosserat model [COS 09]. In the following, we will mainly use the second gradient model developed in Grenoble [CHA 98, CHA 01], but the obtained conclusions can be generalized to other regularization techniques.

The extension of these regularization techniques to multiphasic materials and multiphysical problems leads to the question of the interactions between the physical problems and the localization process. Loret *et al.* have shown that diffusion equation (fluid or thermal) introduces an internal length scale [LOR 91]. Zhao, Schrefler *et al.* [ZHA 99], [ZHA 01] studied the potential interaction between the different lengths. They showed that the interaction between the different phenomena could appear for a given range of parameters; nevertheless, a robust mechanical model is still needed even for coupled problems.

9.4. Numerical modeling

Among the different regularization techniques, we have proposed the following to use the second gradient model [CHA 98, CHA 01]. The second grade model is extended to biphasic medium [COL 06] in order to show the possible interaction between the internal lengths introduced by the model and the diffusion process. In this model, the porous medium is considered as the superposition of several continua [COU 95]: the solid skeleton (grain assembly) and the fluid phases (water, air, oil, etc.). Based on the averaging theories [HAS 79a, HAS 79b, LEW 00], the governing equations for the full dynamic behavior of a partially saturated porous medium have been proposed. Hereafter, these equations will be restricted to quasi-static problem in unsaturated conditions, under Richard's assumptions (constant air pressure). This assumption may be irrelevant in the particular case of low and ultra-low permeable porous media. For this study, isothermal condition and incompressible solid grains are assumed. The unknowns of the mechanical and flow problems are the displacements u_i and the pore water

pressure p_{w} (possibly negative in unsaturated case), respectively. In the following developments, the balance equations are written in the current solid configuration denoted as Ω^t (updated Lagrangian formulation).

9.4.1. *Momentum balance equation*

In the mixture balance of momentum equation, the interaction forces between fluid phases and grain skeleton get canceled. In a weak form (virtual work principle), the following equation can be employed for any kinematically admissible virtual displacement field:

$$\int_{\Omega^t} \sigma_{ij}^t \varepsilon_{ij}^* \mathrm{d}\Omega^t = \int_{\Omega^t} \left(\rho_{\mathrm{s}}(1-\phi^t) + S_{\mathrm{r,w}}^t \rho_{\mathrm{w}}^t \phi^t \right) g_i u_i^* \mathrm{d}\Omega^t + \int_{\Gamma_\sigma^t} \overline{t}_i^t u_i^* \mathrm{d}\Gamma^t, \qquad [9.2]$$

where $\varepsilon_{ij}^* = 0.5\left(\left(\partial u_i^* / \partial x_j^t\right) + \left(\partial u_j^* / \partial x_i^t\right)\right)$, is the kinematically admissible virtual strain field, ϕ^t the porosity defined as $\phi^t = \Omega^{v,t} / \Omega^t$, where Ω^t is the current volume of a given mass of skeleton and $\Omega^{v,t}$ the corresponding porous volume, ρ_{s} the solid grain density, $S_{\mathrm{r,w}}^t$ the water relative saturation, ρ_{w}^t the water density, g_i the gravity acceleration, and Γ_σ^t the part of the boundary where tractions $\overline{t}_i^t$ are known.

The total stress σ_{ij}^t is defined as a function of the kinematics. Here, we first assume that the Bishop's definition of effective stress holds [NUT 08]:

$$\sigma_{ij}^t = \sigma_{ij}'^t - S_{r,\mathrm{w}}^t p_{\mathrm{w}}^t \delta_{ij} \qquad [9.3]$$

with $\sigma_{ij}'^t$ being the effective stress, p_{w}^t representing the pore water pressure, and δ_{ij} denoting the Kronecker symbol.

9.4.2. *Mass balance equation*

The water mass balance equation in a weak form can be given as follows:

$$\int_{\Omega^t} \left(\dot{M}^t p_{\mathrm{w}}^* - m_i^t \frac{\partial p_{\mathrm{w}}^*}{\partial x_i^t} \right) \mathrm{d}\Omega^t = \int_{\Omega^t} Q^t p_{\mathrm{w}}^* \mathrm{d}\Omega^t - \int_{\Gamma_q^t} \overline{q}^t p_{\mathrm{w}}^* \mathrm{d}\Gamma^t, \qquad [9.4]$$

where p_{w}^{*} is the virtual pore water pressure field, Q^t a sink term, and Γ_q^t the part of the boundary where the input water mass per unit area $\overline{q}^t$ prescribed. M^t and m_i^t are the mass of the water inside the current configuration of the skeleton Ω^t and the mass flow, and are defined in equations [9.5] and [9.7], respectively.

Water mass balance equation (equation [9.4]) has to hold for any time t, and the virtual quantities in this equation are dependant on the history of the boundary conditions and time t.

The mass flow m_i^t is defined as follows:

$$m_i^t = -\rho_{\mathrm{w}}^t \frac{\kappa\, k_{r,\mathrm{w}}^t}{\mu_{\mathrm{w}}} \left(\frac{\partial p_{\mathrm{w}}^t}{\partial x_i^t} + \rho_{\mathrm{w}}^t g_i \right), \qquad [9.5]$$

where κ is the intrinsic permeability, $k_{\mathrm{r,w}}^t$ the water relative permeability, and μ_{w} the water dynamic viscosity.

The compressible fluid is assumed to respect the following relationship [LEW 00]. This predicts an increase in the water density as a function of the pore water pressure, defining χ_{w} as the water bulk modulus:

$$\dot{\rho}_{\mathrm{w}}^t = \frac{\rho_{\mathrm{w}}^t}{\chi_{\mathrm{w}}} \dot{p}_{\mathrm{w}}^t. \qquad [9.6]$$

If the grains are assumed to be incompressible (which means ρ_{s} is constant), then the time derivative of the water mass is obtained directly by using equation [9.6] and mass balance equation for the solid phase. This yields the following for a unit mixture volume:

$$\dot{M}^t = \rho_{\mathrm{w}}^t \left[\frac{\dot{p}^t}{\chi_{\mathrm{w}}} S_{\mathrm{r,w}}^t \phi^t + \dot{S}_{\mathrm{r,w}}^t \phi^t + S_{\mathrm{r,w}}^t \frac{\dot{\Omega}^t}{\Omega^t} \right]. \qquad [9.7]$$

9.4.3. *Local second gradient model for monophasic medium*

Let us first recall the governing equations of a monophasic medium with a microstructure. This kind of model can be traced back to the pioneering

works of the Cosserat brothers [COS 09, GER 73, MIN 64]. In the framework of microstructure continuum theory, a microkinematic gradient field v_{ij} is introduced to describe strain and rotation at the microscale. With respect to classical continuum mechanics, additional terms are then added in the internal virtual work of a given body [GER 73]. The following expression holds for any virtual quantities:

$$W_i^* = \int_{\Omega^t} \left(\sigma_{ij}^t \frac{\partial u_i^*}{\partial x_j^t} + \tau_{ij}^t (v_{ij}^* - F_{ij}^*) + \Sigma_{ijk}^t h_{ijk}^* \right) \mathrm{d}\Omega^t, \qquad [9.8]$$

where F_{ij}^* is the virtual macrodeformation gradient, v_{ij}^* the virtual microkinematic gradient, τ_{ij}^t, known as microstress, is an additive stress associated with the microstructure, h_{ijk}^* the virtual microsecond gradient, and Σ_{ijk}^t the double stress dual of h_{ijk}^*.

In the local second gradient model used, an assumption is included: the microkinematic gradient is equal to the macrodeformation gradient:

$$v_{ij} = F_{ij}. \qquad [9.9]$$

As a consequence: $v_{ij}^* = F_{ij}^*$. Finally, the principle of virtual work can be rewritten as follows:

$$W_i^* = \int_{\Omega^t} \left(\sigma_{ij}^t \frac{\partial u_i^*}{\partial x_j^t} + \sum\nolimits_{ijk}^t \frac{\partial^2 u_i^*}{\partial x_j^t \partial x_k^t} \right) \mathrm{d}\Omega^t. \qquad [9.10]$$

By assuming that the boundary Ω^t is regular, the external virtual work W_{e}^* can be defined as follows:

$$W_{\mathrm{e}}^* = \int_{\Omega^t} \rho g_i u_i^* \mathrm{d}\Omega^t + \int_{\Gamma_\sigma^t} \left(\overline{t}_i u_i^* + \overline{T}_i D u_i^* \right) \mathrm{d}\Gamma^t, \qquad [9.11]$$

where $\overline{t}_i$ is the external (classical) forces per unit area and $\overline{T}_i$ an additional external (double) force per unit area, both applied on a part Γ_σ^t of the boundary of Ω^t. D denotes the normal derivative of any quantity q ($Dq=(\partial q/\partial x_k)n_k$). To the authors' knowledge, the additional boundary condition (on $\overline{T}_i$) allows us to produce solutions with boundary layers.

One of the advantages of local second gradient is the fact that constitutive equations remain local, and therefore it is straightforward to formulate a second gradient extension of any classical models. The previous virtual work equation of second gradient models can, of course, be used in a finite element code. However, this equation needs the use of C^1 functions for the displacement field because second derivatives of the displacement are involved. In order to avoid such functions in the virtual work principle [9.10], the equalities between v_{ij}^* and F_{ij}^* and between v_{ij} and F_{ij} are introduced through a field of Lagrange multipliers λ_{ij} related to a weak form of the constraint [9.9] [CHA 98]:

$$\int_{\Omega^t}\left(\sigma_{ij}^t\frac{\partial u_i^*}{\partial x_j^t}+\sum\nolimits_{ijk}^t\frac{\partial v_{ij}^*}{\partial x_k^t}\right)\mathrm{d}\Omega^t-\int_{\Omega^t}\lambda_{ij}^t\left(\frac{\partial u_i^*}{\partial x_j^t}-v_{ij}^*\right)\mathrm{d}\Omega^t-W_{\mathrm{e}}^*=0, \qquad [9.12]$$

$$\int_{\Omega^t}\lambda_{ij}^*\left(\frac{\partial u_i^t}{\partial x_j^t}-v_{ij}^t\right)\mathrm{d}\Omega^t=0. \qquad [9.13]$$

9.4.4. *Local second gradient coupled model*

Starting from equations [9.2] and [9.4] of the coupled problem in classical poromechanics, microstructure effects can be introduced in the momentum balance equation by adding microkinematic gradient terms, under the previous assumptions $(v_{ij}^*=F_{ij}^*, v_{ij}=F_{ij})$. By assuming that the pore fluid has no influence at the microstructure level, microkinematic gradients are not generated by pore pressure variations. This latter hypothesis follows the ideas of Ehlers [EHL 98] concerning a Cosserat model for biphasic medium. Cosserat model [COS 09] is in fact a particular case of a microstructured medium.

According to the previous assumptions, we have the following governing equations:

$$\int_{\Omega^t}\left(\sigma_{ij}^t\frac{\partial u_i^*}{\partial x_j^t}+\sum\nolimits_{ijk}^t\frac{\partial^2 u_i^*}{\partial x_j^t\partial x_k^t}\right)\mathrm{d}\Omega^t=\int_{\Omega^t}\rho^{\mathrm{mix},t}g_i u_i^*\mathrm{d}\Omega^t+\int_{\Gamma_\sigma^t}\left(\overline{t}_i u_i^*+\overline{T}_i D u_i^*\right)\mathrm{d}\Gamma^t, \qquad [9.14]$$

$$\int_{\Omega^t}\left(\dot{M}^t p_{\mathrm{w}}^*-m_i^t\frac{\partial p_{\mathrm{w}}^*}{\partial x_i^t}\right)\mathrm{d}\Omega^t=\int_{\Omega^t}Q^t p_w^*\mathrm{d}\Omega^t-\int_{\Gamma_q^t}\overline{q}^t p_{\mathrm{w}}^*\mathrm{d}\Gamma^t, \qquad [9.15]$$

where $\rho^{\mathrm{mix},t}$ is the mass density of the mixture $\rho^{\mathrm{mix},t} = \rho(1-\rho^t) + S_{\mathrm{r}}^{\mathrm{w},t}\rho^{\mathrm{w},t}\phi^t$. By introducing Lagrange multiplier fields (as in the previous section), the governing equations of the local second gradient coupled problem can be given as follows:

$$\int_{\Omega^t}\left(\sigma_{ij}^t\frac{\partial u_i^*}{\partial x_j^t}+\sum\nolimits_{ijk}^t\frac{\partial v_{ij}^*}{\partial x_k^t}\right)\mathrm{d}\Omega^t-\int_{\Omega^t}\lambda_{ij}^t\left(\frac{\partial u_i^*}{\partial x_j^t}-v_{ij}^*\right)\mathrm{d}\Omega^t-W_{\mathrm{e}}^*=0, \qquad [9.16]$$

$$\int_{\Omega^t}\lambda_{ij}^*\left(\frac{\partial u_i^t}{\partial x_j^t}-v_{ij}^t\right)\mathrm{d}\Omega^t=0, \qquad [9.17]$$

$$\int_{\Omega^t}\left(\dot{M}^t p_{\mathrm{w}}^*-m_i^t\frac{\partial p_{\mathrm{w}}^*}{\partial x_i^t}\right)\mathrm{d}\Omega^t=\int_{\Omega^t}Q^t p_{\mathrm{w}}^*\mathrm{d}\Omega^t-\int_{\Gamma_i^t}\overline{q}^t p_{\mathrm{w}}^*\mathrm{d}\Gamma^t. \qquad [9.18]$$

In the present work, the stress tensor σ_{ij} in equation [9.16] is a total stress defined according to Bishop's postulate [9.3]; on the contrary, the double stress Σ_{ijk} has no link with the pore pressure.

Equations [9.16]–[9.18] have to hold for any time t, with the virtual quantities in these equations being dependant on the history of the boundary conditions and time t. Moreover, the constitutive equations also have to hold for any time t.

9.4.5. *Local second gradient model in a multiphysical context*

The procedure to extend the local second gradient model to other multiphysical contexts is more or less the same: additional balance equations appear to model the other processes. The main issue is not a numerical one, but rather a physical one. What are the possible interactions between the second gradient model and the thermal diffusion, suction or chemical reaction? These questions should be first addressed by the experimental campaign. With regard to the internal length introduced by the second gradient model, it has been found to be the ratio of two constitutive moduli (the one related to the second gradient constitutive law and the other related to the classical law). Considering that the classical constitutive moduli are influenced by the different processes (chemical, thermal, suction, etc.), it can be concluded that the internal length scale should be modified by these latter

processes (under the condition that the second gradient law is not influenced by the processes). This should again be confirmed by some experimental evidence!

9.5. Applications

The following example shows the interest of using the theoretical tools presented, but also points out their limitations. We have proposed to study a typical problem of nuclear waste disposal: the excavation of a storage gallery. It has been proposed to model the excavation process with a very simple strain-softening constitutive law capable of reproducing the main phenomena appearing during tunneling: the progressive decrease in material strength during loading and strain localization. This coupled modeling is a benchmark exercise proposed by the GDR-Momas and organized by EDF-CEA [CHA 05].

9.5.1. *Constitutive equation and localization study*

The proposed constitutive law is an elastoplastic strain-softening model. The yield criterion is a Drucker–Prager model given by the following equation:

$$F \equiv \sqrt{\frac{3}{2}} II_{\sigma^*} + m\left(I_\sigma - \frac{3c}{\tan\phi} \right) = 0, \qquad [9.19]$$

where II_{σ^*} is the second deviatoric stress invariant, I_σ the first stress invariant, ϕ the friction angle, parameter m a function of ϕ: $m=2\sin(\phi)/(3-\sin(\phi))$, the cohesion $c=c_0 f(\gamma^p)$ the softening variable, c_0 the initial cohesion, and γ^p the equivalent deviatoric plastic deformation.

For this single-mechanism elastoplastic law, the Rice criterion can be transformed into a fourth-order equation in $\tan(\theta)=z$, with θ being the angle between n and the x-axis, and a_i being the real parameters depending on the constitutive moduli:

$$(a_1 z^4 + a_2 z^3 + a_3 z^2 + a_4 z + a_5) = 0. \qquad [9.20]$$

At the beginning of loading, this equation does not have any real solution. After some load steps, the first real solution is a double one [WAN 93], which then gives two bifurcation directions.

In order to emphasize this theoretical concept with the proposed constitutive law, the homogenous response of a drained biaxial experiment is first studied to observe when the Rice condition is met (Figure 9.5). Moreover, different dilatancy angles are considered to study the effect of this parameter on the response of the material. For all the considered values, the Rice criterion is met during the loading path.

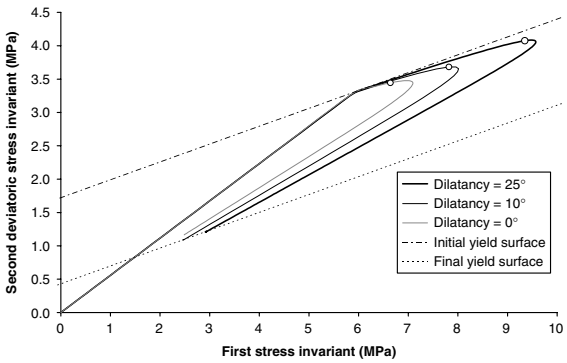

Figure 9.5. *Drained biaxial test response of the constitutive law for several dilatancy angles*

Figure 9.6 presents the evolution of the Rice criterion as a function of the loading history. When the behavior is elastic, the criterion exhibits only one minimum and is always positive. When the behavior becomes elastoplastic, the criterion exhibits two extrema, but remains positive up to a loading level, for which two symmetric directions of bifurcation are predicted. With the loading path going on, a fan of directions exists, where the Rice criterion is met.

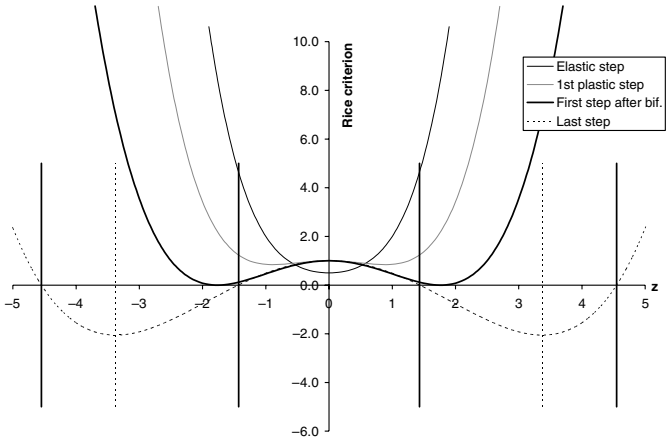

Figure 9.6. *Rice criterion (as a function of z) for several loading steps*

The numerical modeling of a perfect sample remains homogenous even if the Rice criterion is met. In reality, geomaterial samples have some heterogeneity, leading to localization processes. In order to numerically reproduce these processes, it is possible to introduce some defects (soft element, parasite force, etc.) to force the occurrence of localization (Figure 9.7). However, even in a perfect sample, it is possible to find localized solutions, using special techniques.

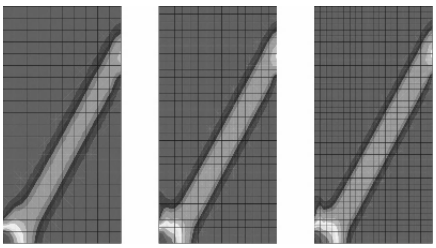

Figure 9.7. *Localized solution for non-perfect sample for different mesh size (dilatancy=25°)*

In a coupled context, the interactions between the mechanical behavior and the fluid diffusion can modify the conclusions of the results obtained for drained biaxial tests. Let us now consider undrained biaxial tests to prove the coupling effects.

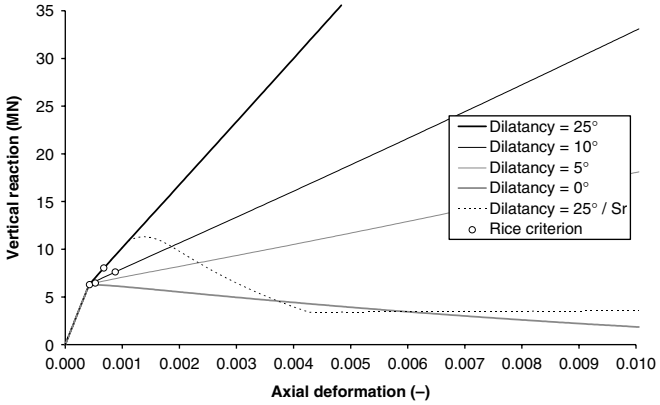

Figure 9.8. *Load vs. axial strain for undrained biaxial tests*

The results (Figure 9.8) show that for highly dilatant materials, the Rice criterion is never met (in this first modeling, it is assumed that the medium remains saturated even for negative pore pressure). This is in agreement with the experimental observations. When the dilatancy is lower (from 10° to 0°), the Rice criterion is met and localization is possible. In order to put the influence of the unsaturated conditions in evidence, a case with a dilatancy of 25° and a retention curve is performed: it is shown that the Rice criterion is met when the sample becomes unsaturated!

By introducing a defect in the structure, it is possible to obtain localized solutions when the Rice criterion is met. Figure 9.9 presents the plastic points in the localized solution for the case of a null dilatancy angle and when desaturation is taken into account. It is important to underline the fact that no localization is possible when the dilatancy is equal to 25° and the sample remains saturated.

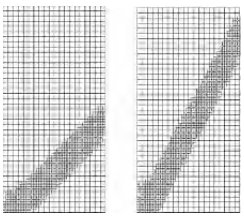

(a) *Dilatancy = 0°* (b) *Dilatancy = 25° and $S_r(s)$*

Figure 9.9. *Plastic loading points during undrained biaxial tests*

9.5.2. *Model predictions for the excavation problem*

A cylindrical unsupported cavity of 3 m diameter is located in a homogenous low permeability formation. The following is the initial state of stress and pore pressure:

$$\sigma'_{xx} = \sigma'_{zz} = -7.74\,\text{MPa} \quad \sigma'_{yy} = -11.64\,\text{MPa} \quad p_{\text{w}} = 4.7\,\text{MPa}.$$

The excavation process is modeled by decreasing both the radial total stress and pore pressure at the cavity wall. The excavation duration T is equal to 1.5 Ms (about 17 days) and the final modeling time is 300 Ms (about 9.5 years).

$$\text{at } r = 3m \begin{cases} 0 \le t \le T \\ \sigma_{xx} = \sigma'_{xx} - bp_{\text{w}} = -11.5\left(1 - \dfrac{t}{T}\right)\text{MPa} \\ \sigma_{yy} = \sigma'_{yy} - bp_{\text{w}} = -15.4\left(1 - \dfrac{t}{T}\right)\text{MPa} \\ p_{\text{w}} = 4.7\left(1 - \dfrac{t}{T}\right)\text{MPa} \\ t > T \\ \sigma_{xx} = \sigma_{yy} = p_{\text{w}} = 0 \end{cases} \quad \text{and} \quad \text{at } r = \infty \begin{cases} \sigma_{xx} = -11.5\,\text{MPa} \\ \sigma_{yy} = -15.4\,\text{MPa}. \\ p_{\text{w}} = 4.7\,\text{MPa} \end{cases}$$

During the excavation, the behavior of the material becomes plastic near the tunnel and permanent strains are created. The yield criterion is first met in the direction where the orthoradial stress is the major principal stress. The dilatancy effects are presented in Figure 9.10(a), where the pore pressure becomes negative at the end of tunneling. Subsequently, during the remaining modeling time, the pore pressure increases progressively. Figure 9.10(b) shows the radial displacement curve: during the tunneling phase, cavity convergence remains around 1.5 cm. Most of the convergence appears later and reaches 22.6 cm. Indeed, negative pore pressure allows an additional cohesive strength; this effect is maximum after 1.5 Ms and decreases progressively up to 300 Ms.

Shear band localization is also influenced by hydromechanical coupling. Indeed, at the end of excavation, there is no clear localization patterning

even if the Rice criterion is verified. After that phase, pore pressure increases progressively and a pattern is gradually created. Figure 9.11(a) presents a map of the equivalent strains, where the different shear bands clearly appear. Vilotte's indicator is shown in Figure 9.11(b); this indicator evidences the strain activity of the shear band. Here, we can see that only the external shear band is active at the end of the simulation and that a chip is finally created.

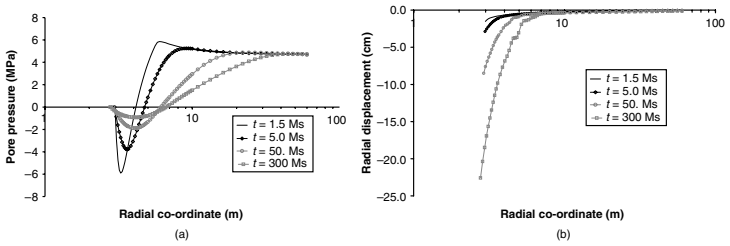

Figure 9.10. *Pore pressure and displacement curve during coupled excavation*

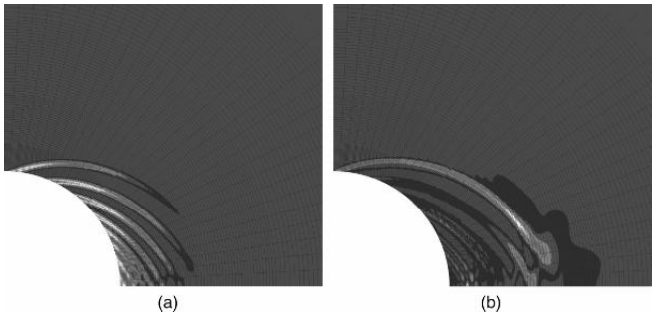

Figure 9.11. *Equivalent strain and Vilotte's indicator for active shear band (t=300 Ms) – Classical medium*

These results (Figure 9.11) have been obtained with classical finite elements and are thus mesh dependent. We propose to perform the same modeling with a coupled second gradient model. We see (Figure 9.12) that the results are independent of the mesh size. Though regularization techniques are a solution for this problem, it should be pointed out that these theories do not restore the uniqueness of the solution.

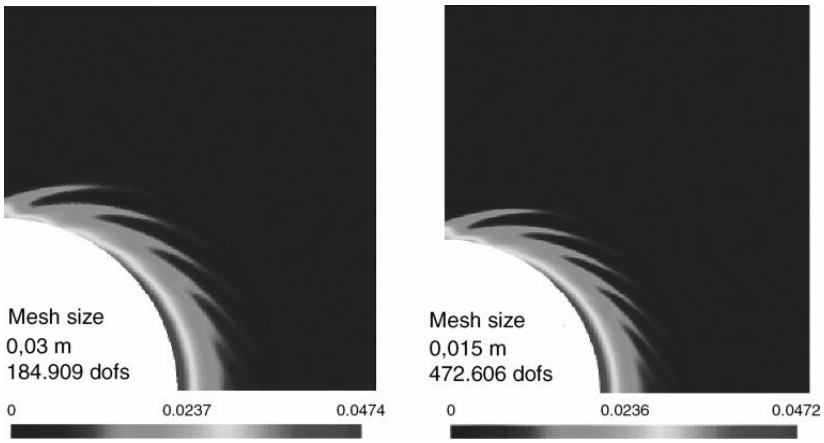

Figure 9.12. *Equivalent strain for two mesh sizes with second gradient dilation model [FER 09]*

9.6. Conclusions

Rupture in geomaterials is often preceded by a localization of the deformations within thin bands. Strain localization is thus an important process, which has been studied both experimentally and theoretically. The developments of geomechanics in the field of coupled multiphysical processes impose the study of strain localization to these new conditions, and interactions between the different processes can indeed occur.

The numerical modeling of shear bands with classical finite elements suffers from mesh dependency problem. An internal length scale has to be introduced in the problem. Among the different regularization techniques, we have proposed a second gradient coupled model for an application to gallery excavation. It has been shown that the model regularizes the solution, but does not restore the uniqueness (see [SIE 09]).

The extension of such theories to other multiphysical context is more of an experimental problem than a numerical one. Further experiments are needed to demonstrate the influence of temperature, suction, or chemical concentration on the occurrence and thickness of strain localization!

9.7. Acknowledgment

The authors are grateful to FNRS and EU (under the TIMODAZ project) for their financial support.

9.8. Bibliography

[AIF 84] AIFANTIS E.C., "On the microstructural origin of certain inelastic models", *Journal of Engineering Materials and Technology, ASME*, vol. 106, p. 326-330, 1984.

[BAZ 84] BAZANT Z.P., BELYTSCHKO T.B., CHANG T.P., "Continuum model for strain softening", *Journal of Engineering Mechanics, ASCE*, vol. 110, p. 1666-1692, 1984.

[CHA 86] CHAMBON R., "Bifurcation and shear band localization an approach for incrementally non linear constitutive equations", *Journal de Mécanique Théorique et Appliquée*, vol. 5, no. 2, p. 277-298, 1986.

[CHA 98] CHAMBON R., CAILLERIE D., EL HASSAN N., "One-dimensional localisation studied with a second grade model", *European Journal of Mechanics A/Solids*, vol. 17, no. 4, p. 637-656, 1998.

[CHA 01] CHAMBON R., CAILLERIE D., MATSUSHIMA T., "Plastic continuum with microstructure, local second gradient theories for geomaterials: localization studies", *International Journal of Solids and Structures*, vol. 38, p. 8503-8527, 2001.

[CHA 05] CHAVANT C., FERNANDES R., "Evaluating the reliability of hydro-mechanical simulation: a benchmark of numerical techniques carried out by Research Group of MoMas", *2nd International Meeting Clays in Natural & Engineered Barriers for Radioactive Waste Confinement, Tours*, 14-18 March, pp 249-250, 2005.

[COL 05] COLLIN F., LALOUI L., CHARLIER R., "Unified approach of coupled constitutive laws", ALERT Autumn School 2005, *Revue Européenne de Génie Civil*, vol. 9, nos. 5-6, p. 713-724, 2005.

[COL 06] COLLIN F., CHAMBON R., CHARLIER R., "A finite element method for poro mechanical modelling of geotechnical problems using local second gradient models", *International Journal for Numerical Methods in Engineering*, vol. 65, no. 11, p. 1749-1772, 2006.

[COS 09] COSSERAT E., COSSERAT F., *Théorie des Corps Déformables*, Paris, Hermann, 1909.

[COU 95] COUSSY O., *Mechanics of Porous Continua*, London, Wiley, 1995.

[DES 84] DESRUES J., La localisation de la déformation dans les matériaux granulaires, PhD thesis, Institut de Mécanique de Grenoble, 1984.

[DES 96] DESRUES J., CHAMBON R., MOKNI M., MAZEROLLES F., "Void ratio evolution inside shear bands in triaxial sand specimens studied by computed tomography", *Géotechnique*, vol. 46, no. 7, p. 529-546, 1996.

[DES 04] DESRUES J., VIGGIANI G., "Strain localization in sand: an overview of the experimental results obtaines in Grenoble using stereophotogrammetry", *International Journal for Numerical and Analytical Methods in Geomechanics*, vol. 28, no. 4, p. 279-321, 2004.

[DES 05] DESRUES J., "Hydro-mechanical coupling and strain localization in saturated porous media", ALERT Autumn School 2005, *Revue Européenne de Génie Civil*, vol. 9, nos. 5-6, p. 619-634, 2005.

[EHL 98] EHLERS W., VOLK W., "On theoretical and numerical methods in the theory of porous media based on polar and non-polar elasto-plastic solid materials", *International Journal of Solids and Structures*, vol. 35, p. 4597-4617, 1998.

[FER 09] FERNANDES R., Modélisation numérique objective des problèmes hydromécaniques couplés dans le cas des géomatériaux, PhD thesis, UJF Grenoble, 2009.

[FIN 96] FINNO R., HARRIS W., MOONEY M., VIGGIANI G., "Strain localization and undrained steady state of sands", *Journal of Geotechnical Engineering, ASCE*, vol. 122, no. 6, p. 462-473, 1996.

[FIN 97] FINNO R., HARRIS W., MOONEY M., VIGGIANI G., "Shear bands in plane strain compression of loose sand", *Géotechnique*, vol. 47, no. 1, p. 149-165, 1997.

[GER 73] GERMAIN P., "The method of virtual power in continuum mechanics. Part 2 Microstructure", *SIAM Journal on Applied Mathematics*, vol. 25, p. 556-575, 1973.

[HAD 03] HADAMAR J., *Leçon sur la propagation des ondes et les équations de l'hydrodynamique*, Paris, Hermann, 1903.

[HAN 91] HAN C., VARDOULAKIS I., "Plane-strain compression experiments on water-saturated fine-grained sand", *Géotechnique*, vol. 47, no. 1, p. 49-78, 1991.

[HAS 79a] HASSANIZADEH M., GRAY W., "General conservation equations for multi-phase systems: 1. Average procedure", *Advances in Water Resources*, vol. 2, p. 131-144, 1979.

[HAS 79b] HASSANIZADEH M., GRAY W., "General conservation equations for multi-phase systems: 2. Mass, momenta, energy, and entropy equations", *Advances in Water Resources*, vol. 2, p. 191-208, 1979.

[HIL 58] HILL R., "A general theory of uniqueness and stability in elastic-plastic solids", *Journal of Mechanics and Physics of Solids*, vol. 5, p. 236-249.

[KHO 06] KHOA H.D.V., GEORGOPOULOS I.O., DARVE F., LAOUAFA F., "Diffuse failure in geomaterials: Experiments and modelling", *Computers and Geotechnics*, vol. 33, no. 1 p. 1-14, 2006.

[KOT 08] KOTRONIS P., AL HOLO S., BÉSUELLE P., CHAMBON R., "Shear softening and localization. Modelling the evolution of the shear zone", *Acta Geotechnica*, vol. 3, no. 2, p. 85-97, 2008.

[LEN 07] LENOIR N., BORNERT M., DESRUES J., BESUELLE P., VIGGIANI G., "Volumetric digital image correlation applied to X-ray micro tomography images from triaxial compression tests on argillaceous rock", *STRAIN*, vol. 43, no. 3, p. 193-205, 2007.

[LEW 00] LEWIS R.W., SCHREFLER B.A., *The Finite Element Method in the Static and Dynamic Deformation and Consolidation of Porous Media*, New York, Wiley, 2000.

[LOR 91] LORET B., PREVOST J., "Dynamic strain localization in fluid-saturated porous media", *Journal of Engineering Mechanics*, vol. 117, no. 4, p. 907-922, 1991.

[MAN 66] MANDEL J., "Condition de stabilité et postulat de Drucker", *Proc. of IUTAM Symposium on Rheology and Soil Mechanics*, Grenoble, p. 58-67, 1966.

[MIN 64] MINDLIN R.D., "Micro-structure in linear elasticity", *Archive for Rational Mechanics and Analysis*, vol. 16, p. 51-78, 1964.

[MOK 99] MOKNI M., DESRUES J., "Strain localisation measurements in undrained plane-strain biaxial test on Hostun RF sand", *Mechanics of Cohesive-Frictional Materials*, vol. 4, p. 419-441, 1999.

[NUT 08] NUTH M., LALOUI L., "Effective stress concept in unsaturated soils: clarification and validation of a unified framework", *International Journal for Numerical and Analytical Methods in Geomechanics*, vol. 32, no. 7, p. 771-801, 2008.

[PIJ 87] PIJAUDIER-CABOT G., BAZANT Z.P., "Non-local damage theory", *Journal of Engineering Mechanics, ASCE*, vol. 39, p. 1512-1533, 1987.

[PEE 96] PEERLINGS R.H.J., DE BORST R., BREKELMANS W.A.M., DE VREE J.H.P., "Gradient-enhanced damage for quasi-brittle materials", *International Journal for Numerical Methods in Engineering*, vol. 15, no. 6, p. 3391-3403., 1996.

[RIC 76] RICE J., "The localization of plastic deformation", *Theoretical and Applied Mechanics*, North-Holland Publishing Company, p. 207-220, 1976.

[ROG 98] ROGER V., DESRUES J., VIGGIANI G., "Experiments on strain localization in dense sand under isochoric conditions", in O.F. (ed.) *Localization and Bifurcation Theory for Soils and Rocks, 4th Workshop on Localization and Bifurcation Theory for soils and Rocks*, Gifu (Japan), 28 September-2 October 1997, Balkema, p. 239-248, 1998.

[RUD 75] RUDNICKI J, RICE J., "Conditions for the localisation of deformation in pressure sensitive dilatant materials", *JMPS*, vol. 23, p. 371-394, 1975.

[SIE 09] SIEFFERT Y., AL HOLO S., CHAMBON R., "Loss of uniqueness of solutions of the borehole problem modelled with enhanced media", *International Journal of Solids and Structures*, vol. 46, no. 17, p. 3173-3197, 2009.

[TOU 62] TOUPIN R., "Elastic materials with couple-stresses", *Archive for Rational Mechanics and Analysis*, vol. 11, p. 385-414, 1962.

[VAR 78] VARDOULAKIS I., GOLDSCHEIDER M., GUDEHUS Q., "Formation of shear bands in sand bodies as a bifurcation problem", *International Journal for Numerical and Analytical Methods in Geomechanics*, vol. 2, p. 99-128, 1978.

[VAR 96] VARDOULAKIS I., "Deformation of water-saturated sand: II. Effect of pore water flow and shear banding", *Géotechnique*, vol. 46, no. 3, p. 457-472, 1996.

[WAN 93] WANG X.C., Modélisation numérique des problèmes avec localisation des déformations en bandes de cisaillement, PhD thesis, University of Liège, 1993.

[ZHA 99] ZHANG H.W., SANAVIA L., SCHREFLER B.A., "An internal length scale in dynamic strain localization of multiphase porous media", *Mechanics of Cohesive-Frictional Materials*, vol. 4, no. 5, p. 443-460, 1999.

[ZHA 01] ZHANG H.W., SCHREFLER B.A., "Uniqueness and localization analysis of elasto-plastic saturated porous media", *International Journal for Numerical and Analytical Methods in Geomechanics*, vol. 25, no. 1, p. 29-48, 2001.

PART IV

Engineering Applications

Chapter 10

Modeling Landslides in Partially Saturated Slopes Subjected to Rainfall Infiltration

10.1. Introduction: the hazard of shallow landslides

Shallow slips and debris flows represent a major threat to human life and property. They are primarily triggered in partially saturated, steep slopes during stormy rainfall events. The triggering process is very rapid, often without any precursory signs, which consequently renders their prediction rather difficult. In the alpine regions, the failure surface is commonly located between 2 and 4 m in soil depth, and the whole sliding mass sums up to a couple of hundred to thousands of cubic meters [MOS 83]. The sliding mass often develops very high velocities (up to several meter per seconds) leading to high impact on obstacles, and sadly, coming in many cases as a surprise to eyewitnesses. In the future, a higher occurrence of shallow slides is expected due to the increasing number of extreme weather events and human activities in landslide-prone areas. In mountainous regions, the melting permafrost, rainfall instead of snowmelt and glacial retreat, will lead to more shallow slope instabilities [OCC 07].

Within the framework of an advanced elastoplastic constitutive model for unsaturated soils, the results from a numerical finite element analysis are presented. They deal with a real test-site slope in partially saturated conditions subjected to rain infiltration [SPR 09]. The results show the

Chapter written by John EICHENBERGER, Mathieu NUTH and Lyesse LALOUI.

usefulness of considering partial saturation in hydraulic and mechanical terms for the modeling of the predominant transient processes and key physical mechanisms, such as soil hardening effect of matric suction, wetting pore collapse, and plastic shearing.

10.2. Physical processes in unsaturated soil slopes

Commonly, two flow regimes are encountered in natural slopes: a deep flow regime, most often parallel to the slope surface with possible complex bedrock interactions, and a superficial flow regime with capillary pressures or positive, compressive pore water pressures controlled by rainfall. Rain infiltration and hydrologic conditions influence the occurrence and type of triggering mechanism in landslides. The slope behavior mainly depends on the rainfall intensity and duration, soil hydraulic characteristics, the thickness of the sliding mass, and antecedent weather conditions [FRE 93, KLU 09]. A flow regime, parallel to the slope surface, installs itself in the upper partially saturated soil layer when the volume of the infiltrated water is large enough, consequently carrying water to the toe region. Several hydromechanical processes act in a destabilizing sense on the slope. The degree of saturation of the upper soil layer increases, thereby reducing the capillary tension between the soil particles, which weakens the slope. Upon that, due to the mobilized fluid flow inside the soil matrix, the fluid exerts a destabilizing, downhill frictional drag. If the rainfall intensity is higher than the capacity of the soil to dissipate the pore water, surface run-off occurs which may erode the slope. Depending on soil permeability and the intensity and duration of rainfall, infiltration will lead to shallow slides or debris flows in the vadose zone, or time-delayed, deep-seated failures due to mounding of the water table [COL 04, RAH 07, TSA 08].

Under strong cyclic variations of ambient environmental conditions, the upper soil layers undergo continuous plastic straining and are exposed to weathering and soil destructuration. This leads to a general weakening of the soil structure and a decay of shear strength [LER 02]. It is also known that the wetting-drying cycles influence the capillary effects and thus soil strength due to the hysteresis observed in the soil water retention curve [NUT 08a].

The above-mentioned processes make it clear that a geomechanical model needs to be capable of simulating the transient flow in saturated and

unsaturated conditions. Capillary effects need to be taken into account in order to capture the possible shallow failure mechanisms in partially saturated soils.

10.3. Theoretical framework for unsaturated soils

It was shown previously that the key physical mechanisms at the origin of slope movements are the infiltration and irreversible strains below the surface. The modeling of the onset of landslides in partially saturated slopes due to rainfall infiltration requires a multiphysics approach and an advanced constitutive framework. This paragraph reviews the main concepts of an elastoplastic constitutive model called Advanced Constitutive Model for Environmental Geomechanics (ACMEGs) and the governing equations in multiphase porous media.

The ACMEGs [NUT 07, NUT 08b] is a Cam-Clay-type elastoplastic model [SCH 68], and is based on the Hujeux's model [HUJ 85]. The increment of strain $\mathrm{d}\varepsilon_{ij}$ is decomposed into:

$$\mathrm{d}\varepsilon_{ij} = \mathrm{d}\varepsilon_{ij}^{\mathrm{e}} + \mathrm{d}\varepsilon_{ij}^{\mathrm{p}}, \qquad [10.1]$$

where $\mathrm{d}\varepsilon_{ij}^{\mathrm{e}}$ is the elastic strain increment and $\mathrm{d}\varepsilon_{ij}^{\mathrm{p}}$ the plastic strain increment.

The elastic deformation can be expressed as:

$$\mathrm{d}\varepsilon_{ij}^{\mathrm{e}} = C_{ijkl}\mathrm{d}\sigma'_{kl}. \qquad [10.2]$$

The tensor C_{ijkl} is the mechanical elastic tensor, and is composed of nonlinear elastic moduli. The elastic strain increment $\mathrm{d}\varepsilon_{ij}^{\mathrm{e}}$ can be decomposed in volumetric and deviatoric increments, which can be given as:

$$\mathrm{d}\varepsilon_{\mathrm{V}}^{\mathrm{e}} = \frac{\mathrm{d}p'}{K_{\mathrm{ref}}\left(\dfrac{p'}{p'_{\mathrm{ref}}}\right)^{n^{\mathrm{e}}}}, \qquad [10.3]$$

$$\mathrm{d}\varepsilon_{\mathrm{d}}^{\mathrm{e}} = \frac{\mathrm{d}q}{3G_{\mathrm{ref}}\left(\dfrac{p'}{p'_{\mathrm{ref}}}\right)^{n^{\mathrm{e}}}}. \qquad [10.4]$$

The material parameters K_{ref}, G_{ref}, and n^{e} are the bulk elastic modulus at a reference mean stress p'_{ref}, the reference shear elastic modulus at p'_{ref}, and the nonlinearity exponent, $n^{e} \in [0,1]$, respectively.

σ'_{kl} in equation [10.2] is the effective stress for unsaturated soils:

$$\sigma'_{kl} = (\sigma_{kl} - u_{\mathrm{a}}\delta_{kl}) + S_{\mathrm{r}}(u_{\mathrm{a}} - u_{\mathrm{w}})\delta_{kl}, \qquad [10.5]$$

where σ_{kl} is the total stress, u_{a} the air pressure, u_{w} the water pressure, S_{r} the degree of saturation, and δ_{kl} the Kronecker's delta (δ_{kl}=1 if k=l; otherwise, 0). The difference between the total stress σ_{kl} and the air pressure u_{a} is called the net stress $\sigma_{kl\,\mathrm{net}}$. The difference between u_{a} and u_{w} is defined as the matric suction s.

The critical state line (CSL) is defined in the plane of deviatoric stress q versus the mean effective stress p', with a slope M. The slope of the CSL in the plane volumetric plastic strain versus the mean effective stress $(\varepsilon_{\mathrm{v}}^{\mathrm{p}} - \ln p')$ is β, and $p'_{\mathrm{CR}\,0}$ is the initial critical state pressure.

$$\ln\frac{p'_{\mathrm{CR}}}{p'_{\mathrm{CR}\,0}} = \beta\varepsilon_{\mathrm{v}}^{\mathrm{p}}. \qquad [10.6]$$

In the ACMEGs model, the plastic irreversible strain increment $d\varepsilon_{ij}^{\mathrm{p}}$ is induced by two coupled dissipative processes: an isotropic and a deviatoric plastic mechanism. The yield limits of each mechanism, bounding the elastic domain in the effective stress space, can be written as:

$$\tilde{f}_{\mathrm{iso}}(p', \varepsilon_{\mathrm{v}}^{\mathrm{p}}, r_{\mathrm{iso}}) = p' - r_{\mathrm{iso}}dp'_{\mathrm{CR}}, \qquad [10.7]$$

$$\tilde{f}_{\text{dev}}(p',q,r_{\text{dev}},\varepsilon_{\text{v}}^{\text{p}},\varepsilon_{\text{d}}^{\text{p}}) = q - Mp'\left(1 - b\ln\frac{p'}{p'_{\text{CR}}}\right)r_{\text{dev}}, \qquad [10.8]$$

where p'_{CR} is the critical state pressure, d, b, r_{iso}, and r_{dev} are the material parameters, and $\varepsilon_{\text{v}}^{\text{p}}$ and $\varepsilon_{\text{d}}^{\text{p}}$ are the volumetric plastic strain and the deviatoric plastic strain, respectively. The critical state pressure in equation [10.6] can be related to the preconsolidation pressure p'_{c} using the material parameter d:

$$p'_{\text{c}} = dp'_{\text{CR}}. \qquad [10.9]$$

Using the space of triaxial stress variables q and p', the elastic domain is enclosed by an ellipsoidal surface that is cut by the isotropic yield limit (see Figure 10.1). Adding suction s as a third axis of the space, Figure 10.1 shows that the elastic domain gets larger with suction. This accounts for the fact that a dryer material will have higher strength and stiffness. Equation [10.10] gives the mathematical formulation of the contribution of the capillary effects to the mechanical behavior. The principle is to introduce a dependency of the preconsolidation pressure p'_{c} on the level of suction s and using a material parameter γ_{s}.

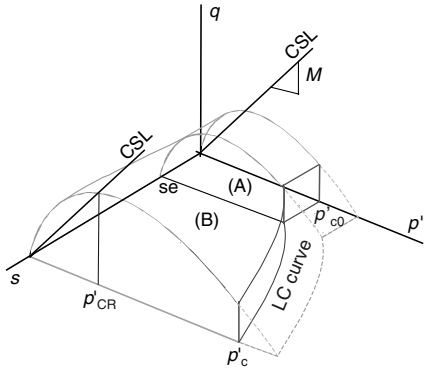

Figure 10.1. *Shape of the yield surface and CSL in a (p', q, s) space*

$$p'_{\mathrm{c}} = \begin{cases} p'_{\mathrm{c0}} & \text{if } s \le s_{\mathrm{e}} \\ p'_{\mathrm{c0}}\left[1+\gamma_{\mathrm{s}}\log(s/s_{\mathrm{e}})\right] & \text{if } s \ge s_{\mathrm{e}} \end{cases}. \qquad [10.10]$$

p'_{c0} is the initial preconsolidation pressure at zero suction and s_{e} is the air entry suction to be defined later. Equation [10.10] defines the loading collapse (LC) curve.

The purpose of the elastoplastic soil water retention model is to model the evolution of the degree of saturation S_{r} with respect to suction s. The increase in the degree of saturation $\mathrm{d}S_{\mathrm{r}}$ is decomposed into an elastic part and a plastic part, and can be given as:

$$\mathrm{d}S_{\mathrm{r}} = \frac{\mathrm{d}s}{K_H \times (s/s_{\mathrm{e}})} + \frac{\mathrm{d}s_D}{\beta_H \times (s_{\mathrm{D}}/s_{\mathrm{D0}})}. \qquad [10.11]$$

K_H is the elastic slope and β_H is the plastic slope defined in Figure 10.2. s_{e} is the air entry value and represents the limit below which the degree of saturation remains 1. s_{e} is a variable that depends on the void ratio. If the suction remains lower than the air entry value, then the degree of saturation equals to 1 and there is no elastic increment. If the residual state is reached (S_{r}=S_{res}, where S_{res} is the residual degree of saturation), then the elastic increment also becomes null. s_D is the drying yield suction, which is the maximum suction ever experienced by the material along a drying path. s_{D0} is the initial value of the drying yield suction.

The process of drying and wetting is not fully reversible and the (S_{r}–s) data usually show the existence of a capillary hysteresis. A given level of suction can indeed correspond to different degrees of saturation. The method chosen to reproduce the hysteresis in the retention model is to make the yield surface evolve by means of kinematic hardening. The elastic domain is delimited by the following yield limit:

$$f = \left\| \ln(s) - \ln(s_{\mathrm{D}}) + \frac{1}{2}\left[\ln(s_{\mathrm{D0}}) - \ln(s_{\mathrm{e}})\right] \right\| - \frac{1}{2}\left[\ln(s_{\mathrm{D0}}) - \ln(s_{\mathrm{e}})\right]. \qquad [10.12]$$

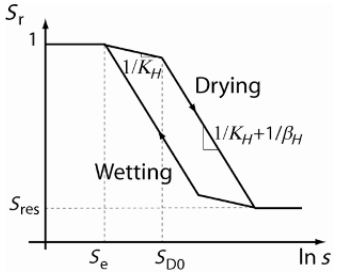

Figure 10.2. *The model for the soil water retention curve*

The constitutive model presented earlier is implemented into the finite element code called LAGAMINE [CHA 87, COL 03]. The code features hydromechanically coupled finite elements. The field equations of the hydromechanical problem are:

– Momentum conservation:

$$\operatorname{div}\boldsymbol{\sigma} + \rho\mathbf{g} = 0, \qquad [10.13]$$

where $\boldsymbol{\sigma}$ is the total (Cauchy) stress tensor with tensile stresses taken as negative, ρ the mass density of the medium, and $\mathbf{g}$ the gravity vector.

– Mass conservation of water:

$$\dot{S}_{\mathrm{w}} + \operatorname{div}(\mathbf{V}_{\mathrm{w}}) - Q_{\mathrm{w}} + \dot{S}_{\mathrm{v}} + \operatorname{div}(\mathbf{V}_{\mathrm{v}}) - Q_{\mathrm{v}} = 0, \qquad [10.14]$$

where S_{w} and S_{v} are the quantities of stored water in the liquid (w) and vapor (v) phases, respectively, $\mathbf{V}_{\mathrm{w}}$, $\mathbf{V}_{\mathrm{v}}$ are the mass fluxes of fluid, and Q_{w}, Q_{v} are the sources of fluid.

The generalized Darcy's law is used to describe the relative velocity of the fluid:

$$\mathbf{q}_{\mathrm{w}} = \frac{\mathbf{K}_{\mathrm{w}}}{\rho_{\mathrm{w}}\mathbf{g}}(\operatorname{grad}(u_{\mathrm{w}}) + \rho_{\mathrm{w}}\mathbf{g}\operatorname{grad}(z)), \qquad [10.16]$$

where $\mathbf{q}_{\mathrm{w}}$ is the vector of the velocity of the fluid phase with respect to the solid phase, $\mathbf{K}_{\mathrm{w}}$ the tensor of water permeability, u_{w} the pore water pressure,

and z the vertical coordinate taken positive upwards. In general, the permeability tensor $\mathbf{K}_w$ depends on the degree of saturation S_r. By assuming isotropic conditions for the numerical simulation presented in this chapter, the water relative permeability coefficient k_{rw} can be defined according to the following relationship, with CKW1 being a material parameter:

$$k_{rw} = \sqrt{S_r}\left[1-\left(1-S_r^{1/CKW1}\right)^{CKW1}\right]^2. \qquad [10.17]$$

10.4. Numerical modeling of an unsaturated soil slope subjected to rainfall events

The previously presented elastoplastic constitutive framework for multiphysical processes in unsaturated soils is subsequently applied to the study of the behavior of a steep slope subjected to rain infiltration. As a generic case study, we base our analysis on realistic geometrical [ASK 09] and material parameters close to those of a real test-site case study in Rüdlingen, Switzerland (Swiss Competence Center Environment and Sustainability, project TRAMM). A detailed description of this landslide triggering experiment is presented by S. Springman *et al*. [SPR 09]. We do not intend here to reproduce the in-situ experiment neither to compare the performance of our model with the measured in-situ data. The material parameters for the ACMEGs model, summarized in Table 10.1, were calibrated on the basis of our laboratory tests, such as triaxial tests and water retention test. The geometry of the slope is presented in Figure 10.3. The steep slope of 38° is composed of silty sand deposits (soil cover) of 2–5 m thickness and a beneath laying bedrock. The principal objective of this study is to show the effect of rain infiltration on the stability of a partially saturated slope and its failure mechanisms.

10.4.1. *Definition of the geomechanical model and the calculation procedure*

The finite element mesh presented in Figure 10.3 is composed of 4672 six-noded quadratic triangles. The ACMEGs constitutive model is applied to both bedrock and soil cover, using the parameters of Table 10.1. The behavior of the bedrock is assumed to be elastic. Therefore, the preconsolidation pressure p'_c is set high enough in this layer to avoid any

plastic deformations to occur. The mesh is strongly refined in the upper soil layer in order to properly model the transient hydromechanical processes and the development of plastic zones during rain infiltration. Conventional kinematic boundary conditions are imposed on the model: displacements in the horizontal direction are blocked on the left, right, and bottom boundary; in the vertical direction, displacements are blocked along the bottom boundary.

		Symbol	Description	Value
Stress-strain model	Elastic parameters	K_{ref}	Bulk modulus	1×10^9 Pa
		G_{ref}	Shear modulus	6×10^8 Pa
		n^e	Elastic exponent	0.1
	Plastic parameters	φ'	Friction angle	32°
		β_0	Compressibility coefficient	30
		*α	Dilatancy coefficient	0.7
		*a		0.05
		b	see equation [10.8]	0.1
		*c		0.08
		d	see equation [10.7]	1.3
	Limits of elastic domain	r^e_{dev}	Initialization of deviatoric mechanism	0.3
		r^e_{iso}	Initialization of isotropic mechanism	0.3
Capillary effects		γ_s	Coefficient of LC curve	0.78173
		*Ω	Coefficient of compressibility change	2×10^{-5}
		s_e	Air entry value	3000 Pa
Retention model		K_H	Elastic coefficient	8.8
		β_H	Plastic coefficient	10
		s_{D0}	Drying yield suction	6000 Pa
		S_{res}	Residual degree of saturation	0.3
Permeability		$k_{w,sat}$	Intrinsic water permeability	10^{-5} m/s
		CKW1	Parameter for the water rel. permeability function	0.123

*see [NUT 07] for the explanation of the parameters.

Table 10.1. *Parameters for the elastoplastic ACMEGs and the water retention model*

Initially, a uniform negative pore pressure corresponding to a suction value of 50 kPa is imposed on all nodes before gravity loading is applied linearly. This numerical strategy for a Cam-Clay type of model is applied to avoid the appearance of negative mean effective stresses in the sense of traction, which tend to occur typically at the slope toe when gravity loading is imposed. In a second step, hydrostatic pore pressures are imposed on the

left and right boundaries, as shown in Figure 10.3. The pore pressure profile is cut at –100 kPa in order to avoid the generation of excessively high matric suctions. A coupled flow and deformation analysis is subsequently run until a steady state is reached. The resulting water table runs inclined from the top-left to the bottom-right model boundary. Matric suction is distributed hydrostatically in the partially saturated zone above the water table and the degree of saturation reaches its residual value of S_r=0.3 along the slope surface.

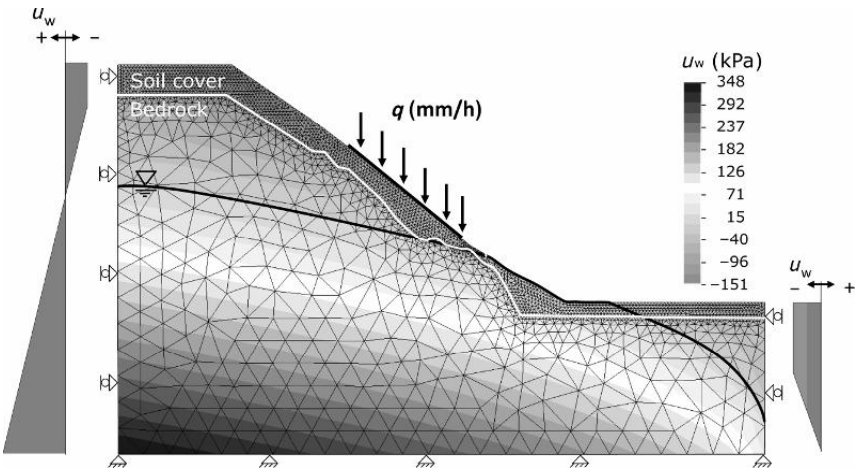

Figure 10.3. *Finite element mesh, boundary and initial conditions*

At this step, i.e. before rain infiltration, the overconsolidation ratio (OCR) varies across the model. The slope surface is an overconsolidated zone, while at the interface with the bedrock, especially in the proximity of the bedrock abutment (Figure 10.3), the OCR is close to 1. The latter is a zone that is *a priori* more likely to undergo plastic volumetric deformations during a wetting process.

In the final step, rain infiltration is simulated by means of an imposed boundary flux of 15 mm/h for 3.5 days (the rain input is virtual and does not correspond to the real experiment). Figure 10.4(a) shows the penetration of the saturation front at the end of the calculation. Clearly, the superficial soil layer has been quasi-completely saturated. The soil water retention curve illustrated in Figure 10.4(b) has three points at different depths indicating that the matric suction has decreased to reach zero or close to zero values.

In conformity with the schematic description of the soil water retention curve presented in Figure 10.2, the point of capillary state in the (S_r–s) plane of points A and B migrate within the hysteresis to join the main wetting curve at S_r=0.52.

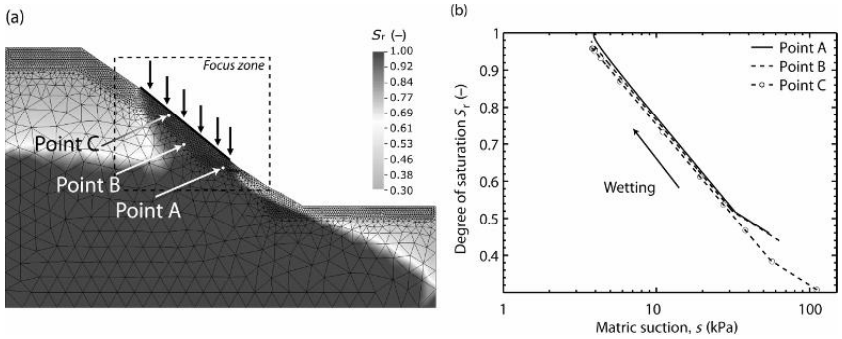

Figure 10.4. *Rain infiltration in a partially saturated slope: spatial distribution of the degree of saturation (a) and soil water retention curve (b)*

10.4.2. *Plastic mechanisms during rain infiltration in a partially saturated slope*

The supply of water in a partially saturated slope acts negatively on its stability. With the increasing water content, the capillary forces reigning between the soil particles decrease. This debonding effect of wetting is taken into account in the model through the effective stress (equation [10.5]), which decreases during rain infiltration, and the soil looses its strength in terms of classical soil mechanics.

In Figure 10.5, the contours of deviatoric strains are shown for the "focus zone" indicated in Figure 10.4, where rain infiltration of 15 mm/h takes place over 3.5 days. Shear strains are localized along the interface between the bedrock and soil layer for the lower and middle part of the slope, and run up biased to the slope surface in the upper part. The extent of the shear zone coincides with the zone of increased degree of saturation (Figure 10.4(a)), clearly showing a localized effect of the infiltrated water.

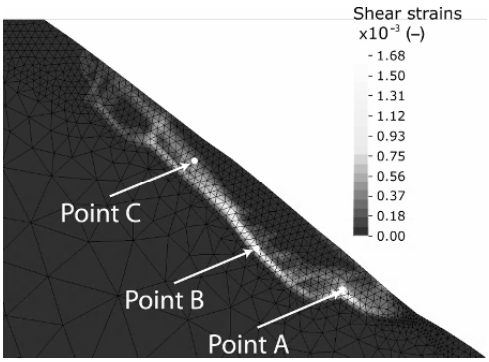

Figure 10.5. *Contour of deviatoric strains after 3.5 days of rain infiltration. Light zones indicate a concentration of shear strains*

The deformation history of three selected points, A, B and C, defined in Figure 10.5, indicates which plastic mechanism, among the isotropic (equation [10.7]) and deviatoric (equation [10.8]), is predominant in different parts of the slope at different time instances. Point A is located immediately at the interface between the bedrock and soil cover in the lower part of the slope, which presents an abutment of the bedrock. The soil in that region was almost normally consolidated prior to infiltration. In this zone, water infiltration was at the origin of strong shearing associated with noticeable positive (compressive) plastic volumetric deformations (Figure 10.6). These plastic deformations occurred after 10^5 s and kept increasing until the end of the calculation, and when compared with the other observation points, the volumetric behavior could be clearly distinguished. Point B located in the middle part of the slope underwent strong shearing of the same order of magnitude as point A. However, the compressive plastic volumetric deformation at point B was negligible. Point C located in the shearing zone running up to the slope surface reacted only after 2×10^5 s.

In accordance with the other observation points, this suggests that the shearing mechanism starts in the lower part of the slope, above the abutment, then moves upwards along the bedrock interface, and finally runs up to the slope surface, consequently delimitating a potentially instable soil mass. The plastic volumetric strains in point C are negative in the sense of extension and are associated with the occurrence of plastic deviatoric strains. The extension of the soil can be either due to dilatancy during shearing,

considering that the soil is overconsolidated, or due to a downward movement of the potentially unstable soil mass leading to the formation of a tension crack in the upper part of the slope.

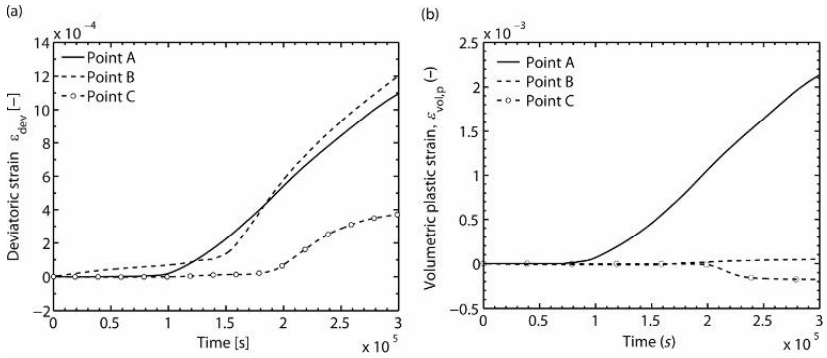

Figure 10.6. *Evolution of deviatoric (a) and plastic volumetric (b) deformations*

As mentioned earlier, the soil state is initially close to normal consolidation in the lower part of the slope. This region is a priori susceptible to plastic deformations in the sense of a wetting pore collapse. The wetting pore collapse is the property of the soils to get denser when soaked under a sufficient mechanical load. As shown in Figure 10.7(a), for points A and B, the stress paths during wetting initially remain within their respective elastic domains. The isotropic yield limits are reached at lower values of the matric suction. The stress paths then follow the current isotropic yield surfaces without moving them noticeably. Yet, this process corresponds to soil hardening and generation of compressive volumetric plastic strains. This behavior was experimentally observed in confined testing conditions and is coherent with the simulated conditions in the soil slope. A considerable loss in the mean effective stress associated with the wetting pore collapse could be observed in point A after 7×10^4 s, indicating a strength decrease in the lower part of the slope (Figure 10.7(b)). The mean effective stress reached a constant value of around 60 kPa after 1.5×10^5 s. At this time, matric suction decreased to a steady constant value of around 5 kPa.

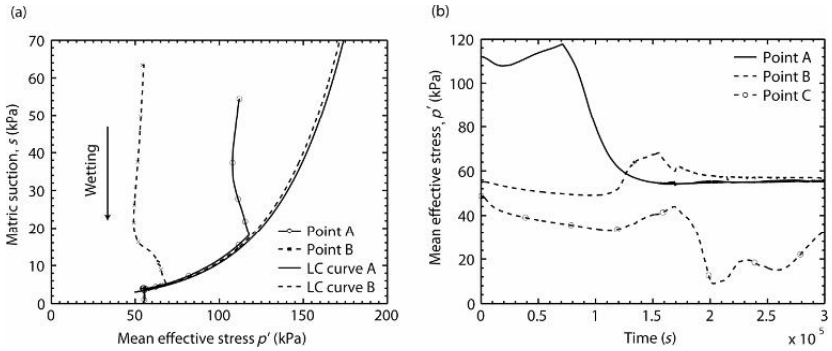

Figure 10.7. *Stress paths and LC curves (isotropic yield loci) for two points (a) and evolution of mean effective stresses (b)*

As noticed in Figure 10.6, the deviatoric deformations are far more important than the volumetric deformations for points B and C. By plotting the stress path expressed in terms of deviatoric stress q against matric suction s for those points as well as the evolution of the deviatoric yield loci with suction, it could be noticed that the stress point B is actually located on the deviatoric yield surface during complete simulation (Figure 10.8). Stress point C is first located in the elastic domain until suction decreases below a value of 70 kPa, where both yield locus and stress point join each other.

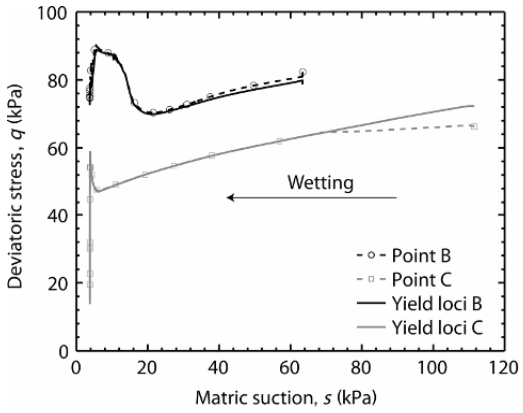

Figure 10.8. *Changes in deviatoric stress q and plastic deviatoric mechanism f_{dev} with suction decrease due to wetting. Superposition of both the lines indicates plasticity*

The deviatoric plastic mechanism is clearly predominant in the upper and middle part of the slope, while in the lower part of the slope, the isotropic plastic mechanism governs the behavior.

10.5. Conclusion

An introduction to the mechanics of unsaturated soils has been presented. It was shown that a consistent stress framework is an essential prerequisite for the constitutive modeling of unsaturated soils. It was also demonstrated how the material behavior strongly depends on the interaction between the mechanical stress-strain response and the water retention aspect.

Results from a numerical finite element simulation for a partially saturated slope subjected to rain infiltration allowed us to assess the performance of the elastoplastic constitutive model and the coupled hydromechanical approach to model the transient infiltration process and the ongoing physical mechanisms in the shallow soil cover. The analysis of the active plastic mechanisms within the soil mass allowed us to conclude that the most probable failure mechanism during rain infiltration develops in the lower part of the slope as a consequence of a wetting pore collapse, and then spreads upwards along the bedrock and through the soil cover to the slope surface as a predominant shear mechanism.

10.6. Bibliography

[ASK 09] ASKARINEJAD A. “A method to locate the slip surface and measuring subsurface deformations in slopes”, *4th Intern. Young Geotechnical Engineers’ Conf.*, Alexandria, Egypt, p. 171-174, 2009.

[CHA 87] CHARLIER R. Approche unifiée de quelques problèmes non linéaires de mécanique des milieux continus par la méthode des éléments finis, PhD thesis, University of Liège, 1987.

[COL 03] COLLIN F. Couplages thermo-hydro-mécaniques dans les sols et les roches tendres partiellement saturés, PhD thesis, University of Liège, 2003.

[COL 04] COLLINS B.D., ZNIDARCIC D. “Stability analyses of rainfall induced landslides”, *Journal of Geotechnical and Geoenvironmental Engineering*, vol. 130, no. 4, p. 362-372, 2004.

[FRE 93] FREDLUND D.G., RAHARDJO H. *Soil Mechanics for Unsaturated Soils*, John Wiley and Sons, New York, 1993.

[HUJ 85] HUJEUX J. *Une loi de comportement pour le chargement cyclique des sols*. Génie Parasismique. Paris, Les éditions de l'E.N.P.C., p. 287-353, 1985.

[KLU 09] KLUBERTANZ G., LALOUI L., VULLIET L. "Identification of mechanisms for landslide type initiation of debris flows", *Engineering Geology*, vol. 109, no. 1-2, p. 114-123, 2009.

[LER 02] LEROUEIL S. "Natural slopes and cuts: movement and failure mechanisms", *Geotechnique*, vol. 51, no. 3, p. 197-243, 2001.

[MOS 83] MOSER M., HOHENSINN F. "Geotechnical aspects of soil slips in alpine regions", *Engineering Geology*, vol. 19, p. 185-211, 1983.

[NUT 07] NUTH M., LALOUI L. "New insight into the unified hydro-mechanical constitutive modelling of unsaturated soils", *Unsat Asia*, Nanjing, p. 109-125, 2007.

[NUT 08a] NUTH M., LALOUI L. "Advances in modelling hysteretic water retention curve in deformable soils", *Computers and Geotechnics*, vol. 35, no. 6, p. 835-844, 2008.

[NUT 08b] NUTH M., LALOUI L. "Effective stress concept in unsaturated soils: clarification and validation of a unified framework", *International Journal for Numerical and Analytical Methods in Geomechanics*, vol. 32, p. 771-801, 2008.

[OCC 07] OcCC/ProClim, *Klimaänderungen und die Schweiz 2050: Erwartete Auswirkungen auf Umwelt, Gesellschaft und Wirtschaft*, Bern, 2007.

[RAH 07] RAHARDJO H., ONG T.H., REZAUR R.B., LEONG E.C. "Factors controlling instability of homogeneous soil slopes under rainfall", *Journal of Geotechnical and Geoenvironmental Engineering*, vol. 133, no. 12, p. 1532-1543, 2007.

[SCH 68] SCHOFIELD A. N., WROTH C. P. *Critical State Soil Mechanics*, McGraw-Hill, 1968.

[SPR 09] SPRINGMAN S.M., KIENZLER P., CASINI F., ASKARINEJAD A. "Landslide triggering experiment in a steep forested slope in Switzerland", *17th Intern. Conf. of Soil Mech. & Geot. Eng*., Alexandria, Egypt, p. 1698-1701, 2009.

[TSA 08] TSAI T.L., CHEN H.E., YANG J.C. "Numerical modeling of rainstorm-induced shallow landslides in saturated and unsaturated soils", *Environmental Geology*, vol. 55, no. 6, p. 1269-1277, 2008.

Chapter 11

Thermally Induced Moisture Transport and Pore Pressure Generation in Nearly Saturated Geomaterials

11.1. Introduction

This chapter examines certain aspects of the modeling of porous geomaterials that are nearly unsaturated. It deals with the problem of coupled heat and moisture transport in unsaturated porous geomaterials where the skeletal deformations are neglected, and describes the computational modeling and an experimental simulation that is relevant to a borehole emplacement-type heating of compacted clay.

The chapter also examines the problem of the surface heating of a porous cementitious material, which takes into consideration the coupled thermo-hydro-mechanical (THM) effects in a geomaterial, and accounts for the nearly unsaturated behavior of the medium through the modification of fluid compressibility. This adjustment is required to match the experimental observations of the time-dependent generation of pore fluid pressures during the boundary heating of a cementitious solid, where the degree of saturation is not known with certainty.

Chapter written by Antony P.S. SELVADURAI.

11.2. Modeling background

The mechanics of unsaturated geomaterials has important applications in geomechanics, in general, and the study of environmental geomechanics dealing with problems such as engineered geological barriers for deep geological disposal of heat-emitting nuclear fuel waste and geothermal energy extraction, in particular. In these situations, heating can induce further desaturation of an already unsaturated material. In an all-encompassing treatment of this class of problems, it is necessary to take into consideration the interactive processes of heat transfer, moisture transport, and mechanical deformations. The degree of coupling will change with the materials involved, and the mechanical deformations can be significantly influenced by the moisture state and transport processes. Advances in the area of coupled THM processes in geological media, where the mechanical deformations have irreversible effects and coupling extends to all multiphases of the fluid, are too numerous to be documented in the context of this introduction, and their accounts can be found in [ALO 90], [HUE 90a], [HUE 90b], [KHA 01], [COU 04] and [LAL 08]. References to further studies are given in [GEN 10]. The exclusion of mechanical deformations from the coupled processes is a gross simplification that needs to be applied within the context of an engineering application, where the porous medium is either completely rigid or constrained to allow the processes of fluid movement without the generation of mechanical deformations. Specific situations where such simplifications are warranted are rare and these can include either relatively rigid porous geological materials or geological materials that are externally constrained to allow moisture movement without skeletal deformations. Even within this context, the absence of boundary deformations in a specific THM problem should not be construed as evidence of null internal deformations because heat and moisture transport takes place. Despite the limitations of the absence of skeletal deformations, the purely coupled processes of heat and moisture transport can provide a useful limiting solution for examining the general class of problem that accounts for coupled THM effects. The seminal work in this area was carried out by [PHI 57], and since this initial work, a number of authors have used the modeling of heat and moisture transport to examine problems related to geothermal energy storage and recovery, and the behavior of engineered geological clay barriers to be used in nuclear waste management endeavors [GER 86, RAD 84, THO 87]; references to further literature can be found in [SEL 96a] and [SEL 96b].

The isothermal theory of poroelasticity, as proposed by [BIO 41], represents a major development in the subject of geomechanics [ATK 76, RIC 76, SEL 96c, SEL 07]. The extension of the theory to include thermal phenomena was presented by a number of authors including [SCH 71], [MOR 78], [DER 79], [PAL 82], [NOO 84], [BOO 85], [McT 86], and [SEL 95a]; references to further developments are given in [SEL 96c, SEL 07]. These classical developments invariably assume that the pore space of the deformable porous medium is saturated with the permeating fluid. Consideration of a pore space that is partly saturated is necessary either due to the effects of heating or the influences of natural fluid flow that limits the complete saturation of the pore space in relatively low permeability geomaterials. The modeling of partial saturation of the pore space can be approached using the general continuum formulations based on the theory of mixtures [BOW 67, BOW 82, GRE 65, GRE 67, KRI 97, RAJ 95]. There are instances where the degree of fluid saturation is sufficient to warrant the classification of the permeating fluid as saturating the pore space, but with its compressibility adjusted to account for the presence of a distributed undissolved gaseous phase. This enables the use of the thermo-poroelasticity model as developed in the conventional THM modeling, to examine the influence of near-saturation on the behavior of the pore fluid pressure response. This chapter presents two examples; one that relates to the heat and moisture transport in a non-deformable medium, and the second that deals with the coupled THM pore pressure behavior of a nearly saturated porous medium. In addition, the results of the experiments and computational predictions associated with each problem are also presented.

11.3. Coupled heat and moisture diffusion

The dependent variables in the theory of heat and moisture transport in a non-deformable porous medium are the volumetric moisture content $\theta(\mathbf{x},t)$ and temperature $T(\mathbf{x},t)$, where $\theta = w\gamma_d/\gamma_w$, w is the gravimetric water content, γ_d is the dry unit weight, and γ_w is the unit weight of water. The definition of both the dependent variables applies to a representative elementary volume, and no deformability of the porous skeleton implies that the porosity, and hence γ_d, are constant. The coupled partial differential equations governing the moisture diffusion and heat transfer given by [PHI 57] take the form of:

$$\frac{\partial \theta}{\partial t} = \nabla(D_\theta \nabla \theta) + \nabla(D_{\mathrm{T}} \nabla T) + \frac{\partial K_\theta}{\partial z}, \qquad [11.1]$$

$$\rho c \frac{\partial T}{\partial t} = \nabla(\lambda \nabla T) - \rho L \nabla(D_{\theta \mathrm{v}} \nabla \theta), \qquad [11.2]$$

where D_θ is the isothermal moisture diffusivity and D_T the thermal moisture diffusivity, which are composed of the components related to the liquid (l) and vapor (v) phases (i.e. $D_\theta = D_{\theta \mathrm{v}} + D_{\theta \mathrm{l}}; D_{\mathrm{T}} = D_{\mathrm{Tl}} + D_{\mathrm{Tv}}$), ρc is the volumetric heat capacity, λ is the effective thermal conductivity, L is the latent heat of vaporization, ∇ is the gradient operator, and the last term on the right-hand side of equation [11.1] can be neglected if gravitational effects on the moisture transport process can be ignored. If the physical and mechanical parameters encountered in equations [11.1] and [11.2] are constant, then these equations can be considered to be of the parabolic type, and the existence and Hadamard stability of the solutions under suitable essential (Dirichlet) and natural (Neumann or Robin) boundary conditions can be proved. For example, the essential boundary condition for the volumetric moisture content field can be written as:

$$\theta(\mathbf{x}, t) = \overline{\theta}; \quad \mathbf{x} \in S_1. \qquad [11.3]$$

and the generalized Neumann–Robin boundary condition for the volumetric moisture content field can be written as:

$$D_{\mathrm{T}} \frac{\partial T}{\partial \hat{n}} + D_\theta \frac{\partial \theta}{\partial \hat{n}} + K_\theta n_z + a_\theta T + b_\theta \theta + c_\theta = 0 \quad \text{on} \quad x \in S_2, \qquad [11.4]$$

where a_θ, b_θ and c_θ are constants chosen to fit a certain type of boundary; $\hat{n}$ represents the outward unit normal to S_2 and $S_1 \cup S_2 = S$, where S is the surface of the region and $S_1 \cup S_2 = 0$, indicating that the surfaces on which the boundary conditions are prescribed are non-moving boundaries.

Similarly, the essential boundary condition for the temperature field can be written as:

$$T = \overline{T} \quad \text{on} \quad \mathbf{x} \in S_3, \qquad [11.5]$$

and the generalized Neumann–Robin boundary condition for heat lost at a surface is given by:

$$\lambda \frac{\partial T}{\partial \hat{n}} - LD_{\theta v} \frac{\partial \theta}{\partial \hat{n}} + a_{\mathrm{T}} T + b_{\mathrm{T}} \theta + c_{\mathrm{T}} = 0 \quad \text{on} \quad \mathbf{x} \in S_4, \qquad [11.6]$$

where a_{T}, b_{T} and c_{T} are constants chosen to fit a certain type of boundary; $\hat{n}$ represents the outward unit normal to S_4 and $S_3 \cup S_4 = S$, with $S_3 \cup S_4 = 0$, indicating that the boundaries on which the moisture contents are prescribed need not correspond to the boundaries on which the temperatures are prescribed, and also indicating that the surfaces on which the boundary conditions are prescribed are non-moving boundaries. The formulation of the initial boundary value problem is complete when suitable initial conditions are prescribed for the dependent variables in the domain Ω, i.e.:

$$T(\mathbf{x},0) = \overline{T}_0(\mathbf{x}); \quad \theta(\mathbf{x},0) = \overline{\theta}_0(\mathbf{x}). \qquad [11.7]$$

The initial boundary value problem described by equations [11.1]–[11.7] can be solved using both the analytical and computational methods. The classes of problems that lend themselves to analytical treatment usually involve relatively simple geometries, and deal with linear partial differential equations with one spatial variable. Most of the practical problems involving complicated geometries and nonlinearity arising from material parameters that depend on the dependent variables themselves need to be solved using a computational approach. Examples of these procedures are given in [COM 76], [DEM 78], [THO 80], [LEW 83] and [SEL 96b]. Briefly, by introducing an arbitrary weighting function $\delta\theta$, and by using equations [11.1], [11.4] and Green's theorem, we can obtain:

$$\begin{aligned} &\iiint_{\Omega} \left\{ \nabla(\delta\theta)(D_{\mathrm{T}} \nabla T + D_{\theta} \nabla \theta) + \frac{\partial(\delta\theta)}{\partial z} K_{\theta} n_z + \delta\theta \frac{\partial \theta}{\partial t} \right\} \mathrm{d}\Omega \\ &+ \iint_{S_2} \delta\theta \left\{ a_{\theta} T + b_{\theta} \theta + c_{\theta} \right\} \mathrm{d}S = 0 \end{aligned} \qquad [11.8]$$

Similarly, by introducing an arbitrary weighting function δT, and by using equations [11.2], [11.6] and Green's theorem, we can obtain:

$$\begin{aligned}&\iiint_{\Omega}\left\{\nabla(\delta T)(\lambda\nabla T-\rho L\nabla\theta)+\rho c(\delta T)\frac{\partial T}{\partial t}\right\}\mathrm{d}\Omega\\&+\iint_{S_4}(\delta T)\{a_T T+b_T\theta+c_T\}\mathrm{d}S=0\end{aligned}\quad . \qquad [11.9]$$

These functional forms can be converted to their matrix equivalents through the use of a suitable matrix of interpolation functions $[\mathbf{N}]$ and the resulting systems of matrix equations take the form:

$$\begin{aligned}&[\mathbf{K}_{\mathrm{TT}}]\{T\}+[\mathbf{K}_{\mathrm{T}\theta}]\{\theta\}+[\mathbf{M}_{\mathrm{T}}]\{\dot{T}\}=\{\mathbf{P}_{\mathrm{T}}\}\\&[\mathbf{K}_{\theta\theta}]\{\theta\}+[\mathbf{K}_{\theta\mathrm{T}}]\{T\}+[\mathbf{M}_{\mathrm{T}}]\{\dot{\theta}\}=\{\mathbf{P}_{\theta}\}\end{aligned}\quad , \qquad [11.10]$$

where the dot denotes the time derivative. The time integration schemes are of the type applicable to parabolic schemes, i.e.:

$$\begin{aligned}&\{\dot{\theta}\}=\frac{\{\theta_{t+\Delta t}\}-\{\theta_t\}}{\Delta t};\ \{\dot{T}\}=\frac{\{T_{t+\Delta t}\}-\{T_t\}}{\Delta t}\\&\{\theta\}=\alpha\{\theta_{t+\Delta t}\}+(1-\alpha)\{\theta_t\};\ \{T\}=\{T_{t+\Delta t}\}+(1-\alpha)\{T_t\}\end{aligned}\quad , \qquad [11.11]$$

where Δt is the single time step and α is the weighting factor between 0 and 1. For $0<\alpha<0.5$, the integration scheme is conditionally stable, indicating that the time step has to be less than a certain critical value. For $0.5<\alpha<1$, the system is unconditionally stable, which indicates that the time step can be large. For example, the solution scheme can be accelerated at time scales approaching the steady-state solution. Other improved Crank–Nicolson schemes have been proposed in the literature and their details are given in [LEW 83], [BOR 88], and a recent article [KOS 10]. Using equation [11.11], result [11.10] can be written as:

$$\begin{bmatrix}\{[\mathbf{M}_{\theta}]+\alpha(\Delta t)[\mathbf{K}_{\theta\theta}]\} & \alpha(\Delta t)[\mathbf{K}_{\theta T}]\\ \alpha(\Delta t)[\mathbf{K}_{\theta T}] & \{[\mathbf{M}_{\theta}]+\alpha(\Delta t)[\mathbf{K}_{\theta\theta}]\}\end{bmatrix}\begin{bmatrix}\theta_{t+\Delta t}\\ \theta_{t+\Delta t}\end{bmatrix}=\begin{bmatrix}\mathbf{Q}_{\theta}\\ \mathbf{Q}_{T}\end{bmatrix}, \qquad [11.12]$$

where

$$\begin{bmatrix}\mathbf{Q}_{\theta}\\ \mathbf{Q}_{\mathrm{T}}\end{bmatrix}=\begin{bmatrix}\mathbf{F}_{\theta\theta} & \mathbf{F}_{\theta\mathrm{T}}\\ \mathbf{F}_{\mathrm{T}\theta} & \mathbf{F}_{\mathrm{TT}}\end{bmatrix}\begin{bmatrix}\theta_t\\ T_t\end{bmatrix}+\Delta t\begin{bmatrix}\mathbf{P}_{\theta}\\ \mathbf{P}_{\mathrm{T}}\end{bmatrix}, \qquad [11.13]$$

and

$$\begin{aligned}&\mathbf{F}_{\mathrm{TT}}=\left\{[\mathbf{M}_{\mathrm{T}}]-(1-\alpha)\Delta t[\mathbf{k}_{\mathrm{TT}}]\right\};\quad \mathbf{F}_{\theta\theta}=\left\{[\mathbf{M}_{\theta}]-(1-\alpha)\Delta t[\mathbf{k}_{\theta\theta}]\right\}\\&\mathbf{F}_{\mathrm{T}\theta}=-(1-\alpha)\Delta t[\mathbf{k}_{\mathrm{T}\theta}];\quad \mathbf{F}_{\theta\mathrm{T}}=-(1-\alpha)\Delta t[\mathbf{k}_{\theta\mathrm{T}}]\end{aligned}, \quad [11.14]$$

Result [11.12] represents the system equation for the volumetric moisture content and temperature at time $t+\Delta t$. The terms on the right-hand side of equation [11.12] can be obtained from the boundary conditions and from the values of $\{T\}$ and $\{\theta\}$. At the first time step, the initial conditions [11.7] apply. Owing to the coupled nature of the problem, the system matrix defined by equation [11.12] will, in general, be non-symmetric. For computational efficiency, a Gaussian iteration scheme can be used, i.e.:

$$\begin{aligned}&\left[[\mathbf{M}_{\theta}]+\alpha(\Delta t)[\mathbf{K}_{\theta\theta}]\right]\left\{\theta_{t+\Delta t}\right\}^{n+1}=\left\{\mathbf{Q}_{\theta}\right\}_1-\alpha(\Delta t)[\mathbf{K}_{\theta\mathrm{T}}]\left\{\theta_{t+\Delta t}\right\}^{n}\\&\left[[\mathbf{M}_{\mathrm{T}}]+\alpha(\Delta t)[\mathbf{K}_{\mathrm{TT}}]\right]\left\{T_{t+\Delta t}\right\}^{n+1}=\left\{\mathbf{Q}_{\mathrm{T}}\right\}_1-\alpha(\Delta t)[\mathbf{K}_{\mathrm{T}\theta}]\left\{T_{t+\Delta t}\right\}^{n}\end{aligned}, \quad [11.15]$$

where $\{\ \}^n$ denotes the iteration number. The convergence of the iteration procedure employed in equation [11.15] depends on the values of the hygrothermal parameters in a specific problem. For no coupling, $LD_{\theta\mathrm{v}}=D_{\mathrm{T}}=0$, and only a single iteration is needed. For the coupled problem, special procedures are needed to improve the convergence and accuracy of the solution.

11.4. Heat-induced moisture transport in a bentonite-sand mixture

The computational approach presented in the previous section has been applied to develop computational results for a large-scale laboratory experiment conducted to simulate the internal heating of a compacted sand-bentonite mixture in a borehole emplacement environment. The complete documentation of the experimental configuration and results are given in [SEL 96a, SEL 02]. A granite block measuring 918 mm×926 mm in cross-section and 2446 mm in height was used to model the rock mass. An axisymmetric borehole measuring 262 mm in diameter and 975 mm in depth was located along the axis of the granite block. The function of the granite block was primarily to create the environment for compacting the bentonite-sand mixture and to allow conductive heat transfer during internal heating. The granite block was instrumented with arrays of thermocouples that could measure the temperature distribution during heating (Figure 11.1). The outer surfaces of the granite block were insulated and the surface temperatures of

the granite block were monitored at salient locations. The buffer was a mixture of crushed sand and bentonite in equal proportions at a gravimetric moisture content of $w \approx 17.5\%$. The specific gravity of the buffer mixture was $G_s \approx 2.70$, initial void ratio was $e_0 \approx 0.62$; dry unit weight was $\gamma_d \approx 16.6$ kN/m^3, and the volumetric moisture content was $\theta_0 \approx 0.29$. The buffer was compacted within a geotextile liner that allowed the supply of moisture to the boundary of the buffer, and moisture retention within the buffer was ensured by incorporating a geosynthetic liner at the interface between the geotextile liner and granite (Figure 11.2).

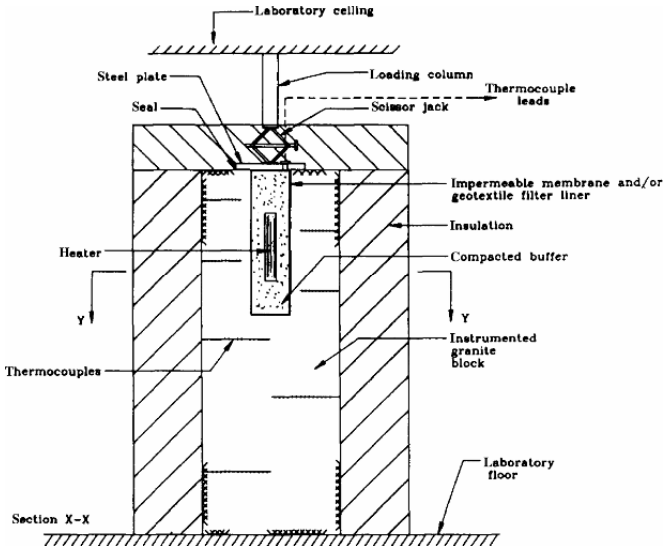

Figure 11.1. *A schematic view of the granite block test facility*

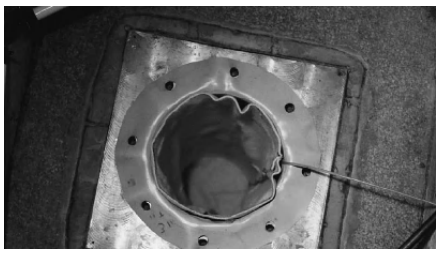

Figure 11.2. *The geotextile interface and geosynthetic liner*

The heater used in the experiments was constructed using a high-grade stainless steel and measured 72.5 mm in diameter and 435 mm in length. The heating was provided by two parallel helically wound coils around a ceramic core. The space between the core and the outer shell was filled with DEVCON aluminum epoxy to minimize thermal convection gradients within it, to reduce the thermal inertia of the system as well as to eliminate any moisture influx to the heater region. The stages in the placement of the heater within the sealed cavity in the granite block are shown in Figure 11.3.

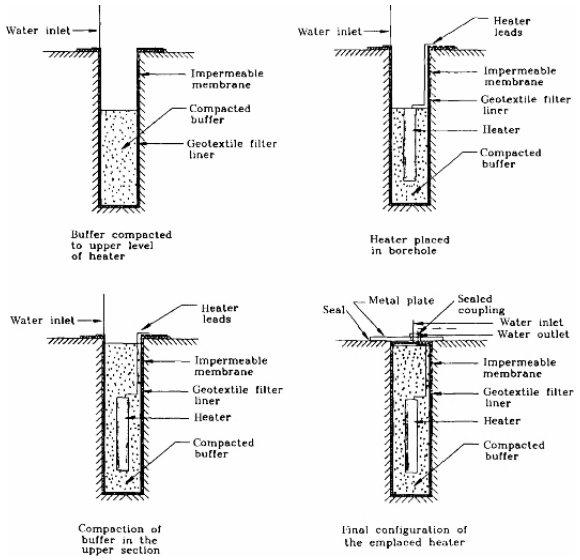

Figure 11.3. *Placement of the heater in the compacted bentonite*

The interface between the buffer and the heater was filled with fine sand to an average thickness of 2–3 mm, which provided thermal contact during heating. The compacted buffer region was also instrumented with thermocouples that can measure the temperature at salient locations. The geotextile liner was used to provide moisture supply to the boundary of the compacted bentonite mixture. Several types of tests were conducted in the experimental facility and these are described in detail in [SEL 96a, SEL 02]. Here, however, we have focused on an experiment where the boundary of the buffer had no moisture influx and the temperature at the boundary of the heater at its mid-plane was maintained at 80°C, for 2000 h. At the termination of the tests, samples from the compacted bentonite were cored out to determine the distribution of the volumetric moisture content.

11.5. Computational simulations of the behavior of bentonite-sand mixture

The computational procedure outlined previously was used to establish the temperature distribution in the compacted bentonite and granite, and the distribution of moisture in the compacted bentonite-sand mixture. The parameters required for computational modeling were determined from separate experiments involving one-dimensional heating of compacted columns. The experiments performed by [MOH 90] gave the following estimates for the hygrothermal parameters:

$$\begin{aligned} D_\theta &= (0.0122 + 0.00132T)\mathrm{e}^{0.104\theta} \times 10^{-8}\ \mathrm{m}^2/\mathrm{s} \\ D_{\mathrm{T}} &= (-0.108 + 0.0200T + 1.805\theta) \times 10^{-11}\ \mathrm{m}^2/\mathrm{s\,K} \\ D_{\theta\mathrm{v}} &= (-0.216 + 0.040T + 3.61\theta) \times 10^{-14}\ \mathrm{m}^2/\mathrm{s} \\ \lambda &= (-2.685 + 0.00205T - 0.215\theta)\ \mathrm{J/m\,s\,K} \end{aligned} \quad . \qquad [11.16]$$

Furthermore, the experiments performed by [SEL 92] on the same bentonite-clay mixture gave the following estimates for the hygrothermal parameters:

$$\begin{aligned} D_\theta &= (0.0320 + 0.00296T + 0.9322\theta) \times 10^{-8}\ \mathrm{m}^2/\mathrm{s} \\ D_{\mathrm{T}} &= (0.6852 + 0.0591T - 2.138\theta) \times 10^{-9}\ \mathrm{m}^2/\mathrm{s\,K} \\ D_{\theta\mathrm{v}} &= 0 \\ \lambda &= (-0.2539 + 0.00352T + 0.6261\theta)\ \mathrm{J/m\,s\,K} \end{aligned} \qquad [11.17]$$

In general, the volumetric heat capacity of the compacted bentonite-sand mixture can vary with θ; in this study, it was assumed to be constant, i.e. $\rho c = 3 \times 10^{-6}\ \mathrm{J/m^3K}$. The granite block was modeled as a cylinder with an external diameter of 920 mm. The thermal conductivity and heat capacity of granite, as determined from transient tests, are as follows:

$$\lambda = 2.50\ \mathrm{J/m\,K}; \quad \rho c = 2.38 \times 10^6\ \mathrm{J/m^3K}. \qquad [11.18]$$

In the experiments, the granite block rested on the concrete floor of the laboratory, and the thermal conductivity and heat capacity of the concrete were assigned the following values:

$$\lambda = 1.28\ \mathrm{J/m\,s\,K}; \quad \rho c = 1.50 \times 10^6\ \mathrm{J/m^3K}. \qquad [11.19]$$

The insulation at the outer boundary of the granite block was polystyrene bead insulation, and the thermal properties of the material were as follows:

$$\lambda = 0.155\,\mathrm{J/m\,s\,K}; \quad \rho c = 0.20 \times 10^6\ \mathrm{J/m^3K}. \qquad [11.20]$$

The details of the finite element discretization are shown in Figure 11.4, and eight-noded isoparametric elements are used to model the three regions. Complete continuity of temperature is assumed at the interfaces, and the temperature at the outer boundary of the insulation and the concrete is set at the average temperature in the laboratory environment (approx. 20°C). As the time history of the surface temperatures of the heater are measured, the temperature and no moisture flux boundary conditions are prescribed as follows:

$$\begin{aligned} &T(r,z,t_0 = T_{\mathrm{h}}(t); \quad (r,z) \in S_{\mathrm{bh}} \\ &D_\theta \nabla\theta + D_{\mathrm{T}} \nabla T = 0; \quad (r,z) \in S_{\mathrm{bh}} \end{aligned} \qquad [11.21]$$

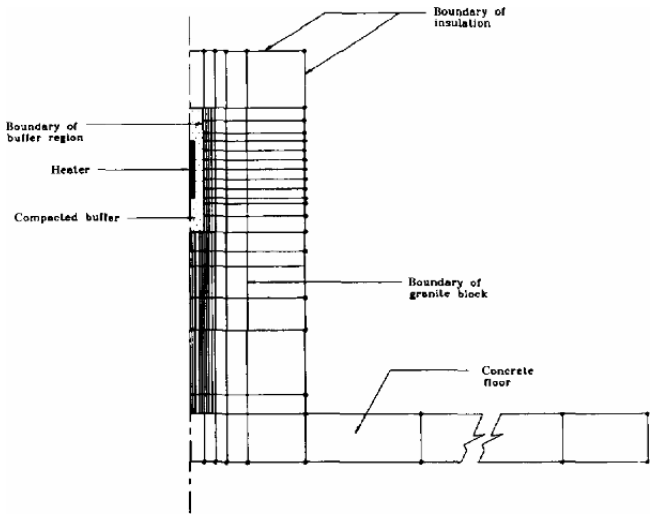

Figure 11.4. *The finite element discretization of the granite block test facility*

The hygrothermal parameters for the granite block region are set to zero. The initial temperature in the system is set to the ambient laboratory temperature, and the volumetric moisture content in the buffer region is set to the initial value of θ_0=0.29. Computational modeling is used to estimate

the time-dependent temperature distributions as well as the residual volumetric moisture content distributions in the compacted bentonite-buffer mixture at the termination of the experiment. The results of the comparisons indicate that, in general, the temperature distributions within the system can be predicted quite accurately without the need for fully coupled modeling that involves both heat conduction and moisture transport. The rationale for this is the relatively minor change in the thermal conductivity and heat capacity of the compacted bentonite-sand mixture that can result from moisture migration within it. Unless there is complete drying of the material that results in excessive shrinkage and loss of contact at the interface between the heater and the compacted material as well as at its outer surface, the thermal conductivity values remain relatively constant, leading to good predictions of heat conduction. This conclusion is also supported by results obtained from large-scale field tests of compacted bentonite-sand mixtures in galleries and emplacement boreholes [ALO 05]. The results of the experiments are mainly used to assess the capabilities of computational modeling to predict the distribution of residual moisture at the termination of the experiment. Figure 11.5 illustrates the distribution of normalized residual volumetric moisture content within the compacted bentonite mixture at the termination of the test. The notations NUM 1 and NUM 2 refer to the computational estimates derived from the material parameter data sets given by equations [11.16] and [11.17], respectively. There is reasonable correlation between the experimental data and computational predictions.

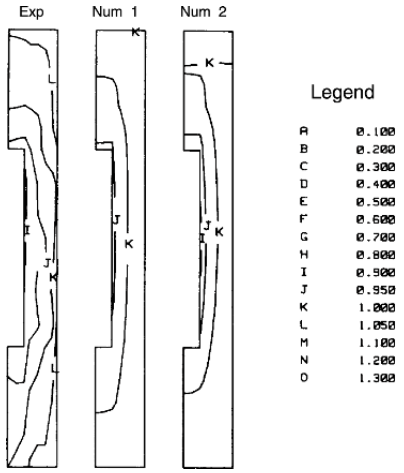

Figure 11.5. *Distribution of normalized volumetric moisture content in the compacted bentonite-sand mixture after 2000 h heating and comparison with computational estimates*

11.6. THM processes in a porous medium

In this section, we consider the non-isothermal mechanics of a porous medium that contains a compressible pore fluid. The partial differential equations governing the displacement field u(x,*t*), temperature T(x,*t*), and pore fluid pressure *p*(x,*t*) can be obtained by combining the Duhamel–Neumann extensions to Hookean elasticity, Darcy's law applicable to the flow of the fluid through the pore space, Fourier's law for pure heat conduction through the saturated medium, and the appropriate conservation laws applicable to mass, momentum, and energy. These equations can be written as:

$$\kappa\nabla^2 T = \rho C\frac{\partial T}{\partial t}, \qquad [11.22]$$

$$G\nabla^2\mathbf{u} + (G+\lambda)\nabla(\nabla\bullet\mathbf{u}) + \alpha_0\nabla p - \beta K_D\nabla T + \mathbf{F} = 0, \qquad [11.23]$$

$$\begin{aligned}&\frac{k}{\mu}\nabla^2 p - \left(\frac{n}{K_{\mathrm{f}}} - \frac{n}{K_{\mathrm{f}}} + \frac{\alpha_0}{K_{\mathrm{s}}}\right)\frac{\partial p}{\partial t} + \alpha_0\frac{\partial}{\partial t}(\nabla\bullet\mathbf{u})\\ &+\left[(1-\alpha_0)\beta - (1-n)\beta_{\mathrm{s}} - n\beta_{\mathrm{f}}\right]\frac{\partial T}{\partial t} = 0\end{aligned}, \qquad [11.24]$$

where G and λ are the linear elastic Lame' constants; κ the thermal conductivity of the bulk poroelastic medium; ρC the heat capacity of the bulk porous medium; k the permeability of the porous medium; n the porosity of the medium; β, β_{s}, and β_{f} are the drained thermal expansion of the porous fabric, solid phase, and pore fluid, respectively; K_{D}, K_{s}, and K_{f} are the bulk moduli of the drained material, solid phase, and fluid, respectively (we note that if the fluid contains air voids, then this term should be interpreted as the effective bulk modulus of the fluid); μ is the kinematic viscosity; $\alpha_0 = [1-(K_D/K_s)]$; F is a body force vector; and ∇ is the gradient operator. In the development of these partial differential equations, certain key constitutive and kinematic assumptions are invoked; the first relates to the effective stress concept used in the formulations. Here, we assume that the effective or inter-granular stresses $\boldsymbol{\sigma}'$ are given by:

$$\boldsymbol{\sigma}' = \boldsymbol{\sigma} - \alpha_0 p\mathbf{I}, \qquad [11.25]$$

where $\mathbf{I}(=\mathbf{ii}+\mathbf{jj}+\mathbf{kk})$ is the unit dyadic. Second, the poroelastic deformations require that Darcy's law be modified to take into consideration relative motion between the pore fluid and porous skeleton, i.e.:

$$\mathbf{v}_{\mathrm{f}}-\mathbf{v}_{\mathrm{s}}=\frac{k}{n\mu}\nabla p, \qquad [11.26]$$

where $\mathbf{v}_{\mathrm{f}}$ and $\mathbf{v}_{\mathrm{s}}$ are the velocities of the pore fluid and solid phase, respectively. In order to complete the formulation of a specific boundary value problem, it is necessary to prescribe appropriate boundary conditions for the dependent variables **u**, T, and p. These can be the usual Dirichlet and Neumann boundary conditions applicable to the dependent variables. In addition, appropriate initial conditions should also be prescribed. Considering the thermodynamic requirements for a positive definite strain energy potential (see e.g. [RIC 76]), it can be shown that the material parameters should satisfy the following constraints:

$$G>0;\quad 0\le\tilde{B}\le 1;\quad -1<\nu<\nu_{\mathrm{u}}\le 0.5;\quad k>0;\quad \kappa>0, \qquad [11.27]$$

where $\tilde{B}$ is the pore pressure parameter defined by [SKE 54], and both $\tilde{\alpha}$ and $\tilde{\beta}$ are related to the undrained Poisson's ratio ν_{u} and $\tilde{B}$ as follows:

$$\alpha_0=\frac{3(\nu_{\mathrm{u}}-\nu)}{\tilde{B}(1-2\nu)(1+\nu_{\mathrm{u}})}\quad \beta=\frac{2G(1-2\nu)(1+\nu_{\mathrm{u}})^2}{9(\nu_{\mathrm{u}}-\nu)(1-2\nu_{\mathrm{u}})}. \qquad [11.28]$$

In addition to the above-mentioned constraints, we can introduce the relationship that is applicable to the effective compressibility of a fluid containing low concentration of dissolved air. From phase relationships, we have:

$$V_{\mathrm{a}}=V_{\mathrm{w}}(1-S_{\mathrm{r}}), \qquad [11.29]$$

where V_{a} is the volume fraction of air in a volume of water V_{w} and S_{r} the degree of saturation. From the theory of mixtures, the effective compressibility of an imperfectly saturated fluid containing air voids can be written in terms of the Voigt average:

$$C_{\mathrm{aw}}=C_{\mathrm{w}}S_{\mathrm{r}}+(1-S_{\mathrm{r}})C_{\mathrm{a}}=\frac{1}{K_{\mathrm{f}}}, \qquad [11.30]$$

where K_f is the effective bulk modulus of the fluid introduced in equation [11.24].

The compressibility of air can be determined by considering the ideal gas laws, and for high degrees of saturation, $S_r \in (0.8,1.0)$, the capillary and surface tension effects can be neglected, thus obtaining:

$$C_a = \frac{1}{(p + p_{atm})}, \qquad [11.31]$$

where p_{atm} is the atmospheric pressure and p the conventional pore water pressure. As the effective bulk modulus of the fluid is now dependent on the pressure p, the governing equation [11.24] is *nonlinear*. The solution of the set of partial differential equations (PDEs) must necessarily be approached by considering an iterative scheme. In this chapter, however, the objective is to use the elementary poroelastic model in a parametric analysis of the THM response of a specific initial boundary value problem. In this sense, the problem is linearized by assigning *a priori* a spatial variation in the degree of saturation.

11.7. Computational modeling of the THM processes

Computational modeling of the classical poroelasticity problem is a standard development in computational geomechanics, which is described in a number of texts and articles devoted to both finite element and boundary element analysis. Comprehensive discussions of these developments are given in [DES 77], [LEW 95], [SEL 01], [SEL 07], and [EHL 02]. Computational modeling of the THM problem described in the preceding section has been discussed by a number of authors, and detailed accounts of these studies are also given in [SEL 95a], [NGU 95] and [GAT 97]. The governing equations are approximated by their matrix equivalents by adopting a standard Galerkin finite element procedure. We consider a bounded region where standard finite element procedures [ZIE 06] are used to discretize the region with plane isoparametric elements. The displacements within the element are interpolated as functions of the displacements at all the eight nodes, whereas pore pressures and temperatures are interpolated as functions of their values at only the corner nodes. The justification for the procedure is well documented in the literature, and further discussions of the numerical treatment of both isothermal and non-isothermal problems involving coupled processes of a double diffusive nature

are presented in the literature of computational geomechanics [LEW 95]. The appropriate matrix equations applicable to the partial differential equations [11.22]–[11.24] can be written as follows:

$$\begin{aligned}&\left[\alpha[\mathbf{KH}]\right]+(\rho C/\Delta t)[\mathbf{CM}]\{\mathbf{T}\}^1\\&=\{\mathbf{FH}\}+\{\mathbf{FQ}\}+\left[(\alpha-1)[\mathbf{KH}]+(\rho C/\Delta t)[\mathbf{CM}]\right]\{\mathbf{T}\}^0,\end{aligned}\qquad[11.32]$$

$$\begin{aligned}&\begin{bmatrix}[\mathbf{K}] & \alpha_0[\mathbf{CP}]\\ \alpha_0[\mathbf{CP}] & -\alpha\Delta t[\mathbf{KP}]-c_{\mathrm{e}}[\mathbf{CM}]\end{bmatrix}\begin{Bmatrix}\{\mathbf{d}\}^1\\ \{\mathbf{p}\}^1\end{Bmatrix}=\{\mathbf{f}\}\\&\begin{bmatrix}\dfrac{(\alpha-1)}{\alpha}[\mathbf{K}] & \alpha_0\dfrac{(\alpha-1)}{\alpha}[\mathbf{CP}]\\ \alpha_0[\mathbf{CP}]^{\mathrm{T}} & (1-\alpha)[\mathbf{KP}]-c_{\mathrm{e}}[\mathbf{CM}]\end{bmatrix}\begin{Bmatrix}\{\mathbf{d}\}^0\\ \{\mathbf{p}\}^0\end{Bmatrix},\\&+\begin{bmatrix}\dfrac{\beta K_{\mathrm{D}}}{\alpha}[\mathbf{K}] & [\mathbf{0}]\\ [\mathbf{0}] & \beta_{\mathrm{e}}[\mathbf{CM}]\end{bmatrix}\begin{Bmatrix}(1-\alpha)\{\mathbf{T}\}^0+\alpha\{\mathbf{T}\}^1\\ \{\mathbf{T}\}^1-\{\mathbf{T}\}^0\end{Bmatrix}\end{aligned}\qquad[11.33]$$

where the unknowns are the displacements $\{\mathbf{d}\}^1$, nodal temperatures $\{\mathbf{T}\}^1$, and nodal pore pressures $\{\mathbf{p}\}^1$ at the current time step, and $\{\mathbf{d}\}^0$, $\{\mathbf{T}\}^0$, and $\{\mathbf{p}\}^0$ are the nodal displacements, nodal temperatures, and nodal pore fluid pressures at the previous time step, respectively, $\{\mathbf{f}\}$ is a vector of generalized "forces", $\{\mathbf{FQ}\}$ and $\{\mathbf{FH}\}$ are the heat flux vectors, α is the time integration constant, and [**K**], [**CP**], etc. are assembled from element matrices, which are dependent on thermal, mechanical, and hydrological properties of the individual elements and the interpolation functions used. In addition:

$$c_{\mathrm{e}}=\frac{n}{K_{\mathrm{f}}}-\frac{n}{K_{\mathrm{s}}}+\frac{\alpha_0}{K_{\mathrm{s}}};\quad \beta_{\mathrm{e}}=(1-\alpha_0)\beta-(1-n)\beta_{\mathrm{s}}-n\beta_{\mathrm{f}}.\qquad[11.34]$$

As has been noted previously, the time integration constant α varies between 0 and 1. However, stability of the solution can be realized within the first three to four steps by setting α=0.75. The accuracy of the finite element technique has been verified through comparison with classical analytical solutions for: (i) the isothermal problem of the surface loading of a halfspace region by a uniform circular loading [McN 60] and (ii) the internal heating of a saturated poroelastic medium by a volumetric heat source [BOO 85]. Details of these calibration exercises are given in [NGU 95].

11.8. Experimental modeling of the THM processes in a cementitious block

In this section, we have outlined the experimental procedures that were employed to determine the thermo-poroelastic response of a "saturated" synthetic porous material made of a cementitious grout, fabricated to give hydraulic conductivities comparable with those for either a dense unfractured sandstone or shale. The poroelastic material was made of a cementitious grout consisting of a mix of water:cement:mortar sand:superplasticizer in the ratios of 2:4:10:0.1 by weight. Extensive tests were conducted to obtain the above-mentioned mix proportions [SEL 95b]. The cylinder used in the experimental investigations measured 500 mm in diameter and 500 mm in height. The use of the superplasticizer provided sufficient workability of the mix, enabling the installation of instrumentation for the measurement of the pore water pressure and temperature at salient points within the cylinder. The miniature pore pressure transducers used in the instrumentation were of the diaphragm type with an active surface of diameter 2 mm. Precautions were taken to ensure that the diaphragm of the transducer was isolated from the cementitious grout both during the hardening stages and during the thermal surface loading of the cylinder. This was achieved by fitting the transducers with a highly porous cap. It was found that by keeping the porous tip moist during the placement of the cement grout, there is no possibility of infiltration of cement particles into the porous tip region. Each transducer was fluid-pressure tested separately to assess their accuracy. Thermocouples were also installed at the locations of the pore pressure transducers. The test grout cylinder was fabricated as a single unit and allowed to cure under humid conditions for 28 days. In addition to the test cylinder, several smaller cylinders of 75 mm in diameter and 150 mm in height were fabricated to determine the poroelastic properties that are required for computational modeling. These included the thermoelasticity parameters, thermal conductivity and heat capacity values, and hydraulic conductivity values. The results of the experimental investigations gave the following values for the cementitious grout: thermal conductivity: κ=0.563 J/m/sec/°C; heat capacity: ρC=2×10^6 J/m^3/°C; Young's modulus: E=26.65 GPa; Poisson's ratio: ν=0.24; coefficient of thermal expansion: β=2×10^{-5}/°C; and hydraulic conductivity: $k \cong 10^{-12}$ m/s. The cured cement grout cylinder was first subjected to heating on its plane surface in close proximity to the pressure sensors. Heating was achieved using a flexible coil heater that gave nearly uniform temperatures over the entire surface of contact. This was verified during the calibration of the

heater. The contact was maintained through the application of a flexible surcharge load in the form of a layer of sand of 5 cm in thickness. The response of the pore pressure transducers and the thermocouples embedded in the cylinder were recorded during the heating sequence where the boundary temperature was approximately 92°C. The temperature increases recorded within the cylinder were consistent with the temperatures applied at the plane surface. Unfortunately, the pore pressure sensors at locations 1 and 3 were damaged during the fabrication of the cementitious grout cylinder. During the heating of the cured cementitious grout cylinder, the pore pressure transducers recorded virtually no pressure changes during the heating sequence, indicating that the pore pressure sensors would respond when pore fluid pressures were present. The complete cylinder was subjected to vacuum saturation for 10 days after the curing period. The regular testing of the thermo-poroelastic response of the cementitious grout cylinder commenced 72 h after the termination of the vacuum saturation process. Figure 11.6 illustrates the general layout of the cylinder during the boundary heating sequence.

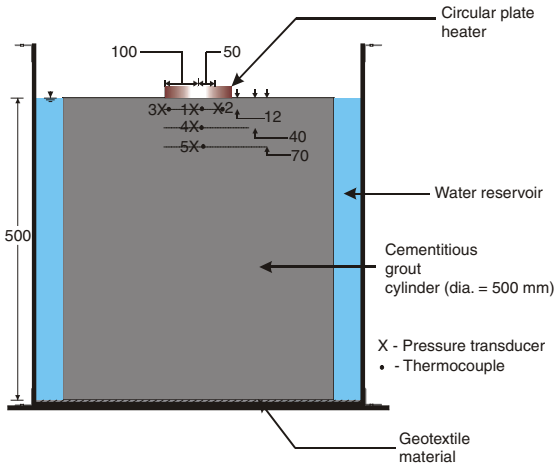

Figure 11.6. *General layout of the cementitious cylinder during boundary heating (all dimensions are in mm)*

A series of experiments were performed on the "saturated" cementitious cylinder, with the progressive increase in the peak temperature associated with boundary heating. Figures 11.7–11.9 indicate typical experimental

results that were recorded by the temperature and pressure sensors located within the cementitious grout cylinder.

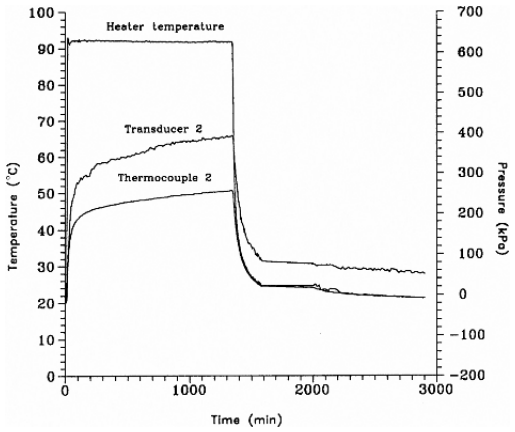

Figure 11.7. *Experimental results for the time-dependent pore water pressure and temperature at the sensor location 2*

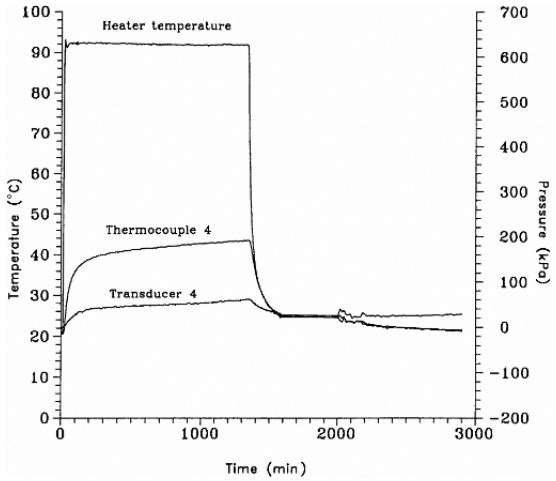

Figure 11.8. *Experimental results for the time-dependent pore water pressure and temperature at the sensor location 4*

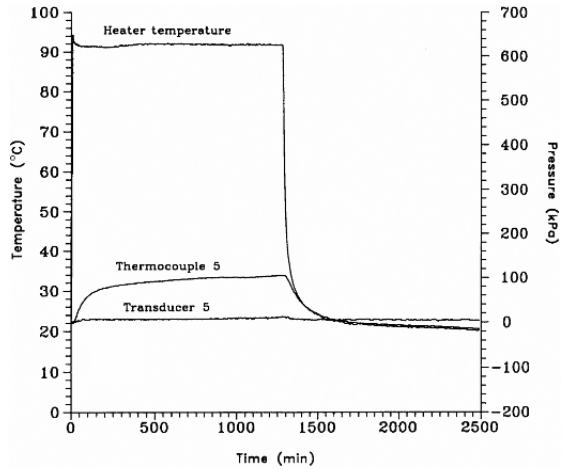

Figure 11.9. *Experimental results for the time-dependent pore water pressure and temperature at the sensor location 5*

11.9. Comparison of experimental results and computational estimates

The computational procedures outlined briefly in section 11.5 were employed to develop estimates for the temperatures and pore water pressures at the sensor locations associated with experimental modeling. In the computational developments, the compressibility of the fluid was assumed to vary with the degree of saturation of the pore fluid. Therefore, in order to develop the computational results, it is necessary to assign the inhomogeneous variation in the degree of saturation throughout the cylinder. Such an assessment, however, requires the evaluation of the degree of saturation achieved during the vacuum saturation phase. This in itself necessitates the analysis of a moisture diffusion problem, which is not routine. In the case of the cementitious material, such an approach is a difficult exercise, particularly in view of the fact that the moisture uptake can be influenced by the hydration effects of the cement and can be subject to continuous variation. Instead, the approach adopted in this study is to consider a plausible variation in the degree of saturation of the material in the vicinity of the plane boundary that would result in a computational estimate close to those of the experimental results. As the objective of the computational exercise is to estimate the influence of the unsaturation effects on the temperature and pore pressure development within the cylinder, the compressibility of the pore fluid is assumed to vary in a prescribed manner

with 100% saturation at the surface, to 98.9% at the sensor location 2 and decreasing linearly to approximately 94% at the depth of the pore pressure transducer location 5 (Figure 11.6). Figure 11.10 illustrates the time-dependent variation in the temperatures at the sensor locations 2, 4, and 5. Based on the results of previous THM studies performed in connection with granite and bentonite barrier systems [SEL 96a, SEL 96b, SEL 02], the temperature distributions within the region are not substantially influenced by the degree of saturation of the poroelastic medium. The discrepancies between the experimental and computational results for the temperatures at the sensor locations shown in Figure 11.10 are within the range of accuracy of the thermocouples used to measure the temperature at these locations. Figure 11.11 illustrates the time-dependent variation of pore pressures recorded at the sensor locations 2, 4, and 5, and the corresponding computational results obtained for the case of the poroelastic medium with the prescribed variation in the degree of saturation, and hence, the prescribed variation in the compressibility of the pore fluid of the poroelastic medium. In this case, there is a reasonable correlation between the experimental and computational results. Figure 11.12 shows the time-dependent variation in the pore fluid pressure at the sensor location 4 as a function of the saturation value, which varies from 99 to 97.5% at sensor location 4. It is evident that the computational estimate for the pore pressure development at sensor location 4 is particularly sensitive to the degree of saturation at that location.

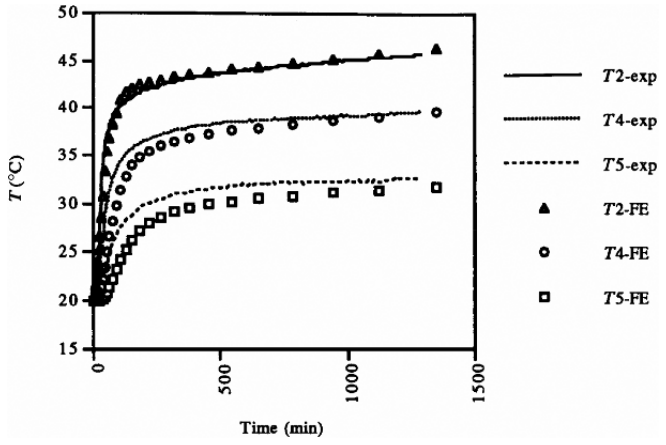

Figure 11.10. *Time-dependent variation in the temperatures at sensor locations 2, 4, and 5*

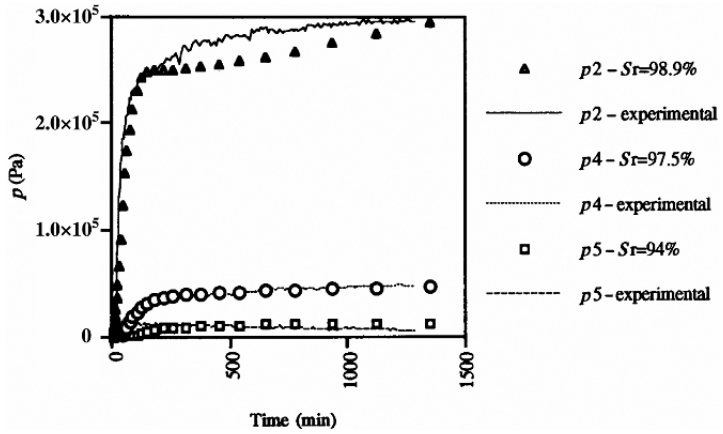

Figure 11.11. *Time-dependent variation in the pore fluid pressures at sensor locations 2, 4, and 5*

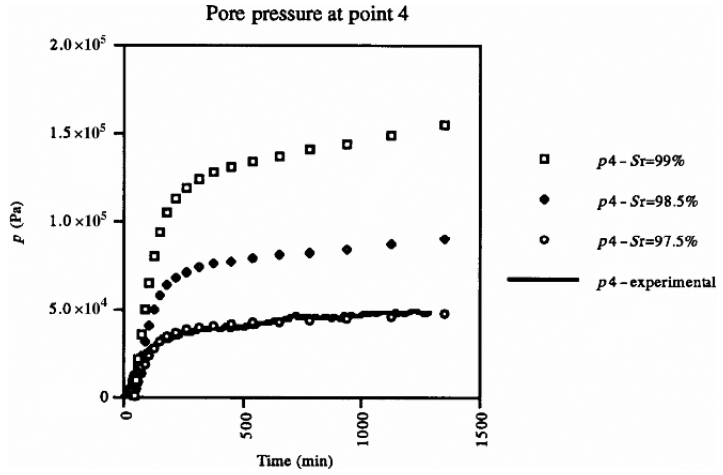

Figure 11.12. *Influence of the compressibility of the pore fluid pressure on the pore pressure development at the sensor location 4*

11.10. Concluding remarks

The thermo-hydro-mechanics of unsaturated porous geomaterials can be approached at various levels of theoretical and experimental sophistication. The more advanced theories for modeling these materials rely on complete thermodynamic treatments for the development of constitutive equations

that account for irreversible processes associated with a porous skeleton that undergoes irreversible mechanical deformations in the presence of mixed-phase fluid flow processes. The theoretical advances in these formulations are not consistent with the practical reality of developing experimental techniques that can determine the coupling effects spanning all the processes. Alternative approaches to the modeling of unsaturated porous materials that account for restricted forms of coupling are highly simplified approaches for examining coupled processes in thermo-hydro-mechanics. The exclusion of mechanical deformations is warranted only in limited situations where the porous skeleton is sessile either through its mechanical properties or through the confinement of the porous medium that prevents deformation. In such cases, attention can be focused only on the movement of moisture and conduction of heat in a coupled fashion. This chapter examines the problem of internal heating of a compacted bentonite-sand mixture in a confined configuration. The geometry of the problem and the confined conditions lend themselves to the application of theories that involve only the hygrothermal processes. The results for the residual volumetric moisture content distribution within the heated geomaterial indicates that the heat-induced moisture distribution can be examined using reduced coupling. The chapter also addresses the problem of surface heating of a cementitious porous medium that contains a pore fluid with a volume fraction of air. The pore pressure generated during the surface heating of the cementitious material is measured using an embedded transducer. It has been shown that the classical theory of thermo-hydro-mechanics developed by extending Biot's classical approach to include thermal effects is a suitable model for examining this problem, provided the compressibility of the pore fluid is modified to include the compressibility of the dissolved air.

11.11. Acknowledgments

The work described in this chapter was supported by a grant from the Natural Sciences and Engineering Research Council of Canada, and research contracts awarded by Atomic Energy of Canada Limited and the Canadian Nuclear Safety Commission. The author is grateful to the Technical Staff at Carleton University, Ottawa, Canada, for their assistance in conducting the experiments described in this chapter.

11.12. Bibliography

[ALO 90] ALONSO E.E., GENS A., JOSA A., "A constitutive model for partially saturated clays", *Geotechnique*, vol. 40, p. 405-430, 1990.

[ALO 05] ALONSO E.E., *et al.*, "The FEBEX benchmark test: case definition and comparison of modelling approaches", *International Journal of Rock Mechanics and Mining Sciences*, vol. 42, p. 611-638, 2005.

[ATK 76] ATKIN R.J., CRAINE R.E., "Continuum theories of mixtures: basic theory and historical development", *Quarterly Journal of Mechanics and Applied Mathematics*, vol. 29, p. 209-244, 1976.

[BIO 41] BIOT M.A., "General theory of three-dimensional consolidation", *Journal of Applied Physics*, vol. 12, p.144-164, 1941.

[BOO 85] BOOKER J.R., SAVVIDOU C., "Consolidation around a point heat source", *International Journal for Numerical and Analytical Methods in Geomechanics*, vol.9, p. 173-184, 1985.

[BOR 88] BORJA R.I., "The analysis of consolidation by a quasi-Newton technique", *International Journal of Numerical and Analytical Methods in Geomechanics*, vol. 12, p. 221-229, 1988.

[BOW 67] BOWEN R.M., "Towards a thermodynamics and mechanics of mixtures", *Archive for Rational Mechanics and Analysis*, vol. 24, p. 370-403, 1967.

[BOW 82] BOWEN R.M., "Compressible porous media models by the use of the theory of mixtures", *International Journal of Engineering Science*, vol. 20, p. 697-735, 1982.

[COM 76] COMINI G., LEWIS R.W., "A numerical solution of two-dimensional problems involving heat and mass transfer", *International Journal of Heat and Mass Transfer*, vol. 19, p. 1387-1392, 1976.

[COU 04] COUSSY O., *Poromechanics*, John Wiley, New York, 2004.

[DEM 78] DEMPSEY B.J., "A mathematical model for predicting coupled heat and water movement in unsaturated soil", *International Journal for Numerical and Analytical Methods in Geomechanics*, vol. 2, p. 19-36, 1978.

[DER 79] DERSKI W., KOWALSKI S.J., "Equations of linear thermo-consolidation", *Archiwum Mechaniki*, vol. 31, p. 303-316, 1979.

[DES 77] DESAI C.S., CHRISTIAN, J.T. (eds.), *Numerical Methods in Geotechnical Engineering*, John Wiley, New York, 1977.

[EHL 02] EHLERS W., BLUHM J. (eds.), *Porous Media: Theory, Experiments and Numerical Applications*, Springer-Verlag, Berlin, 2002.

[GAT 97] GATMIRI B., DELAGE P., "A formulation of fully coupled thermal-hydraulic-mechanical behavior of saturated porous media-numerical approach", *International Journal for Numerical and Analytical Methods in Geomechanics*, vol. 21, p. 199-225, 1997.

[GEN 10] GENS A., "Soil-environment interactions in geotechnical engineering", *Geotechnique*, vol. 60, p. 3-74, 2010.

[GER 86] GERAMINEGAD M., SAXENA S.K., "A coupled thermo-elastic model for saturated-unsaturated porous media", *Geotechnique*, vol. 36, p. 539-550, 1986.

[GRE 65] GREEN A.E., NAGHDI P.M., "A dynamical theory of interacting continua", *International Journal of Engineering Science*, vol. 3, p. 231-241, 1965.

[GRE 67] GREEN A.E., NAGHDI P.M., "A theory of mixtures", *Archive for Rational Mechanics and Analysis*, vol. 24, p. 243-263, 1967.

[HUE 90a] HUECKEL T., BALDI G., "Thermoplasticity of saturated clays: experimental constitutive study", *Journal of Geotechnical Engineering, ASCE*, vol. 116, p.1778-1796, 1990.

[HUE 90b] HUECKEL T., BORSETTO M., "Thermoplasticity of saturated soils and shales: experimental constitutive study", *Journal of Geotechnical Engineering, ASCE*, vol. 116, p. 1765-1777, 1990.

[KHA 01] KHALILI N., LORET B., "An elastic-plastic model for non-isothermal analysis of flow and deformation in unsaturated porous media formulation", *International Journal of Solids and Structures*, vol. 38, p. 8305-8330, 2001.

[KOS 10] KHOSHGHALB A., KHALILI N., SELVADURAI A.P.S., "A three-point time discretization technique for parabolic partial differential equations", *International Journal of Numerical and Analytical Methods in Geomechanics*, doi:10.1002/nag.902, 2010.

[KRI 97] KRISHNASWAMY S., BATRA R.C., "A thermomechanical theory of solid-fluid mixtures", *Mathematics and Mechanics of Solids*, vol. 2, p. 143-151, 1997.

[LAL 08] LALOUI L., CEKEREVAC C., "Non-isothermal plasticity model for cyclic behaviour of soils", *International Journal for Numerical and Analytical Methods in Geomechanics*, vol. 30, p. 437-460, 2008.

[LEW 83] LEWIS R.W., MORGAN K., ZIENKIEWICZ O.C. (eds.), *Numerical Methods in Heat Transfer*, John Wiley, New York, 1983.

[LEW 95] LEWIS R.W., SCHREFLER B.A., *The Finite Element Method in the Static and Dynamic Deformation and Consolidation of Porous Media*, John Wiley, New York, 1998.

[McT 86] McTIGUE D.F., "Thermoelastic response of fluid-saturated porous rock", *Journal of Geophysical Research*, vol. 91, p. 9533-9542, 1986.

[McN 60] McNAMEE J., GIBSON R.E., "Plane strain and axisymmetric problems of the consolidation of a semi-infinite clay stratum", *Quarterly Journal of Mechanics and Applied Mathematics*, vol. 13, p. 210-227, 1960.

[MOH 90] MOHAMED A.M.O., YONG R.N., XU D.-M., "Application of an identification technique to evaluate diffusion parameters in coupled flow", *Proceedings of the International Association for Scientific and Technological Development*, Montreal, p. 1-4, 1990.

[MOR 78] MORLAND L.W., "A theory of slow fluid flow through a porous thermoelastic matrix", *Geophysical Journal of the Royal Astronomical Society*, vol. 55, p. 393-410, 1978.

[NGU 95] NGUYEN T.S., SELVADURAI A.P.S., "Coupled thermal-mechanical-hydrological behaviour of sparsely fractured rock: implications for nuclear waste disposal", *International Journal of Rock Mechanics and Mining Sciences*, vol. 32, p.465-479, 1995.

[NOO 84] NOORISHAD J., TSANG C.-F., WITHERSPOON P.A., "Coupled thermo-hydraulic-mechanical phenomena in saturated fractured porous rocks: numerical approach", *Journal of Geophysical Research*, vol. 89, p. 10365-10373, 1984.

[PAL 82] PALCIAUSKAS V.V., DOMENICO P.A., "Characteristics of drained and undrained response of thermally loaded repository rocks", *Water Resources Research*, vol. 18, p. 281-290, 1982.

[PHI 57] PHILIP J.F., DE VRIES D.A. "Moisture movement in porous materials under temperature gradients", *Transactions of the American Geophysical Union*, vol. 38, p. 222-232, 1957.

[RAD 84] RADHAKRISHNA H.S., LAU K.C., CRAWFORD A.M., "Coupled heat and moisture flow through soils", *Journal of Geotechnical Engineering, Proceedings, ASCE*, vol. 110, p. 1766-1784, 1984.

[RAJ 95] RAJAGOPAL K.R., TAO L., *Mechanics of Mixtures*, World Scientific Publishing, Singapore, 1995.

[RIC 76] RICE J.R., CLEARY M.P., "Some basic stress diffusion solutions for fluid-saturated elastic porous media with compressible constituents", *Reviews of Geophysics and Space Physics*, vol. 14, p. 27-241, 1976.

[SCH 71] SCHIFFMAN R.L., "A thermoelastic theory of consolidation", *Environmental and Geophysical Applications of Heat Transfer*, ASME, New York, p. 78-84, 1978.

[SEL 92] SELVADURAI A.P.S., "Experimental determination of parameters governing heat-induced moisture movement in a clay buffer", in SOMBRET G.C. (ed.), *Proceedings XVth Symposium on the Scientific Basis for Nuclear Waste Management*, Strasbourg, Materials Research Society, Boston, vol. 257, p. 539-545, 1992.

[SEL 95a] SELVADURAI A.P.S., NGUYEN T.S., "Computational modelling of isothermal consolidation of fractured media", *Computers and Geotechnics*, vol. 17. p. 39-73, 1995.

[SEL 95b] SELVADURAI, A.P.S., Experimental modelling of thermal consolidation effects around a high level waste repository, Atomic Energy Control Board Project Report 5.146.1, Ottawa, Canada, 1995.

[SEL 96a] SELVADURAI A.P.S., "Heat-induced moisture movement in a clay barrier. I. Experimental modelling of borehole emplacement", *Engineering Geology*, vol. 41, p. 239-256, 1996.

[SEL 96b] SELVADURAI A.P.S., "Heat-induced moisture movement in a clay barrier. II. Computational modelling and comparisons with experimental results", *Engineering Geology*, vol. 41, p. 219-238, 1996.

[SEL 96c] SELVADURAI A.P.S. (ed.), *Mechanics of Poroelastic Media*, Kluwer Academic Publ., Dordrecht, Netherlands, 1996.

[SEL 01] SELVADURAI A.P.S., "On some recent developments in poroelasticity, IACMAG 2001", Desai C.S. *et al.* (eds.), *Proceedings of the 10th International Conference on Computer Methods and Advances in Geomechanics*, Tucson, Arizona, A.A. Balkema, Netherlands, vol. 2, p. 1761-1769, 2001.

[SEL 02] SELVADURAI A.P.S., "Influence of pressurized water influx on the hygrothermal behaviour of an engineered clay barrier in a waste emplacement borehole", *Engineering Geology*, vol. 64, p. 157-178, 1996.

[SEL 07] SELVADURAI A.P.S., "The analytical method in geomechanics", *Applied Mechanics Reviews*, vol. 60, p. 87-106, 2007.

[SKE 54] SKEMPTON A.W., "The pore pressure coefficients A and B", *Geotechnique*, vol. 4, p.143-147, 1954.

[THO 80] THOMAS H.R., MORGAN K., LEWIS R.W., "A fully non-linear analysis of heat and mass transfer problems in porous bodies", *International Journal for Numerical Methods in Engineering*, vol. 15, p. 1381-1393, 1980.

[THO 87] THOMAS H.R., "Nonlinear analysis of heat and moisture transfer in unsaturated soils", *Journal of Geotechnical Engineering, Proceedings, ASCE*, vol. 113, p. 1163-1180, 1987.

[ZIE 06] ZIENKIEWICZ O.C., TAYLOR R.L., *The Finite Element Method*, vols. 1-3, Butterworth-Heinemann, Massachusetts, 2006.

Chapter 12

Mechanics of Unsaturated Geomaterials Applied to Nuclear Waste Storage

12.1. Introduction

In many countries using nuclear power for electricity generation, the construction of a deep geological repository is the preferred option for storage or disposal of high-level nuclear waste (HLW). An important feature of HLW is that it is strongly heat emitting. The aim of geological disposal is to remove the radioactive waste from human environment and to ensure that any radionuclide release rates remain below the prescribed limits [CHA 87]. Figure 12.1 shows a typical scheme for an underground mined repository. It involves the sinking of deep shafts (or ramps) down to a depth of several hundred meters. The depth is controlled by local geological conditions. The shafts provide access to a network of horizontal drifts that constitute the main repository area. A part of those drifts will be access tunnels and a part will be devoted to nuclear waste disposal. The waste itself may be placed in the disposal horizontal drifts themselves, or alternatively, in vertical boreholes. At present, hard crystalline rocks, argillaceous rocks, and saline rocks are the type of host formations most likely to be selected, although other rock types such as unsaturated tuff are also considered.

As an example of conceptual design, Figure 12.2 shows the longitudinal section of a disposal tunnel in granite. It can be observed that the canisters

---

Chapter written by Antonio GENS.

containing high-level waste are emplaced at the center of a horizontal drift. The space between the canisters and the host rock is filled with a suitable material to constitute an engineered barrier. The material most usually considered is compacted swelling clay, normally some kind of bentonite on its own or mixed with other materials like sand. However, cement-based materials (special concretes) and crushed salt (for repositories in salt rock) are also being examined.

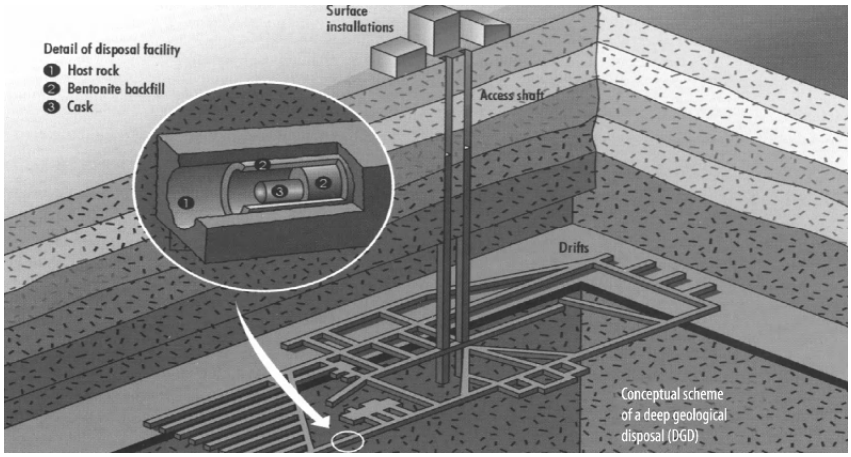

Figure 12.1. *Scheme of a deep geological repository for high-level nuclear waste*

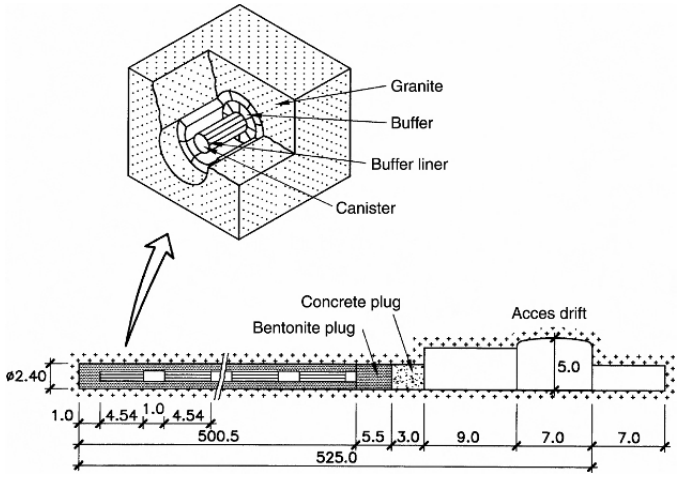

Figure 12.2. *Longitudinal section of a disposal drift in a deep geological repository*

All disposal designs for HLW resort to the multi-barrier concept to achieve the required degree of waste isolation. If we observe the potential path of a radionuclide from inside the canister to the biosphere, it is clear that it will need to cross several barriers, including the canister itself, the backfill (engineered barrier), and the host rock (geological barrier). Each one of these elements will provide a degree of safety to the overall disposal system. Originally, it was thought that each barrier should be designed in such a way to provide sufficient isolation on its own, so that a simultaneous failure of all barriers would be required for significant radioactive releases to occur. In fact, this is too restrictive, and in cases involving long-lived wastes, possibly impossible to achieve. It is more realistic to consider all the barriers acting together in a single repository system.

Figure 12.3 shows a scheme of the multi-barrier system for a deep repository of HLW using an engineered barrier of bentonite. Ideally, each barrier should provide favorable conditions for the isolation and controlled release of radionuclides. The bentonite barrier fulfills several important functions. In the first instance, a very low hydraulic conductivity restricts water penetration and significantly retards solute transport due to its low diffusion coefficient and additional sorption effects. It should also provide a favorable chemical environment and be able to self-heal if subjected to physical disturbance, such as cracking and fissuring events. In addition to the bentonite barrier, additional sealing must be provided to prevent preferential radionuclide migration through access tunnels and shafts or ramps. Often, the sealing agent is a compacted material with a significant (sometimes full) amount of bentonite.

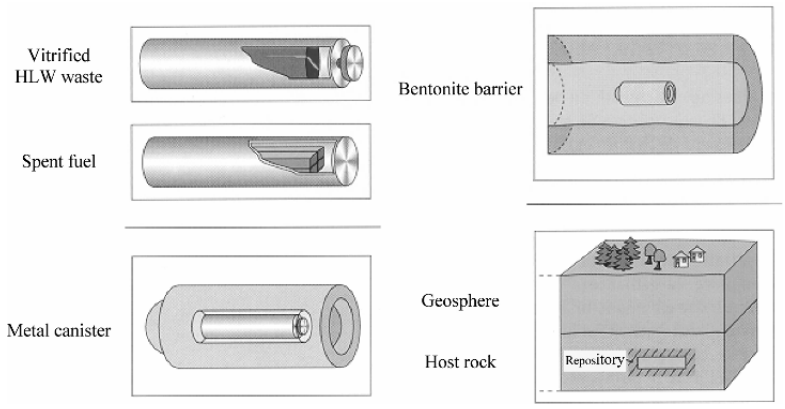

Figure 12.3. *Multi-barrier concept for a deep geological repository for HLW*

To study the problems associated with a deep geological repository, it is convenient to differentiate the near field from the far field. The near field can be defined as the zone altered by the presence of radioactive waste. It includes the engineered barriers and a portion of the host rock adjacent to the waste location. The far field extends from the end of the near field (not a precise location) to the ground surface. As expected, geomechanics plays a key role in the selection, design, and performance assessment of a deep geological repository [GEN 03, GEN 09a, GEN 10]. More specifically, geomechanics of unsaturated materials is especially relevant for the following situations:

– Thermo-hydro-mechanical (THM) behavior of the bentonite barrier. Compacted bentonite is used as the prime material, and consequently, the initial state of the barrier is unsaturated.

– THM behavior of the host rock in the near field. The host rock may be unsaturated or, more commonly, may become unsaturated due to thermal effects and bentonite suction.

– Hydromechanical behavior of shafts and tunnel seals, where, again, the material is placed compacted and, therefore, unsaturated.

In this chapter, only the near-field THM behavior of the bentonite barrier and adjacent rock is examined. Specifically, the results of a series of coupled THM analyses will be presented and discussed in order to highlight some of the features of the combined behavior of bentonite barrier and rock in the near field. Refer to [OLI 05] for a case in which the host rock is initially unsaturated, or to [VAN 07] for a hydrodynamic analysis of borehole sealing.

12.2. THM phenomena in the near field

The near field is an area of complex phenomena and interactions. The swelling clay making up the barrier is compacted, and hence, initially, it is in an unsaturated state. After placing the canisters, the main actions that affect the bentonite barrier (at least in the short term) are the heating arising from the canisters and hydration from the surrounding rock. At the inner boundary, the barrier receives a very strong heat flux from the canister. The dominant heat transfer mechanism is conduction that occurs through the three phases of the material. A temperature gradient will therefore develop in the near field, and heat dissipation will be basically controlled by the thermal conductivity of the

barrier and host rock. The maximum temperatures envisaged in the repository design can be quite high. Some designs limit the maximum temperature to 100°C, but other concepts allow significantly higher temperatures.

In the inner zone of the barrier, the heat supplied by the heater results in a temperature increase and strong water evaporation that induces drying of bentonite. The degree of saturation and water pressure will reduce significantly in this region. Vapor arising from bentonite drying will diffuse outwards until finding a cooler region where vapor will condense, causing a local increase in water saturation. Vapor diffusion is a significant mechanism of water transfer mechanism, and to a much lesser extent, heat transport. Owing to the low water pressures existing initially in the unsaturated material that constitutes the backfill, hydration will take place with water moving from the host rock to the barrier. The distribution of water potential is also affected by the phenomena of bentonite drying and vapor transport described earlier. Hydration will eventually lead to saturation of the barrier, but saturation times can often be very long due to the low permeability of bentonite and/or host rock. Figure 12.4 shows a scheme of the main thermo-hydraulic processes occurring in the bentonite barrier and rock in the near field. In the figure, the rock has been assumed to be saturated, but in fact, it can desaturate in some circumstances.

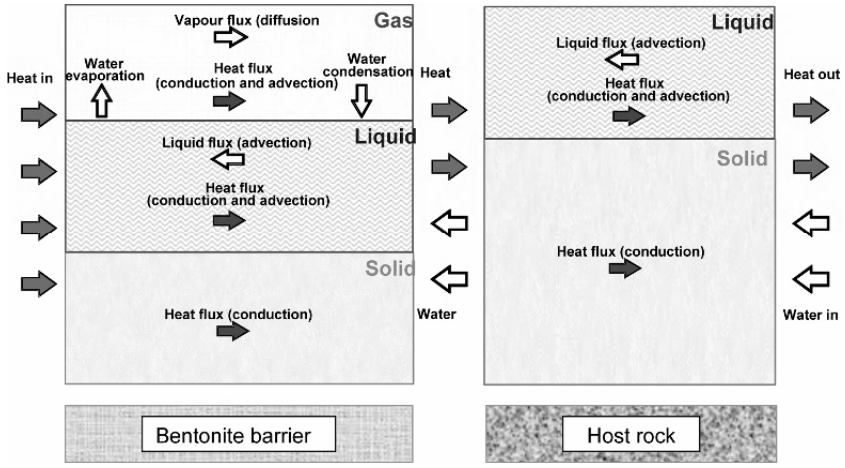

Figure 12.4. *Thermo-hydraulic processes occurring in the near field*

In addition to the thermo-hydraulic behavior, there are also other important mechanical phenomena that occur. Drying of bentonite causes shrinking of the material, whereas hydration produces swelling that may be quite strong in the bentonite barriers. As the barrier is largely confined between canister and rock, the main result of hydration is the development of swelling pressures, in a process quite similar to the swelling pressure test. The magnitude of the stresses developed is critically dependent on the emplacement density of bentonite and may reach values of several MPa.

The above-mentioned discussion strongly indicates that all those phenomena are strongly coupled, interacting with each other in a complex manner. The complexity of THM behavior increases further when the interaction of the bentonite barrier with the host rock is taken into account. This issue is explored in detail in this chapter.

12.3. Theoretical formulation and coupled analysis

The coupled THM formulation required to carry out the analyses has been presented elsewhere [GEN 10, OLI 94]. However, for completeness, a brief description is given here. The formulation is based on a multiphase, multispecies approach, and it is assumed that the porous medium is composed of three species: mineral, water, and air, distributed in three phases: solid, liquid, and gas. The liquid phase contains water and dissolved air, and the gas phase contains dry air and water vapor. The formulation takes into account the basic thermal, hydraulic, and mechanical phenomena that are relevant to the coupled THM analysis for porous materials. Specifically, the following have been explicitly incorporated:

– Heat transport: heat conduction, heat advection (by liquid water, water vapor, and gaseous air), and phase changes.

– Water flow: liquid phase and water vapor diffusion.

– Air flow: gas phase and dissolved air diffusion.

– Mechanical behavior: behavior of porous material dependent on stresses suction and temperature.

The following assumptions are made in the formulation of the problem:

– Dry air is considered as a single species, and usually, it is the main component of the gaseous phase.

– Thermal equilibrium between the phases is assumed. This means that the three phases are at the same temperature.

– Balance of momentum for the medium as a whole is reduced to the equation of stress equilibrium together with a mechanical constitutive model to relate stresses with strains. Strains are defined in terms of displacements.

– Small strains and small strain rates are assumed for solid deformation. Advective terms due to solid displacement are neglected after the formulation is transformed in terms of material derivatives (basically, material derivatives are approximated as eulerian time derivatives). In this way, volumetric strain is properly considered.

– Physical parameters in constitutive laws are the function of pressures and temperature.

The equations that govern this problem can be categorized into three main groups: balance equations, constitutive equations and equilibrium relationships. The balance equations establish the conditions for water mass conservation, air mass conservation, energy conservation, and momentum conservation (equilibrium). They are solved simultaneously to take into account, in a proper manner, the various couplings between the phenomena. The unknowns (state variables) are liquid pressure, gas pressure, temperature, and displacements.

The constitutive equations establish the link between the state variables (or unknowns) and the dependent variables. There are several categories of dependent variables based on the complexity with which they are related to the unknowns. The governing equations are finally written in terms of the unknowns when the constitutive equations are substituted in the balance equations.

Another type of relationships that relate dependent variables with unknowns is the equilibrium restrictions. They are obtained by assuming the chemical equilibrium for the dissolution of different species (air and vapor) in different phases (liquid and gas). This assumption is sufficiently adequate because these chemical processes are fast when compared with the transport processes that take place in this type of porous media, and therefore, they are not rate controlling.

Constitutive equations and equilibrium restrictions are described in [GEN 00]. The following points should be highlighted:

– Heat conduction is governed by Fourier's law. Thermal conductivity depends on the porosity and state of hydration of the material.

– Specific heat is considered additive with respect to the various components of a porous medium.

– Liquid and gas flow are governed by Darcy's law. Hydraulic conductivity depends on the porosity, degree of saturation, and temperature (via water viscosity).

– Vapor diffusion is governed by Fick's law. A tortuosity coefficient is included to take into account the fact that diffusion takes place in a porous medium [OLI 00].

The formulation has been discretized using Galerkin's approach for space discretization and finite differences for time discretization. A computer code, CODE_BRIGHT [OLI 96], has been developed to perform coupled THM analyses in two and three dimensions. The analyses reported herein have been performed using this code.

12.4. Coupled THM analyses of the unsaturated barrier and adjacent rock

12.4.1. *Reference case*

A completely general examination of the combined behavior of bentonite barrier and adjacent rock is not feasible because of the large number of variables involved as well as their very wide range of values. In a particular instance, it is necessary to focus on preferably the one that provides a realistic scenario. In this respect, large-scale tests reproducing repository conditions are especially useful because they provide intensely instrumented full-scale models of actual conditions. These tests also supply specific cases in which the effects of various parameters and processes can be investigated in situations that have practical relevance.

One such full-scale test, FEBEX, is used here as the basic case for exploring the interaction between the host medium and clay barrier. The FEBEX in situ test is a large-scale heating test that is being carried out at the Grimsel Test Site (GTS) in the Swiss Alps. The test tries to reproduce the main features of a Spanish concept for deep underground disposal of high-level radioactive waste [ENR 00].

The test layout (Figure 12.5) consists of placing two heaters at the end of a drift of 2.28 m diameter and 70.4 m length particularly bored for this purpose. The diameter and length of the heaters (0.9 and 4.54 m, respectively) correspond to the actual dimensions of the canister envisaged for radioactive waste storage. The heaters are placed in the axis of the drift at a 1 m distance from each other. The space between the drift and the heaters is filled with blocks of compacted bentonite with smectite content in the range of 88–96%. The mean values of the initial dry density and water content are 1.7 g/cm^2 and 14.4%, leading to an initial degree of saturation of about 65%. The host rock is a good quality Central Aare granite crossed, in the test zone, by a lamprophyre dyke. The 17 m long test zone at the end of the drift is sealed by a concrete plug.

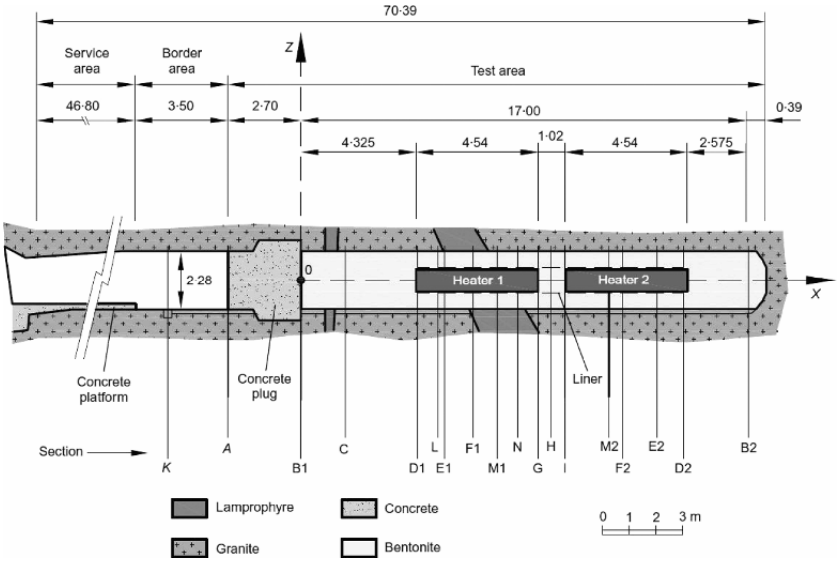

Figure 12.5. *Layout of the FEBEX in situ test*

The test schedule involved switching on the heaters with a prescribed power schedule until the temperature reaches a value of 100°C at some point in the bentonite. From that moment on, the power of the heaters is constantly adjusted in order to keep the maximum temperature in the bentonite barrier at the 100°C mark.

The THM properties of the compacted bentonite and the rock have been determined by means of a comprehensive characterization program including laboratory and *in situ* tests. Figure 12.6 shows the very low intrinsic permeability value of bentonite and its dependency on porosity. The retention (characteristic) curve linking suction and degree of saturation is presented in Figure 12.7, where drying and wetting curves are distinguished. It can be observed that the permeability of the rock (including the contribution of discontinuities) is significantly higher, in the order of 8×10^{-18} m^2. Even the mass permeability of granite, 10^{-18} m^2, is higher than that of bentonite. The retention curve for granite, as determined in the laboratory, is shown in Figure 12.8. It is interesting that the granite appears to have a rather low air entry value, certainly lower than that of the bentonite. Additional information on the performance and interpretation of the FEBEX test and on the material parameters is given in [GEN 09b].

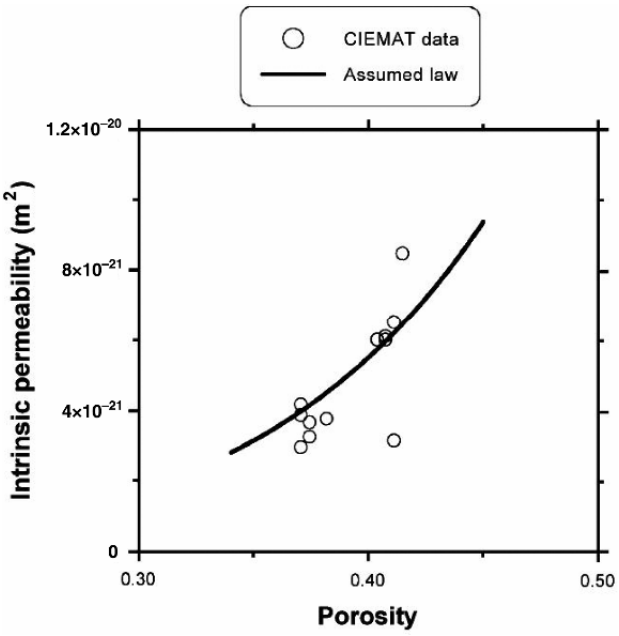

Figure 12.6. *Variation of the intrinsic permeability of the FEBEX bentonite with porosity [VIL 96]*

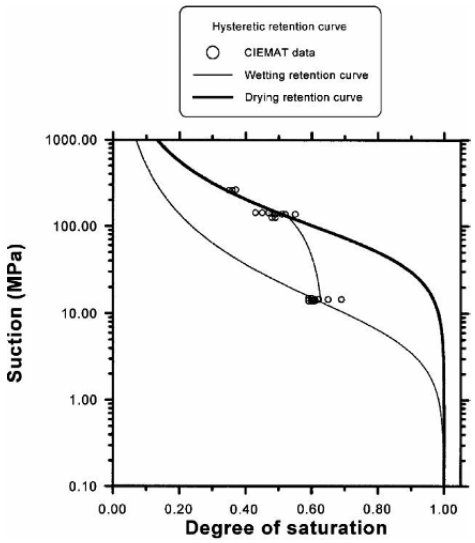

Figure 12.7. *Retention curves of bentonite [VIL 96]*

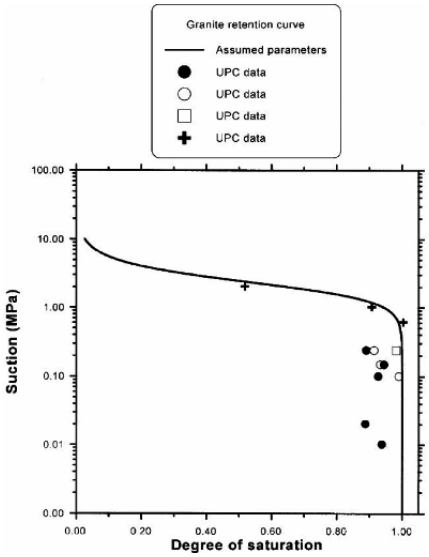

Figure 12.8. *Retention curve of granite [PIN 96]*

12.4.2. *Features of the analyses*

The analyses were carried out using a 1D geometry with radial symmetry. Initial conditions, boundary conditions, and constitutive law parameters were derived from an extensive field and laboratory testing program carried out before the performance of the test. According to the hydrogeological investigations, the water flow close to the tunnel was mainly radial tending gradually towards the regional flow direction over a distance of 50 m. Accordingly, the outer domain boundary was fixed at a radial distance of 50 m where a water pressure of 0.7 MPa (typical of the values measured before tunnel excavation) was prescribed. A temperature of 12°C and a radial stress of 28 MPa were specified at the outer boundary.

The thermal boundary conditions applied at the heater location (r=0.385 m) were: (i) a constant power of 1200 W/heater from day 0 to 21, (ii) a constant power of 2000 W/heater from day 21 to 42, (iii) a constant power of 2400 W/heater from day 42 to t_{100}, and (iv) a constant temperature equal to 100°C from day t_{100} up to 3 years. t_{100} is the time required to reach 100°C at some point in bentonite. These thermal boundary conditions aimed to reproduce the planned heating schedule.

The analyses performed started simulating the excavation of the tunnel, allowing sufficient time for equilibration, both hydraulic and mechanical. Regarding mechanical variables, an initially uniform and isotropic stress field of 28 MPa was assumed. The initial granite porosity was taken as 0.01.

As indicated earlier, the initial water content of bentonite was 14.4%, which corresponded to a degree of saturation of 0.65 and, from the retention curve adopted, an initial value of suction of 84 MPa. The initial stress was assumed to be isotropic and equal to 0.5 MPa in bentonite. Finally, a uniform initial temperature of 12°C was adopted throughout the domain. The mechanical behavior of bentonite was modeled by a thermoplastic constitutive model specifically developed for unsaturated materials [GEN 95]. For the host rock, a simple linear elastic model was deemed acceptable.

12.4.3. *Results of the Base Case*

A series of parametric analyses have been performed to check the effect of individual parameters and processes on the overall behavior of the barrier.

This parametric study provides important information on a number of aspects of the interaction of the host geological medium with the clay barrier. The results are given for three representative points in the engineered barrier: first near the heater, second in the central part of the buffer, and third near the rock.

For comparison, a Base Case analysis was performed using the best estimation of test conditions and parameters available at the time of performing the analyses, as discussed in [GEN 98]. The analysis provided the basic pattern of behavior, against which the results of the parametric studies were compared. The analyses were extended over 3 years of the heating stage. The following points can be noted:

– The temperature increases quickly throughout the barrier until reaching a value of 100ºC close to the heater. It rises slowly afterward, reflecting the change in thermal boundary condition (Figure 12.9).

– The bentonite near the heater dries, whereas the degree of saturation increases close to the rock. The barrier as a whole is far from saturation at the end of 3 years (Figures 12.10 and 12.11).

– Practically, no rock desaturation occurs with the parameters selected for the Base Case (Figure 12.11).

– The bentonite near the heater contracts due to drying, whereas the material near the rock swells due to wetting (Figure 12.12).

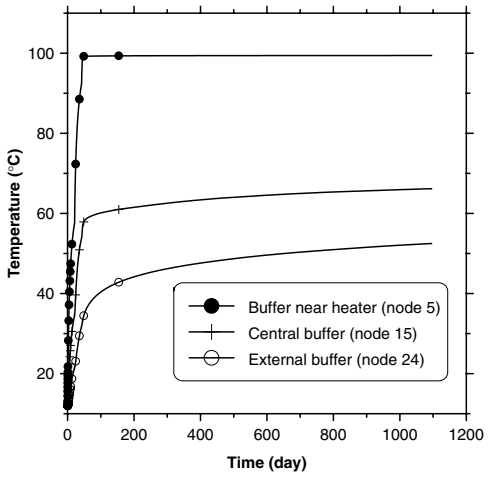

Figure 12.9. *Variation of temperature with time. Base Case analysis*

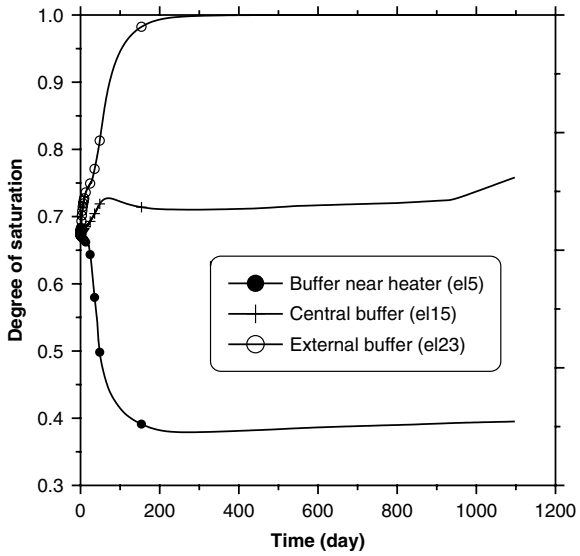

Figure 12.10. *Variation of the degree of saturation with time. Base Case analysis*

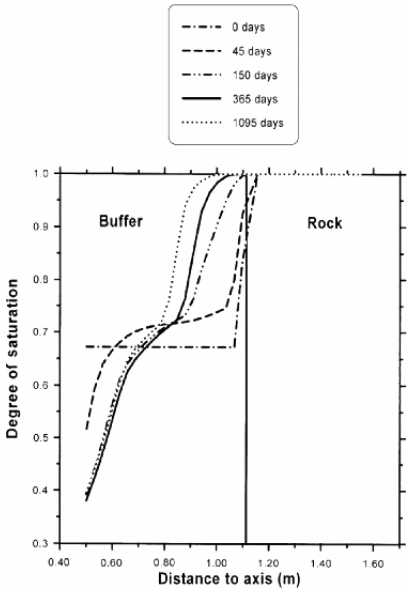

Figure 12.11. *Distribution of the degree of saturation at various times. Base Case analysis*

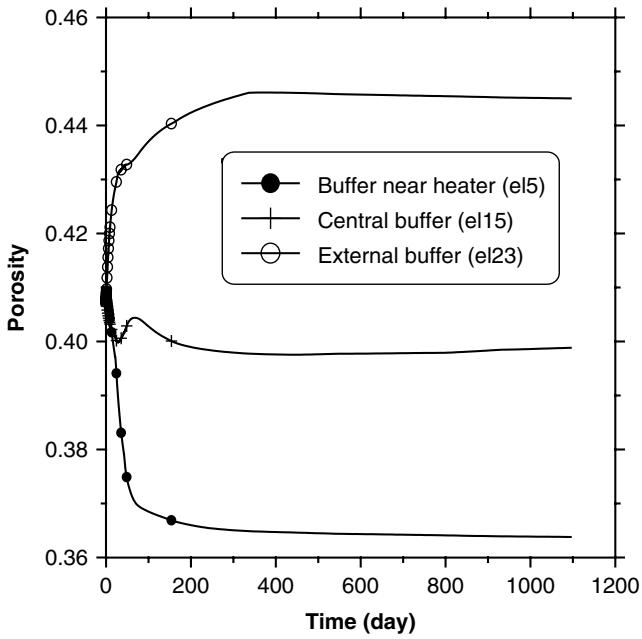

Figure 12.12. *Variation of porosity with time. Base Case analysis*

12.4.4. *Results of the parametric study*

In this section, selected results of the complete parametric study are presented. Specifically, the effects of vapor diffusion of bentonite and rock permeability as well as retention curves are discussed.

12.4.4.1. *Vapor diffusion*

In the analysis coded TB, the vapor diffusion velocity is diminished by an order of magnitude. As shown in Figure 12.13, the effect of a reduced vapor diffusion rate is particularly noticeable near the heater. It can be noted that the dynamic equilibrium between the inflow of liquid water coming from the outer buffer areas and the vapor outflow is established at a much higher value of degree of saturation. As a consequence, the pattern of porosity variation is also significantly affected with little drying contraction occurring in the inner part of the barrier (Figure 12.14). Thus, vapor diffusion rate exerts an important influence, especially on the state of the barrier close to the heater.

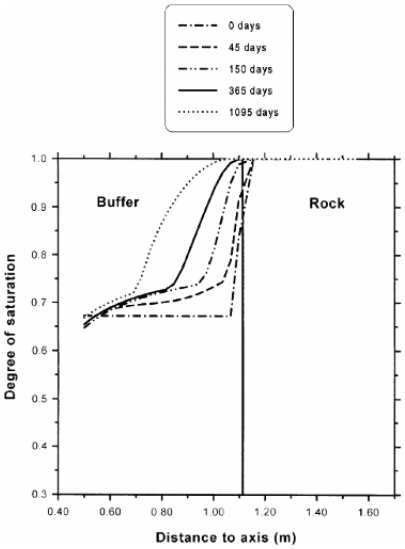

Figure 12.13. *Distribution of the degree of saturation at various times. TB analysis (reduced vapor diffusion)*

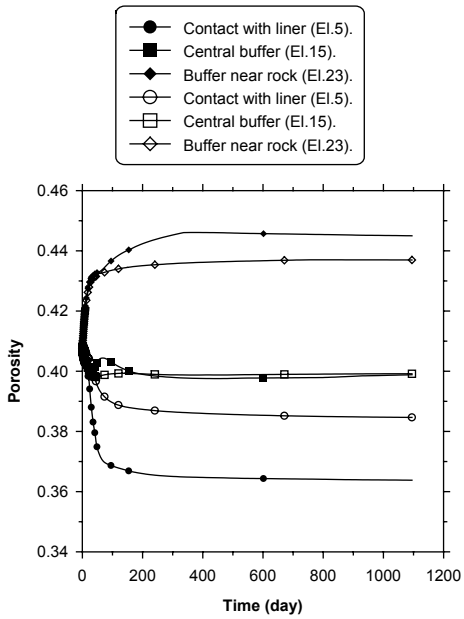

Figure 12.14. *Variation of porosity with time. TB analysis (reduced vapor diffusion). Black symbols correspond to Base Case*

12.4.4.2. *Bentonite permeability*

The analysis coded KB has been performed using an intrinsic permeability of 2×10^{-20} m^2, about three times higher than that employed in the Base Case. The effect of this higher bentonite permeability is striking. As shown in Figure 12.15, a strong desaturation of granite occurs because the rock is unable to provide the increased inflow of water demanded by the larger hydraulic conductivity of bentonite. At that point, a quasi-impermeable barrier is created in the rock that practically prevents the inflow of water into the buffer. As time goes on, the rock becomes saturated again and the progressive hydration of the buffer can then take place. This process can be clearly seen in Figure 12.16, in which the hydration stoppage due to rock desaturation can be observed. Once resaturation of granite is achieved, hydration takes place more quickly than in the Base Case because of greater bentonite permeability.

In this context, it is interesting to examine the results of the analysis coded KBPG in which the higher value of bentonite permeability has been used, but rock desaturation has been prevented by adopting a high air entry value in the retention curve of granite. As shown in Figure 12.17, no hydration delay is observed and the higher hydraulic conductivity of bentonite results in a more hydrated barrier at the end of the analysis.

12.4.4.3. *Rock permeability*

The granite intrinsic permeability used in the Base Case, 8×10^{-18} m^2 was derived as an average value by taking into account the rock mass as well as the discontinuities. Although the overall water entry value into the test area is thus preserved, it is implicitly assumed that this inflow takes place in a uniform way, which might not be the case. Therefore, there is a need to carry out an alternative analysis (KG) in which the permeability corresponding more closely to the rock mass value (10^{-18} m^2) is used. This case would then be more representative of a zone in which water inflow from large discontinuities is absent.

The distributions of the degree of saturation obtained using this lower value of rock permeability are shown in Figure 12.18. It can be noted that granite desaturation initially takes place because the rock is now unable to supply enough water to bentonite. However, eventually, the rock resaturates and hydration subsequently takes place (Figure 12.19). At the end of the analysis, the final state of saturation of the barrier is only just below that of

the Base Case. Other parametric analyses have demonstrated that the specific effect of rock permeability is, in this case, small.

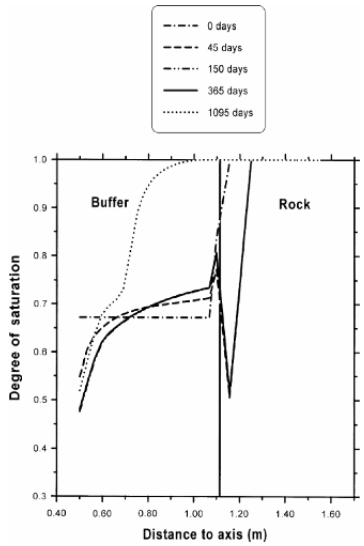

Figure 12.15. *Distribution of the degree of saturation at various times. KB analysis (increased bentonite permeability)*

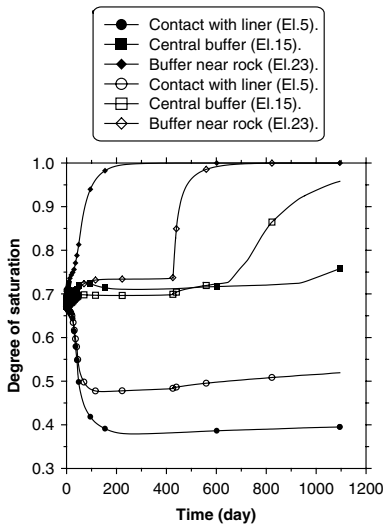

Figure 12.16. *Variation of the degree of saturation with time. KB analysis (increased bentonite permeability). Black symbols correspond to Base Case*

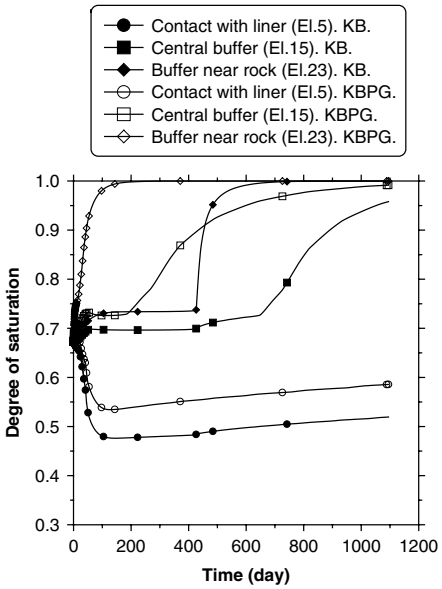

Figure 12.17. *Variation of the degree of saturation with time. KB (granite desaturation) and KBPG (no granite desaturation) analyses*

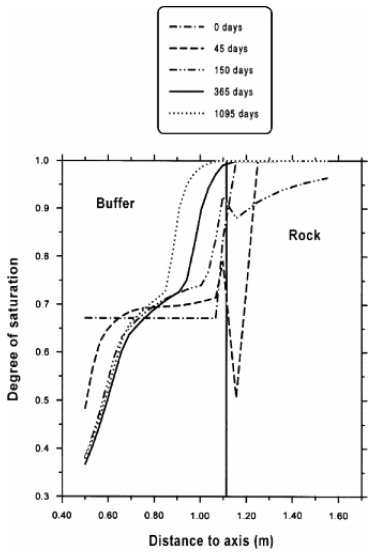

Figure 12.18. *Distribution of the degree of saturation at various times. KG analysis (lower granite permeability)*

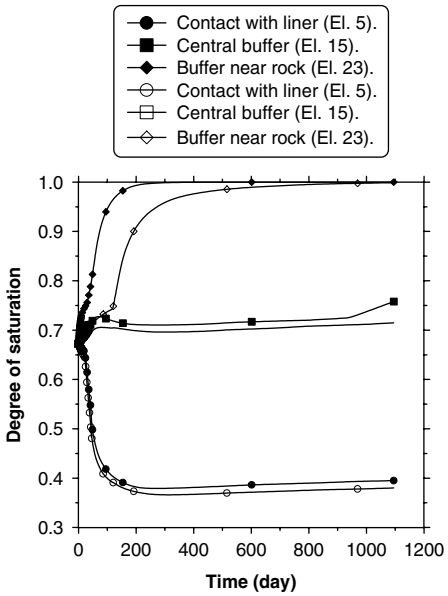

Figure 12.19. *Variation of the degree of saturation with time. KG analysis (lower granite permeability). Black symbols correspond to Base Case*

12.4.4.4. *Retention curves of granite and bentonite*

The intricacy of the interaction between the buffer and host rock becomes strikingly apparent when examining the effect of the retention curve of bentonite using only the dry branch of the basic relationship without considering any hysteresis effects, in contrast to the Base Case, where retention curve hysteresis was incorporated in the analysis. The analysis coded SH clearly demonstrated the significance of a possible rock desaturation in this case (Figure 12.20). Desaturation of the granite occurred, which was driven by the high suction values associated with the new retention curve. As desaturation was maintained throughout the analysis, a very limited amount of hydration occurred; the average increase in the degree of saturation was only 4.1%. Contrasting results were obtained in the equivalent analysis where no rock desaturation was allowed (PGSH). Here, not only did hydration proceed unimpeded, but total saturation of the buffer was achieved at the end of the analysis. The temperature field was also significantly changed owing to the increased thermal conductivity associated with a more saturated barrier.

Thus, the retention curve of bentonite plays an important role in the analysis. However, the effects are totally different depending on whether the rock desaturates or not. The interplay of the hydraulic regimes in the bentonite barrier and rock gives a high degree of complexity to the problem analyzed.

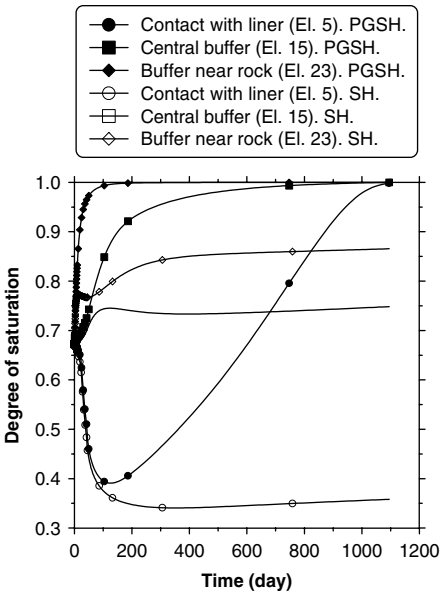

Figure 12.20. *Variation of the degree of saturation with time. Analyses SH (granite desaturation) and PGSH (no granite desaturation)*

12.5. Conclusions

The interaction between the engineered barrier and the host rock of a potential deep repository for HLW was explored by means of a series of parametric studies carried out in relation to a large-scale *in situ* heating test currently underway in the underground GTS. The study revealed a high degree of complexity in the behavior of the rock/barrier system due to the coupled nature of the thermal, hydraulic, and mechanical phenomena that occur. It was shown that vapor diffusion and hydraulic parameters have a very strong influence on the patterns of computed behavior.

It is interesting to note that a major contribution to this complexity arises from the interplay of saturated and unsaturated regimes. The large variation of

permeability and storage coefficient in the two states results in behavior patterns that could not be easily predicted beforehand. An example is the apparently paradoxical observation that a change in the retention curve may accelerate or delay hydration depending on weather the rock can be desaturated or not. Therefore, it is risky to extrapolate the effects observed with a set of parameters to another situation in which the materials may have quite different properties. The study also demonstrated the importance of performing coupled analyses with an appropriate formulation that takes into account the characteristic features of the THM behavior of unsaturated materials.

12.6. Acknowledgments

The support given by ENRESA and the European Commission to carry out this work is gratefully acknowledged. Additional assistance has been given by the Spanish Ministry of Science and Innovation through research grant BIA2008-06537.

12.7. Bibliography

[CHA 87] CHAPMAN N.A., MC KINLEY I.G., *The Geological Disposal of Nuclear Waste*, Wiley, Chichester, 1987.

[ENR 00] ENRESA, Full-scale engineered barriers experiment for a deep geological repository for high level waste in crystalline host rock, Technical Publication 01/2000. Enresa, Madrid, 2000.

[GEN 95] GENS A., "Constitutive laws", in GENS, JOUANNA, AND SCHREFLER (eds.), *Modern Issues in Non-saturated Soils*, Springer-Verlag, Vienna, p. 129-158, 1995.

[GEN 98] GENS A., GARCÍA-MOLINA A.J., OLIVELLA S., ALONSO E.E., HUERTAS, F., "Analysis of a full scale in situ test simulating repository conditions", *Int. J. Numer. Anal. Methods Geomech.*, vol. 22, p. 515-548, 1998.

[GEN 00] GENS A., OLIVELLA S., "Non isothermal multiphase flow in deformable porous media. Coupled formulation and application to nuclear waste disposal", in DAVID W. SMITH AND JOHN P. Carter (eds.), *Developments in Theoretical Geomechanics – The John Booker Memorial Symposium*, A.A. Balkema, Rotterdam, p. 619-640, 2000.

[GEN 03] GENS A.. "The role of geotechnical engineering for nuclear energy utilisation". *Proc. 13th. Europ. Conf. on Soil Mechanics and Geotech. Eng.*, Prague, vol. 3, p. 25-67, 2003.

[GEN 09a] GENS A., GARITTE, B., OLIVELLA, S., VAUNAT, J. "Application of multiphysical geomechanics un underground nuclear waste storage", *European Journal of Environmental and Civil Engineering*, vol. 13, no. 7-8, p. 937-962, 2009.

[GEN 09b] GENS A., SÁNCHEZ M., GUIMARÃES L. DO N., ALONSO E.E., LLORET A., OLIVELLA S., VILLAR M.V., HUERTAS F., "A full-scale *in situ* heating test for high-level nuclear waste disposal: observations, analysis and interpretation", *Géotechnique*, vol. 59, p. 377-399, 2009.

[GEN 10] GENS A. "Soil-environment interactions if geotechnical engineering. 47th Rankine Lecture", *Geotechnique*, vol. 60, p. 3-74, 2010.

[OLI 94] OLIVELLA S., CARRERA J., GENS A., ALONSO E.E., "Non-isothermal multiphase flow of brine and gas through saline media", *Transport in Porous Media*, vol. 15, p. 271-293, 1994.

[OLI 96] OLIVELLA S., GENS A., CARRERA J., ALONSO E.E., "Numerical formulation for a simulator (CODE_BRIGHT) for the coupled analysis of saline media", *Engineering Computations*, vol. 13, p. 87-112, 1996.

[OLI 00] OLIVELLA S., GENS A. "Vapour transport in low permeability unsaturated soils with capillary effects", *Transport in Porous Media*, vol. 40, p. 219–241, 2000.

[OLI 05] OLIVELLA S., GENS A., "Double structure THM analysis of a heating test in a fractured tuff incorporating intrinsic permeability variations", *International Journal of Rock Mechanics and Mining Sciences*, vol. 42, p. 667-679, 2005.

[PIN 96] PINTADO X., LLORET A., THM laboratory tests in FEBEX phase I. Report 70-UPC-L-3-01, Universitat Politècnica de Catalunya, Barcelona, 1996.

[VAN 07] VAN GEET M., VOLCKAERT G., BASTIENS W., MAES N., WEETJENS E., SILLEN X., VALLEJAN B., GENS A., "Efficiency of a borehole seal by means of pre-compacted bentonite blocks", *Physics and Chemistry of the Earth*, vol. 32, p. 123-134, 2007.

[VIL 96] VILLAR M.V., PELAYO M., Characterization of 'La Serrata' clay used in the FEBEX project, Technical Report. 54A1411196, CIEMAT, Madrid, 1996.

Chapter 13

Soil–Pipeline Interaction in Unsaturated Soils

13.1. Introduction

Pipelines used for the transport of energy and services are very important lifelines to modern society. The vital role that they play in our present economy is reflected in the many kilometers of pipelines laid in onshore and offshore locations worldwide. They are often buried in the ground, which provides protection and support, but ground movements can induce unwanted loading on the pipelines. Progressive differential ground movements, such as those caused by landslides, can initiate pipeline deformations that may impact serviceability or trigger failure, such as buckling or wrinkling. Hence, in order to maintain the integrity of pipelines under various conditions, it is important to evaluate soil loading on pipelines in response to the relative movement of the surrounding soil.

Pipelines are generally placed in unsaturated soils (Figure 13.1). However, pipeline design guidelines [ASC 84] are based on the assumption that the soil is either dry or fully saturated. For many years, the mechanical behavior of unsaturated soils was either ignored or approached inappropriately by using the traditional framework of saturated soil mechanics. For certain geotechnical problems, it may not be acceptable to have such assumptions because the meniscus formed between soil particles (see Figure 13.1) creates an additional normal force between the particles

---

Chapter written by Dilan ROBERT and Kenichi SOGA.

by suction, which in turn forms temporary bonds. For earth structures, partial saturation can enhance the stability. Conversely, underground infrastructure systems, such as buried pipelines can be adversely affected by the increased soil loading.

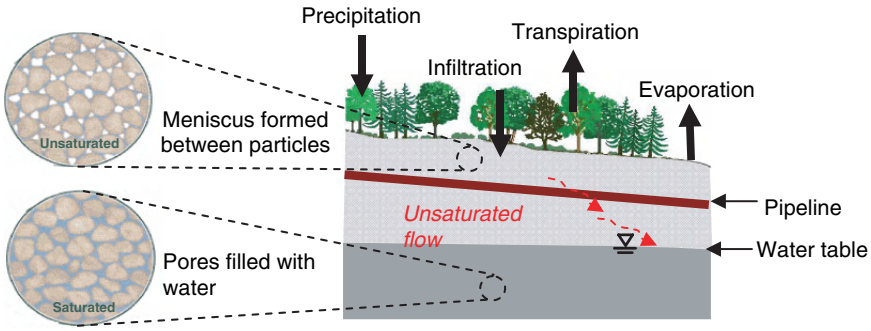

Figure 13.1. *Pipeline buried in unsaturated zone*

A recent series of large-scale physical model experiments at Cornell University (CU) showed that the soil loads by lateral pipeline movement in dry and unsaturated sands are virtually the same [ORO 08]. In contrast, other recent experiments performed at the Pipeline Engineering Research Laboratory (PERL) of Tokyo Gas, Japan, showed a higher peak load under unsaturated conditions when compared with dry conditions. Thus, the effect of partial saturation on soil loading to pipeline may be different depending on the soil type, moisture condition, and density. The current study investigates this problem through constitutive modeling of the unsaturated soils used for testing and finite element (FE) analysis of soil–pipeline interactions in unsaturated soils.

13.2. Large-scale physical model experiments

Physical model experiments were conducted recently at PERL and CU to investigate the effect of partially saturated soil on soil loading to the pipeline when there are relative lateral displacements. Some of the results are presented here, but further details can be found in [ROB 10].

13.2.1. *Experimental setup*

The test setup used in the PERL experiments is shown in Figure 13.2. The experiment facilities were designed to conduct lateral pipeline loading tests at a H/D (H, the height from the ground surface to the center of the pipe; D, the diameter of the pipe) of 6 with large pipe displacements (~400 mm). The tests were conducted using a 114.6 mm diameter pipe. As shown in Figure 13.2, the testing tank was fixed to the moving base to which the displacement was applied to induce pipe displacement relative to the soil. The pipe was connected to a load cell via a steel rope to measure the soil load. Displacement sensors were used to monitor the pipe displacements in both horizontal and vertical directions. Soil pressure sensors were placed at the model boundaries to examine the boundary effects at the base of the test tank and in the soil at the pipe level. The pipe was restricted at both the ends using counter weights (each 40 kg in weight) in order to limit the differential settlements of the pipe due to its self-weight.

The experimental setup used in the CU experiments (Figure 13.3) is comparable with that used in the PERL experiments. The tests were conducted using a 124 mm diameter pipe. The horizontal force was applied using two long-stroke hydraulic actuators and the magnitude was measured using load cells. The loading arm was designed so that the test pipe could rise without vertical restraint as it was displaced laterally through the soil.

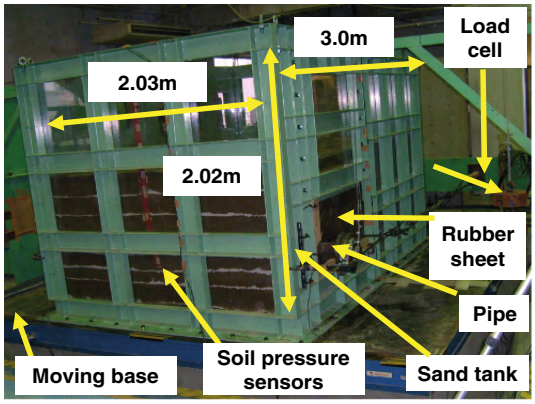

Figure 13.2. *Experimental setup for PERL experiments*

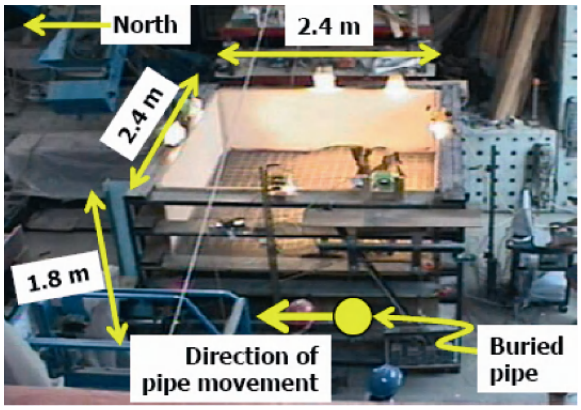

Figure 13.3. *Experimental setup for CU experiments [ORO 08]*

13.2.2. *Experimented sands*

Here, the soils used in the experiments are referred to as Cornell sand (G_s=2.694, e_{max}=0.705, and e_{min}=0.393) and Tokyo Gas sand (G_s=2.646, e_{max}=0.946, and e_{min}=0.5) for CU and PERL experiments, respectively.

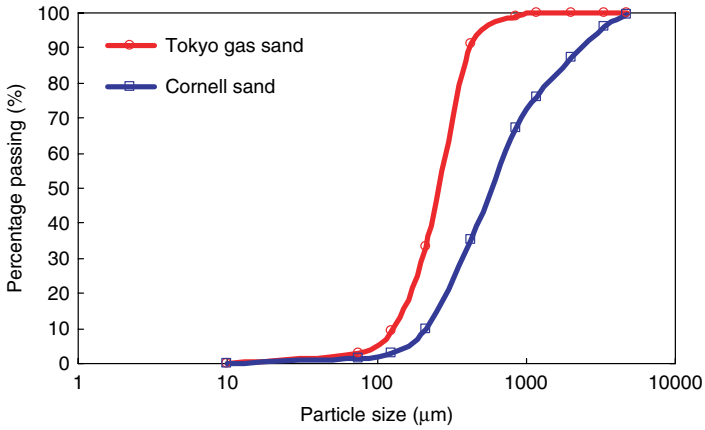

Figure 13.4. *Particle size distribution for Tokyo Gas and Cornell sands*

The particle size distributions of the sands are presented in Figure 13.4. It can be observed that the grain sizes of Tokyo Gas sand are uniformly distributed within the range of 0.9–0.08 mm (C_c=1.06, C_u=2.1), whereas those of Cornell sand (C_c=0.9, C_u=3.3) are relatively well graded. The percentage of finer particles with grain size smaller than 0.42 mm is about 90% for Tokyo Gas sand and approximately 30% for Cornell sand. Therefore, Tokyo Gas sand can be considered to be finer and comparably more well-sorted than Cornell sand.

13.2.3. *Experimental results*

Some of the loading displacement curves obtained from the experiments are shown in Figures 13.5 and 13.6 for the PERL and CU experiments, respectively. Two curves are shown: one obtained in dry conditions, and the other obtained in unsaturated conditions. The initial conditions of the sands used in the experiments are shown in the figure legend. S_r and γ_d are the degree of water saturation and the dry density of sands, respectively. The soils (either dry or moist) were compacted to comparable energy inputs.

In the PERL experiments, the dry density of the dry sand model was 15.6 kN/m^3, whereas that of the unsaturated sand model (S_r=61.8%) was 15.2 kN/m^3. Hence, the moist conditions in the unsaturated model created looser soil structure than the dry conditions. Despite this, pipe loading was greater in the unsaturated sand model when compared with the dry sand model, as shown in Figure 13.5.

In the CU experiments, the dry density of the dry sand model was 16.9 kN/m^3, whereas that of the unsaturated sand model (S_r=17.1%) was 16.3 kN/m^3. Again, the moist conditions in the unsaturated sand model created a looser structure when compared with the dry sample. However, in this case, contrary to what was observed in the PERL experiments, the pipe loading in the unsaturated sand model was about the same as in the dry sand model, as shown in Figure 13.6. These results illustrate the potentially complicated soil–pipeline interaction that occurs in unsaturated soils.

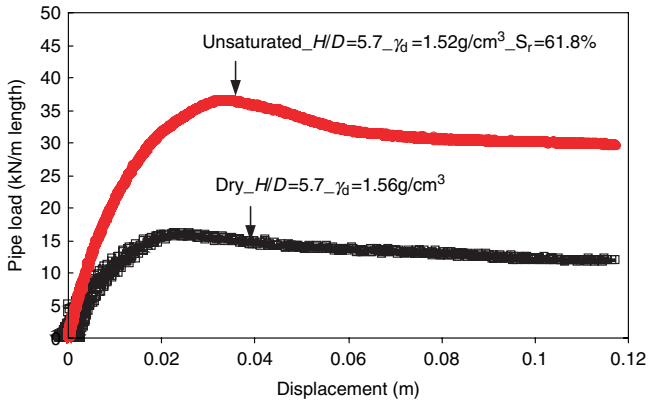

Figure 13.5. *PERL experiment results*

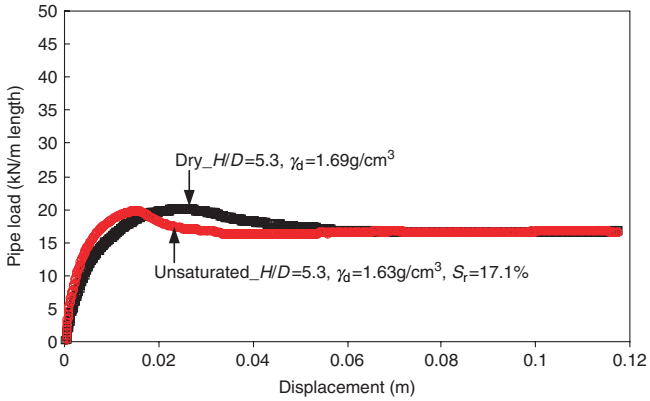

Figure 13.6. *CU experiment results*

13.3. Behavior of unsaturated sands

13.3.1. *Compaction and soil moisture tests*

Soil compaction tests were conducted on the two sands. Four different energy levels were applied including the standard and modified proctor compaction tests. Figures 13.7 and 13.8 show the test results for Tokyo Gas and Cornell sands, respectively. The amount of energy applied to the soils is indicated in the legend.

As expected, compaction curves depict the same trend of varying dry densities with moisture contents. As the moisture content decreases from fully saturated condition to a lower value, the dry density increases to a maximum before decreasing again. The test results also show that the fully dry sand tends to have a greater dry density than the dry density at the optimum water content for both the sands under all energy levels tested, except in the case of the modified proctor compaction.

Figures 13.7 and 13.8 also show the soil states at which the large-scale pipeline experiments were conducted (open circle for the dry test and cross symbol for the unsaturated test). The results show that the amount of energy applied to the soil in the physical model experiments is less than the lowest possible energy level tested in determining the compaction curves.

In both PERL and CU experiments, the soil model used in the dry sand model had a better packing structure and higher density than the unsaturated sand model for a given compaction effort, which was also observed in the compaction test data.

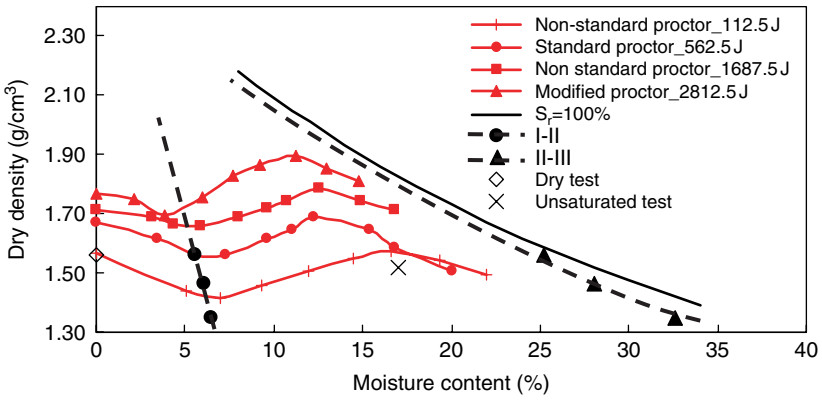

Figure 13.7. *Compaction curves for Tokyo Gas sands*

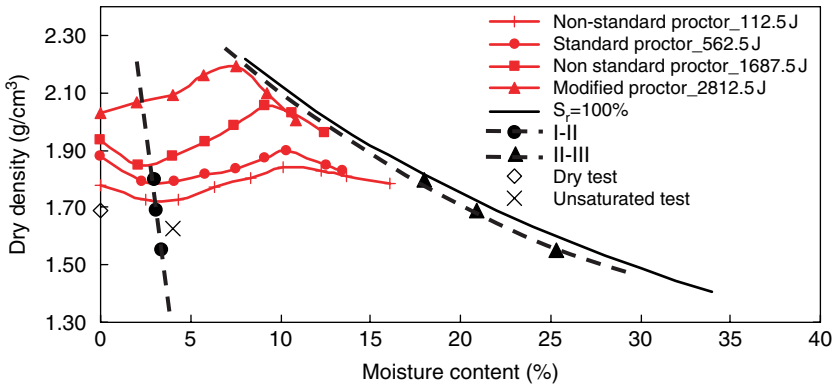

Figure 13.8. *Compaction curves for Cornell sands*

The full saturation line (S_r=100.0%) as well as the transition lines between the pendular region (I) and funicular region (II), and between the funicular region (II) and capillary region (III), are also shown in the compaction curve plots. The transition lines are derived based on the soil water characteristic curves (SWCCs) obtained by the suction plate technique, as shown in Figures 13.9 and 13.10.

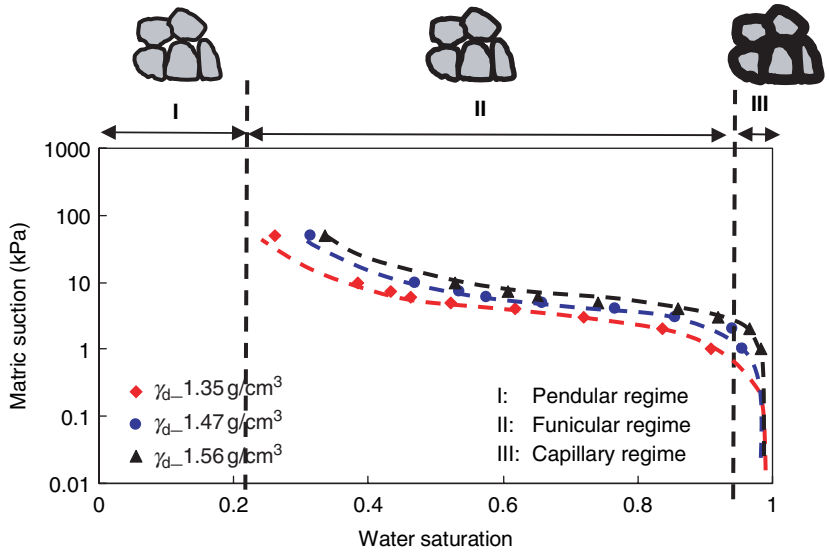

Figure 13.9. *SWCC for Tokyo Gas sand*

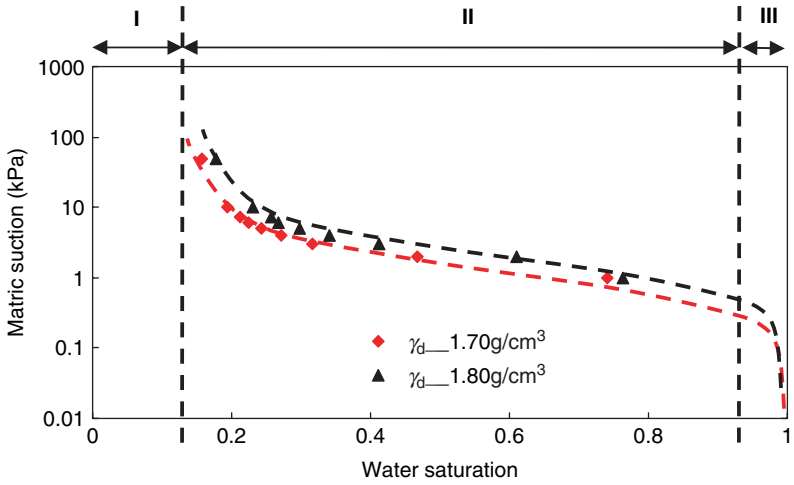

Figure 13.10. *SWCC for Cornell sand*

As described earlier, Cornell sand is coarser and well graded, whereas Tokyo Gas sand is finer and well sorted. Owing to the higher amount of fine particles present in Tokyo Gas sand, larger amount of energy (suction) is required to withdraw a specified amount of water from the pore spaces, as shown in Figures 13.9 and 13.10.

13.3.2. *Triaxial compression tests*

Consolidated drained triaxial compression tests were performed on the two sands in saturated and unsaturated conditions. The experiments were conducted at a fixed dry density (Tokyo Gas sand: 1.58 g/cm^3; Cornell sand: 1.69 g/cm^3) and for a range of moisture contents (suction pressures), with the results presented in Figures 13.11 and 13.12. The tests were conducted at a net confining stress of 10 kPa.

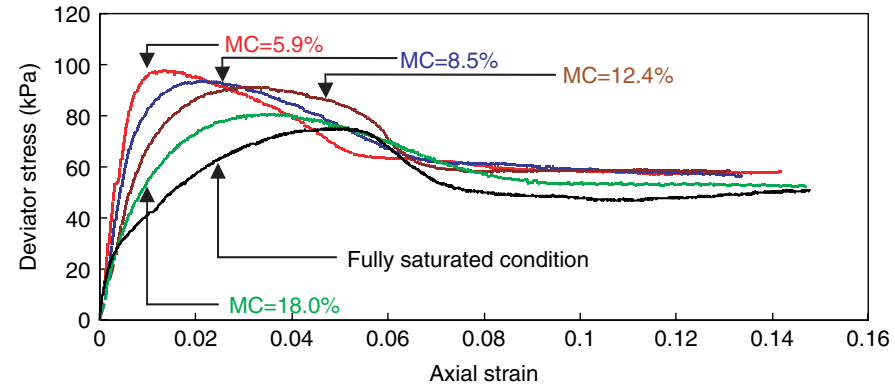

(a) *Stress–strain characteristics*

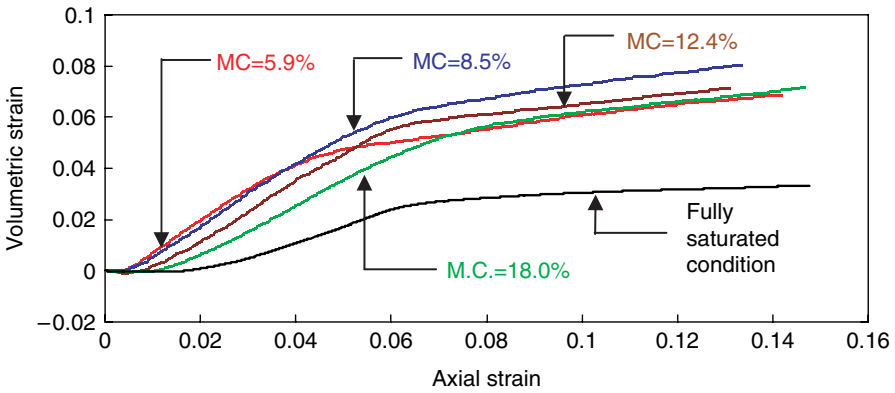

(b) *Volume change characteristics*

Figure 13.11. *Stress–strain (a) and volume change (b) characteristics of Tokyo Gas sand at the dry density of 1.58 g/cm^3 and net confining stress of 10 kPa*

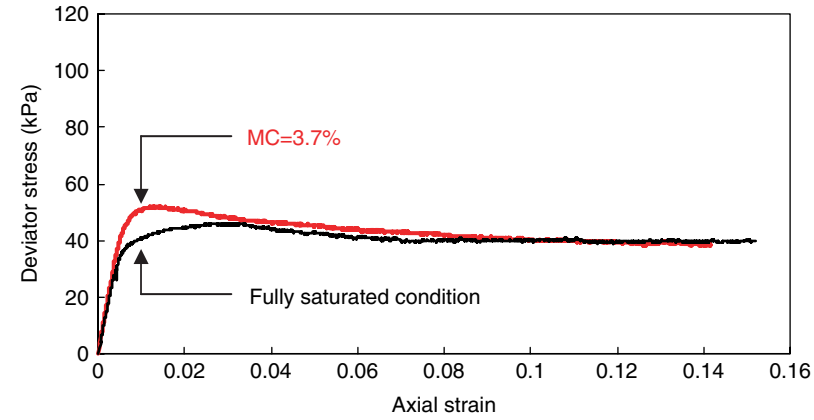

(a) *Stress–strain characteristics*

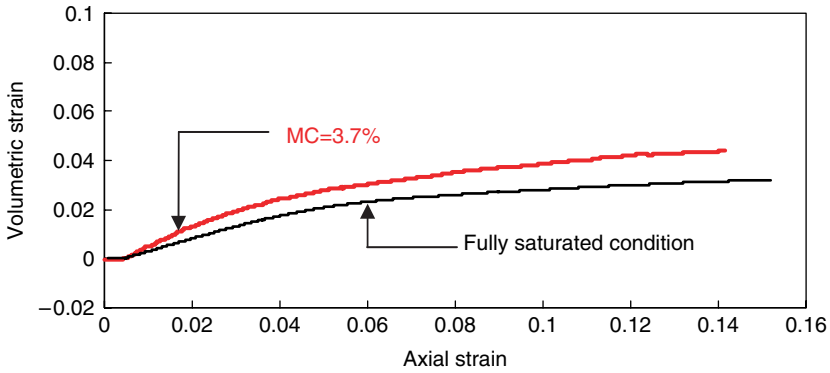

(b) *Volume change characteristics*

Figure 13.12. *Stress–strain (a) and volume change (b) characteristics of Cornell sand at the dry density of 1.69 g/cm^3 and net confining stress of 10 kPa*

When tested at the same dry density, the Cornell sand (Figure 13.12) gave slightly higher strength measurements at 3.7% moisture content than for fully saturated conditions. For Tokyo Gas sand (Figure 13.11), the strength increased as the moisture content decreased for a given dry density. The apparent cohesion due to the presence of fine particles seems to have influenced the strength at low confining pressures.

The dilation characteristics for both the sands were related to the amount of suction. As shown in Figures 13.11(b) and 13.12(b), greater dilation is observed when suction increases (i.e. decreasing moisture content).

As suction increases, sand particles tend to adhere together to form larger aggregates, which produces larger dilation when sheared.

13.4. Numerical modeling of the behavior of unsaturated sands

13.4.1. *Stress state of unsaturated sands*

The state of stress in unsaturated soil is fundamentally different from that of stress in dry or fully saturated soil. Unlike dry or saturated soils that are two-phase systems essentially comprising soil particles and pore air or pore water (depending on dry or saturated condition), unsaturated soils are three-phase systems comprising solids (soil particles), liquid (pore water), and gas (pore air). The relative amounts and corresponding pressures of the pore water and pore air have a direct impact on the state of stress acting at the particle-particle contacts, and consequently, on the macroscopic mechanical behavior of the soil mass (shear resistance and volume change).

Owing to the fact that Terzaghi's effective stress is valid only for the limit state of the total saturation of pores with one fluid alone (water or air), the concept of Bishop's effective stress [BIS 59] converts a multiphase and a multi-stress medium into a mechanically equivalent single-phase and stress-state continuum. It uses the following equation to define the effective stress:

$$\sigma'_{ij} = \sigma^{\text{net}}_{ij} + \chi s \delta_{ij}, \qquad [13.1]$$

where $\sigma^{\text{net}}_{ij} = \sigma_{ij} - u_{\text{a}}\delta_{ij} = \text{net stress}$, $s = u_{\text{a}} - u_{\text{w}} = \text{matric suction}$, χ=effective stress parameter, $\sigma'_{ij} = \text{effective stress tensor}$, σ_{ij}=total stress tensor, u_{w}=pore water pressure, u_{a}=pore air pressure, and δ_{ij}=Kronecker's delta $(\delta_{ii} = 1; \delta_{i \neq j} = 0)$. The first term on the right-hand side of equation [13.1] represents the component of net normal stress applicable to bulk soil (which is the case for a completely dry system). The product $\chi(u_{\text{a}}–u_{\text{w}})$ represents the interparticle stress (suction stress) due to suction.

Although there is some criticism in the literature regarding the use of Bishop's effective stress concept for modeling the behavior of unsaturated soils, especially the volume change characteristics (e.g. [JEN 62]), much of the arguments are invariably formulated within the context of a linearly elastic theoretical framework. More recent works [BOL 96, JOM 00, NUT 09,

SHE 04, TAM 04, WHE 03] show that the inclusion of product $S_r \times s$ in the effective stress formulation makes the hydromechanical coupling straightforward, featuring a direct modification in effective stress upon suction change. The non-recoverable deformations, such as collapse, can be modeled within this effective stress framework by defining the yield surface as a function of suction (e.g. [BOL 96, KHA 01, KOH 93, LOR 00, MOD 94]).

In the current study, the generalized effective stress has been defined within a consistent stress–strain framework as defined by equation [13.2] [SHE 04].

$$\begin{pmatrix} \sigma'_{ij} = \sigma^{\text{net}}_{ij} + S_r s \delta_{ij} \\ s = u_a - u_w \end{pmatrix} \quad \text{and} \quad \begin{pmatrix} \varepsilon_{ij} \\ S_r \end{pmatrix}, \qquad [13.2]$$

where S_r is the degree of saturation and ε_{ij} is the strain tensor.

The plastic behavior is modeled using appropriate elastoplastic constitutive models (in this study, Mohr–Coulomb and Nor–Sand plasticity models) and considering the suction hardening effect. In the current research, it is shown that this generalized effective stress framework coupled with an appropriate unsaturated soil model is capable of providing accurate predictions of soil–pipeline interaction in unsaturated soils.

13.4.2. *Modified Mohr–Coulomb model to simulate the unsaturated soil behavior*

The Mohr–Coulomb soil model is a simple linear-elastic, perfectly plastic model, which is widely used for design applications in geotechnical engineering requiring simulation of material response under monotonic loading. The Mohr–Coulomb failure criterion assumes that failure occurs when the shear stress on any point in a material reaches a value that depends linearly on the normal stress in the same plane, as defined by equation [13.3]:

$$\tau_f = c' + \sigma' \tan \phi'. \qquad [13.3]$$

The material constant c′ defines the cohesion yield stress for the hardening behavior of the material, and the friction angle ϕ controls the

shape of the yield surface in the deviatoric plane. τ_f and σ' are the failure shear stress and the normal effective stress on the failure plane.

The unsaturated soil version of Mohr–Coulomb model uses the generalized effective stress as follows:

$$\tau_f = c' + \chi_f (u_a - u_w)_f \tan\phi' + (\sigma - u_a)_f \tan\phi'. \quad [13.4]$$

$$= c' + c'' + (\sigma - u_a)_f \tan\phi'. \quad [13.5]$$

where $c'' = \chi_f (u_a - u_w)_f \tan\phi'$. c' has two components: (i) the classical cohesion c'_s, which is the shearing resistance arising from interparticle locking and interparticle physicochemical forces, and (ii) the capillary cohesion c'_u, which is considered to be due to the suction-induced hardening occurring at the microscopic particle contact level. For both the sands, the term c'_s is found to be zero. The term c'' is the macroscopic capillary cohesion term, which describes the mobilization of macroscopic suction stress $[\chi(u_a–u_w)]$ in terms of shearing resistance. Hence, the apparent cohesion of unsaturated soils is represented by $(c'_u + c'')$.

Triaxial test results on Tokyo Gas sand show that the maximum dilation angle (ψ_{max}) and the effective apparent cohesion (c'_u) are strongly affected by the changes in water saturation. Figures 13.13 and 13.14 show the variation of ψ_{max} and c'_u, respectively, with water saturation at a dry density of 1.58 g/cm^3.

Initially, the values of c'_u increase with decreasing water saturation from full saturation conditions. After reaching a peak, the value of c'_u then decreases with further decrease in water saturation. At residual water conditions, the contribution of microscopic capillary cohesion is almost negligible. For Cornell sand, it was found that the magnitude of c'_u is very small when compared with the contribution of the macroscopic cohesion c'' (not shown).

For the dilation characteristic, the dilation angle peaks when the water saturation is close to residual saturation. Both the sands showed similar behavior.

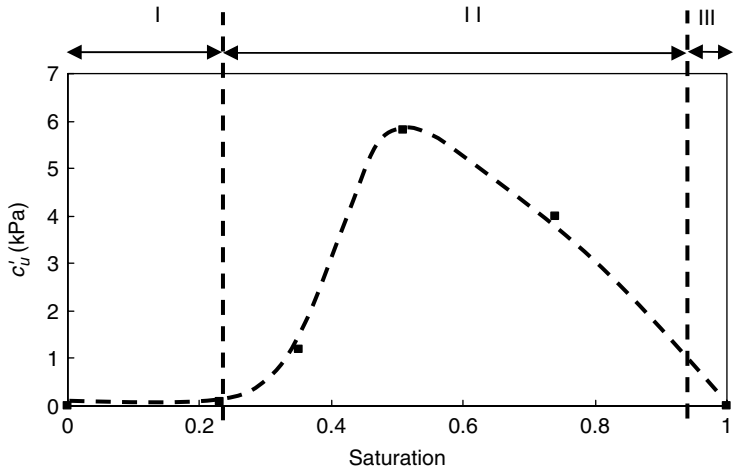

Figure 13.13. *Variation of effective cohesion* c'_u *with saturation for Tokyo Gas sand at the dry density of 1.58 g/cm*^{3}

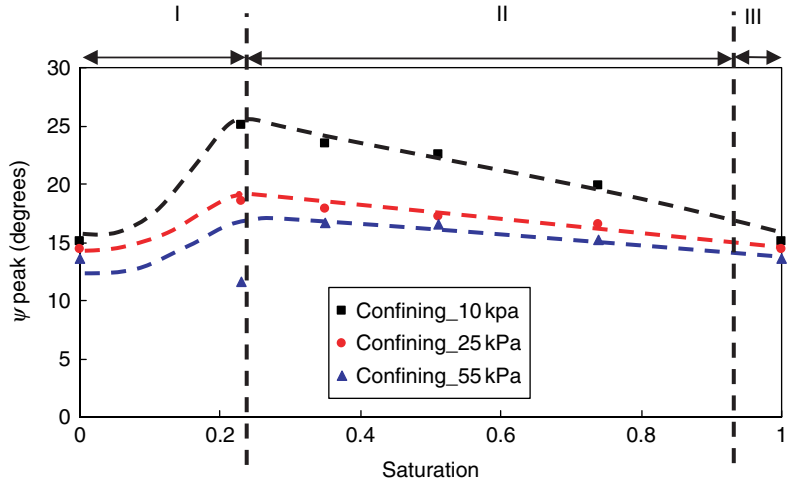

Figure 13.14. *Variation of peak dilation* ψ_{peak} *with saturation for Tokyo Gas sand at the dry density of 1.58 g/cm*^{3}

To model the observed softening behavior and the constant volume shearing at critical state, the mobilized friction (ϕ_{mob}), dilation angle (ψ_{mob}), and apparent cohesion (c'_u) were defined to vary with plastic deviatoric

shear strain (γ^{p}_{dev}). Figure 13.15 schematically depicts the variation of ϕ_{mob} and ψ_{mob} as a function of γ^{p}_{dev}. ϕ_{mob} and ψ_{mob} vary from peak values (ϕ_p, ψ_p) to the critical state friction angle (ϕ_{cs}) and zero dilation, respectively. γ^{p}_{f} defines the plastic deviatoric shear strain at softening completion. Further details of the model, including the formulations and validations against element test data can be found in [ROB 10].

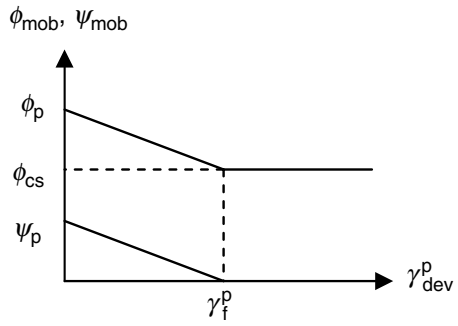

Figure 13.15. *Variation of mobilized friction (ϕ_{mob}) and dilation angle (ψ_{mob}) with plastic deviatoric shear strain*

13.4.3. *Modified Nor-Sand model to simulate the unsaturated soil behavior*

The Nor-Sand model is a generalized Cambridge-type constitutive model for sand, which is based on the critical state theory. It uses the state parameter concept [BEE 85] and attempts to accurately reproduce dilation and softening on the dry side of the critical state. This is achieved by postulating infinite isotropic normal consolidation loci, which allows separation of the intrinsic state from the over-consolidation state. The main feature of the Nor-Sand model is the use of rate-based hardening using the state parameter, ψ, to size the yield surface. The Nor-Sand model adopts the associated flow rule, yet predicts realistic dilation.

In this study, the saturated version of the Nor-Sand model has been modified in conjunction with the generalized effective stress framework [ROB 10]. The unsaturated version includes the effect of increasing apparent tensile strength by water meniscus at particle contacts (cohesion enhancement) as well as enhanced dilation (dilation enhancement). These two hardening effects as well as the classical plastic hardening effect make

the proposed model a triple-hardening model. The magnitudes of the former two hardening mechanisms depend on both water saturation and plastic strain, whereas the latter hardening mechanism depends only on the plastic strains. Further details of the model can be found in [ROB 10].

13.5. Numerical modeling of the physical model experiments

13.5.1. *Finite element analysis*

The FE simulations of the laterally loaded pipeline experiments conducted at PERL and CU was carried out using ABAQUS/EXPLICIT [ABA 08]. The unsaturated models presented in the previous section were implemented. The simulations were performed in plane strain conditions. The soil and pipe elements were four-node bilinear, plane strain, reduced integration with hourglass control (CPE4R) elements. Sand behavior was modeled using the modified Mohr–Coulomb model as well as the modified Nor-Sand model, whereas the pipe was assumed to be a linear elastic material (ASTM Grade A-36 steel).

The model parameters for both the constitutive models were evaluated from the triaxial drained compression test data, some of which were presented earlier. The input parameters for the modified Mohr–Coulomb model were derived by interpolating the calibrated model parameters with varying dry densities, moisture contents, and confining stresses. Hence, the model demands different sets of model parameters depending on its initial soil density, water saturation, and pipe embedment depth. In contrast, the modified Nor-Sand soil model requires only one set of model parameters to simulate the sand behavior over the range of void ratios, confining stresses, and water saturations, which make the model versatile.

13.5.2. *Finite element results*

The load-displacement relationships calculated from the FE simulations are presented in Figure 13.16(a) and (b) for the PERL and CU cases, respectively. The results of the two soil models are presented.

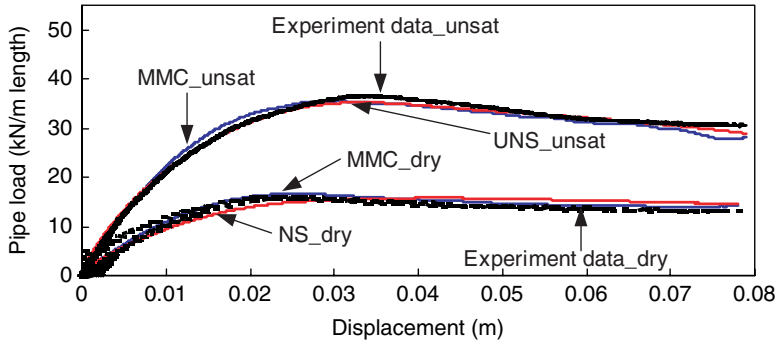

(a) *Tokyo gas sand analyses*

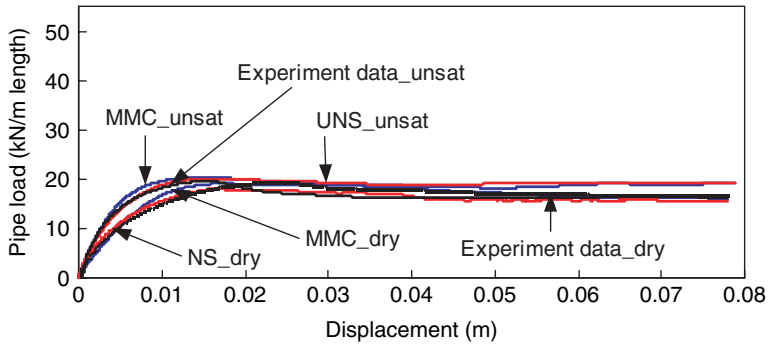

(b) *Cornell sand analyses*

Figure 13.16. *Results of the FE analyses conducted to simulate the physical model experiments based on (a) Tokyo Gas sand and (b) Cornell sand*

It was found that soil loading on a pipeline can be accurately predicted using the developed constitutive models in dry and unsaturated conditions of both the sands. The loading responses match in the regimes of stiffness, peak, and softening when compared with the experimental results. Hence, the models are capable of capturing the increase in strength and dilatancy of sands in unsaturated conditions.

13.6. Dimensionless force – *H*/*D* relationship for pipelines in unsaturated soils

Further FE analyses were conducted to investigate the behavior of pipelines under different embedment depths at varying moisture contents of both Tokyo Gas and Cornell sands. The current study focuses on the behavior of a steel pipeline of 0.1146 m diameter embedded into the sands having an initial dry density of 1.61 g/cm^3. The sand was modeled using the unsaturated version of the Nor-Sand model and the pipe was assumed to be a linear elastic material.

The results of the FE analyses are presented by normalizing the maximum pipe load and embedment depth, as shown in Figure 13.17(a) and (b) for Tokyo Gas and Cornell sand, respectively. The maximum dimensionless load, N_q^{sat} applied to the pipeline is defined as:

$$N_q^{\text{sat}} = \frac{F_{\max}}{\sigma' DL} = \frac{F_{\max}}{\gamma_{\text{d}} HDL}, \qquad [13.6]$$

where $F_{\max}$ is the maximum lateral force on the pipe, γ_{d} is the dry density of the saturated sand, H is the height from the ground surface to the level of the pipe, D is the diameter of the pipe, L is the length of the pipe, and σ' is the effective stress at the pipe level as defined by equation [13.7].

$$\sigma'_{ij} = \sigma_{ij}^{\text{net}} - S_{\text{r}} s, \qquad [13.7]$$

where s=u_{a}–u_{w}=matric suction (negative) and other symbols hold the same definition as defined in section 13.4.1. Accordingly, N_q^{unsat} expresses the pipeline load that is normalized by suction, soil density, embedment depth, pipeline diameter, and length.

Figure 13.17 shows the variation of N_q^{unsat} with H/D obtained from the FE analysis. The diameter of the pipe used in the analyses was 114.6 mm and the embedment ranged from 0.23 m (H/D=2.0) to 1.32 m (H/D=11.5).

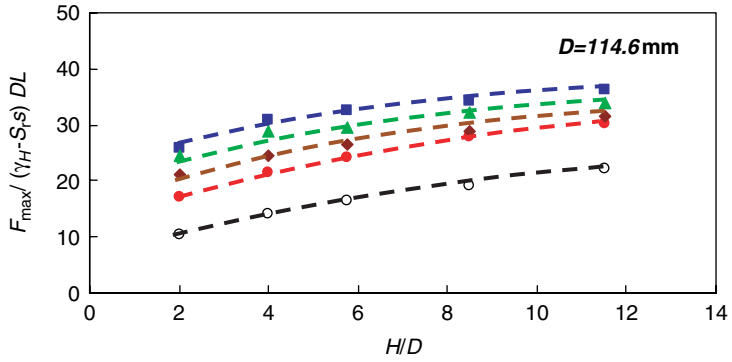

Figure 13.17(a). *Results of the FE analyses conducted to investigate the effect of moisture content on the behavior of pipelines at different H/Ds in Tokyo Gas sand*

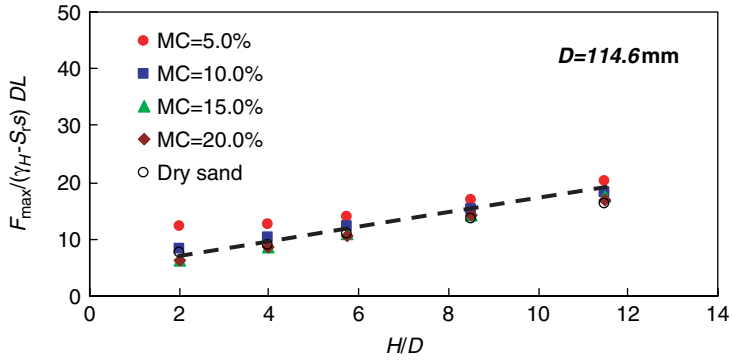

Figure 13.17(b). *Results of the FE analyses conducted to investigate the effect of moisture content on the behavior of pipelines at different H/Ds in Cornell sand*

For Tokyo Gas sand, the dimensionless pipeline loading, N_q^{unsat} is clearly affected by moisture content (suction pressure) due to the contribution of the apparent cohesion ($c_u^{'}$) that is present in this soil (see Figure 13.13). The soil loading increases with moisture content and then decreases when the moisture content increases from 10% (40% water saturation) to 15% (60% water saturation), which is reflected by a similar behavior observed in the triaxial compression tests (Figure 13.13). The largest c_u' was measured when the moisture content was 13.4% (55% water saturation).

In contrast, for Cornell sand, N_q^{unsat} was more or less independent of moisture content (or suction) as shown in Figure 13.17(b). That is, the soil loading in dry sand is similar to that in unsaturated sand. This is mainly due to the absence of apparent cohesion effect, as discussed previously. However, N_q^{unsat} below the 5% moisture condition lie slightly above the dry sand envelope, apparently due to the existence of very small c'_{u} at low moisture contents.

13.7. Conclusions

An understanding of pipeline response in unsaturated soil can be important in pipeline design, because its suction effect may strengthen the soil. Rational designs require knowledge of the soil force resulting from relative soil–pipeline movement in unsaturated soil. Recent investigation at CU through a series of large-scale physical model experiments showed that the soil loads by lateral pipeline movement in dry and unsaturated sands are virtually the same [ORO 08]. In contrast, other recent experiments performed at the PERL of Tokyo Gas, Japan, showed a higher peak load under unsaturated conditions when compared with dry conditions. The causes for this discrepancy were investigated by conducting a series of laboratory experiments on the two sands used for the pipeline experiments as well as through performing FE analysis of the soil–pipeline interaction.

The results showed that the behavior of unsaturated sands depends on the grain size characteristics. The effect of partial saturation on the mechanical behavior was more pronounced in finer and well-sorted Tokyo Gas sand when compared with coarser and well-graded Cornell sand.

The pipeline behavior in unsaturated soil was successfully simulated using Bishop's effective stress, and advanced elastoplastic constitutive soil models. Soil loading using Tokyo Gas sand varied significantly with the moisture content because of larger suction pressures and apparent cohesion effects. In contrast, the soil loading results of dry Cornell sand was comparable with the tests using unsaturated Cornell sand because of smaller suction and negligible apparent cohesion. These findings suggest that careful characterization of soil in the unsaturated state is necessary for soil–pipeline interaction problems.

13.8. Acknowledgments

This research is the outcome of the effort and continuous support from many interested parties. Tokyo Gas Co. Ltd, Japan, and Cornell University, USA kindly provided the results of their large-scale physical model experiments. In particular, the authors would like to thank Professor Tom ORourke and Mr Takashi Sananoue, who have offered continuous support to this project. Financial support provided by Tokyo Gas Co. Ltd and the Cambridge Commonwealth Trust is greatly appreciated.

13.9. Bibliography

[ABA 08] ABAQUS, Inc. *ABAQUS V.6.8 User's Manual*, Providence, Rhode Island, 2008.

[ASC 84] ASCE, *Guidelines for the Seismic Design of Oil and Gas Pipeline Systems*, Committee on Gas and Liquid Fuel Lifelines of the ASCE Technical Council on Lifeline Earthquake Engineering, ASCE, New York, 1984.

[BEE 85] BEEN, K., JEFFERIES, M.G., "A state parameter for sands", *Geotechnique*, vol. 35, no. 2, p. 99-112, 1985.

[BIS 59] BISHOP, A.W., "The principles of effective stress", *Tecnisk Ukeblad*, vol. 39, p. 859-863, 1959.

[BOL 96] BOLZON, G., SCHREFLER, B.A., ZIENKIEWICZ, O.C., "Elastoplastic soil constitutive laws generalised to partially saturated states", *Geotechnique*, vol. 46, no. 2, p.270-289, 1996.

[JEN 62] JENNINGS, J.E.B., BURLAND, J.B., "Limitations to the use of effective stresses in unsaturated soils", *Geotechnique*, vol. 12, p.125-144, 1962.

[JOM 00] JOMMI, C., "Remarks on constitutive modelling of unsaturated soils. Experimental evidences and theoretical approaches in unsaturated soils", *Proc. of an International Workshop*, Trento, p. 139-153, 2000.

[KHA 01] KHALILI, N., LORET, B., "An elasto-plastic model for nonisothermal analysis of flow and deformation in unsaturated soils: formulation", *International Journal of Solids Structures*, vol. 38, p. 8305-8330, 2001.

[KOH 93] KOHGO, Y., NAKANO, M., MIYAZAKI, T., "Theoretical aspects of constitutive modelling for unsaturated soils", *Soil Mechanics Foundation Engineering* (English Translation), vol. 33, no. 4, p.49-63, 1993.

[LOR 00] LORET, B., KHALILI, N., "A three phase model for unsaturated soils", *International Journal for Numerical and Analytical Methods in Geomechanics*, vol. 24, no. 11, p.893-927, 2000.

[NUT 09] NUTH, M., Advanced modelling of unsaturated soils: constitutive and hydro-mechanically coupled finite element analysis, PhD Thesis, Ecole Polytechnique Federale De Lausanne, 2009.

[MOD 94] MODARESSI, A., ABOU-BERK, N., "A unified approach to model the behaviour of saturated and unsaturated soils", SIRUWARDANE (ed.), *Proc. 8th international Conference in Computer Methods and Advances in Geomechanics*, Morgantown, Balkema, Rotterdam, p. 1507-1513, 1994.

[ORO 08] O'ROURKE, T.D., JEZERSKI, J.M., OSLON N.A., BONNEAU, A.L., PALMER, M.C., STEWART, H.E., O'ROURKE, M.J., ABDOUN, T., "Geotechnics of pipeline system response to earthquakes". *Proc. Geotechnical Earthquake Engineering and Soil Dynamics IV Congress*, ASCE Geotechnical Earthquake Engineering and Soil Dynamics (GSP 181) Sacramento, California, p. 193, 2008.

[ROB 10] ROBERT, D.J. Soil-pipeline interaction in unsaturated soils, PhD Thesis, University of Cambridge.

[SHE 04] SHENG, D., SLOAN S.W., GENS, A., "A constitutive model for unsaturated soils: thermomechanical and computational aspects", *Computational Mechanics*, vol. 33, no. 6, p.453-465, 2004.

[TAM 04] TAMAGNINI, R., "An extended Cam-clay model for unsaturated soils with hydraulic hysteresis", *Geotechnique*, vol. 54, no. 3, p.223-228, 2004.

[WHE 03] WHEELER, S.J., SHARMA, R.S., BUISSON, M.S.R., "Coupling of hydraulic hysteresis and stress-strain behaviour in unsaturated soils", *Geotechnique*, vol. 53, no. 1, p. 41-54, 2003.

Chapter 14

Coefficient *B*, Consolidation, and Swelling in Fine Soils Near Saturation in Engineering Practice

14.1. Introduction

The aim of this chapter is to give a simplified model that can be used for engineering projects, based on standard experimental measurements (oedometer tests, triaxial tests) for fine soils near saturation (S_r>80-90%).

The model can be used to estimate:

– instant and differed settlement under an embankment,

– instant and differed swelling after excavation, and

– swelling and shrinking cycle.

The chapter is organized in four sections: (a) the model assumptions; (b) the method to determine the parameters from standard oedometric tests; (c) example of application to the experimental embankment at Cubzac-les-Ponts: oedometric parameters – comparison with field measurement, and (d) conclusions.

Chapter written by Luc BOUTONNIER.

14.2. Model assumptions

In this chapter, four domains of saturation for fine soils are defined. The importance of the occluded air domain is shown for natural soils and compacted soils. In each of these domains, the general equations are given, and based on additional assumptions, we have provided the equations for the B coefficient (ratio between increment of pore pressure and increment of total stress on an undrained stress path) and the coefficient of consolidation C_v.

14.2.1. *The four domains of saturation, D1, D2, D3 and D4*

Boutonnier and Virollet [BOU 03] distinguished four domains: unsaturated dry soils (D1 domain), quasi-saturated soils (D2 and D3 domains), and saturated soils (D4 domain).

14.2.1.1. *D1 domain*

The air phase is continuous (Figure 14.1). The suction s is larger than the air entry suction s_{air} (Figure 14.2). Experimental measurements gave a wide range of s_{air} values from 10 kPa (silts) to more than 1000 kPa for clays [BIA 87]. At air entry suction, according to experimental results available in the literature [BIA 87, CHE 95, FLE 02, SCH 66, ZER 98], the degree of saturation $S_{r\,air}$ is between 75 and 100%, depending on the preparation and initial water content (compacted soils at optimum Proctor, saturated soils, etc.). Instead of suction, the negative pore water pressure can be used according to the relationship:

$$s = u_a - u_w, \qquad [14.1]$$

where u_a is the air pressure and u_w is the water pressure.

The air and water pressures are relative pressures set to zero at atmospheric air pressure P_a. In most of the applications, air at the soil domain boundary is at atmospheric pressure, and at air entry suction, we can write:

$$u_{a\,air} = 0 \quad \text{and} \quad u_{w\,air} = -s_{air}. \qquad [14.2]$$

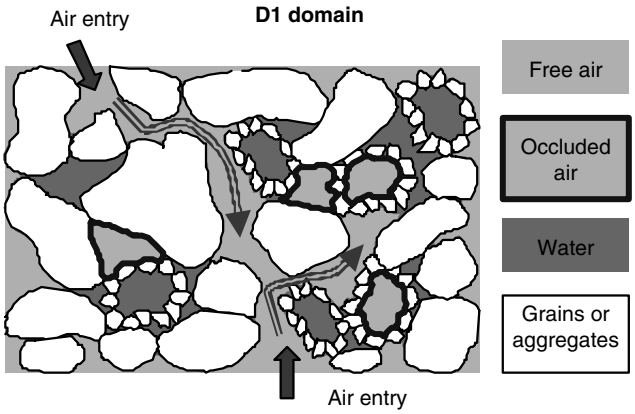

Figure 14.1. *D1 domain: air is free in the soil*

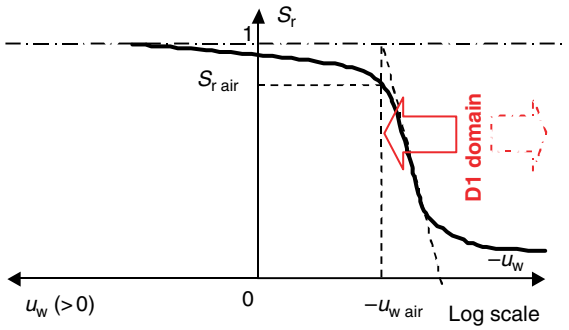

Figure 14.2. *D1 domain: negative water pressure $-u_w$ is greater than negative water pressure at air entry $-u_{w\,air}$*

14.2.1.2. *D2 domain*

The occluded air is in contact with the soil particles, and the negative water pressure u_w increases the interparticle contact strength (Figure 14.3). By definition, S_{re} is the degree of saturation corresponding to zero capillary tension (Figure 14.4). With standard conditions (atmospheric pressure outside soil), zero water pressure is observed at this point. Experimental measurements [BAR 74, FLE 02, LIN 95] show that optimum Proctor belongs to the D2 domain. In natural soils, the capillary fringe also belongs to the D2 domain.

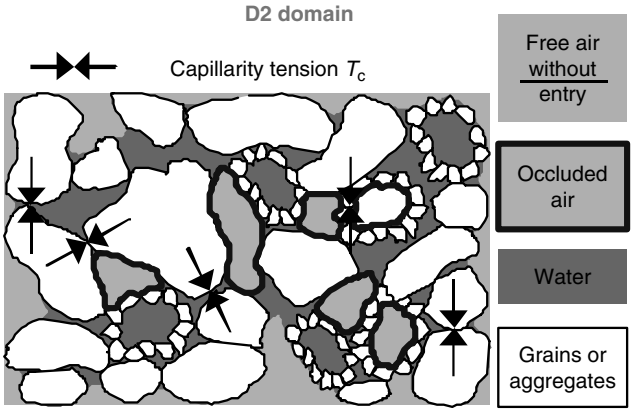

Figure 14.3. *D2 domain: air is occluded. Capillary tension increases interparticle contact strength*

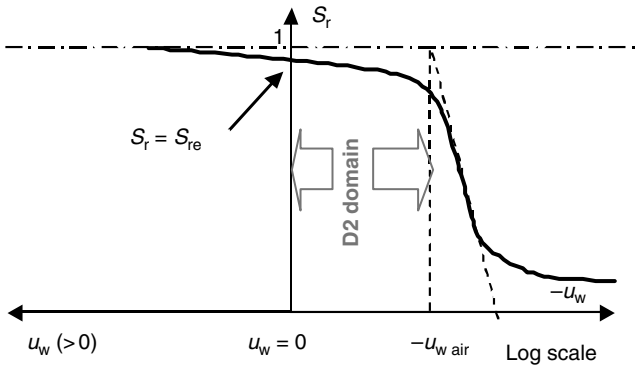

Figure 14.4. *D2 domain: negative water pressure is between zero and negative water pressure at air entry -$u_{w\,air}$*

14.2.1.3. *D3 domain*

In this domain, occluded air bubbles exist as in the domain D2, but macroscopic measurements give a zero suction (s=0, see Figure 14.5). The water pressure is positive (equation [14.3] and Figure 14.6):

$$u_w > 0. \qquad [14.3]$$

This does not mean that tension strength does not exist on each bubble surface at the microscopic level.

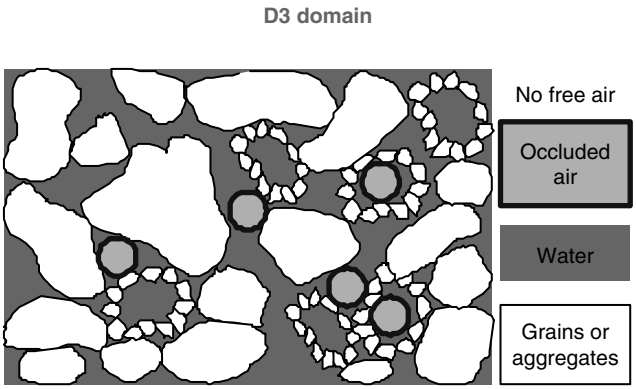

Figure 14.5. *D3 domain: air is occluded. Capillary tension does not exist at the macroscopic level*

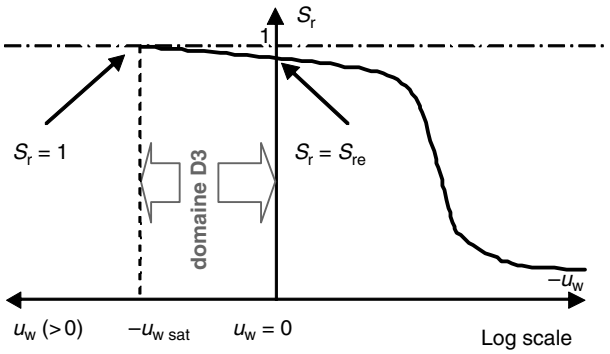

Figure 14.6. *D3 domain: water pressure is between zero and saturation water pressure* $u_{w\,sat.}$

14.2.1.4. *D4 domain*

In this domain, the soil is perfectly saturated (Figure 14.7). The limit between domains D3 and D4 can be characterized by the water pressure $u_{w\,sat}$, which has to be reached to obtain full saturation S_r=1 (Figure 14.8).

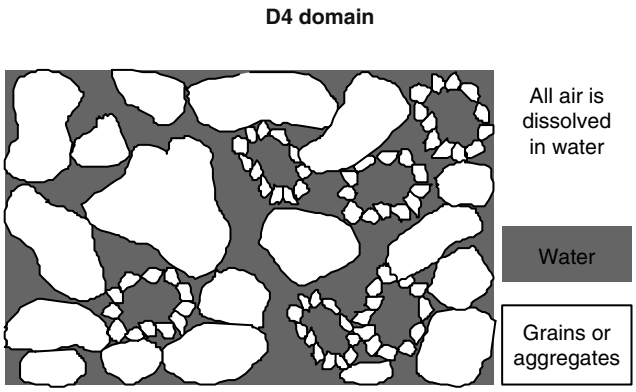

Figure 14.7. *D4 domain: air is dissolved in water. The soil is saturated*

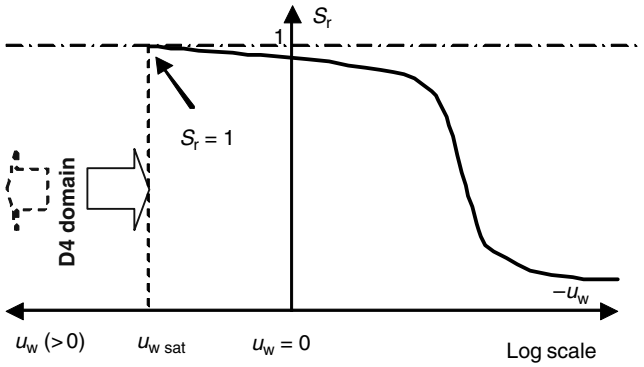

Figure 14.8. *D4 domain: water pressure is greater than saturation water pressure*

14.2.2. *The different saturation domains in compacted soils*

The detailed review of different data available in the literature [BAR 74, CAB 93, LIN 95, FLE 02, LEO 02] gives a qualitative view of the different domain limits in compacted soils, as shown in Figure 14.9. As sensitive fine soils are compacted at nearly optimum water content or on the wet side of the curve, we can see that many embankments in temperate climates are built with soils with occluded air. Moreover, the free air in soils on the dry side of the optimum during construction can become occluded in high embankments because of void ratio reduction under high stresses.

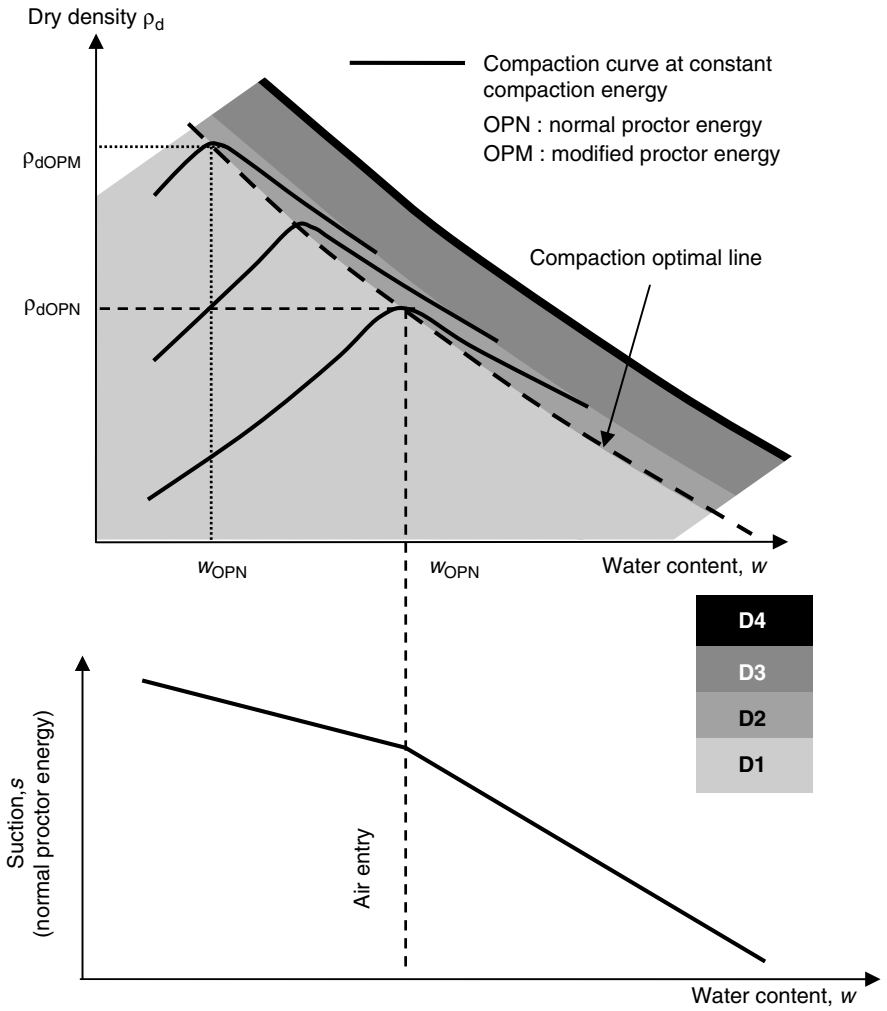

Figure 14.9. *Qualitative position of the D1, D2, D3, and D4 domains in compacted soils according to literature experimental results.*

14.2.3. *Different saturation domains in natural (intact) soils*

Most of the time, natural soils in temperate climates are in the D2 domain (capillary fringe) or in the D3/D4 domain (under the water table), as shown in Figure 14.10.

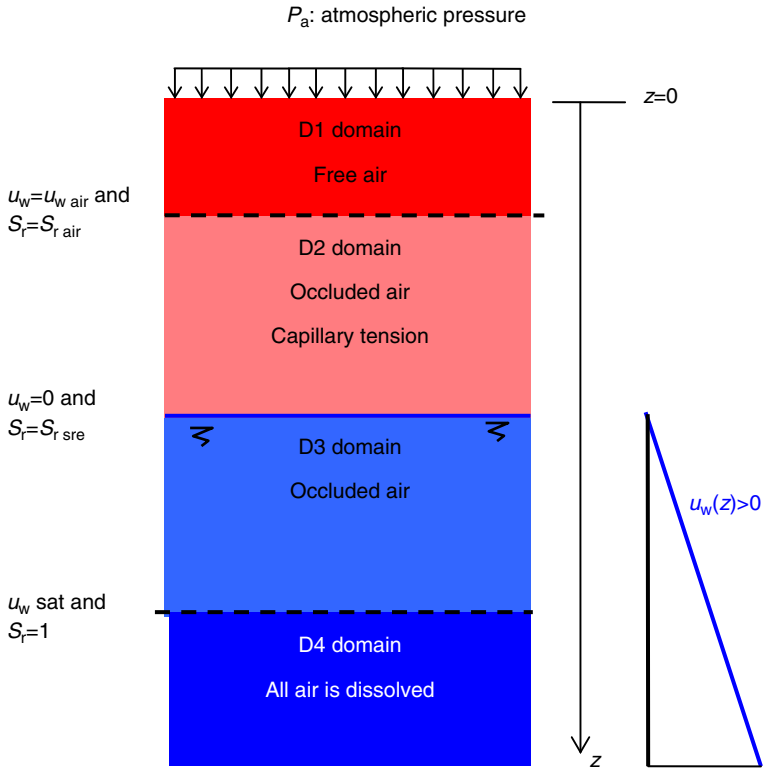

Figure 14.10. *Qualitative position of the D1, D2, D3, and D4 domains in natural soils*

14.2.4. *Physical assumptions in near-saturation domain*

In the D2, D3 and D4 domains, the following physical assumptions are made:

(1) Air is an ideal gas.

(2) Dissolved air in water follows Henry's law. The coefficient of solubility h is equal to 0.02 (see [FRE 93] for details). However, tests by

Black and Lee [BLA 73] show that a long period of time is needed for dissolution. Therefore, for a short loading time period, Henry's law can be neglected by taking into account h=0 instead of h=0.02.

(3) In the air/water mixture, the ratio between the mass of air and the mass of water is constant (Figure 14.11). The diffusion of air through water is not taken into account at the macroscopic level even if it exists locally at the microscopic level.

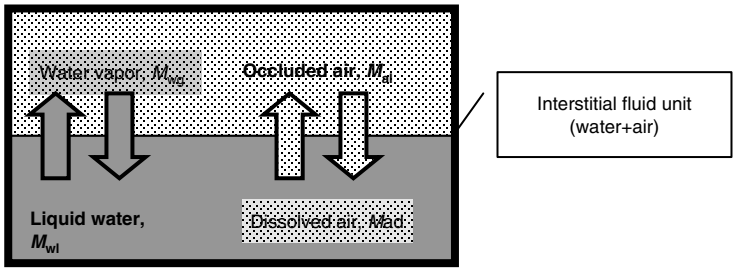

Figure 14.11. *The ratio $(M_{wg}+M_{wl})/(M_{al}+M_{ad})$ is constant*

(4) Occluded air is saturated with water vapor. Water vapor pressure is uwg.

(5) The soil stays in the domains D2, D3, or D4. In these domains, the effective stress principle can be used [BIA 87, KHA 98, LOR 02, LAL 09].

(6) In the D2 domain, the degree of saturation S_r is a one-to-one function of negative water pressure, $-u_{w,}$ and we can denote it as $S_r(u_w)$.

(7) The parameters ($u_{w\,sat}$, S_{re}, $S_{r\,air}$, $u_{w\,air}$) defining the limits between the different domains (D1, D2, D3, and D4) are supposed to be constant.

(8) In the D3 domain, air bubbles are supposed to have a constant radius r_{bm}. Indeed, at a microscopic scale, diffusion occurs and the small bubbles tend to disappear to create big bubbles that stay in the biggest pores [MUR 02, VAU 03]. The air pressure u_a and water pressure u_w then follow the equation

$$u_a - u_w = 2\frac{T_c}{r_{bm}} = s_{bm}, \qquad [14.3]$$

(9) The water compressibility is c_w. The soil particles are considered incompressible when compared with water.

(10) The water permeability k_v (D1, D2, D4) or air/water mixture permeability k_f (D3) is a one-to-one function of void ratio, e, not only in the domains D3 and D4, but also D2. The functions in the D2 domain and the D3/D4 domain can be different. In the domain D1, the water permeability is a function of negative water pressure and void ratio.

(11) The relative air pressure u_a is equal to zero at absolute air pressure P_a=100 kPa. Similarly, the relative water pressure u_w follows the same rule.

[BOU 07] considered almost the same assumptions. The only difference is that suction s is used instead of water pressure u_w in the relation between S_r and u_w. However, there is no significant difference between the two assumptions in numerical applications.

14.2.5. *The relationship between S_r and u_w*

The first relationship is between the degree of saturation S_r and air pressure u_a. Hypotheses 1–5 from section 14.2.4 yield:

$$\frac{\mathrm{d}u_a}{(u_a + P_a - u_{wg})} = \frac{\mathrm{d}S_r}{S_r(1 - S_r + hS_r)}. \qquad [14.4]$$

This equation can be used with h=0 for short time loadings. Integration of this equation yields:

$$S_r = \frac{1}{1 - h + \left(\frac{1 - S_{r\,ref} + hS_{r\,ref}}{S_{r\,ref}}\right)\left(\frac{u_{a\,ref} + P_a - u_{wg}}{u_a + P_a - u_{wg}}\right)}, \qquad [14.5]$$

where $S_{r\,ref}$ and $u_{a\,ref}$ are the reference degree of saturation and air pressure, respectively.

To calculate the relationship between the degree of saturation and water pressure in the domain D3, we used assumption 8 from section 14.2.4:

$$S_r = \frac{1}{1-h+\left(\frac{1-S_{re}+hS_{re}}{S_{re}}\right)\left(\frac{s_{bm}+P_a-u_{wg}}{u_w+s_{bm}+P_a-u_{wg}}\right)} \quad if \quad 0<u_w<u_{w\,sat}, \quad [14.6]$$

$$u_{w\,sat} = \left(s_{bm}+P_a-u_{wg}\right)\frac{1-S_{re}}{hS_{re}}, \quad [14.7]$$

where $u_{w\,sat}$ is the water pressure at the point of full saturation if dissolution of air into water occurs ($h \neq 0$).

By considering assumption 6 from section 14.2.4, we obtained a relationship between S_r and u_w in the D2–D4 domains. We can suppose, for instance, that $S_r(u_w)$ is a linear function in the D2 domain:

$$S_r(u_w) = S_{re} - \frac{u_w}{u_{w\,air}}(S_{re}-S_{r\,air}). \quad [14.8]$$

Figure 14.12 gives an example of the numerical application. The shape of the curve is mainly a function of S_{re} and the slope of the line $S_r(u_w)$ in the D2 domain [BOU 07]. The influence of the bubble radius can become important for soil without macropores (bubble radius<5 μm).

The air/water mixture compressibility c_f can be calculated in domain D3 (V_v: void volume per unit volume of soil):

$$c_f = \frac{1}{\rho_f}\frac{d\rho_f}{du_w} = \frac{-1}{V_v}\frac{dV_v}{du_w} = c_w\frac{1-S_r+hS_r}{u_w+s_{bm}+P_a}. \quad [14.9]$$

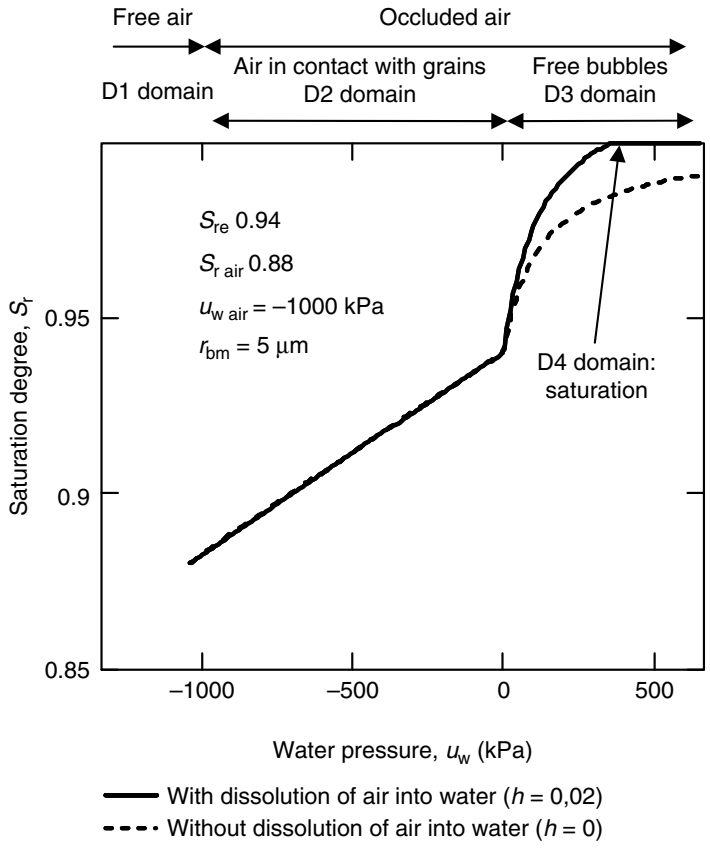

Figure 14.12. *Example of the relationship between S_r and u_w. Here, the number of parameters is limited*

14.2.6. *General equations between water pressure and void ratio*

Using mass conservation and Darcy's law with Hubbert potential for compressible fluids [HUB 40], the following are the general equations relating water pressure, degree of saturation, and void ratio:

$$\frac{\delta u_w}{\delta t}\frac{e}{1+e}\left(\frac{\delta S_r}{\delta u_w}+c_w S_r\right)+\frac{\delta e}{\delta t}\frac{S_r}{1+e}=\frac{k_w}{\rho_w g}\Delta u_w-k_w c_w\frac{\delta u_w}{\delta z}\quad \text{D1 and D2 domain,}$$

$$\frac{\delta u_{\mathrm{w}}}{\delta t}\frac{e}{1+e}c_{\mathrm{f}}+\frac{\delta e}{\delta t}\frac{1}{1+\mathrm{e}}=\frac{k_{\mathrm{f}}}{\rho_{\mathrm{f}}g}\Delta u_{\mathrm{w}}-k_{\mathrm{f}}c_{\mathrm{f}}\frac{\delta u_{\mathrm{w}}}{\delta \mathrm{z}} \quad \text{D3 domain,}$$

$$\frac{\delta u_{\mathrm{w}}}{\delta t}\frac{e}{1+e}c_{\mathrm{w}}+\frac{\delta e}{\delta t}\frac{1}{1+\mathrm{e}}=\frac{k_{\mathrm{w}}}{\rho_{\mathrm{w}}g}\Delta u_{\mathrm{w}}-k_{\mathrm{w}}c_{\mathrm{w}}\frac{\delta u_{\mathrm{w}}}{\delta \mathrm{z}} \quad \text{D4 domain,}$$

$$\Delta u_{\mathrm{w}}=\frac{\delta^2 u_{\mathrm{w}}}{\delta x^2}+\frac{\delta^2 u_{\mathrm{w}}}{\delta y^2}+\frac{\delta^2 u_{\mathrm{w}}}{\delta z^2}. \qquad [14.10]$$

14.2.7. *Application to one-dimensional hydromechanical coupling in the D2, D3 and D4 domains*

We considered that the soil skeleton follows the effective stress principle. The soil behavior law can be written using the following equation:

$$\mathrm{d}e=-\frac{1-e}{E_{\mathrm{oedo}}}\mathrm{d}\sigma_z+\frac{\delta_{\mathrm{lc}}e}{\delta t}\mathrm{d}t, \qquad [14.11]$$

where E_{oedo} is the tangent oedometric modulus. It can be calculated following any soil behavior law. For instance, Boutonnier [BOU 07] gave the equations for the Cam Clay model. The following is the association with the standard oedometric parameters C_{c} and C_{s}:

$$E_{\mathrm{oedo}}=\frac{(1+e)\sigma_z\ln(10)}{C_x}. \qquad [14.12]$$

The creep behavior is given by the other coefficient of equation [14.11]. The following is the association with the parameter $c_{\alpha\mathrm{e}}$ that can be estimated easily from the oedometric creep test:

$$\frac{\delta_{\mathrm{lc}}e}{\delta t}=-\frac{c_{\alpha\mathrm{e}}}{t_{\mathrm{f}}\ln(10)}=\frac{c_\alpha}{t_{\mathrm{f}}}, \qquad [14.13]$$

with:

$$t_{\mathrm{f}} = 10\frac{C_{\mathrm{c}}\log\left(\frac{\sigma' p}{\sigma' z}\right) - C_{\mathrm{s}}\log\left(\frac{\sigma' p}{\sigma' z}\right)}{c_{\alpha \mathrm{e}}}, \qquad [14.14]$$

σ'_{p} : preconsolidation pressure

By using relations [14.10] and [14.11], the equations of one-dimensional hydromechanical coupling can be obtained for the D2, D3 and D4 domains. The following are the main features that are taken into account:

(I) diffusion/consolidation (analogy with C_{v} from Terzaghi equation [TER 43]),

(II) undrained B coefficient (analogy with Skempton B coefficient on isotropic loading [SKE 54]),

(III) creep,

(IV) effect of water compressibility ($c_{\mathrm{l}}=c_{\mathrm{w}}$ in D2 and D4 domains) or air/water mixture compressibility ($c_{\mathrm{l}}=c_{\mathrm{f}}$ in D3 domain).

$$\left\{\begin{array}{c} \qquad\quad \textbf{(I)} \qquad \textbf{(II)} \qquad\quad \textbf{(III)} \qquad\quad \textbf{(IV)} \\ \dfrac{\delta u_{\mathrm{w}}}{\delta \mathrm{t}} = C_{\mathrm{v}}\dfrac{\delta^2 u_{\mathrm{w}}}{\delta z^2} + B\dfrac{\delta \sigma_z}{\delta t} + B\dfrac{E_{\mathrm{oedo}}}{t_{\mathrm{f}}\ln(10)} - \rho_{\mathrm{l}} g c_{\mathrm{l}} C_{\mathrm{v}}\dfrac{\delta u_{\mathrm{w}}}{\delta z} \\ \dfrac{\delta \sigma'_z}{\delta \mathrm{t}} = \dfrac{\delta \sigma_z}{\delta \mathrm{t}} = \dfrac{\delta u_{\mathrm{w}}}{\delta \mathrm{t}} \\ \dfrac{\delta \mathrm{e}}{\delta \mathrm{t}} = -\dfrac{1+e}{E_{\mathrm{oedo}}}\dfrac{\delta \sigma'_z}{\delta t} - \dfrac{c_{\alpha \mathrm{e}}}{t_{\mathrm{f}}\ln(10)} \end{array}\right., \qquad [14.15]$$

with:

D2 domain:

$$C_{\mathrm{v}} = \frac{B}{S_{\mathrm{r}}}\frac{k_{\mathrm{w}} E_{\mathrm{oedo}}}{\rho_{\mathrm{w}} g} = \frac{B}{S_{\mathrm{r}}} C_{\mathrm{v\_Terzaghi}}, \qquad [14.16]$$

$$B = \frac{1}{1 + \frac{e}{1+e} E_{oedo} \left(\frac{1}{S_r} \frac{\delta S_r}{\delta u_w} + c_w \right)}, \quad [14.17]$$

$\rho_l = \rho_w$ and $c_l = c_w$

D3 domain:

$$C_v = B \frac{k_f E_{oedo}}{\rho_f g} = B C_{v\_Terzaghi}, \quad [14.18]$$

$$B = \frac{1}{1 + \frac{e}{1+e} E_{oedo} c_f}, \quad [14.19]$$

$\rho_l = \rho_f$ and $c_l = c_f$

D4 domain:

$$C_v = B \frac{k_w E_{oedo}}{\rho_w g} = B C_{v\_Terzaghi}, \quad [14.20]$$

$$B = \frac{1}{1 + \frac{e}{1+e} E_{oedo} c_w}, \quad [14.21]$$

$\rho_l = \rho_w$ and $c_l = c_w$

If we consider that water is incompressible (c_w=0), the Terzaghi equation of consolidation [TER 43] appears to be a particular case of equations [14.15] and [14.21].

If we consider an undrained stress path (k_f=0 or k_w=0) and no creep ($c_{\alpha e}$=0), then the Skempton B coefficient for oedometric loading (instead of isotropic loading) can be extended to negative pore pressures (D2 domain). The equations for the B coefficient can be used on isotropic undrained

loading with an isotropic tangent modulus $E_{\text{iso,}}$ instead of the oedometric tangent modulus E_{oedo}.

14.3. How to determine the model?

It is not possible to carry out direct and accurate measurement of parameters S_{re}, r_{bm}, $S_{\text{r air}}$, and $u_{\text{w air}}$. However, as the number of parameters is limited, it is possible to estimate them indirectly from standard oedometric test with loading and unloading steps. The parameters can also be obtained from undrained isotropic loading and unloading in an oedometric or triaxial cell.

In this chapter, we have developed the procedure to determine the parameters from standard oedometric tests with loading and unloading steps.

14.3.1. *First step: calculation of B, C_v, E_{oedo} and $c_{\alpha e}$ on each loading or unloading step*

For each loading or unloading step, the void ratio variation is the sum of the undrained, consolidation, and creep components, as shown in Figure 14.13:

$$\Delta e = \Delta e_{\text{ins}} + \Delta e_{\text{dif}} + \Delta e_{\text{f}}, \qquad [14.22]$$

At first, the Taylor method [TAY 48] can be used to determine C_{v}, t_{90}, Δe_{ins}, and Δe_{dif} (see also [AFN 05]). For one loading or unloading step, we assumed that all the parameters are constant. Subsequently, we estimated B and the oedometric modulus:

$$E_{\text{oedo}} = \frac{-(1+e)}{\Delta e_{\text{ins}} + \Delta e_{\text{dif}}}(\sigma_{z\_\text{fin}} - \sigma_{z\_\text{ini}}), \qquad [14.23]$$

$$B = 1 + \frac{\Delta e_{\text{inst}} E_{\text{oedo}}}{(1+e)(\sigma_{z\_\text{fin}} - \sigma_{z\_\text{ini}})}, \qquad [14.24]$$

with:

σ_{z_ini}, initial vertical stress before the loading step (or unloading step);
σ_{z_fin}, final vertical stress after the loading step (or unloading step).

The creep coefficient can easily be measured if the constant load lasts long enough, as shown in Figure 14.13.

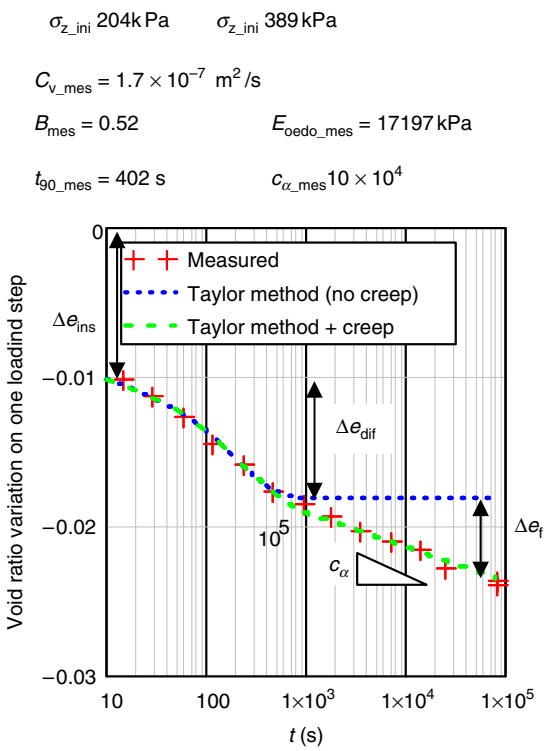

Figure 14.13. *Calculation of B, C_v, E_{oedo}, and c_a from one loading step on oedometric test*

14.3.2. *Second step: estimation of the parameters of the model S_{re}, r_{bm}, $S_{r\,air}$, $u_{w\,air}$*

The estimation of the parameters of the model is obtained by comparing, on each loading or unloading step, the theoretical and measured secant B modulus (equations [14.24] and [14.25]).

$$B_{\text{sec}} = \frac{\Delta u_{\text{w}}}{\Delta \sigma_z} = \frac{\int_{\sigma_{z\_\text{ini}}}^{\sigma_{z\_\text{fin}}} B \, \mathrm{d}\sigma_z}{\sigma_{z\_\text{fin}} - \sigma_{z\_\text{ini}}}. \qquad [14.25]$$

There is no analytical expression for the theoretical secant B modulus, but it can be easily calculated with good accuracy using a step-by-step integration to calculate the integrals.

There are four main parameters to determine. Fortunately, two of these parameters are used for the loading steps (S_{re} and r_{bm}), and only one parameter is needed for the unloading steps (the slope of equation [14.8] can be adjusted by choosing $u_{\text{w air}}$ and $S_{\text{r air}}$). For oedometric tests, the loading is very quick and it appears that dissolution of air can be neglected (h=0).

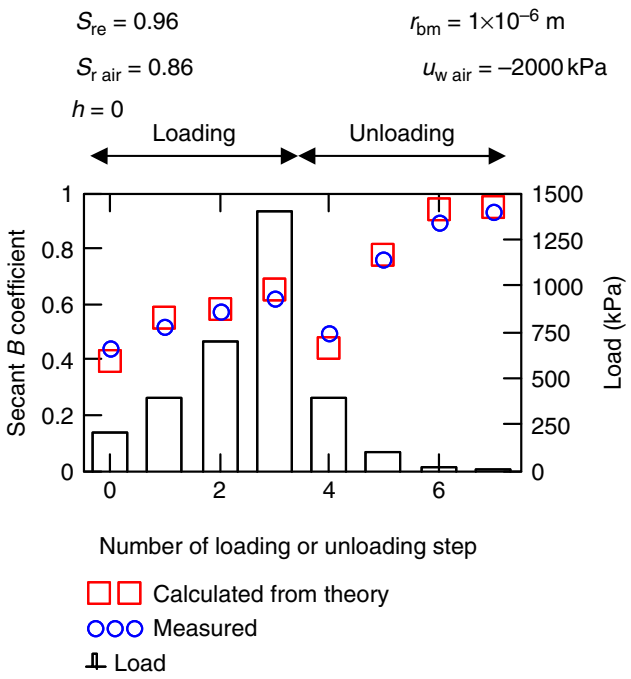

Figure 14.14. *Set of parameters S_{re}, $S_{r\,air}$, $u_{w\,air}$, and r_{bm} allowing a complete simulation of loading and unloading steps on an oedometric test (intact sample of marl from LGV Rhin-Rhône high-speed train project)*

Generally, one set of parameters can work for many loading or unloading steps, as shown in Figure 14.14. [BOU 07] found that one set of parameters works for a variable specimen of a natural soil (marl from the LGV Rhin-Rhône high-speed train project).

14.3.3. *Third step: estimation of permeability in D2 ad D3 domains*

The permeability can be estimated from C_v measurements (see section 14.2.2) and C_v equations [14.16] and [14.18]. For each loading or unloading step, we obtained an estimation of permeability. It is then possible to look for a relation between void ratio and permeability in the domain D2 or D3 as shown in Figure 14.15.

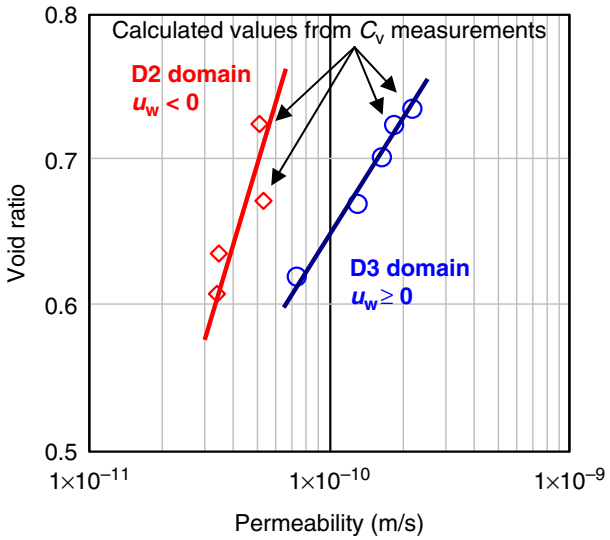

Figure 14.15. *Permeability calculated from C_v on different loading ($u_w \geq 0$) or unloading ($u_w < 0$) steps. Permeability is logically lesser in the D2 domain where the degree of saturation is smaller. Moreover, the classical relationship between permeability and void ratio is verified in each domain: $e=e_k+c_k\ ln(k_w)$*

14.4. Why is it interesting for engineers?

The main interest of the model is to capture the main features of hydromechanical coupling with only three additional parameters: S_{re}, r_{bm} and the slope given by the couple ($u_{w\ air}$, $S_{r\ air}$) in the D2 domain. Moreover, these

parameters can be determined from standard oedometric tests. Once these parameters are known, it is possible to simulate a wide range of problems: development of pore pressure in embankments and dams, undrained, and drained settlement under embankments, swelling after excavation, swelling and shrinking cycles, etc.

14.5. Application to Cubzac-les-Ponts experimental embankment

Cubzac-les-Ponts is a famous compressible soil site near Bordeaux in France, where numerous experimental embankments (embankment A, B, C, and D) have been built [HAG 83, MAG 83]. We propose to simulate experimental embankment D. This embankment is only 1-m high, as the aim was to observe the behavior of over-consolidated soils. The oedometric parameters of the site [HAG 83] are available in Table 14.1.

	γ (kN/m^3)	C_s	C_c	e_0	σ'_p (kPa)	$c_{\alpha e}$
Embankment (1 m)	21					
0–1.3 m	16.9	0.06	0.4	1.1	90	0.01
1.3–2.4 m	14.5	0.15	1.3	2.5	68	0.01
2.4–5.2 m	15	0.04	0.7	1.6	58	0.02
5.2–7.4 m	14.6	0.07	1	1.8	64	0.02
7.4–9 m	15	0.08	1	1.9	85	0.02

Table 14.1. *Oedometric parameters from experimental embankment D (from [HAG 83])*

The soil can be described as soft clay, very much over-consolidated from zero to 1.3 m (effect of swelling/shrinking cycles) and with organic matter from 1.3 to 2.4 m. The water table can vary from the surface to 1.5 m in depth.

On the same site, undrained oedometric tests have been carried out on a soil sample from the layer between 6 and 7 m depth [MAG 77]. These tests can be used to determine the D3 parameters S_{re} and r_{bm}. However, detailed data are only available for one test. An excellent adjustment can be obtained with S_{re}=0.908, r_{bm}=0, and h=0 as shown in Figure 14.16.

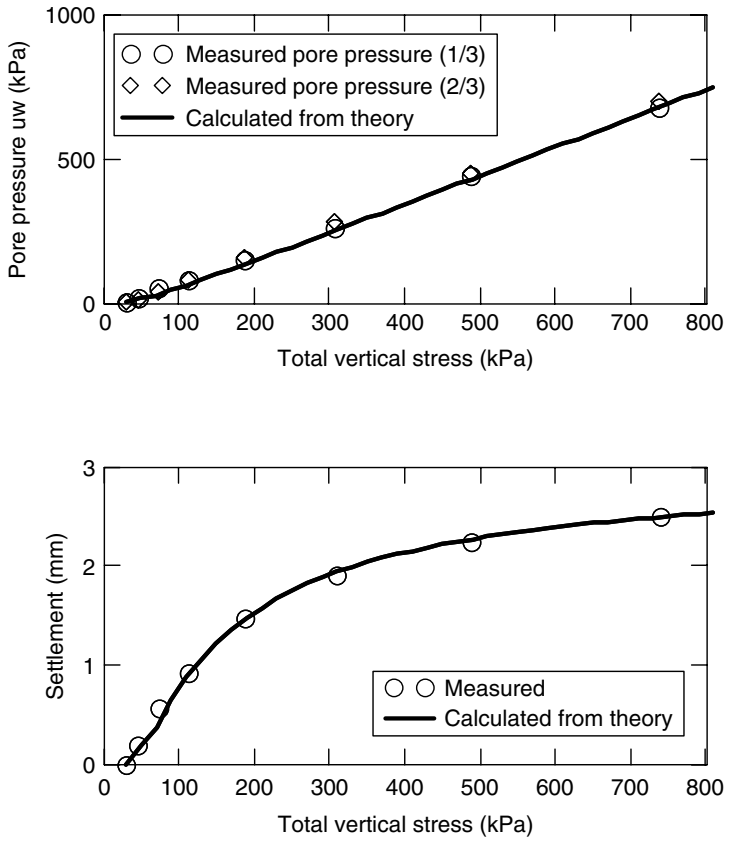

Figure 14.16. *Undrained oedometric test from Cubzac-Les-Ponts. The parameters S_{re}=0.908, r_{bm}=0, and h=0 give an excellent adjustment between the theoretical values and real measurements*

These parameters can be used to simulate the behavior of experimental embankment D. Settlement and pore pressure measurements were carried out [HAG 83]. Figure 14.17 gives a comparison between measured and calculated settlement and pore pressure. As the embankment is only 1 m high ($\Delta\sigma$=21 kPa), the results are very scattered because the variation in pore pressure and settlement is very limited. Nevertheless, the model has the ability to give a good prediction of undrained settlement (see Figure 14.17). We can consider that the construction period is undrained because it only lasted for 1 day. The calculated pore pressure appears to be slightly greater

than the measured values. This may be linked to the difficulty in measuring the tiny variations of pore pressures.

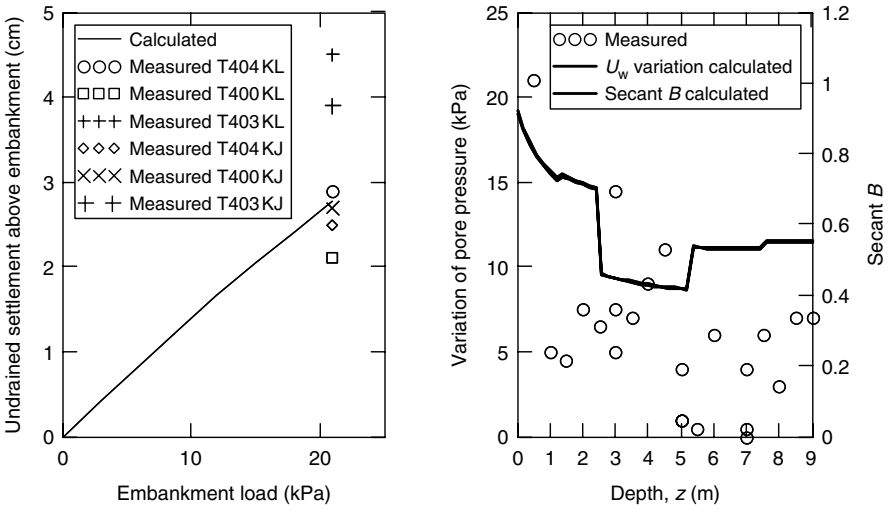

Figure 14.17. *Calculated and measured settlements and pore pressures after embankment D construction. Better results are obtained for settlement. The tiny variations in pore pressure may be difficult to measure*

14.6. Conclusion

Fine soils with occluded air are very common in intact natural soils and compacted soils (embankments, dams, etc.). Nevertheless, there is no method with a reasonable number of parameters to take this phenomenon into account in engineering practice.

In this chapter, we have given the theoretical developments and a simplified tool for engineers to estimate the pore pressure on undrained or drained stress paths. This method can be used in a wide range of applications:

– instant and differed settlement under embankment,

– pore pressure in compacted soils (high embankments or dams),

– instant and differed swelling after excavation (cuts, tunnels), and

– swelling and shrinking cycle.

The method can be used with any soil skeleton behavior law defined in the saturated domain with the effective stress principle. The step-by-step procedure to determine the parameters of hydromechanical coupling from standard oedometric test with loading and unloading steps has been detailed.

The model has the ability to properly match with various experimental results from laboratory and *in situ* measurements from the experimental embankment of Cubzac-les-Ponts.

Furthermore, other validations have been carried out and further experimentations and theoretical developments are underway. In addition, the method should be extended to three-dimensional calculations with finite element codes in the near future.

14.7. Bibliography

[AFN 05] AFNOR. XP CEN ISO/TS 17892-5, August 2005, indice de classement P 94-512-5. *Reconnaissances et essais géotechniques, Essais de sol en laboratoire, Partie 5: Essai à l'oedomètre sur sol saturé*, AFNOR, Paris, 2005.

[BAR 74] BARDEN L., "Consolidation of clays compacted 'dry' and 'wet' of optimum water content", *Géotechnique*, vol. 24, no. 4, p. 605-625, 1974.

[BIA 87] BIAREZ J., FLEUREAU J.-M., ZERHOUNI M.-I., SOEPANDJI B.S., "Variations de volume des sols argileux lors de cycles de drainage-humidification", *Revue Française de Géotechnique*, vol. 41, p. 63-71, 1987.

[BLA 73] BLACK D. K., LEE K. L., "Saturating laboratory samples by back pressure", *Journal of the Soil Mechanics and Foundations Division, ASCE*, vol. 99, no. 1, p. 75-93, 1973.

[BOU 03] BOUTONNIER L., VIROLLET M., "Tassements et gonflements instantanés dans les sols fins proches de la saturation", *Revue Française de Géotechnique*, vol. 104, p. 3-19, 2003.

[BOU 07] BOUTONNIER L., Comportement hydromécanique des sols fins proches de la saturation. Cas des ouvrages en terre: coefficient B, déformations instantanées et différées, retrait/gonflement. INPG Grenoble, thesis, http://geotec-luc.blogspot.com.

[CAB 93] CABOT L., LE BIHAN J.-P., "Quelques propriétés d'une argile sur la ligne optimale de compactage", *Revue Canadienne de Géotechnique*, vol. 30, p. 1033-1040, 1993.

[CHE 95] CHEN Y.J., YU P.J., "Pore pressure dissipation features of an unsaturated compacted soil", *Proc. of the 1st Conference on Unsaturated Soils, Unsat'95*, Paris, vol. 2, p. 439-445, 1995.

[FLE 02] FLEUREAU J.M., VERBRUGGE J.-C., HUERGO P.J., GOMES CORREIA A., KHEIRBEK-SAOUD S., "Aspects of the behavior of compacted clayey soils on drying and wetting paths", *Canadian Geotechnical Journal*, vol. 39, p.1341-1357, 2002.

[FRE 93] FREDLUND D.G., RAHARDJO H., *Soil Mechanics for Unsaturated Soils*, Wiley-Interscience Publication, John Wiley & Sons, 1993.

[HAG 83] HAGHGOU M., Etude du comportement d'un remblai expérimental sur sols compressibles, Thesis, UPMC, Paris VI, 1983.

[HUB 40] HUBBERT M.K., "The theory of ground water motion", *Journal of Geology*, vol. 48, no. 8, Part I, p. 785-944, 1940.

[KHA 98] KHALILI N., KHABBAZ M.H., "A unique relationship for χ for the determination of the shear strength of unsaturated soils", *Géotechnique*, vol. 48, no. 5, p. 681-687, 1998.

[LAL 09] LALOUI L., NUTH M., "On the use of the generalised effective stress in the constitutive modelling of unsaturated soils", *Computers and Geotechnics*, vol. 36, p. 20-23, 2009.

[LEO 02] LEONG, E.C., RAHARDJO, H., "Soil-water characteristic curves of compacted residual soils", in JUCA DE CAMPOS & MARINHO (eds.), *Unsaturated Soils*, Swets & Zeitlinger, Lisse, p. 271-276, 2002.

[LIN 95] LINS A.H.P., SANDRONI S.S., SILLS G.C., "An experimental analysis of the development of pore-water pressure in an unsaturated compacted soil". *Proc. of the 1st Conf. on Unsaturated Soils, Unsat' 95*, Paris, vol. 2, p. 759-764, 1995.

[LOR 02] LORET B., KHALILI N., "An effective stress elastic-plastic model for unsaturated porous media", *Mechanics of Materials*, vol. 34, p. 97-116, 2002.

[MAG 77] MAGNAN J.P., DANG M.T., "Etude théorique et expérimentale de la compressibilité du fluide interstitiel dans un sol argileux presque saturé", *Bulletin de liaison des Laboratoires des Ponts et Chaussées*, Paris, no. Spécial VI F, p. 129-137, 1977.

[MAG 83] MAGNAN J.P., MIEUSSENS C., QUEYROI D., "Etude de remblai sur sols compressibles: le remblai B du site expérimental de Cubzac-les-Ponts", *Rapport de recherche* LPC no. 127. LCPC. Paris, 1983.

[MUR 02] MURRAY, E.J., "An equation of state for unsaturated soils", *Canadian Geotechnical Journal*, vol. 39, p. 125-140, 2002.

[SCH 66] SCHUURMAN IR. E., "The compressibility of an air/water mixture and a theoretical relation between the air and water pressures", *Géotechnique*, vol. 16, p. 269-281, 1966.

[SKE 54] SKEMPTON A.W., "The pore-pressure coefficients A and B", *Géotechnique*, vol. 4, p. 143-147, 1954.

[TAY 48] TAYLOR, D.W., *Fundamentals of Soil Mechanics*, John Wiley & Sons, New York, p. 238-242, 1948.

[TER 43] TERZAGHI K., *Theoretical Soil Mechanics*, John Wiley & Sons, New York, 510p, 1943.

[VAU 03] VAUGHAN P.R., "Observations on the behaviour of clay fill containing occluded air bubbles", *Géotechnique*, vol. 53, no. 2, p. 265-272, 2003.

[ZER 98] ZERHOUNI M.I., GERARD C., FLEUREAU J.M., "Etude du retrait de deux sols argileux naturels", *Actes du colloque Magi'50*, Vandoeuvre, p. 15-20, 1998.

Chapter 15

Geomechanical Analysis of River Embankments

15.1. Introduction

Unsaturated geomechanics has been seldom applied to the design and control of river embankments, even in developed countries. This is rather surprising, considering that these structures are constructed by compaction, and thus under unsaturated conditions, and that – for their hydraulic protection function – typically remain unsaturated throughout all their working life.

This is a direct consequence of the fact that river embankments may be classified as *poor structures*, in the sense that their cost must be reduced as much as possible, due to their huge extension. On the other hand, river embankments are not innovative structures. Traditional technologies – *poor technologies* – are still being used, relying on local experience and rules of thumb, which are still considered to be sufficient to guarantee sufficient margin of safety against failure and adequate working performance during the embankment lifetime.

Chapter written by Cristina JOMMI and Gabriele DELLA VECCHIA.

As a matter of fact, this will probably still be the practice in the near future, having in mind the following considerations:

– Huge amounts of soil are required to build river levees; therefore, contrary to other typical applications of unsaturated soil mechanics, the choice for optimal characteristics of the material is definitely limited by the requirement of soil availability on-site.

– Laboratory investigation with dedicated equipment is not feasible, both due to costs in terms of expense and time, and to limited availability of similar equipment compared to the widespread requirements.

– Control tests on soil samples retrieved from the compacted earth structure on-site are not allowed usually, as the public authorities, who typically manage the construction, discourage sampling after construction to preserve structural integrity.

– Representativeness of samples compacted in the laboratory against the behavior of the soil compacted *in situ* has not yet been verified in detail.

Thus, what role will unsaturated soil mechanics play in this context?

Going back to the earth structure itself, and to its fundamental function, which is land hydraulic protection, the following considerations may help in envisaging a role for unsaturated soil mechanics at present:

– Among all the soil characteristics which may be of interest in design and control, the retention properties are of fundamental importance, both for the hydraulic behavior of the structure and to understand and describe properly the mechanical behavior of the compacted soil.

– River embankments are always built by compaction, in general after having performed standard tests to determine optimal compaction conditions following a heuristic procedure; any information which may help in the rational interpretation of compaction conditions, and which may help inferring the main hydraulic and mechanical properties of the compacted soil from compaction variables, will certainly increase confidence in compaction specifications.

– A rational theoretical interpretation of the behavior of the soil under unsaturated conditions will help in the interpretation of *in situ* control measurement, at least from a qualitative viewpoint.

– Finally, if a sound interpretation framework were available, calibrated by means of few easily available data, suitability of the soils which may be used

in new constructions could be inferred and preliminary specifications could be suggested, especially in developing countries.

To complete the description of the problem under examination, it is worth noting that the stress levels of interest in this kind of application are almost constant and rather low, due to limited height of levees, and to the absence of any relevant surcharge loading. On the contrary, levees are exposed to significant *environmental* loads, characterized by an increasing number of wetting–drying cycles over time, due both to interaction with the atmosphere in the outer part of the structure, and to continuously variable river water level.

After recalling the main design objectives of a river levee, some experimental data from a widespread investigation performed on the soils used in the construction of the Po river levees will be presented in following. The data are then interpreted in the light of unsaturated soil mechanics, adopting a simple mechanical model and paying special attention to the water retention properties.

15.2. Design specifications and materials

The main function of a river levee is obviously the hydraulic protection of the landscape. To this aim, the fundamental requirement of the structure is a sufficiently low hydraulic conductivity. As already recalled, river levees must be constructed, in general, with the soil largely available *in situ*, and thus, sometimes, with soils which cannot satisfy the impermeability requirements themselves. In these cases, a coating must be designed to guarantee adequate performance of the structure. Soils having an hydraulic conductivity – after compaction – of the order of $k = 10^{-8} \div 10^{-9}$ m/s may guarantee sufficient hydraulic performance, and, therefore, they may be used directly as construction materials. These are typically silty–clayey soils, possibly with a limited percentage of sand, to which we will refer solely in the following.

The most relevant *failure* mechanisms, which have to be considered in the design and control of river protection systems, are schematically indicated in Figure 15.1. Failure, in this case, is intended as any condition reaching the serviceability limits of the embankment, causing the protection function requirement to be lost.

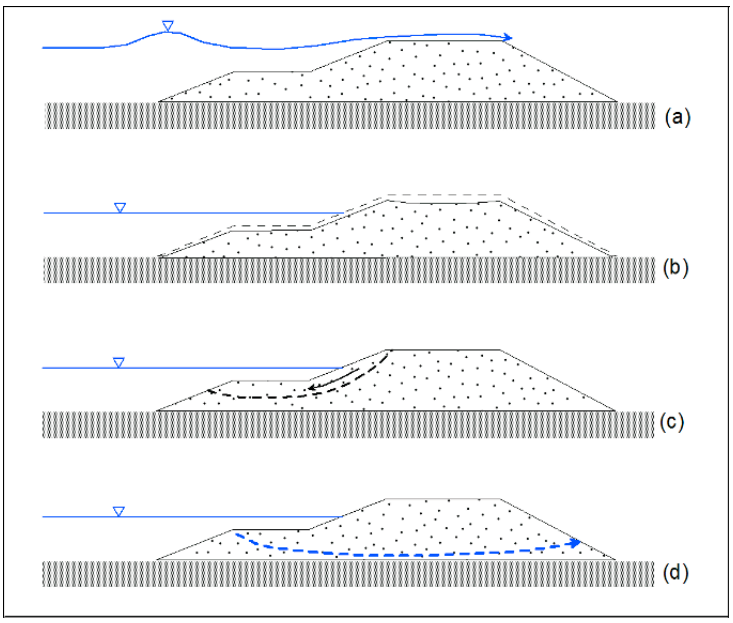

Figure 15.1. *Principal failure mechanisms of a river levee: (a) overtopping, (b) excessive deformation, (c) scarp instability, and (d) piping*

Overtopping (Figure 15.1(a)) may result from incorrect determination of the hydrologic behavior of the whole river basin, or from exceptional events from historical statistics or from uncorrelated interventions on the river basin. Hydrologic studies have to cope with this problem, to provide the *design hydraulic load*, based on probabilistic arguments. Piping (Figure 15.1(d)) is a well-known failure mechanism, which is conventionally tackled by prescribing given limits on the grain size distribution of the soil used for the construction. The latter mechanism is most likely in saturated soils. Once again, the evolution of the hydraulic state of the levee turns out to be an important datum of the problem.

The two mechanisms that are directly linked to the behavior of the unsaturated compacted soil are instability of the levee scarps and deformation of the construction (Figure 15.1(b) and (c)). The two mechanisms may be activated by interaction of the embankment with the river, with the atmosphere, and with the groundwater level, which is usually found at low depths below the levee foundation. These mechanisms are usually contrasted by suitable rules of thumb on the compaction specifications. In the following, it will

be shown how a comprehensive framework for the behavior of soils under unsaturated conditions may help in the rational interpretation of these rules of thumb, and how it may be exploited to provide more general design specifications.

15.2.1. *Some experimental observations on undisturbed samples*

The data presented in the following come from long lasting studies on typical soils and earthworks from the low Po river embankments, performed starting from the 1950s, after a major flood that took place in 1952, which caused significant damage to the whole landscape. These studies provide an experimental database which can be considered rather exceptional, in terms of the amount of information available on undisturbed samples collected from the embankments after their construction.

The soils investigated are typically silts with a clay percentage ranging from 10% to 30% and a sand fraction that must not exceed a percentage of 40%. Usually, clay minerals of medium activity, with predominant illitic fraction, characterize the available soils. Design specifications suggest to cast in place the soil at the optimal water content and at least 95% of the optimum dry density, determined from compaction tests performed with half the energy of the Proctor standard test. A scatter of 2% on water content is considered to be tolerable. The suggested low energy tends to overcome the possibility of having significant swelling upon water content increase, during the lifetime of the construction.

Typical data of compaction control measurements [COL 80, COL 99] are reported in Figure 15.2. The data were determined on samples collected on-site, both during the construction and 250 days after its end. The aim of the investigation was to verify the changes in dry density and water content occurring after the end of the construction.

In spite of the fact that the design specifications are satisfied, the data show that the actual compaction conditions are ruled by seasonal changes in water content. In the wet season, the compaction procedures lead to a soil compacted mostly on the wet of optimum for half the standard energy, thus at low dry density. In the dry season, higher density is obtained, but the water content tends to be lower than the optimum for the corresponding energy. Therefore,

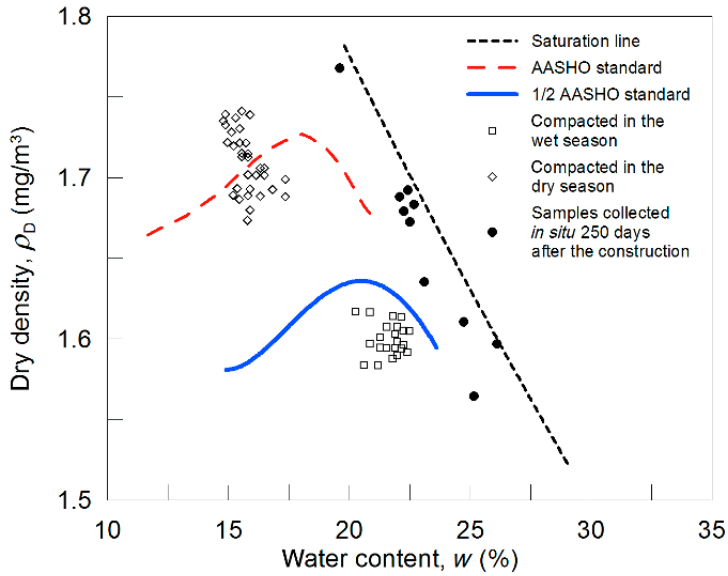

Figure 15.2. *Compaction data and control measurements after the construction (redrawn from Colleselli et al. [COL 99])*

the final construction presents some degree of inhomogeneity, which may affect its following performance. Interestingly, control data 250 days after the end of the construction suggest that the soil tends always to saturate under the environmental actions to which it is exposed. The dry density changes too, and higher or lower densities are encountered at different depths.

To provide further insight into the effects of environmental loads, data for dry density and water content are plotted in Figure 15.3 on samples collected at different heights from the base of an embankment a few months after the construction. The central part of the embankment, less exposed to interaction with the boundary, shows the highest density and the lowest water content. Near to the base, where the embankment may absorb water both from the river and the ground, the water content tends to increase. The dry density is rather low, even if the stress is the highest. In the upper part of the embankment, values of dry density and water content are found to be similar to those observed in the lowest part, although the interaction mechanisms with the environment are different and can be ascribed mostly to climatic rainfall infiltration and evaporation, under standard working conditions.

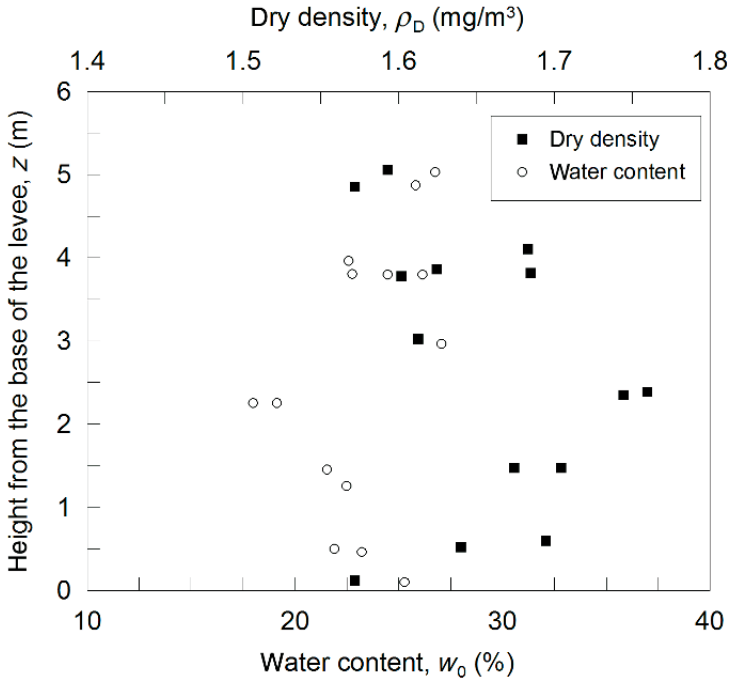

Figure 15.3. *Dry density and water content along the height of the embankment a few months after the end of the construction (redrawn from Colleselli et al. [COL 99])*

To gain first information on the interaction mechanisms between the compacted soil and water, free swelling tests were performed in the laboratory [COL 80], on samples compacted at different initial dry densities. The relevant data are summarized in Figure 15.4, where the volumetric strain and the final water content are plotted as a function of the initial compaction water content. As expected, at null stress, all the samples swell, and the amount of swelling strain is governed by the initial water content. Upon soaking, the soil tends to saturate, and the final water content is similar for all the samples tested. It is worth noting that in the experimental investigation, performed 30 years ago, the effects of the stress levels on swelling were not investigated. The latter will be discussed in the following by means of theoretical simulations of typical stress paths which the soil may undergo after construction.

To provide a rational basis for slope stability analysis, the influence of compaction conditions on the shear strength of the material has been traditionally investigated by means of simple unconfined compression tests,

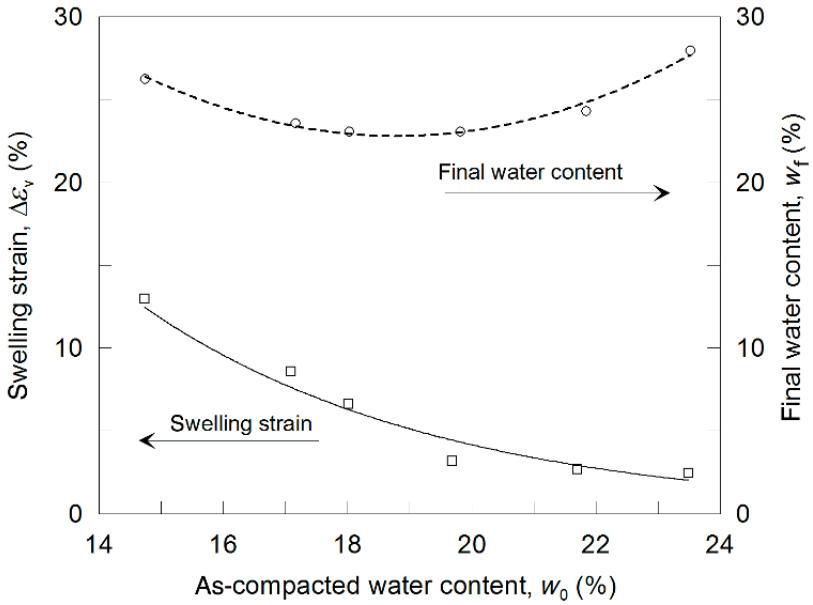

Figure 15.4. *Swelling strain and final water content at the end of one-dimensional soaking of laboratory as-compacted samples (redrawn from Colleselli et al. [COL 99])*

performed on samples at different water contents. At that time, simple unconfined compression tests provided a series of information on the dependence of shear strength on water content and dry density. The conclusion was that both parameters influenced shear strength in a relevant way, and heuristic experimental correlations were given to estimate shear strength as a function of the as-compacted dry density and water content.

Nonetheless, it was already clear that the actual stress level, and possible changes in water content and dry density, would have affected the shear strength of the soil throughout the life of the structure. Shear strength envelopes determined for the compacted soil from constant water content triaxial tests performed at different confining stress are presented in Figure 15.5. The experimental results showed that the shear strength of the soil just after compaction was clearly determined by its water content. Nonetheless, after a few months, the soil had already softened, and its shear strength was almost independent from the confining stress, which was interpreted as a consequence of the tendency of the soil to saturate with time.

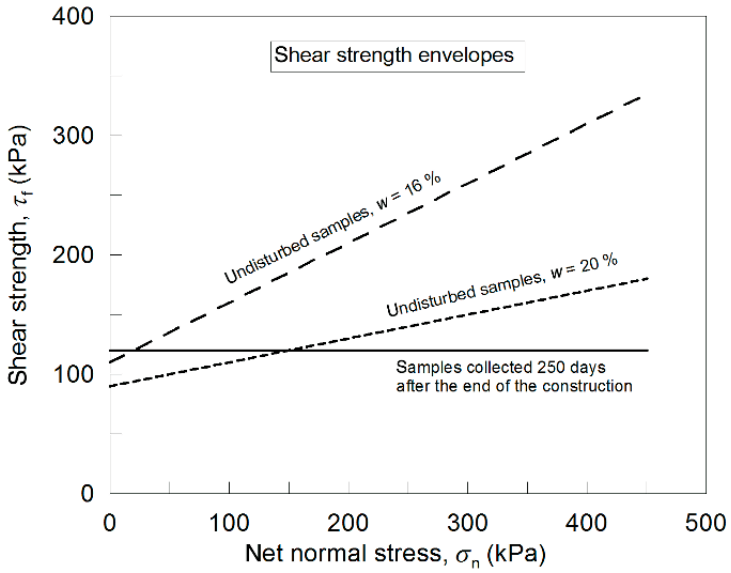

Figure 15.5. *Shear strength envelopes from constant water content triaxial tests on undisturbed samples collected after compaction and a few months after the construction (redrawn from Colleselli et al. [COL 99])*

15.3. Coupled hydro-mechanical modeling

Consideration of both hydraulic and mechanical properties and of their coupled evolution helps in providing a comprehensive framework of the behavior of these soils under unsaturated conditions. As already suggested in the previous sections, in the case of river embankments, the most relevant aspects for the design and control are the retention properties of the compacted soil and a description of strength and of volumetric behavior under water content changes. In the following sections, the key aspects of a possible formulation able to describe the unsaturated behavior of compacted soils will be briefly presented. The formulation will be used to simulate and interpret the data previously presented.

15.3.1. *Mechanical model: stress–strain behavior*

For the sake of simplicity, the basic principle of a possible mechanical model formulation is presented with reference to axisymmetric conditions, and adopting the common geotechnical stress variables $p = (\sigma_a + 2\sigma_r)/3$

and $q = \sigma_{\rm a} - \sigma_{\rm r}$, with the associated strain variables $\epsilon_{\rm v} = \epsilon_{\rm a} + 2\epsilon_{\rm r}$ and $\epsilon_{\rm s} = 2(\epsilon_{\rm a} - \epsilon_{\rm r})/3$.

To reduce the number of constitutive parameters, a convenient model may be formulated in the framework of elasto-plasticity with generalized hardening, following the suggestion by Jommi and di Prisco [JOM 94] and Jommi [JOM 00]. An anisotropic formulation, such as that proposed by Romero and Jommi [ROM 08], may be advantageous to account for the effects of directional compaction.

The average soil skeleton stress (generalized effective stress [NUT 08]), $\sigma'_{ij} = \sigma_{ij} - u_{\rm a}\delta_{ij} + S_{\rm r}(u_{\rm a} - u_{\rm w})\delta_{ij}$, and the suction, $s = u_{\rm a} - u_{\rm w}$, are adopted as stress variables. In the previous expressions, σ_{ij} is the total stress tensor, $u_{\rm w}$ and $u_{\rm a}$ are the pressures of water and air, respectively, and δ_{ij} is the Kronecker delta.

For fine-grained soils, Modified Cam Clay may provide a simple basic choice for the yield function. To account for anisotropy in the triaxial plane, Romero and Jommi [ROM 08] proposed to extend its definition in the simple form suggested by Dafalias [DAF 86]. As a first approximation, an associated plastic potential may be adopted:

$$f = g = \left(q - M_\alpha p'\right)^2 - \left(M^2 - M_\alpha^2\right) p'(\hat{p}_0 - p') = 0, \qquad [15.1]$$

where $\hat{p}_0$ is the apparent preconsolidation pressure under unsaturated conditions (linked with isotropic hardening), M_α is the inclination of the current rotated yield surface with respect to the p' axis (linked to rotational hardening), and M is the slope of the critical state line.

The effect of loading history is described by the set of internal variables $\hat{p}_0$ and M_α. Starting from the proposal of Jommi and di Prisco [JOM 94] and exploiting the work of Gallipoli *et al.* [GAL 03], the preconsolidation pressure $\hat{p}_0$ under unsaturated conditions is assumed to be a function of its saturated counterpart, p_0^*, governed by volumetric plastic strain, and of the degree of saturation $S_{\rm r}$:

$$\hat{p}_0 = p_0^* \left\{1 + b_1[\exp\left[b_2(1 - S_{\rm r})\right] - 1]\right\} = p_0^* \varphi(S_{\rm r}), \qquad [15.2]$$

where b_1 and b_2 are model parameters.

Isotropic hardening is ruled by the classical evolution law for p_0^*:

$$\dot{p}_0^* = \frac{(1+e)p_0^*}{\lambda - \kappa}\dot{\epsilon}_{\text{vol}}^p, \qquad [15.3]$$

where λ and κ are, respectively, the slope of the normal consolidation line and the slope of the unloading-reloading lines.

Rotational hardening may be governed by the difference between the current stress ratio $\eta = q/p'$ and the current inclination of the yield surface M_α, following the original proposal by Dafalias [DAF 86]:

$$\dot{M}_\alpha = c\left|\dot{\epsilon}_{\text{vol}}^p\right|(\eta - \xi M_\alpha)\,. \qquad [15.4]$$

The dimensionless parameter c governs the rate of evolution of M_α and ξ controls the target value of M_α for a given stress ratio.

A classical nonlinear isotropic elastic law of the type,

$$\begin{aligned}\dot{\epsilon}_{\text{vol}}^e &= \kappa\frac{\dot{p'}}{p'},\\ \dot{\epsilon}_{\text{d}}^e &= \frac{\dot{q}}{3G},\end{aligned} \qquad [15.5]$$

with constant shear modulus G, may be adopted as a convenient basic choice.

It is worth noting that, following this approach, the water retention model enters in the description of the mechanical behavior through the product $S_{\text{r}}s$.

The formulation allows for an intrinsic description of the evolution of the critical state shear strength with water content, based on the generalized effective stress definition [NUT 08].

Plastic volumetric strains develop when the stress state lies on the yield surface, which tends to shrink when a wetting process occurs, and to increase at the onset of drying. The dimensions of the elastic domain are expressed as a function of the degree of saturation. If hysteresis of the water retention domain is taken into consideration, uniqueness of the $\hat{p}_0 - S_{\text{r}}$ relationship leads to different curves $\hat{p}_0 - s$. This feature allows for simulating accumulation of plastic strain during drying–wetting cycles [DEL 09, ROM 08].

15.3.2. *Hydraulic model: the retention domain*

Different variables may be adopted to quantify the amount of water in soil. Among them, the more common are volumetric water content θ (volume of water over total volume of soil), degree of saturation S_{r} (volume of water over volume of voids), and gravimetric water content w (weight of water over weight of the solid particles). Nonetheless, none of these variables is able to fully normalize the role of void ratio on the water retention curve [ROM 10]. For compacted clays, experimental evidences (e.g. [DEL 96, ROM 99]) suggest the presence of two distinct water retention regions, intra-aggregate and inter-aggregate. The two retention regions show distinct evolutions along hydro-mechanical paths, as reported by Koliji *et al.* [KOL 06], Della Vecchia [DEL 09], and Romero *et al.* [ROM 10], among others. At low water contents, the influence of initial and current porosity is negligible, and the relationship between suction and the amount of water in the aggregates mainly depends on the mineralogical composition of the clay and on the water chemical composition. In the inter-aggregate region a storage mechanism, dependent on void ratio and void structure, dominates.

To model this behavior, a key point is the conceptual separation of the amount of water stored in the intra-aggregate void space from that exchanged in the inter-aggregate void space. A suitable choice is the definition of intra- and inter-aggregate water ratios, e_{wm} and e_{wM}, which provides an additive decomposition of the total amount of water.

In fact, a useful normalized variable to describe the evolution of water content is the water ratio, e_{w}, defined as the ratio between the volume of water in the pore space and the volume of solid particles:

$$e_{\mathrm{w}} = \frac{V_{\mathrm{w}}}{V_{\mathrm{s}}} = S_{\mathrm{r}} \cdot e = w \cdot G_{\mathrm{s}}. \qquad [15.6]$$

The subdivision between water in the intra-aggregate voids and water in the inter-aggregate voids gives:

$$e_{\mathrm{w}} = \frac{V_{\mathrm{w}}}{V_{\mathrm{s}}} = \frac{V_{\mathrm{wm}}}{V_{\mathrm{s}}} + \frac{V_{\mathrm{wM}}}{V_{\mathrm{s}}} = e_{\mathrm{wm}} + e_{\mathrm{wM}}, \qquad [15.7]$$

where V_{wm} is the volume of water in the micro-voids and V_{wM} is the volume of water in the macro-voids.

Micro- and macro-void retention mechanisms may be described separately, yet guaranteeing continuity of the whole retention model and of its first derivatives, as proposed by Della Vecchia [DEL 09]. To describe the intra-aggregate retention mechanism, a suitable function, independent of the void ratio, can be written as a function of a single independent parameter, b, describing the average slope of the curve for high values of suction:

$$e_{\mathrm{w}} = \frac{b e^*_{\mathrm{m}}}{\log\left(\dfrac{s_{\max}}{s^*_{\mathrm{m}}}\right)} \left[\frac{b + \log\left(\dfrac{s_{\max}}{s^*_{\mathrm{m}}}\right)}{b + \log\left(\dfrac{s}{s^*_{\mathrm{m}}}\right)} - 1 \right], \qquad [15.8]$$

where $s_{\max} = 1$ GPa is a reasonable physical limit for suction, corresponding to oven drying, and s^*_{m} is the suction corresponding to e^*_{wm}, which represents the smallest value of the water ratio for which micro-voids are saturated and macro-voids are completely dry. For water ratios exceeding e^*_{wm}, the intra-aggregate voids are assumed to be always saturated.

Dependence of the macroscopic part of the curve on void ratio may be achieved by adopting the proposal by Romero and Vaunat [ROM 00], and adding a suitable continuous dependence of the air entry value on the void ratio [KAW 00]. Scaling the macroscopic part of the water retention curve in the range $e \geq e_{\mathrm{w}} \geq e_{\mathrm{m}}$ gives

$$e_{\mathrm{w}} = e_{\mathrm{m}} + (e - e_{\mathrm{m}}) \left[1 - \frac{\log\left(1 + \dfrac{s}{s_{\mathrm{m}}}\right)}{2} \right] \left[\frac{1}{1 + (\alpha s)^n} \right]^m. \qquad [15.9]$$

The two parameters m and n are the only independent parameters of the model in the macro-porosity range. In fact, imposing that the two analytical expressions (equations [15.8] and [15.9]) have to be continuous, together with their first derivatives in $s = s_{\mathrm{m}}$, $e_{\mathrm{w}} = e_{\mathrm{wm}}$, gives a unique dependence of α on the set of independent parameters, and naturally leads to a reasonable dependence of the air entry value on the macroscopic void ratio.

To enhance the predictive capabilities of the water retention model, it is worth considering that the aggregates tend to swell and shrink with the current amount of available water, as a function of the activity of the clay fraction of the soil. Therefore, the intra-aggregate porosity e_{m} evolves with water

content, and its evolution should be considered in the water retention model. Experimental data of the evolution of the microstructure of compacted soils having different activities suggest that the evolution of e_{m} may be described by a bilinear reversible envelope, as a function of two independent parameters, e_{m}^{*} and β, the latter representing the swelling tendency of the aggregates.

The response inside the main retention domain was assumed by Della Vecchia [DEL 09] to be incrementally linear in terms of degree of saturation and suction:

$$\mathrm{d}S_{\mathrm{r}} = -k_s \, \mathrm{d}s, \qquad [15.10]$$

where k_s is a constant parameter.

It is reasonable to assume that, for compacted fine-grained soils, the parameters of the model depend on the activity of the clay fraction and on the grain size distribution. The parameters of the water retention model, used to perform the numerical simulations presented in the following section, were chosen by similarity with compacted soils of similar grain size distribution and similar activity. The main drying and the main wetting curves delimiting the water retention domain at the constant dry densities of $\rho_{\mathrm{D}} = 1.6$ Mg/m^3

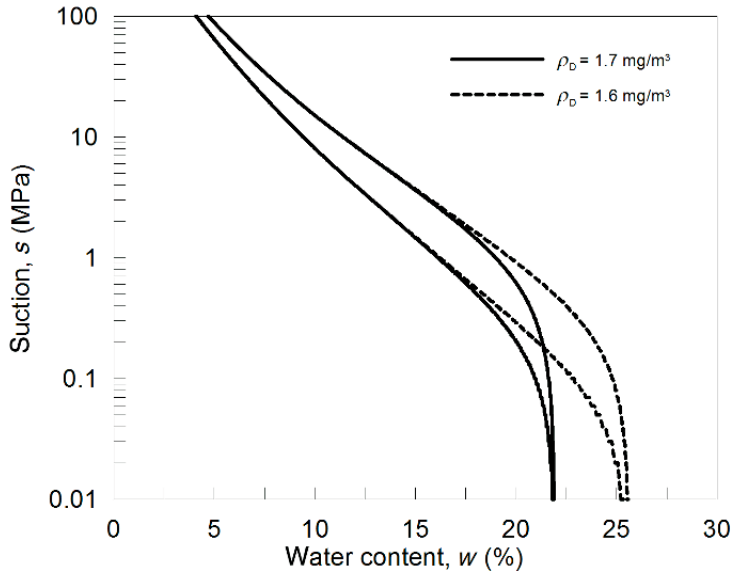

Figure 15.6. *Simulated water retention domains for different constant densities*

and $\rho_{\mathrm{D}} = 1.7$ Mg/m^3 are represented in Figure 15.6, on the plane suction–gravimetric water content, to be consistent with previous experimental data. The figure shows that the formulation adopted is able to account for the dependency of the current water retention domain on the void ratio, for increasing air entry value and for decreasing hysteresis with decreasing void ratio. For more details on the model formulation and calibration reference can be made to [DEL 09].

15.4. Simulation and interpretation of experimental data

The results presented in the following are intended to provide a qualitative unified interpretation of the data previously presented, through numerical simulation of typical laboratory or *in situ* stress paths. No effort was made to calibrate the mechanical and hydraulic parameters on the specific soils tested. The parameters were just chosen based on simulations previously run on soils of similar physical characteristics.

As dynamic compaction *in situ* on these soils tends to give an almost isotropic initial structure (see [JOM 02]), anisotropy was not considered for the sake of simplicity, and to limit to a minimum the number of parameters to be chosen. Therefore, the isotropic version of the model, which can be simply obtained by assuming M_α and the parameter c equal to zero, was used.

Two different initial water contents for each density were considered to simulate the observed experimental scatter under the as-compacted seasonal conditions, namely w = 16% and w = 18% for a dry density of $\rho_{\mathrm{D}} = 1.7$ Mg/m^3, and $w = 20\%$ and $w = 22\%$ for a dry density of $\rho_{\mathrm{D}} = 1.6$ Mg/m^3. Compaction was simulated by increasing the load at constant water content and atmospheric air pressure. The preconsolidation pressure after compaction was determined. The hydraulic state was assumed to lie on the main wetting curve at the end of compaction.

After compaction, one-dimensional loading was imposed to simulate the stress applied by the upper part of the construction. Three stress levels were considered, namely $\sigma_{\mathrm{v}} = 10$, 50, and 100 kPa, which correspond to the upper, middle, and lower parts of the embankment. Two series of numerical tests were then performed. In the first one, a wetting–drying–wetting cycle was simulated, to analyze volumetric strain and water content changes due to the interaction with the environment. The second test series simulated undrained

compression tests on samples collected after the end of the construction, and samples collected on-site after cyclic wetting–drying had occurred.

The simulated as-compacted states are reported in Figure 15.7, together with the reference experimental compaction curves. In the figure, the simulated dry densities and water contents after cyclic wetting–drying are also reported. The results of the simulations fall in the same range of the samples collected *in situ* 250 days after the end of the construction, confirming that water content increases and dry density tends to decrease due to cyclic wetting–drying cycles experienced at the stress levels investigated.

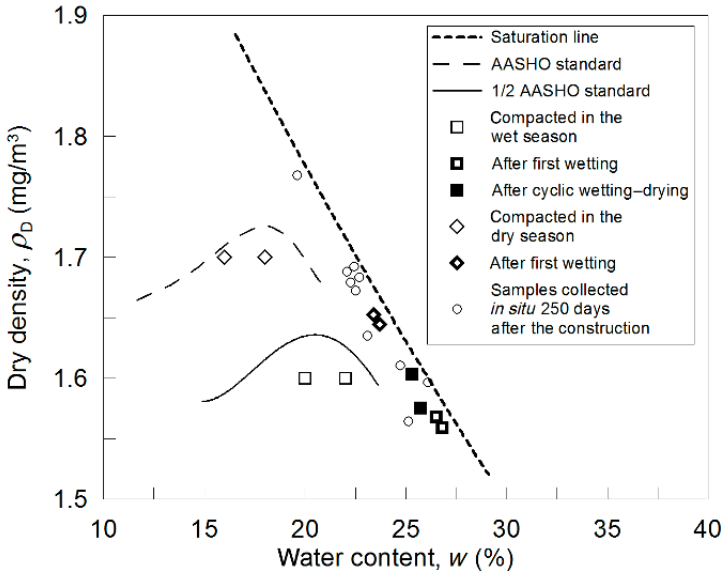

Figure 15.7. *Simulated as-compacted states and states after single and cyclic wetting stages*

Numerical results for void ratio variation and final water content at the end of a soaking test are reported in Figure 15.8. Results for soaking at the two stress levels bounding the range for possible stresses in the embankment are compared.

The simulations confirm that, for the typical stress levels of a levee, the soil tends to swell in the first wetting cycle. Swelling strain is more pronounced for samples compacted at low water contents. The applied stress influences the amount of swelling strain, especially for samples starting from higher water

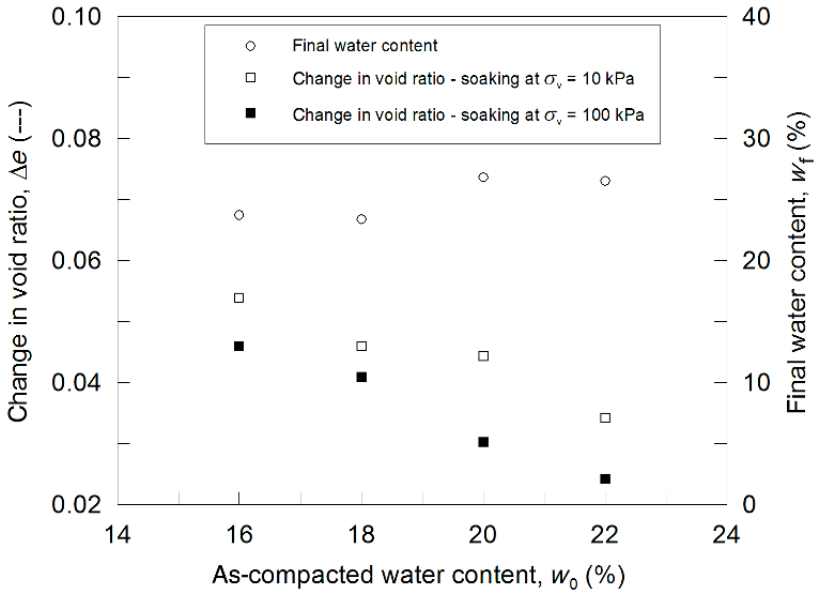

Figure 15.8. *Change in void ratio and final water content after simulated one-dimensional soaking*

contents. Compaction at water contents equal to or greater than the optimum value significantly reduces swelling upon wetting, which is a rather obvious observation, confirmed by a number of experimental data. The latter feature is invoked usually to suggest compaction at water contents higher than the optimum. The final water content after soaking is rather independent of the compaction water content, confirming the trend shown by experimental data (see Figure 15.4).

A deeper insight into the coupled volumetric mechanisms may be provided by analyzing the results of the numerical simulation of a wetting–drying–wetting cycle in detail. Results of the numerical simulations for the tests run imposing a net vertical stress of $\sigma_v = 10$ kPa are reported in Figures 15.9 and 15.10.

The results shown in Figure 15.9 well describe the time evolution of water content. Irreversible increment of water content is always to be expected as a result of the hysteretic retention mechanisms of compacted soils. Independently of the initial state of the compacted soil, the first wetting stage promotes an irreversible increase in water content. In the following drying and

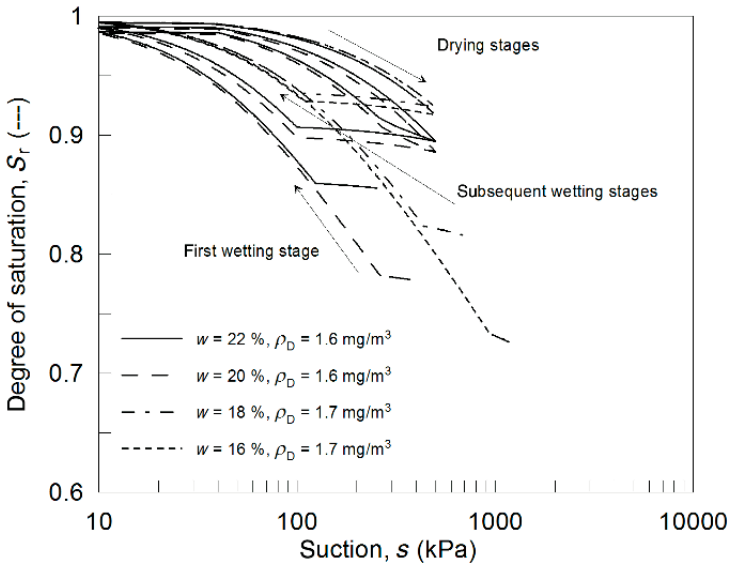

Figure 15.9. *Simulated degree of saturation in a wetting–drying–wetting cycle*

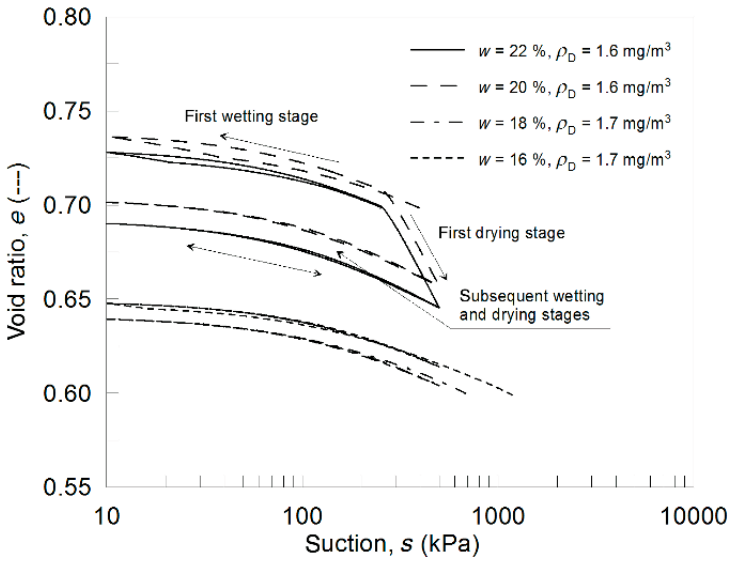

Figure 15.10. *Simulated void ratio variation in a wetting–drying–wetting cycle*

wetting paths, the water content cycles in a smaller range. With the retention model adopted (Figure 15.6), the degree of saturation would remain in the range between 90% and 98%

The results for void ratio, reported in Figure 15.10, highlight an important aspect of the mechanical behavior, which is seldom considered in the design of river embankments by rules of thumb. If the soil is compacted on the wet of optimum, it may undergo significant shrinkage upon first drying. As for swelling strains, the amount of shrinkage depends slightly on the applied stress, but it is mostly governed again by the retention properties of the soil. In fact, the main effect of suction for values below the air entry value of the soil is to act as an external load, hence inducing positive plastic volumetric strains. When compaction is performed at high water contents and low densities, the risk for shrinkage increases. It is worth noting that this is probably the most dangerous mechanism for the river embankments degradation. Therefore, countermeasures must be provided to reduce the risk of progressive damage associated with possible propagation of cracks, which are likely to open starting from the outer surface layers of the construction, directly exposed to the atmosphere.

Finally, the constitutive formulation was adopted to simulate triaxial undrained compression tests at constant water content (TXUU), with reference to the as-compacted conditions and after a soaking stage. The shear strength envelopes reported in Figure 15.11 replicate the trend shown by experimental data. Obviously, the lower the water content, the higher the mobilized shear strength. It is worth noting, anyway, that changes in the values of the intercept and of the slope of the envelopes are simply due to the constant water content constraint conditions. The model assumes, in fact, a constant friction angle describing the critical state in terms of the adopted generalized effective stress [NUT 08].

15.5. Final remarks

The few examples reported in the previous section demonstrate that unsaturated soil mechanics, at present, may help in the interpretation of the behavior of soils used to build river protection embankments, hence may be a valuable tool in the design an control of this kind of structure.

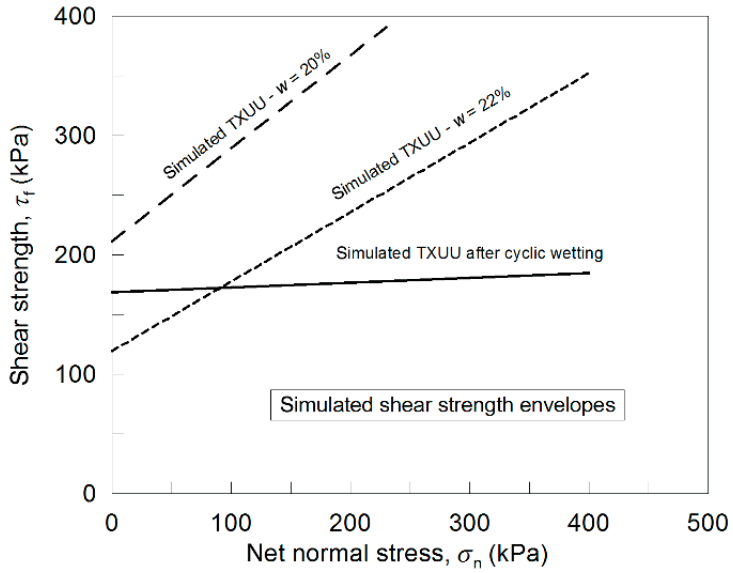

Figure 15.11. *Simulated shear strength envelopes from constant water content triaxial tests (TXUU) on as compacted samples and soaked samples*

The key ingredient for a correct interpretation of behavior of compacted soils is a reliable description of their water retention properties. It has to be remarked that water retention is also the fundamental property ruling hydraulic conductivity and seepage in the embankment. Therefore, it allows for a reliable analysis of the water fluxes promoted by the forcing boundary conditions. In this respect, it is worth mentioning that, still nowadays, reference to steady-state seepage conditions is frequently made in the analysis of the safety conditions of the embankments. This choice usually turns out to be overconservative, implying an overestimation of the dimensions of the embankment, hence of the amount of soil, needed to guarantee a sufficient factor of safety against the possible failure mechanisms, which may be activated during the working life of the structure.

Due to the lack of dedicated experimental tests, for unsaturated soil mechanics to be useful in the future, models as simple as possible should be proposed, depending on few parameters, which could be possibly calibrated by means of simple common laboratory tests. This is especially true with reference to developing countries, or where less experience has been accumulated in the past.

For the purpose of calibration, constant water content tests may be a valuable possibility, if a consistent back-analysis may be performed to evaluate the values for the fundamental mechanical and hydraulic parameters.

15.6. Bibliography

[COL 80] COLLESELLI F., MAZZUCATO A., TRIPICIANO L.M., "Compaction and behaviour of two fills along the Po river built of silty and clayey materials", *International Conference on Compaction*, vol. 2, Paris, p. 227-233, 1980.

[COL 99] COLLESELLI F., CORTELLAZZO G., JOMMI C., LAGIOIA R., "Control tests and measurements during and after the construction of fills in the Po river delta (in Italian)", *XX Italian National Congress of Geotechnics*, Parma, Italy, Pètron Editore, p. 435-443, September 22-25, 1999.

[DAF 86] DAFALIAS Y., "An anisotropic critical state soil plasticity model", *Mechanics Research Communications*, vol. 13, no. 6, p. 341-347, 1986.

[DEL 96] DELAGE P., AUDIGUIER M., CUI Y., HOWAT M., "Miscrostructure of a compacted silt", *Canadian Geotechnical Journal*, vol. 33, p. 150-158, 1996.

[DEL 09] DELLA VECCHIA G., Hydro-mechanical coupling in unsaturated clayey soils, PhD Thesis, Politecnico di Milano, 2009.

[GAL 03] GALLIPOLI D., GENS A., SHARMA R., VAUNAT J., "An elasto-plastic model for unsaturated soil incorporating the effects of suction and degree of saturation on mechanical behaviour", *Géotechnique*, vol. 53, no. 1, p. 123-135, 2003.

[JOM 94] JOMMI C., DI PRISCO C., "A simple theoretical approach to model the mechanical behaviour of unsaturated granular soils (in Italian)", *Il ruolo dei fluidi nei problemi di ingegneria geotecnica*, Mondovì, Italy, p. 167-188, 1994.

[JOM 00] JOMMI C., "Remarks on the constitutive modelling of unsaturated soils", *Experimental Evidence and Theoretical Approches in Unsaturated Soils: Proceeding of an International Workshop*, Trento, Italy, Balkelma, Rotterdam, 2000.

[JOM 02] JOMMI C., SCIOTTI A., "A study of the microstructure to assess the reliability of laboratory compacted soils as reference material for earth constructions", in BONTEMPI F., (ed), *System-Based Visions for Strategic and Creative Design – Proceedings of ISEC-02*, vol. 3, A.A. Balkema, p. 2409-2415, 2002.

[KAW 00] KAWAI K., KATO S., KARUBE D., "The model of water retention curve considering effects of void ratio", in RAHARDJO H., TOLL D.G., LEONG E.C., (eds), *Unsaturated Soils for Asia. Proceedings of the 1st Asian Conference on Unsaturated Soils*, A.A. Balkema, Rotterdam, p. 329-334, May 18-19, 2000.

[KOL 06] KOLIJI A., LALOUI L., CUSINIER O., VULLIET L., "Suction induced effects on the fabric of a structured soil", *Transport in Porous Media*, vol. 64, p. 261-278, 2006.

[NUT 08] NUTH M., LALOUI L., "Effective stress concept in unsaturated soils: clarfication and validation of a unified framework", *International Journal for Numerical and Analytical Methods in Geomechanics*, vol. 32, p. 771-801, 2008.

[ROM 99] ROMERO E., GENS A., LLORET A., "Water permeability, water retention and microstructure of unsaturated compacted Boom clay", *Engineering Geology*, vol. 54, p. 117-127, 1999.

[ROM 00] ROMERO E., VAUNAT J., "Retention curves of deformable clays", in TARANTINO A., MANCUSO C., (eds), *Experimental Evidence and Theoretical Approaches in Unsaturated Soils*, *Proceedings of the International Workshop on Unsaturated Soils*, Trento, Italy, AA. Balkema, Rotterdam, p. 91-106, April 10-12, 2000.

[ROM 08] ROMERO E., JOMMI C., "An insight into the role of hydraulic history on the volume changes of anisotropic clayey soils", *Water Resources Research*, vol. 44, p. 1-16, 2008.

[ROM 10] ROMERO E., DELLA VECCHIA G., JOMMI C., "An insight into the water retention properties of compacted clayey soils", Submitted to *Géotechnique*, 2010.

List of Authors

Ronaldo I. BORJA
Stanford University
Stanford
USA

Luc BOUTONNIER
Egis Géotechnique
Seyssins
France

René CHAMBON
Laboratoires 3S-R
Joseph Fourier University
Grenoble
France

Robert CHARLIER
University of Liège
Belgium

Frédéric COLLIN
FRS-FNRS
University of Liège
Belgium

Pierre DELAGE
Ecole des Ponts
ParisTech (UMR Navier/CERMES, CNRS 8502)
Paris-Est University
France

Gabriele DELLA VECCHIA
Politecnico di Torino
Turin
Italy

John EICHENBERGER
Soil mechanics laboratory
Swiss Federal Institute of Technology (EPFL)
Lausanne
Switzerland

Alessio FERRARI
Soil mechanics laboratory
Swiss Federal Institute of Technology (EPFL)
Lausanne
Switzerland

Bertrand FRANÇOIS
University of Liège
Institute of Mechanics and Civil Engineering
Belgium

Antonio GENS
Universitat Politècnica de Catalunya
Spain

Pierre GERARD
University of Liège
Belgium

Liang-Bo HU
University of Vermont
Burlington
USA

Tomasz HUECKEL
Duke University
Durham, North Carolina
USA

Cristina JOMMI
Politecnico di Milano
Milan
Italy

Lyesse LALOUI
Soil mechanics laboratory
Swiss Federal Institute of Technology (EPFL)
Lausanne
Switzerland

Mathieu NUTH
Soil mechanics laboratory
Swiss Federal Institute of Technology (EPFL)
Lausanne
Switzerland

Hervé PERON
Soil mechanics laboratory
Swiss Federal Institute of Technology (EPFL)
Lausanne
Switzerland

Jean-Pol RADU
University of Liège
Belgium

Dilan ROBERT
University of Cambridge
UK

Simon SALAGER
Soil mechanics laboratory
Swiss Federal Institute of Technology (EPFL)
Lausanne
Switzerland

Antony P.S. SELVADURAI
McGill University
Montreal
Canada

Yannick SIEFFERT
Joseph Fourier University
Grenoble
France

Kenichi SOGA
University of Cambridge
UK

Alessandro TARANTINO
University of Strathclyde
Glasgow
UK

Joshua A. WHITE
Lawrence Livermore National Laboratory
California
USA

Index